Christobel T Gondwe

Department of Mechanical Engineering

Supervisors

Dr. Xinshan Li

Dr. PN Watton

Dr. C Mazzá

A Novel Framework to Model the Short and Medium Term Mechanical Response of the Medial Gastrocnemius

A thesis submitted in partial fulfilment of the degree of Doctor of Philosophy in Biomechanical Engineering

August 2018

Abstract

Musculoskeletal disorders (MSDs) are the second largest cause of disability worldwide and cost the UK National Health Service (NHS) over £4.7 billion yearly. One holistic approach to alleviate this burden is to create *in silico* models that provide insight into MSDs which will improve diagnostic and therapeutic procedures.

This thesis presents a modelling framework that analyses the mechanical behaviour of anatomical skeletal muscles. The anatomical geometry and fibre paths of the medial gastrocnemius muscle were acquired from the Living Human Data Library (LHDL). The medial gastrocnemius model was further sophisticated by incorporating morphological representations of the aponeurosis and myotendon transition region. Having carried out a finite element analysis on the medial gastrocnemius, it was found that the morphology and size of the transition region significantly affected the mechanical response of the muscle. Three illustrative simulations were subsequently carried out on the model, to better understand the muscle's mechanical response in differing mechanical environments: (1) the effects of high extensions on the muscle's mechanical response, (2) lengthening of the aponeurosis - a phenomenon often observed following aponeurosis regression - and (3) the stress-strain regime of the muscle when the tendon experiences a laceration and heals over 21 days. These models show the regions that experienced the highest strains were the muscle-tendon transition regions.

As MSDs tend to be of a degenerative nature and progress over time, the temporal changes of the mechanical response of skeletal muscle tissue is of great interest. In the penultimate chapter, the medial gastrocnemius was assessed across various remodelling regimes. It was found that the muscle returned to homeostasis only when both the muscle and tendon remodelled – albeit, at different remodelling rates. Whilst this observation seems intuitive, most other growth and remodelling models of skeletal muscles have only remodelled either the muscle or tendon constituent. The model developed in this thesis therefore has the potential to inform multi-scale musculo-skeletal muscle models thus providing a significant contribution to understanding MSDs.

Acknowledgements

'The function of education is to teach one to think intensively and to think critically. Intelligence plus character – that is the goal of true education'

***Dr. Martin Luther King Jr, Civil Rights Activist (*1929 – 1968)**

I am deeply indebted to the many people that have been a part of my doctoral journey. I would like to thank the research team at Insigneo and ThemBio – specifically, Shaktidhar Dandapani for being a great friend and providing technical assistance throughout the work of this thesis.

I greatly appreciate the constructive criticism received from my supervisors Dr. Paul Watton, Dr. Xinshan Li and my doctoral development supervisor Dr. Claudia Mazza. I am humbled by the patience, support, and guidance Dr. Li provided and the guidance, mentorship and support Dr. Watton offered me. It was often their understanding, time and empathy that kept me persevering. In retrospect, I can see it has been both the triumphs and hard times endured that have made this journey what it has been.

I would like to thank my dearest partner Kevin for enduring my stress-ridden storms yet still finding a way to make me laugh through them – he has been my rock and support. Lady Francine, my cat and my spirit animal, maintained my sense of sanity and gave me motivation to keep going each time she purred and fell asleep in my arms. Her calmness brought me peace and mindfulness.

Finally, I would like to acknowledge the sacrifice, support and love from my family, in particular, Flora Gondwe. She is an amazing mother and best friend who has supported and provided for me unconditionally and selflessly.

My father is the primary driving force that ignited my ambitions to pursue a doctorate, and to him I dedicate this thesis; for loving me and believing that I was 'clever' and capable, even from my earliest days.

'Reach for the stars, and you will reach the tree tops, but reach for the heavens and you will reach the stars… There will always be drawbacks in life - so let it be your dreams that carry you to your destiny.'

Christopher José Gondwe, Civil Engineer and Loving Father (1947 – 2003)

Statement of Originality

I hereby declare that this submission is my own work and to the best of my knowledge it contains no materials previously published or written by another person, or substantial proportions of materials which have been accepted for the award of any other degree or diploma at the University of Sheffield or any other educational institution, except where due acknowledgement is made in the thesis. Any contribution made to the research by others, with whom I have worked at the University of Sheffield or elsewhere, is explicitly acknowledged in the thesis.
I also declare that the intellectual content of this thesis is the product of my own work, except to the extent that assistance from others in the project's design and conception or in style, presentation and linguistic expression is acknowledged.

……

CHRISTOBEL T GONDWE 31st of August 2018

List of Figures

List of Notations

F	Operational Force/Tension Produced by the muscle
$PCSA$	Physiological Cross-Sectional Area
m	Muscle mass
θ	Mean pennation angle of the fibre, in relation to the loading direction
l	Muscle length
ρ	Muscle density
V	Velocity of contraction
b	Fitted material parameter from experimental data for Hills muscle model
F_0	Maximum isometric tension generated in the muscle
a	Fitted material parameter from experimental data for Hills muscle model
F_T	Total force produced of Muscle
F_{SE}	Force contribution of the series element
F_{PE}	Force contribution of the parallel element
F_{CE}	Force contribution of the contractile element
$f_t(t)$	Function of time that contributes to the force produced in the contractile element of Hills muscle model
$f_v(v)$	Velocity of contraction that contributes to the force produced in the contractile element of Hills muscle model
$f_\lambda(l)$	Force-length relationship that contributes to the force produced in the contractile element of Hills muscle model
L_{PE}	Length of the parallel element in hills muscle model
L_{CE}	Length of the contractile element in hills muscle model
L_{SE}	Length of the series element in hills muscle model
$\boldsymbol{\sigma}$	Cauchy Stress

σ_{matrix}	Matrix contribution of the Cauchy Stress
σ_{fiber}	Fibre contribution of the Cauchy Stress
$\sigma_{incompressibility}$	Volumetric contribution of the Cauchy Stress
F_1	Force contribution of the base matrix material
F_2	Force contribution of the collagenous fibre family
F_3	Force contribution of the interactions between fibres and base matrix
S_T	Total Second Piola-Kirchhoff stress of muscle
$S_{Passive}$	Passive contribution of Second Piola-Kirchhoff stress of muscle
S_{Active}	Active contribution of Second Piola-Kirchhoff stress of muscle
ψ_{NH}	Neo-hookean strain energy density function
ψ_{MR}	Mooney Rivlin strain energy density function
C_1	Neohookean Material constant
C_2	Mooney Rivlin Material constant
$I_i, i \in 1-9$	Invariants 1 to 9 of the right Cauchy-Green Deformation tensor
$\mathbf{F}$	Total deformation gradient or Jacobian Matrix
$\mathbf{F}_e$	Elastic deformation gradient
$\mathbf{F}_g$	Growth Tensor
$\mathbf{X}$	Position vector of a point on a material in the initial reference position. (‘Spatial’ or ‘Eulerian’ co-ordinates)
X_I	The components of the position vector in the reference configuration (‘spatial’ or ‘Eulerian’ co-ordinates)
$\mathbf{E}^{\mathbf{I}}$	The unit base vectors of a rectangular Cartesian coordinate system in the reference position. (‘spatial’ or ‘Eulerian’ co-ordinates)
$\mathbf{x}$	The components of the position vector in the current configuration (‘Lagrangian’ co-ordinates)
x_I	The components of the position vector in the current configuration (‘Lagrangian’ co-ordinates)

$\mathbf{e}^{\mathbf{I}}$	The unit base vectors of a rectangular Cartesian coordinate system in the current position. ('Lagrangian' co-ordinates)
$\varphi(\mathbf{X},t)$	a matrix which defines the deformation of the body through a Lagrangian co-ordinate system
$u(\mathbf{X},t)$	A matrix which defines the deformation of the body through a Eulerian co-ordinate system (reference configuration)
φ	Mapping function
t	time
J	Jacobian = det[**F**]
$\mathbf{F}_{vol}$	Volumetric or isochoric change of the deformation gradient
$\mathbf{F}_{dev}$	Deviatoric or distortional shape change of the deformation gradient
$\mathbf{E}$	Green strain tensor
$\mathbf{I}$	Second order unit tensor
δ_{ij}	Kronecker delta where: $\delta_{ij} = 1 \; if \; i = j$; and $\delta_{ij} = 0 \; if \; i \neq j$
$\mathbf{C}$	The right Cauchy – Green Deformation tensor
$\mathbf{B}$	The left Cauchy – Green deformation tensor
$\overline{\mathbf{C}}$	Volumetric – eliminated version of the right Cauchy- Green deformation tensor
$\overline{\mathbf{B}}$	Volumetric – eliminated version of the left Cauchy- Green deformation tensor
W	D'Alembert's virtual work of a rigid body
∂u	Field of virtual displacements
b	Body force per unit mass
Tr	Surface traction vector
Vol	Volume of a rigid body
$\mathbf{P}$	First Piola-Kirchhoff Stress
D_1	Incompressibility parameter
ρ_h	Hydrostatic pressure
W_{SEF}	Strain Energy Density function with respect to the right Cauchy - Green deformation tensor
λ_f	The fibre stretch ratio in the direction of the undeformed fibre

n	Unit vector of the representative fibre family in the current configuration
$\mathbf{N}$	Unit vector of the representative fibre family in the reference undeformed configuration
$\mathbf{m}$	Unit vector of the first fibre family in the current configuration
$\mathbf{n}$	Unit vector of the second fibre family in the current configuration
$\lambda_1, \lambda_2, \lambda_3$	Principle stretches of the deformation gradient $\mathbf{F}$
$W_i, i \in 1-5$	The derived term of strain energy density function, with respect to its corresponding Invariant
W_{vol}	The volumetric or isochoric change of the deformation gradient
W_{Dev}	Deviatoric or distortional shape change contribution of the strain energy density function
$k_1 t$	First (tendon) material parameter for the anisotropic or fibre contribution, for the first family of fibres
$k_1 m$	First (muscle) material parameter for the anisotropic or fibre contribution, for the second family of fibres
$k_2 t$	Second (tendon) material parameter for the anisotropic or fibre contribution, for the first family of fibres
$k_2 m$	Second (muscle) material parameter for the anisotropic or fibre contribution, for the second family of fibres
λ	The referential stretch used to unify the principal stretches when incompressibility is enforced
c_i	First Isotropic material constant used in ANSYS
d_i	Second Isotropic material constant used in ANSYS
g_1	First anisotropic material constant used in ANSYS for the first family of fibres
g_2	Second anisotropic material constant used in ANSYS for the first family of fibres
E_1	first anisotropic material constant used in ANSYS for the first family of fibres

E_2	Second anisotropic material constant used in ANSYS for the second family of fibres
$\bar{\chi}_i$	The new node location of node number *i*
N	The number of neighbouring vertices to node number *i*.
x_j	The j-th neighbouring vertex
$\boldsymbol{u}(\boldsymbol{x})$	Unknown vector field to be interpolated
$\mathbf{D}$	Field space being explored with known points
w_i	Known vector direction on the spline (provided data)
$d(x)$	The given distance from each point with an unknown vector to the known vector w_i
$f_T(x)$	Volume fraction of tendon
$f_M(x)$	Volume fraction of muscle
$\bar{\psi}_{\text{Medial Gastrocnemius}}$	Total Strain Energy Density function of the Medial gastrocnemius complex
$\bar{\psi}_T$	Strain Energy Density function of the tendinous constituent
$\bar{\psi}_M$	Strain Energy Density function of the Muscular constituent
c_1^T	Isotropic Material constant of the tendinous constituent
c_1^M	Isotropic Material constant of the muscular constituent
k_1^T	First anisotropic material constant of the tendinous constituent
k_1^M	First anisotropic material constant of the muscular constituent
k_2^T	Second anisotropic material constant of the tendinous constituent
k_2^M	Second anisotropic material constant of the muscular constituent
x_{0-5}	The known x-coordinates that determine the different constituent boundaries in linear dependence
χ_C	The x-coordinate of the centroid along the long axis of the muscle
$\bar{y}_0$	The central averaged y coordinate across a selected plane
η_C	The number of centroids specifically situated on a selected plane
$\bar{z}_0$	The central averaged z coordinate across a selected plane

x_i^C	The x-coordinates along the central line
r	The perpendicular distance of a centroid point to the central line
$f_{AB}^{-1}(x_i^C, r_0)$	The volume fraction of the origin transition zone defined in triangle ABC
$f_{DE}^{-1}(x_i^C, r_0)$	The volume fraction of the insertion transition zone defined in triangle DEF
r_b	Radial Boundary
κ	The structural parameter that represents the symmetry of fibre dispersion
σ_{aniso}	Anisotropic stress contribution
σ_h	Homeostatic range of Cauchy stresses
$\sigma_{h(\min)}$	Minimum bound of homeostatic range of Cauchy stresses
$\sigma_{h(\max)}$	Maximum bound of homeostatic range of Cauchy Stresses
$\sigma_{aniso,h(\min)}$	Anisotropic contribution of minimum bound of homeostatic range of Cauchy stresses
$\sigma_{aniso,h(\max)}$	Anisotropic contribution of maximum bound of homeostatic range of Cauchy Stresses
$\tilde{k}_1^{T,M}$	Modified first anisotropic material constant for Tendon or Muscle, respectively
$\tilde{k}_2$	Modified second anisotropic material constant for tendinous constituents
$\tilde{y}$	Modified second anisotropic material constant for muscular constituents
β^T	Remodelling parameter for tendinous constituent
β^M	Remodelling parameter for muscular constituent

Contents

Chapter 1

Thesis Objectives, Aims and Overview

This chapter briefly covers the motivation and rationale outlined behind this thesis. The primary aim is stated, followed by the objectives, which will set the context of the current work.

1.1 Motivation and Introduction

Musculoskeletal disorders (MSDs) are the second largest cause of disability worldwide. Though convention usually associates MSDs with the ageing population, the disease could also manifest early on in life. At least 1 in 3 people of the world's population will live with a debilitating MSD (WHO, February 2018). This results in sickness, loss of working hours – hence impacting global economy. MSDs in 2013-14 were the third largest area of spending for the National Health Service UK's (NHS) budget as £4.7 billion was spent on directly remedying MSDs, with a further £103-£129 billion spent on issues related to MSDs (Public Health England, 2018). The direct costs to remedy MSDs by the NHS in the UK is expected to increase to £118 Billion over the next decade (York Health Economics, 2017). As such, MSDs are an increasingly demanding problem that needs to be addressed.

Research into MSDs provides an economic benefit, as innovative studies can provide insights that will improve healthcare outcomes, and gradually reduce the cost of MSD strain on global economics. This benefit has been monetised, as it is believed that every £1 invested in MSD research, will deliver a return of around £0.25 every year, forever (Wellcome Trust, 2017).

Skeletal muscle is a major component of movement and support in the human body, and therefore plays a central role in various daily physiological and mobility functions. Therefore, if the mechanisms of healthy skeletal muscle as a mechanical entity can be better understood and simulated, then further insight into the pathophysiology of skeletal muscle can be explored.

The mechanical phenomena of skeletal muscles are predominantly governed by their macro architecture (Lieber & Bodine-Fowler, 1992; Burkholder et al., 1994; Blemker, 2005). Thus, the main area of interest in this thesis is to investigate the mechanical response of skeletal muscles to their mechanical environment by means of an anatomical finite element (FE) model.

Finite element modelling is a computational technique that uses numerical iterative processes to solve problems of engineering and mathematical physics. This method is effective in solving partial differential problems, where differences occur over a spatial (dx) and temporal (dt) scale. As such, finite element modelling discretises the special portion of the problem into small regions called elements, and then provides

an approximated result of the assembly of these regions (mesh). This enables the computation and solution of mechanical problems over a specified temporal domain (Craig, 2002).

Finite element models and skeletal muscle modelling is an emerging field, with only a handful of centres around the world working in this area – in stark contrast to cardiac muscle (Humphrey & Yin, 1989; Ambrosi et al., 2011; Humphrey, 2013) or smooth muscle mechanics (Watton et al., 2004; Watton et al., 2009; Bevan et al., 2018), which has seen advanced development in the past decades. This project proposes to make a significant contribution to the current body of knowledge on skeletal muscle computational modelling by incorporating standard continuum finite element methods to skeletal muscle mechanics, with a high focus on constitutive (muscle and tendon tissue) relationships and representation of the architecture and morphology of the skeletal muscle, which will intrinsically provide insight to MSDs and alleviate its global burden.

1.2 Objectives and Aims

The primary goal of this thesis is to develop an anatomically-based finite element model that will simulate and explore the mechanical (stress and strain) response of passive skeletal muscles. This will provide quantitative values on the mechanical behaviour of skeletal muscles (stresses and strains) under stress. This information will help enhance our understanding of how skeletal muscle tissue works and elucidate its function in diseased state in the future.

Secondary objectives include:

I. Elucidating, analysing and investigating the functional role of the aponeurosis using various methods to represent the muscle-tendon junction, aponeurosis morphology and constituent distribution;

II. Explore the effects that the mechanical environment of a muscle has on its mechanical response - by considering remodelling of the muscle-tendon complex in response to an illustrative application - bone lengthening.

These aims have been deduced upon a review of the literature. The methods, results and processes used to achieve these aims have been demonstrated throughout the thesis. Henceforth, the chapters that form this thesis are outlined below.

1.3 Chapter Outline

Chapter 1 describes the thesis outline, and the translational motivation of the work carried out in the thesis.

Chapter 2 describes the anatomy of the Medial gastrocnemius muscle and physiology of skeletal muscle tissues. The hierarchical structure of skeletal muscle tissue is discussed, and an overview of the active and passive behaviour of skeletal muscle mechanics are outlined, to elucidate the possible processes that lead to the passive response of skeletal muscle. These processes will be considered with respect to the muscle's mechanical environment, which therefore induces the motivation of the studies in this thesis.

Chapter 3 provides a literature review of the state-of-the-art on skeletal muscle modelling, models of the muscle-tendon complex and growth and remodelling of skeletal muscle. Comparisons are made between various types of one-dimensional and three-dimensional models, with insight on the physiological mechanisms that occur during under- and overstretch of skeletal muscle tissue. The contributions to knowledge concerning finite element modelling of the medial gastrocnemius, with respect to its remodelling regimes, are also outlined.

Chapter 4 offers an overview of the finite element and mathematical methods that were used in this thesis to simulate the mechanical response of the medial gastrocnemius, with a brief background of the theory of finite deformation hyperelasticy and continuum mechanics. The constitutive relationships of the full muscle-tendon are described in this chapter, with exploration of the estimation of the material parameters used for the isotropic and non-linear anisotropic relationship of muscle and tendon tissue. The numerical process and finite element set-up carried out

in ANSYS, APDL Inc. are verified in this chapter, against benchmark analytical solutions.

Chapter 5 Illustrates the approach taken to process the anatomical features of the medial gastrocnemius from input data (of a cadaveric specimen). This chapter covers the challenges experienced trying to mesh the acquired geometry, as well as the smoothing process of the geometry surface, and goes on to propose the application of an inverse distance interpolation technique to map anatomically palpated muscle fibre paths into a three-dimensional finite element workflow. An illustrative simulation is performed, and a convergence analysis of the mesh is carried out to determine the optimal element size against computational expense.

Chapter 6 Proposes a novel approach to represent the aponeurosis and muscle-tendon morphology and constituent distribution. This is done by means of several methods (a linear distance-dependence method, a cone radial-dependence method, and an ellipsoid-dependence method). These methods are compared to each other, and to a conventional arbitrary muscle to tendon junction. The simulations carried out show favourable results towards the cone and ellipsoid dependant morphology. Illustrative simulations are carried out to assess the effects of high displacements on the medial gastrocnemius, the effects on the stress-strain distribution of the medial gastrocnemius of longer muscle-tendon junctions – often observed following aponeurosis regression or tendon lengthening surgery. The results show that the way the morphology and material properties of the aponeurosis and muscle-tendon junction are defined in a simulation are imperative to obtaining an accurate stress-strain distribution. This is an important contribution to current finite element simulations of skeletal muscles, since other state-of-the-art models simulate the tendon as a disproportionately stiff tissue (Zellner et al., 2012; Zöllner et al., 2015), or do not consider the morphology or constituent distribution of the aponeurosis and muscle-tendon junction (Böl, et al., 2011; Röhrle & Pullan, 2007; Valentin et al., 2018).

Chapter 7 investigates a simplistic remodelling regime of skeletal muscle, with an ellipsoid shaped muscle-tendon junction. In particular, the remodelling regimes illustrate the changes of the stress-strain relationship during overstretch in leg lengthening. As the muscle remodels and it is hypothesised that the stresses

experienced by the fibres will drive the onset of remodelling to get the fibre stresses back to their homeostatic values. The remodelled muscles show the stress difference from the homeostatic stretch, such that when the muscle has fully remodelled, the stress difference returns to 0, and the evolution of a material parameter (k_2) across the anatomical geometry of the medial gastrocnemius.

Chapter 8 Summarises the findings of this thesis by addressing the main modelling outcomes, limitations and recommendations regarding future work on finite element skeletal muscle modelling.

1.4 Thesis Contributions

1 Fibre paths of a cadaveric specimen used in the Living Human Digital project have been applied using an inverse distance method to determine anatomically detailed vector directions for a finite element work-flow. These vectors have been provided for each element (centroid point) of a 24-year-old female cadaveric medial gastrocnemius, as described in Chapter 5.

2 In Chapter 6, A novel approach to represent the aponeurosis morphology is proposed. The aponeurosis and features of its morphology are applied to a three-dimensional mathematically-based model and used in a finite element model of the medial gastrocnemius muscle-tendon complex. This was done by means of idealised shapes - as an ellipsoid, cone, linear distribution and sharp transition morphology. The various shapes show that the morphology of the aponeurosis and muscle-tendon region has a qualitatively significant effect on its strain-stress response.

3 The muscle-tendon constituents have been defined by means of a volume fraction distribution that are dependent on the morphology and distance of each constituent point from muscle or tendon. As such, the muscle-tendon material properties are defined by incorporating this volume fraction to the Holzapfel et al., (2000) fibre-reinforced soft tissue model, also shown in Chapter 6.

4 The remodelling profile of the passive medial gastrocnemius shows a stiffer muscle, during overstretch (leg lengthening) mechanical environments, hence changing the muscles' peak stress-strain profile, detailed in Chapter 7.

1.5 Dissemination – Conference Presentations and Posters

- Gondwe, C., Patterson, J., Xi, L., Watton P.N. (June 2018), 'A Subject-Specific Approach to Modelling the Remodelling of Skeletal Muscles.' Multi-scale Hard and Soft Tissue Modelling Workshop, Sheffield, UK.

- Gondwe, C., Watton, P.N., Li, X. (May 2017). 'A Subject-Specific Approach to Modelling the Interaction between Form, Function and the Environmental Mechanical Envelope of Skeletal Muscles.' Insigneo Showcase 2017, Sheffield UK.

- Gondwe, C., Watton, P.N., Li, X. (June 2016). 'Skeletal Muscle Mechanics: Modelling the Interaction between the Microstructure and the Environmental Mechanical Envelope'. European Congress on Computational Methods in Applied Sciences and Engineering Conference 2016. Crete, Greece.

- Gondwe, C., Watton, P.N., Li, X. (June 2016) 'Skeletal Muscle Mechanobiology: Modelling the interaction between the muscle's microstructure and its environmental mechanical envelope', Graz University of Technology, Austria, July 4th-8th, 2016.

- Gondwe, C., Lu, Y.T., Mazzà, C., Li, X., Viceconti, M. (July 2015). 'A Numerical Model of Passive Skeletal Muscle Mechanics with Considerations to Fibre Orientations – a Finite Element Study.' 21st Congress of The European Biomechanics Society Conference 2015, Czech Republic conference.

- Gondwe, C., Lu, Y.T., Mazzà, C., Li, X. (June 2015) 'Finite Element modelling of Skeletal Muscles', The 2nd Workshop on Soft Tissue Modelling, Glasgow poster presentation and abstract, Plenary Speakers; RW Ogden, C. Berry, J. Humphrey, G. Holzapfel, A. Menzel, M. Ben Amar, D. Ambrosi. *Student Registration Grant Awarded.*

- Gondwe, C., Lu, Y.T., Mazzà, C., Li, X. (2014) 'The Effect of Fibre Orientation on the mechanical behaviour of Skeletal Muscle – a finite element study', World Academy of Science, Engineering and Technology, International Science Index, Biotechnology and Bioengineering, 2(3), 598.

Chapter 2

Background Anatomy and Physiology

This chapter covers the background anatomy and physiological function of muscle, encompassing both muscle's passive mechanical response as well as the interaction between its active and passive mechanics. The chapter concludes by outlining the complex geometrical morphology of the medial gastrocnemius muscle, which is the main muscle of interest in this study.

2.1 Muscle Anatomy and Physiology

Muscle was first conceptualised as being a mound of mass that increases in breadth and shortens in length as it contracts. This idea was derived from Erasistratus' and Aristotle's idea of locomotion being like puppetry, or neurons and tendons being hollow tubes that premia can occupy (McMahon, (1984)). McMahon acknowledges muscle to have a constant volume as it contracts, which was explicated by his work on the frog leg model. This supports the idea of isometric contraction, where the muscle does not change in length as it contracts. Muscle is now conventionally known to be a hierarchical collection of striated fibres that act in synchronous coordination with electrical signals from the brain. Muscle contraction is primarily elicited through electrical stimulation from nerves, where specific input parameters influence the strength and time course of the contraction (Kesar et al., 2009).

Muscle models can be studied under two main categories; intrinsic biophysical deterministic models (Hodgkin & Huxley, 1952; Huxley, 1957), and phenomenological models (Hill, 1938) (Winters & Stark, 1987). Whilst phenomenological models predict the muscle's response to specific external stimuli by means of experimental measurements, biophysical models (such as structural and functional three-dimensional finite element models of skeletal muscles) attempt to predict the muscle's response by trying to idealise and represent the underlying physiology of the system and describe the behaviour of a system based on empirical observations. The scope of this thesis explores the mechanical behaviour of muscle and looks at using engineering techniques to analyse phenomenological models to assess mechanical muscle function. The first step to this exploration was done by gaining an understanding of the anatomical architecture of skeletal muscle tissues.

2.1.1 Anatomical Architecture

Skeletal muscle is made up of thin actin molecules and thick myosin molecules. Myosin is an ATP dependent motor protein, that works with the actin motor proteins to enable muscle contraction. The myosin consists of the head domain, and the actin consists of the filamentous domain that eventually slide over each other through the process of ATP hydrolysis, hence causing the myosin heads to slide over the actin tails during a power stroke – conventionally known as muscle contraction (Pollard & Korn,

1973). The interaction of the actin (thin) and myosin (thick) filaments govern muscle contraction and primarily establish the sarcomere complex, which is a collection of myofibrils that constitute the muscle fibre cell. These muscle fibre cells are the singular components contained in the fascicle, which together make up the muscle (Lieber, 2002). The skeletal muscle is connected to the rest of the bony skeletal system by tendons and co-ordinates with somatic nerve system stimuli. This hierarchical muscle structure is shown in detail in Figure 2.1 and Figure 2.2.

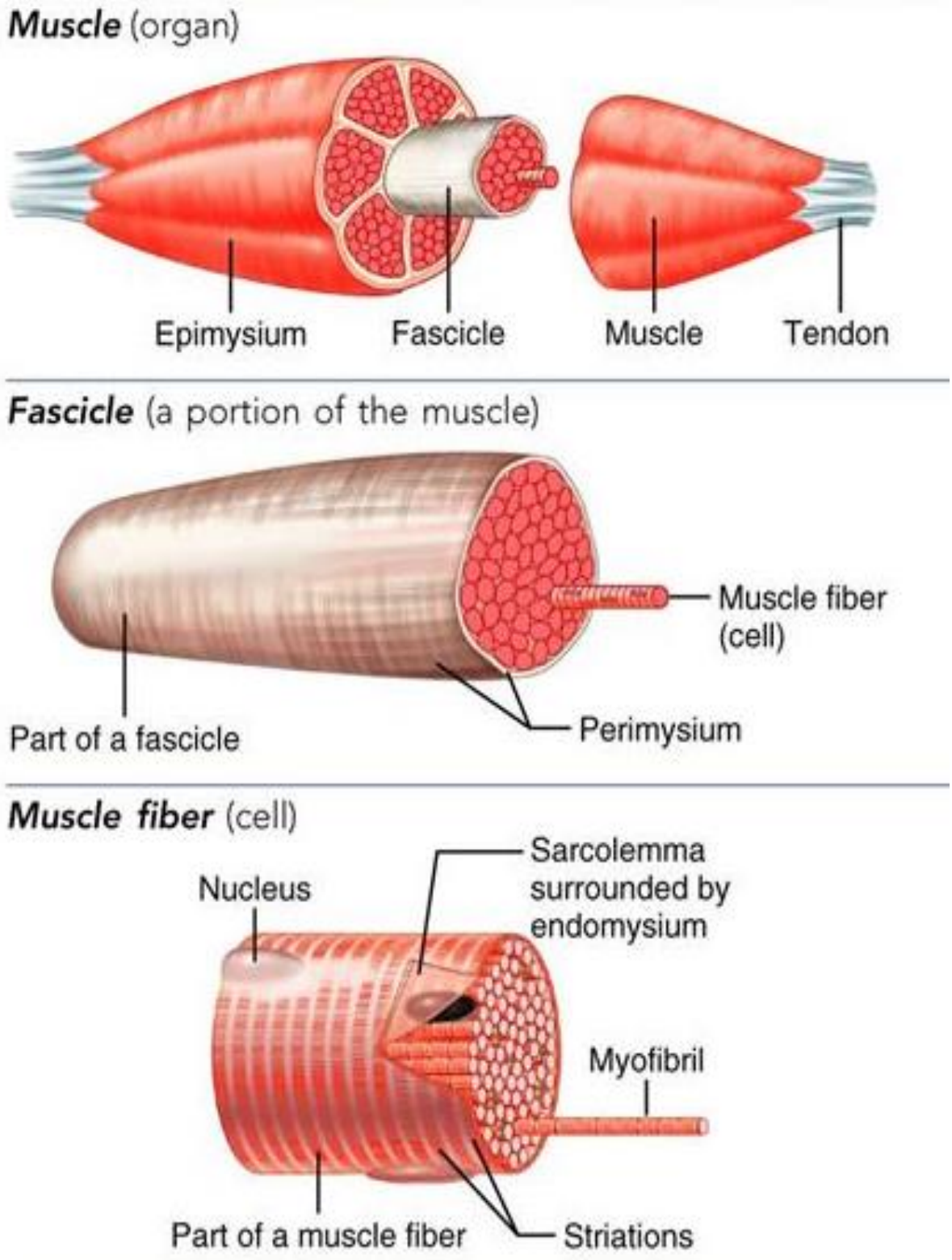

Figure 2.1: Higher muscle organ to muscle fibre cell anatomical structure. Image adapted from: Myofibril complex physiology of a skeletal muscle fibre: PP 288-294. (2014)

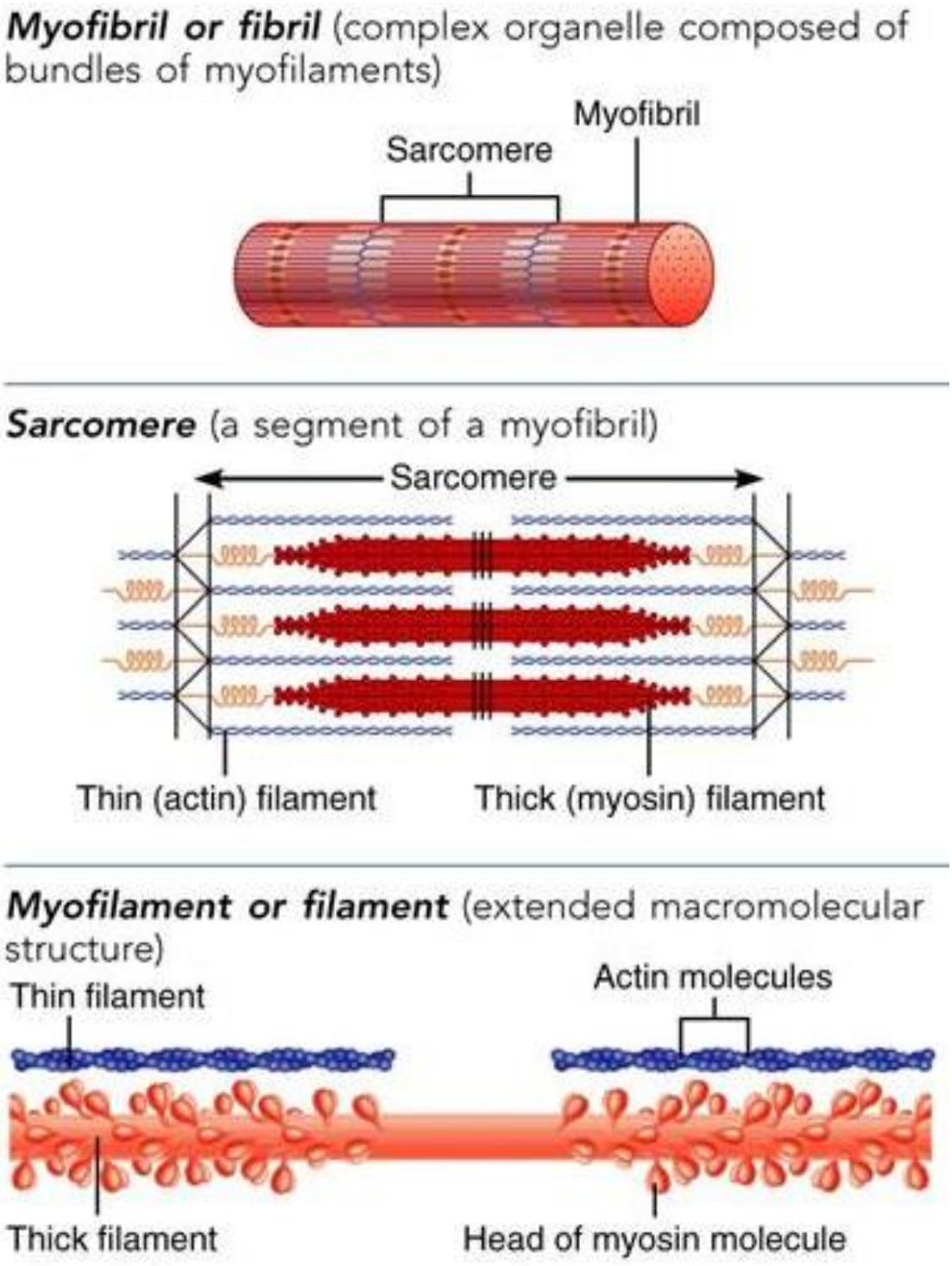

Figure 2.2: Lower skeletal muscle macro structure muscle fibril to myofilament anatomical structure. Image adapted from: Myofibril complex physiology of a skeletal muscle fibre: PP 288-294. (2014)

From the above illustrations we can deduce that muscle tends to be a collaborated collection of tissue structures that allow for neural interaction and stimulation. This stimulation occurs at the neuro-muscular junction therefore allowing for the excitation of the 'motor unit'. As muscle is generally orientated with its antagonistic counterpart, skeletal muscle is known to only actively 'contract' rather than extend; unless passively through its antagonistic partner.

The muscle contracts through a phenomenon called excitation-contraction coupling. The first stage of this cascade of events occurs from the arrival of an action potential from motor neurons and dendrite ends. This stimulates the detachment of a myosin head to actin fibril, which therefore allows for the myosin to bind to a new actin molecule forming a new cross-bridge (Widmaier, et al., 2010). Once the new cross-bridge is formed, the Adenosine Triphosphate (ATP) is hydrolysed by myosin, the process of which releases energy to allow for a partial bond with the actin. The hydrolysed myosin head contains Adenosine Diphosphate (ADP), an extra phosphate group and two Ca^{+2} ions. The remainder of the acting binding sight is blocked by tropomyosin, which leaves the troponin C to bind to the Ca^{+2} heads and the exposed ADP and Phosphate group. This troponin - Ca^{+2} complex causes the tropomyosin to slide over and release the rest of the actin binding site, which allows for the myosin heads to close and strongly bind to actin. This phenomenon results in the shortening of the actin-myosin complex (sarcomere); hence these cyclic occurrences result in further contraction of the sarcomere (Roger & Pearson, 2013). Due to the hierarchical architecture of muscle tissue, this contraction results in the shortening of the muscle fibres, and finally cascades to the contraction of muscle fibres – hence resulting in the contraction of the entire muscle that has been activated.

The macroscopic arrangement of muscles in this context is referred to as the muscle's architecture (Ganz & Bock, 1965), and it is this that is the primary determinant of muscle function. Elucidating the structure-function relationship of muscle is therefore of great importance since it provides the physiological basis of force production and movement. Although much focus has been placed on factors such as fibre-type distribution in determining muscle function there is no question that muscle function is also strongly determined by its architecture and morphology (Burkholder et al., 1994). Skeletal muscle architecture can therefore be defined as "the arrangement of muscle fibres within a muscle relative to the axis of force generation" (Lieber, 2002).

The next section discusses the physical processes that occur within muscle mechanics.

2.1.2 Muscle Physiology

There are four types of contraction phenomenon, depending on the behaviour of the muscle when it contracts: concentric, eccentric, isometric and isotonic contraction.

In **concentric contraction,** the length of the muscle shortens as it contracts, which follows the conventional belief of muscle contraction (Faulkner, 2003). In **eccentric** contraction the force generated is not enough to overcome external loads on muscles, which results in the muscle fibres lengthening as their antagonistic pairs contract (Colliander & Tesch, 1990; Nikolaidis et al., 2012). This type of contraction typically happens when the muscle is trying to decelerate a moving body (for example placing a body gently down rather than letting it fall). In this type of contraction, the muscle is thought to be resisting extension against an external force through contraction.

During **isometric** contraction, the muscle remains the same length, which is characteristic during passive exercise (for example when someone is simply holding up an object but not moving it through space). In this type of contraction, the muscular force generated is equal to the load therefore no movement/strain results from it. Conversely, in **isotonic** contraction the tension in the muscle remains constant despite a change in muscle length (Maton, 1981), which occurs when the muscle reaches its maximal plateau of force generated for contraction (Scherrer & Monod, 1960). A less common contraction phenomenon occurs when the contraction velocity of the muscle remains constant, whilst the force in the muscle varies (Guilhem et al., 2010). This contraction phenomenon is known as **iso-velocity** or **isokinetic** contraction. Tetanic contraction is the phenomenon of contraction where the muscle produces its maximum force at an optimal stretch range. Consequently, tetanic contraction applies to all the contraction phenomena described above, as it is a region within the operational force-length range of the muscle during contraction. Isokinetic muscle phenomena will be considered in this thesis, in order to limit viscous-elastic effects that are often observed *in vivo.*

The active mechanics of the muscle originate from the action potential triggered event of muscle contraction, where a force is generated by the muscle. This has been studied by others but will not be covered comprehensively in this thesis - as this study

mainly focuses on the passive mechanics of the skeletal muscle. The passive behaviour of the muscle arises from the intrinsic mechanical properties of the muscle constituents, including the ground substances and muscle fibres.

2.2 Active and Passive Mechanics of Skeletal Muscle Tissue

The time taken for skeletal muscle contractions can be categorised into twitch and tetanic contractions. In a twitch contraction, neural stimulation causes the muscle to contract very quickly however as the twitch is so short, the muscle begins to relax even before reaching the peak force. McMahon (1984) acknowledges that it is generally easier to measure the resistance to an externally imposed stretch than the development of force (McMahon, (1984)). The resulting descriptive force vs time graphs can elucidate information about the sarcoplasmic reticulum and the calcium release rates. Once this burst of shock occurs, there is no force produced in the muscle, because it is held isometrically; this is because in isometric muscle there is a short/small fall in tension before the active tension is developed (Abbott & Richie, (1951)).

Marey (1874) suggested that the elasticity of muscle is one of the features that determines how the effects of collaborated shocks occur in a tetanic contraction phenomenon. Based on this assumption, the two separate contributions of skeletal muscle can be considered: i.e. the passive and active behaviour of muscle (Marey, (1874)). McMahon acknowledges the passive properties of isolated muscle in that, as a non-linear intrinsically fibrous material, its fibrous elements are redundant at low extension and then become tensed at high extension, which simultaneously accumulates their spring stiffness. The passive and combined (active and passive) tension vs stretch function for a frog Sartorius is shown in Figure 2.3.

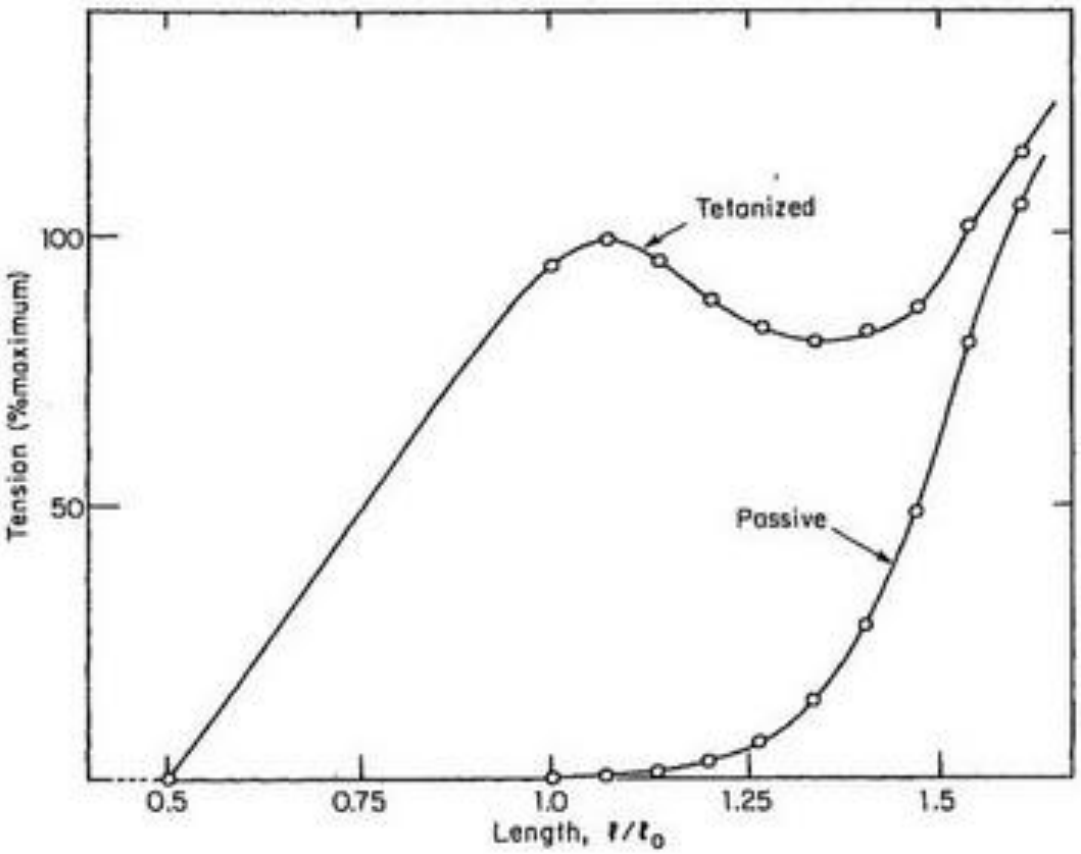

Figure 2.3 Tension –length curve of a frog Sartorius muscle at 0 °C. The passive muscle is based on the resting muscle at a series of different lengths; the total curve has two components: (1) Active tension with the maximum tetanized tension highlighted. This was measured at a series of constant lengths as the muscle was held in isometric contraction. (2) Passive tension, which is also illustrated as a separate curve. Image taken from Aubert et al. (1951). The Tension-length diagram of the frog's Sartorius muscle.

As shown in Figure 2.3, at a small amount of stretch, there was no passive response from the muscle. The force is mainly generated due to tetanized activation of the muscle where the maximum tension is achieved at a relative length of approximately 1. At around a stretch of 1.25, the passive response of the muscle tissue kicks in as the tissues are being stretched close to their physical limit. This sharp increase in the passive response also contributed to the sharp increase in the total force curve, as illustrated in Figure 2.4. The physical limit of the muscle is illustrated to be at around a stretch value of 1.6.

Figure 2.3 shows that the muscle behaves in a generally non-linear fashion, where the passive part behaves as a transversely isotropic fibre reinforced material. As such

it can be idealised as a hyperelastic quasi-incompressible material (Röhrle & Pullan, (2007)). Further, McMahon shows that the pennation angle, defined as the angle each muscle fibre makes with its force-generating axis, affects the passive and total (tetanised) tension-length relationship, as shown in Figure 2.3 (Mahon, 1984).

Figure 2.4 shows force length curves of the pennate fibred gastrocnemius with short fibres and the parallel-fibred Sartorius.

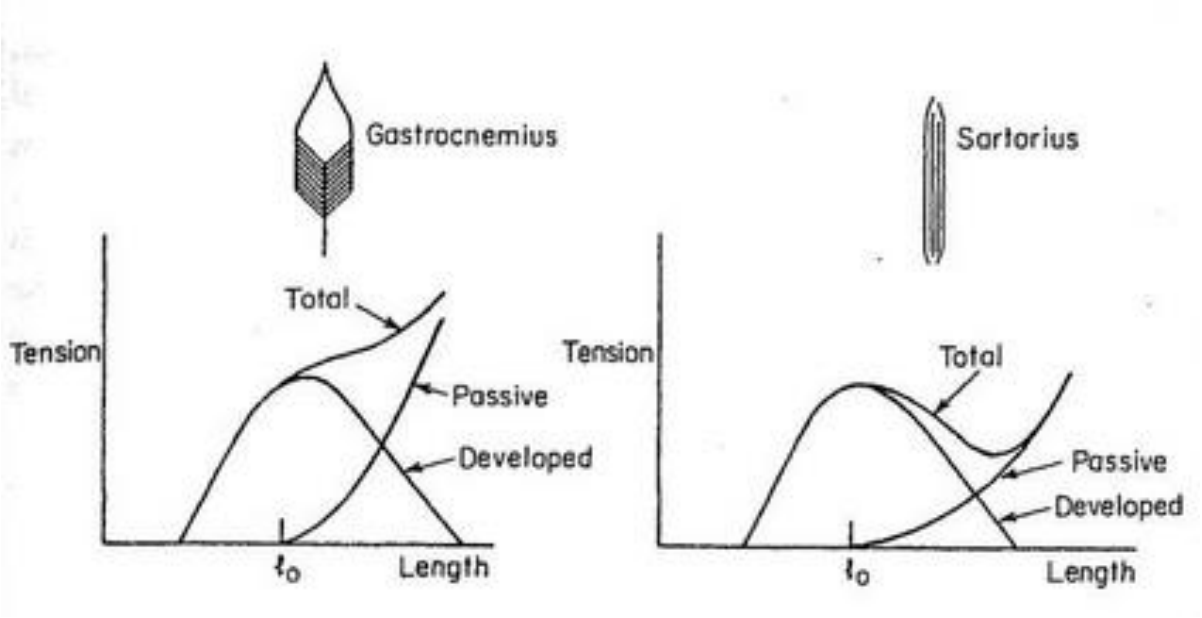

Figure 2.4 Tension – length relationship of a gastrocnemius and Sartorius frog muscle. Image taken from Mahon (1984). Muscles, Reflexes and Locomotion. P11, fig 1.7, Fundamental muscle mechanics.

2.2.1 This clearly illustrates that the fibre orientation of the muscle and its macro-architecture play an important role in the mechanical response of the skeletal muscles, even in a passive state. Furthermore, every muscle in the body has a complex structure that usually consists of muscle, tendon, aponeurosis and transition region. The aponeurosis is not synonymous with the transitional region – here, the aponeurosis is a fibrous sheet made of connective tissue that separates neighbouring muscles, as well as present in the tendon – muscle transition region (Azizi & Roberts, 2009). Each of these structures have a different form, when considering anatomical simulations, it is imperative to focus on a muscle with a specific morphology to better elucidate its mechanical response.

The muscles of the lower extremity are important powerhouse to achieve mobility of the skeleton. Furthermore, given the available literature data and the existing physiology knowledge, the medial gastrocnemius muscle was chosen to be the main muscle of interest in this thesis.

The general anatomy and physiology of skeletal muscles has been described previously. The following section will focus on describing the complex geometrical morphology of the medial gastrocnemius muscle in detail.

2.3 Morphology of the Medial gastrocnemius

The structure of the triceps surae consists of the medial and lateral gastrocnemius muscles which lie superficially of the soleus muscle, and both extend from their tendinous origins by the knee. They both have an aponeurosis region that connects the heads of the muscles to tendon at the distal insertion and merge before transitioning into the Achilles tendon (Blitz & Eliot, 2008). Despite both the gastrocnemius and soleus muscles having aponeuroses which are in direct contact with each other, there is no connection between these aponeuroses until they finally fuse and transition into the Achilles tendon (Blitz & Eliot, 2008). The medial and lateral gastrocnemius bellies are attached to a singular thin aponeurosis on their deep surface, and at the lower end of the gastrocnemius muscle. The aponeurosis extends below the end, however is initially comprised of muscle for a short distance before it merges with the soleus aponeurosis, this is referred to as the gastrocnemius aponeurosis "run-out" and can be seen in Figure 2.5; which shows the general structure of the triceps surae (Blitz & Eliot (2008)).

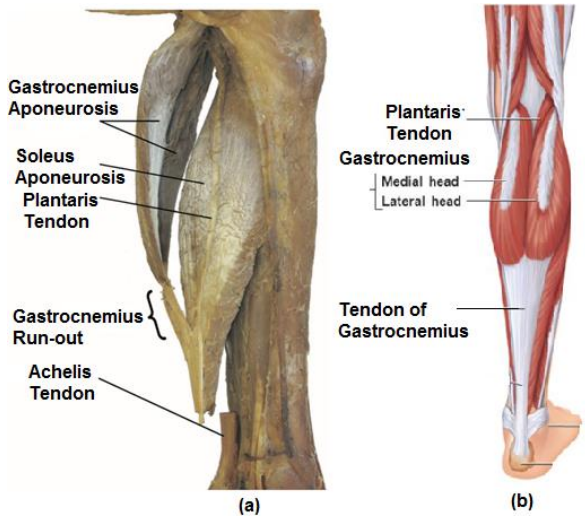

Figure 2.5:(a) Cadaveric specimen and (b) illustrative schematic showing the long gastrocnemius aponeurosis for both the medial and lateral muscle heads. (Blitz & Eliot, 2008).

The limited information of the morphology of the aponeurosis, its morphology and mechanical behaviour has created an impediment to the development of computational

models of the muscle-aponeurosis-tendon complex. Although gastrocnemius aponeurosis length has not been previously quantified, a study by Blitz & Eliot (2008) provides insightful information on the anatomical morphology of the medial gastrocnemius aponeurosis that will be summarised here.

As mentioned previously, the "run-out" is defined as the transition region between the gastrocnemius muscle belly and the Achilles tendon. Variation in the length of this run-out region is defined to have three main categories of differing lengths, categorised as "long", "short", or "direct" attachment to the soleus aponeurosis (Blitz & Eliot, 2007). This region applies to the length of the myotransition region, hence different lengths of this region are of importance to consider.

Figure 1.4.3 (a) Figure 1.4.4 (b) Figure 2.5 (c)

Figure 2.6: (a) Cadaveric specimen of the gastrocnemius aponeurosis for both the medial and lateral heads. (b) Cadaveric specimen showing the short medial aponeurosis. (c) Cadaveric specimen showing the direct attachment for both the medial and lateral heads. Black line shows the muscle tissue boundaries based on points A-E. White line shows insertion boundary onto soleus aponeurosis from points P-T (Blitz & Eliot, 2008).

Figure 2.6 shows the muscular boundary to the aponeurosis (black line) 'cupping' the muscle as a conical region of muscle penetrates the aponeurosis region. The soleus insertion (white line) also shows conical-like type of attachment. These observations

provide useful information regarding how one might attempt to model the morphology of the muscle-aponeurosis-tendon complex.

As well as the morphological issues previously discussed of the aponeurosis, the thickness of the aponeurosis is also important to consider. Studies have shown that the thickness of the gastrocnemius aponeurosis becomes thinner, as it approaches the muscle belly region of the muscle, as schematically illustrated in Figure 2.7.

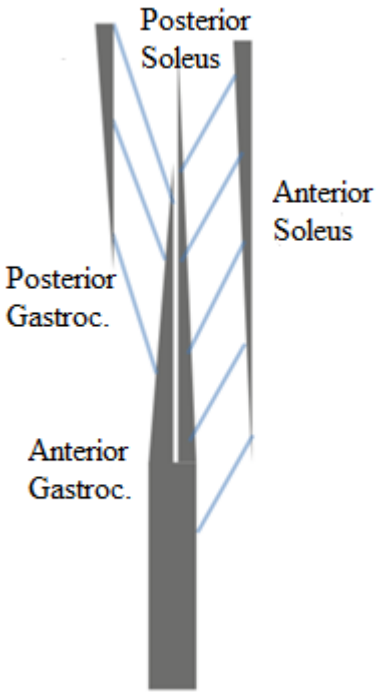

Figure 2.7 Schematic representation of tapering aponeurosis at the posterior end of the soleus. Note that the muscle belly is not shown here. The aponeurosis tissue is shown in shaded grey, and muscle fibre orientation (pennation) are shown in blue lines (Pinney et al., 2004).

It has been demonstrated that the strain distribution across the aponeurosis changes with thickness (Bavel et al., 1996), thus highlighting how changes in thickness may influence the mechanical behaviour as well as the force transmission across the muscle-aponeurosis-tendon complex.

Whilst the above section highlights the complex morphology of the muscle, fibre orientations of the medial gastrocnemius are also a governing feature of the its mechanical response. It is of particular importance at the muscle-tendon junction, and how the muscle tapers as it approaches the middle of the muscle of the muscle and thickens as it approaches the Achilles tendon (Blitz & Eliot, 2007; Blitz & Eliot, 2008)

as shown in Figure 2.7. The types of models that can effectively represent the mechanical response of skeletal muscle in relation to its anatomical geometry are finite element numerical models that incorporate soft tissue constitutive relationships. Therefore, now that the general structure of the muscle of interest (medial gastrocnemius) has been described, the next chapter will cover the current literature concerning finite element models and soft tissue mechanics. These types of models will form the basis of the computational and mathematical techniques used in this thesis to explore the mechanical response of anatomical skeletal muscles.

Chapter 3

Literature Review

This chapter covers the previous research done on skeletal muscle models to elucidate a comprehensive review of the literature and ascertain potential areas in which this thesis might contribute to the current body of knowledge. The mathematical models proposed by various investigators are covered and critically analysed to set out a work-flow for the simulations associated with this work.

3.1 Review of the literature on Models of Skeletal Muscles

The earliest models of skeletal muscles originated from highly idealised lumped parameter models (Hill, 1938) (models that obtain parameters that approximate a number of variables in natural anatomical phenomena), before developing into more complex three-dimensional finite element anatomical models. One of the very earliest sophistications of Hill's model involves incorporating some features of the structure of the muscle and the governance of such features to the muscle's function. This was investigated in 1965 by McPhedran et al., when they acknowledged the difference between the size of individual motor units and their various contractile characteristics (McPhedran et al., 1965; Wuerker et al., 1965). Further studies were undertaken to follow the idea that the excitability of motor neurons was an inverse function of their size (Henneman et al., 1965). A corollary conclusion was that the amount of contractile activity of a motor unit (i.e. the nerve and its corresponding muscle fibre) decreases as its size increases (Henneman & Olson, 1965). Even at this early stage of research in skeletal muscles, it was clear that the structure of the skeletal muscles had a significant influence on its function. This conclusion is reflected in the group of parameters, also known as the size principle parameters that take precedence in skeletal muscle mechanics.

Further work was carried out in 1987 to measure the time-dependant parameters of contraction within the fibres: i.e. motor unit conduction velocity, twitch torque, twitch rise time and half-relaxation time (Andreassen & Arendt-Nielsen, 1987). Andreassen & Arendt-Nielsen demonstrated that there was a high correlation between these four parameters, therefore justifying the inclusion of fibre conduction velocity in the family of size principle parameters when considering the mechanical response of skeletal muscle (Arendt-Nielsen, et al., 1992). This elucidated the fact that skeletal muscle tissue behaves in a viscoelastic nature *in vivo.* The mechanical behaviour is dependent on time – i.e. contraction velocity and relaxation time.

Further detail regarding the muscle-tendon properties and the size considerations of the parameters was explored in Zajac (1989), which acknowledged that the mechanical properties of skeletal muscle and its tendon complex are similar on both a

fibre and sarcomere scale level (Zajac, (1989)). Zajac also studied the creation of nerve signals to muscles through the motor neuron complex nonetheless recognises only one parameter in his studies - the ratio of tendon length (at rest) to muscle fibre length (at rest). This was the basis of his 1D lumped model of a complete musculotendon actuator, with emphasis on fibre orientations and length. From the normalised non-linear force curves produced within his studies, Zajac presents muscle as a transversely isotropic material whose non-linearity supports the sliding filament theory (Zajac, (1989)). A comprehensive review was later done in Monti et al. (2000), regarding the motor unit structure and its definition of function at the neuromuscular junction (Monti, et al., 2000). The muscle fibres, and motor unit components can be considered as different elements within Hill-type models and, for the scope of this review, this literature will be explored separately to the literature pertaining to three-dimensional skeletal muscle finite element models.

Whilst the models developed by Hill (1938), Zajac (1989) and Andreassen & Arendt-Nielsen (1987) were phenomenological lumped parameter models of skeletal muscle, they created the convention of one-dimensional lines of action to represent skeletal muscles. Having compared these models to three-dimensional models (Röhrle & Pullan, (2007); Blemker & Delp, (2005); Blemker et al., (2005)), these one-dimensional lines of action induced significant error when considering the mechanical response of skeletal muscles, reinforcing the importance of considering the anatomy and three-dimensional morphology of the skeletal muscle-tendon complex. As explained above, the muscle fibre orientation will also be considered, since the orientations have a significant effect on their mechanical response. The next section explores the current body of knowledge relating to skeletal muscle fibre architecture, and models that have currently considered this.

3.1.1 Muscle Fibre Orientation

Most mammalian muscle fibres are long cylindrical bodies that span from the tendinous origin to a tendinous insertion (Monti et al., 2000). Some skeletal muscles, however, have a complex structure consisting of short muscle fibres, or fibres that are arranged in series and in overlapping arrays (Bardeen, 1903; Huber, 1917). The specific length of muscle fibres is highly variable across different muscles. However, several investigators have suggested that the length of muscle fibres can be

approximated, as has been done in respect to a range of muscles in other cat models (Loeb et al., 1987). On the other hand, Chanaud et al.'s earlier results in 1991 indicated that in-series short fibres that make up the longer fibres can essentially be considered as separate motor units (Chanaud, et al., 1991), thus playing an important role in the activation component of muscle. While it was found that cat muscle fibres are usually approximately 2.0 cm long, some can be longer than 3.0 cm: such as the cat splenius (Richmond et al., 1985), sartorius (Loeb et al., 1987), tenuissimus (Lev-Tov et al., 1988) and biventer cervivis (Richmond & Armstrong 1988). Previous work suggests that the various fibre lengths reported are essentially based on the different extraction techniques for identifying intercepts of connective tissue (Lieber & Blevins, 1989; Friederich & Brand, 1990), which highlights and may account for the variability of fibre lengths listed in the different cat muscles. One important note to consider, however, is that cat muscle fibres do not normally extend the entire length of the muscle (Sacks & Roy, 1982; Roy & Edgerton, 1992). Monti et al., suggested that the fact that the 'longer fibres' are composed of smaller 'shorter fibres' is not functionally relevant when considering the muscle recruitment and fibre response, (Monti, et al., 2001). Therefore, the supposition that most mammalian fibres span across the full muscle length will be used here.

The significance of functional fibre geometry, and a further justification for its inclusion, is further supported by the observation that the maximum force produced by a muscle can be predicted quite accurately from its physiological cross-sectional area (PCSA), which can be derived by the following relationship (Monti et al., 2000):

$$F \propto PCSA:$$

$$PCSA = \frac{m \bullet \cos\theta}{l\rho} \qquad \textbf{(3.1)}$$

Where the muscle mass is denoted by m, θ is the mean pennation angle of the fibre, the muscle length is represented by l and the muscle density is ρ. As the length of the fibres can be approximated to span across the full length of the muscle, whilst the PCSA will have a functional relationship to the force produced by the muscle.

These functional fibres play an important role in skeletal muscle function and indeed their *active* mechanical response. Since the work carried out in this thesis concerns the passive mechanics of skeletal muscle, the length and PCSA of muscle fibres will be approximated.

The series and parallel mechanics of the muscle (sarcomeres) are affected by the anatomy. One of the first muscle models ever to be developed was done by A V Hill (1938), and this remains the basis of several forward dynamics (Bélaise et al., 2018; Siebert et al., 2018) or inverse kinematics (Carlos et al., 2018) skeletal muscle models today. Hill-type muscle models are therefore briefly discussed below to determine the loose connection between the passive mechanics (series and parallel elements) and the muscles geometrical features (fibre orientations).

3.1.2 Hill-type Models

Hill's model of skeletal muscle originates from phenomenological observations simplified into a one-dimensional dash-pot lumped model developed in 1938 (Hill, 1938).

Hill derived his model by using a thermopile to measure the change in heat of a frog leg. The thermopile converted changes in heat into electrical pulses, which were then read by a galvanometer. As the frog skeletal muscle contracted, there was an influx of potential energy within the muscle. Although blood regulates the heat within the muscle, Hill accounted for the heat dissipation from the system with variables that related to the force generated within the muscle and how fast the muscle was able to contract (Hill, 1938). Hill's derivations covered isotonic contraction of the tetanised muscle.

Although widely used, Hill's one-dimensional model cannot be used as a stand-alone model compared to finite element continuum mechanics models. Whilst it rigorously describes the force-velocity relationships of contracting skeletal muscle, there are issues surrounding the inherent over-simplicity of the model, as highlighted by another author (Winters, 1990). Hence, the need to develop a three-dimensional skeletal muscle model.

As explored by Hill, the contractile phenomenon of skeletal muscle can be accounted for through various components of the models namely the contractile element (CE), the series element (SE) and the parallel element (PE), defined below.

The contractile element (CE) is used to model the active contribution of the muscle where forces originate from actin and myosin cross-bridges at the sarcomere level. Since the CE is the main factor that is responsible for the force generation within the muscle (Winters, 1990), it can be ignored when the muscle is not activated. The

contractile element governs the force-length relationship within the muscle. The force-velocity relationship derived by Hill, also referred to as Hill's rectangular hyperbolic equation, is shown below and it was this that was used to determine the force generation and extrapolation of Hill's results from his thermopile experiment (Hill, 1938; Winters & Stark, 1987).

$$V = b\left[\left(\frac{F_0 + a}{F + a}\right) - 1\right] \qquad \textbf{(3.2)}$$

Where a and b are material parameters fitted from experimental data, F_0 is the maximum isometric tension generated in the muscle, F is the operational tension in the muscle and V represents the velocity of contraction.

The Series Elastic Element (SE) is generally modelled as a non-linear visco-elastic spring in series with the contractile element (Winters & Stark, 1987). This element acts as the refractory element between the passive and active states of the muscle and tends to govern the passive forces of the connective tissues within the muscle, incorporating the soft tissue mechanical behaviour (Fung, 1993). As such, it offers a rapid change of muscle states during contractions of the muscle. It also includes a residual energy storing mechanism, which is often observed in muscle (Hill, 1938; Winters & Stark, 1987; Winters, 1990; Baker, 2015).

The Parallel Element (PE) is modelled as a non-linear spring in parallel with the contractile element and series element. This element is responsible for the passive behaviour of the muscle when stretched since it is related to the elasticity of the connective tissues (Fung, 1993). Although there have been many studies on the CE and SE components, not much is currently known about the PE (Baker, 2015).

The conceptual anatomical fitting of these elements is shown in the diagram below.

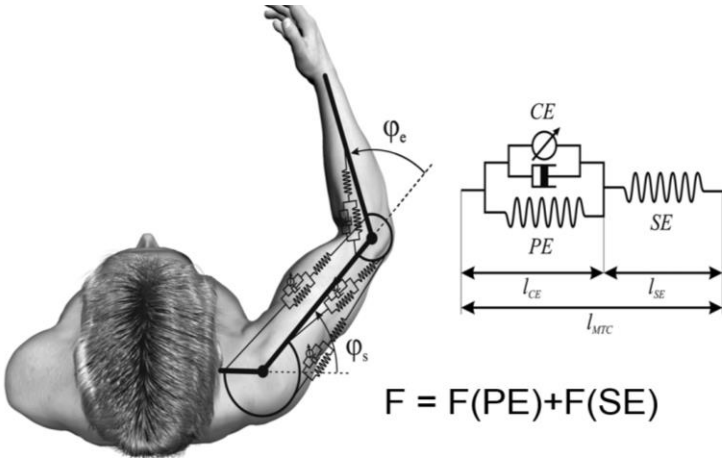

Figure 3.1 A schematic illustration of Hill's model, where φ_e is the elbow joint angle and φ_s is a shoulder joint angle. CE = contractile element length ; lCE = CE length ; PE= parallel elastic element ; SE = series elastic element ; lSE = SE length. Kistermaker et al (2010) : 104(6).

From deduction, the total force would be equal to the summation of the forces of the parallel F_{PE} and contractile elements F_{CE} , which is shown in the relationship below:

$$F_T = F_{PE} + F_{CE} \quad \textbf{(3.3)}$$

where the force generated in the contractile element must be equal to the force generated in the series element F_{SE} (Hill, 1938):

$$F_{CE} = F_{SE} \quad \textbf{(3.4)}$$

The contractile element can therefore be defined as the multiplicative coupling of functions that all contribute to the contractile phenomenon in skeletal muscle, being: time $f_t(t)$, velocity of contraction $f_v(v)$ and the force-length relationship $f_\lambda(l)$. Therefore, the following equation is used (Hill, 1938):

$$F_{CE} = F_0 \times f_t(t) \times f_v(v) \times f_\lambda(l) \quad \textbf{(3.5)}$$

From Hill's approximations, the contractile element, which is the active element, generates a force with a magnitude that depends on the deformation velocity and the respective muscle length. This elucidates the extent of activation over time. Similarly, there is a general relationship that couples the length of the parallel (L_{PE}), contractile (L_{CE}) and series elements (L_{SE}), as shown below:

$$L_{PE} = L_{CE} + L_{SE} \quad \textbf{(3.6)}$$

Whilst this work is conceptualised in components, in 1984, M. Blix carried out a pioneering study to determine the relationship between sarcomere length and force generation within the full muscle, and this set the precedent for cellular scale considerations of skeletal muscle (Blix, 1984). Although the contraction mechanisms of skeletal muscle are highly complex, most models seem to have simplified certain aspects of the physiological processes of muscle by compartmentalising the full system and then modelling each component. In 1998, Martins et al. proposed a numerical model of passive and active behaviour in skeletal muscles that only modelled the time history of a contractile strain as an input for the finite element computations, rather than considering the full activation process (Martins et al., 1998). Zajac et al. (1989) hypothesized that the mechanics at the fibril (sarcomere to fibre) scale can be scaled to the muscle organ scale, and this assumption has been widely adopted since.

An extension of the one-dimensional model Hill proposed can be achieved by compartmentalising the various contributions to the total stress across the volume of the muscle, rather than the forces. The conventional approach involves adding up the longitudinal stresses from the muscle fibres, the stress from the base matrix and the stresses related to the incompressibility of the muscle. This means that the total Cauchy stress (σ) of the muscle can be expressed as the following relationship;

$$\sigma = \sigma_{fibre} + \sigma_{matrix} + \sigma_{volumetric} \quad \textbf{(3.7)}$$

Kojic et al., (1998) proposed that the CE and the SE played the role of the active muscle fibres, where the PE played the role of the surrounding matrix, and their conceptualisation of the SE model considered the PE to behave linearly as an isotropic elastic material. Based on Kojic's foundation, Tang et al. (2005) and Tang et al. (2007) incorporated muscle fatigue into three-dimensional skeletal muscle models. This

fatigue function incorporated the rate of activation and the stretch explored by Stojanovic et al. (2006), which extended the previous models by taking into account different fibre types, as well as including different types of sarcomeres in parallel with the connective tissue. Each sarcomere was modelled by one non-linear elastic element, which was connected in series with one other active contractile element, as shown in Figure 3.2.

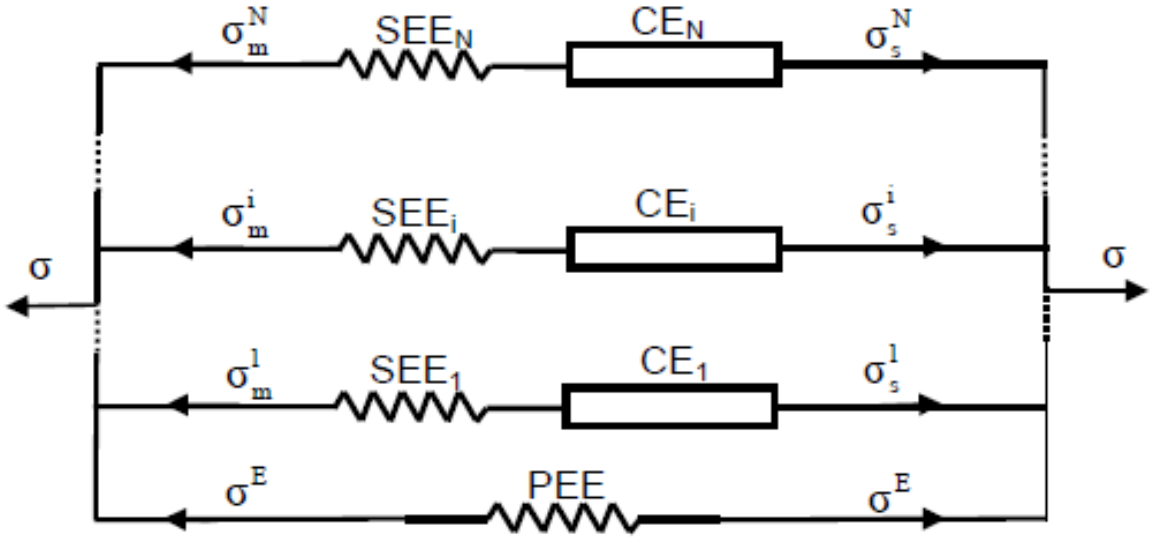

Figure 3.2 Various fibre types in the muscle model placed in parallel to each other, where the summation of each of the fibre types gives the final stress. Stojanovic et al. (2006): 71(7).

As a natural progression of the lumped parameter models reviewed above, the work carried out on three-dimensional skeletal muscle models were of great interest. The next section reviews literature that established the foundation of three-dimensional models, in particular finite element models of skeletal muscle.

3.1.3 Three-Dimensional Anatomical Models of Skeletal Muscle Tissue

Whilst the configuration of fibres in skeletal muscle models has a significant effect on its mechanics, other models have looked to incorporate this in order to attempt to model the muscle-tendon junction and aponeurosis. Examples of computational models of muscle and muscle-tendon complexes exist in abundance, but models that include an aponeurosis structure are far less common. A few examples of such finite element models that include the aponeurosis will be discussed here.

Blemker et al. (2005) created a three-dimensional finite element model of the biceps brachii (arm) to investigate strain distribution across the muscle. The study compared the predicted results obtained from their model with experimental results and found that their model was in good agreement with the experimental data, within one standard deviation. Their muscle geometry (see Figure 3.3) was an idealised geometry of the biceps brachii and was axisymmetric around a centre line.

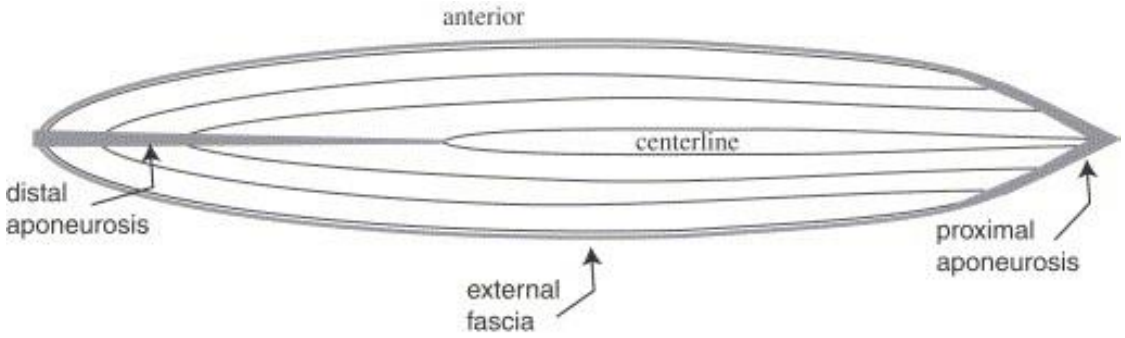

Figure 3.3 Idealised muscle model created in Blemker et al. (2005) showing a simplified model with symmetric muscle geometry and uniform aponeurosis.

This method of creating the muscle geometry is not ideal as it did not accurately reflect the *in vivo* muscle morphology – most notably since the *in vivo* muscle will not be symmetric. An improvement could be made using data from Magnetic Resonance Images (MRI) scans to provide the actual 3D muscle geometry. Furthermore, whilst the aponeurosis was included in this model, no connecting tendon region or muscle-tendon transition was included. Despite this simplification, the aponeurosis induced a non-uniform strain distribution in the finite element muscle simulation. An improvement here could include changing the thickness across the aponeurosis (so that the aponeurosis is not symmetrical), as well as considering an aponeurosis-muscle

transition zone, with the exception that the omittance of a tendon extremity might be compensated for by the application of appropriate boundary conditions.

Other studies have operated at the other extreme to this work, with complex and patient specific models that consequently limit their usability for parameter studies and compromise the ease with which they can be adjusted to model different phenomena. One example of this type of study investigated strain distribution in the biceps femoris longhead, also using a finite element model (Rehorn & Blemker, 2010). Rehorn et al. (2010) made use of MRI to develop the muscle geometry used for the study, which allowed for an accurate definition of muscle geometry – an improvement on the model by Blemker et al. (2005). The anatomical model is shown in Figure 3.4. From Rehorn et al. (2010), it was concluded that the dimensions of the aponeurosis substantially affect deformation within muscle tissue, highlighting the importance of the morphology of the aponeurosis in the stretch distribution throughout the muscle (Rehorn & Blemker, 2010).

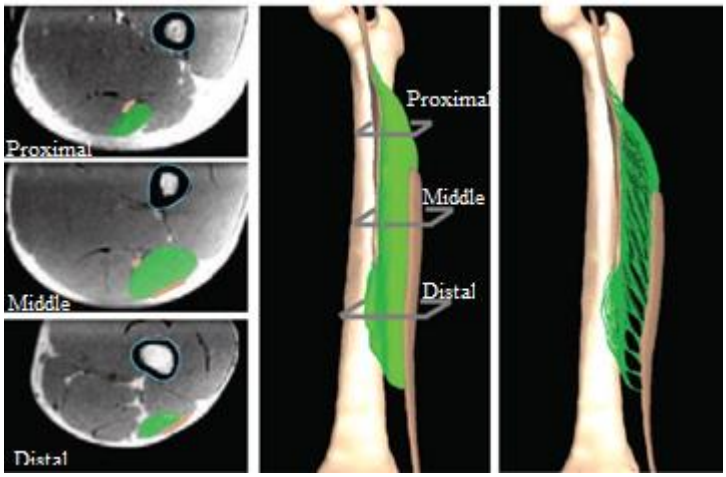

Figure 3.4 MRI-based model of the hamstring from Rehorn et al. (2010). This model is defined via MRI data to provide an accurate geometry of the aponeurosis region's fibres, making it individual specific.

More recently, a three-dimensional finite element model was used in a study, investigating the influence of intramuscular fibre orientation on the curvature of the Achilles tendon during gastrocnemius muscle contraction (Kinugasa et al., 2016). This model included the aponeurosis and tendon, but only at one end (distal) of the muscle. It was found that the aponeurosis transfers force between the muscle and tendon and,

influences the force distribution throughout the muscle complex. This result suggests that including the aponeurosis at both ends (origin and insertion) may influence how force is transferred through the model and thus alter the results. Again, the lack of inclusion of these anatomical features of the muscle-aponeurosis-tendon complex represents a simplification of the modelling methodology, which could have an impact on the results. Furthermore, the models discussed above have not considered the material property distribution of the muscle-tendon junction. Computational models of muscle and muscle-tendon complexes exist in abundance, but models that include an aponeurosis structure at both the distal and proximal ends with a muscle-tendon transition region are far less common, hence the motivation to produce a model that includes such structures.

From the review carried out so far, it is notable that the fibre orientations, and their description have an impact on the mechanical response of skeletal muscle complexes. Whilst there are a number of ways that the fibre of the muscle-tendon fibres can be represented in a finite element workflow (Blemker & Delp, 2005; Zöllner, et al., 2015), the experimental methods required to obtain these fibre orientations must be comprehensive. One of the most comprehensive methods used is Diffusion-weighted magnetic resonance imaging (DW-MRI), that makes use of the diffusion of water molecules to generate contrast colours in MRI (Bihan & Breton, 1985; Merboldt, et al., 1985). DW-MRI allows for the mapping of the diffusion aqueous molecules in vivo, which interact with muscle fibres hence allowing for a clear image of fibres within an organ – such as the medial gastrocnemius. Diffusion Tensor Imaging (DTI) is a sub-set technique of DW-MRI, where the measurement of restricted diffusion of aqueous particles in tissues produce colour-mapped trajectories of the rate of diffusion and preferred diffusion direction. These colour maps allow for the orientation of aqueous molecules that experience restricted diffusion - into a muscle fibre for example. This process therefore provides the orientation of the membrane of muscle fibres, non-invasively. It is important to note, however that this does not elucidate the explicit orientation of the muscle fibre, rather, it represents the aqueous molecules that surround the muscle fibre.

With an emphasis on skeletal muscle architecture as a fibrous material (as explained above), skeletal muscle tissue is modelled as a fibre reinforced material. We can therefore use constitutive relationships of fibrous materials to model fibrous tissues as are those found in skeletal muscles (muscle, tendon and transition tissues).

Constitutive modelling is an important field of research in skeletal muscle modelling that has been adapted from models of similar soft tissues, e.g. vascular tissue, cardiac tissue, tendons or ligaments. The next section looks at the constitutive modelling of soft tissues as fibre reinforced materials, with emphasis on the specific functions that define the energy the constituents store in relation to how they deform, namely the strain energy functions (SEF).

3.1.4 Constitutive Models of Skeletal Muscle with Emphasis on Strain Energy Functions

The general material properties of skeletal muscle are mainly represented by their constitutive equation, which is the relation of a material substance to its external stimuli. The strain energy density of a material can be defined with respect to the invariants of the Cauchy-Green strain tensor, and principal stretches.

For uniaxial stress, therefore, the invariants can be defined as specific relationships with the Cauchy-Green tensor, and each invariant can be used for various structural components. In this context, skeletal muscle is modelled as a fibre-reinforced material, which includes a unit vector in the undeformed configuration that accounts for the direction vectors of the fibres (Weiss, 1996).

Wiess's models have been used extensively for modelling the material behaviour of cardiac muscle (Humphrey & Yin, 1987; Humphrey et al., 1990). Weiss appreciates the compartmentalised components of the skeletal muscle model, where the base matrix is modelled as a basic isotropic material, and the fibre response is modelled as an anisotropic contribution from the interactions between the fibres and the matrix. The fibre contribution is thought to come from the *collagen* fibres embedded in the matrix; or in this context, one family of fibres (whether it be muscle fibres or collagen fibres). This follows the general strain energy function mode:

$$F_T = F_1 + F_2 + F_3 \qquad \textbf{(3.8)}$$

Where F_1 is the base material contribution, F_2 is the collagen fibre family contribution, and F_3 is the mechanical contribution of the interactions between the fibres and the base matrix.

F_1 is usually modelled as an isotropic material, and the anisotropy ($F_{2,3}$) is defined with respect to the first, second and fourth invariants, where their derivatives provide sufficient representation for the structural components.

Although this strain energy function provided comprehensive information for skeletal muscle mechanics, there are several things that cannot be accounted for in this model. These omissions include the active muscle recruitment component, the non-homogeny of the skeletal muscle-tendon tissue and morphology, and the other structural components of skeletal muscle. As such, Röhrle used a different strain energy function that allowed for the incorporation of the *passive* second Piola-Kirchhoff stress component $S_{passive}$ to the *active* second Piola-Kirchhoff stress component S_{Active} in a summative split, with respect to the *total* second Piola-Kirchhoff stress S_T;

$$S_T = S_{Passive} + S_{Active} \quad \textbf{(3.9)}$$

The passive stress component is thought to comprise of a Gaussian linear-like (isotropic) and more non-linear (anisotropic) response. The next section covers the form and behaviour of each of these responses.

3.1.5 Isotropic Response

The isotropic contribution usually accounts for the base matrix response (Holzapfel et al., 2000). The primary, and probably most widely employed isotropic SEF is the Mooney-Rivlin (MR) model, which reduces to the well-known Neo-Hookean (NH) model (Hackett, 2018). The isotropic response is an important contribution to consider, as it represents the intrinsic material properties that make up the muscle and tendon constituents. The isotropic part is generally modelled as a Neo-Hookean or Mooney Rivlin material, expressed in terms of the first two invariants of the Cauchy-Green deformation tensor (mathematically defined in Chapter 4, Equation **4.49**). The Neo-Hookean isotropic model originates from the Gaussian model proposed by Boyce & Arruda, (2000). The Mooney Rivlin model is a more comprehensive and descriptive model than the Neo-Hookean model, since it provides a constant modulus in shear that is not dependent on the shear strain or non-linear deviations from the Gaussian Neo-Hookean uniaxial tension. Other constitutive equations, such as exponential functions, can also be utilised for the isotropic part of

the model. The strain energy density function can be considered as the amount of energy stored in a material constituent, with respect to the way in which it deforms. The Neo-Hookean (ψ_{NH}) and Mooney Rivlin (ψ_{MR}) mathematical relationships are shown in Equation **(3.10**.

$$\psi_{NH} = C_1(I_1 - 3) \quad \textbf{(3.10)}$$

$$\psi_{MR} = C_1(I_1 - 3) + C_2(I_2 - 3) \quad \textbf{(3.11)}$$

In Equation **(3.10**, C_1 is the material constant used in the Neo-Hookean model. In Equation 3.11, C_1 and C_2 are material constants used in the Mooney-Rivlin model. These material constants are typically obtained by fitting the equation to experimental stress-strain data. The first and second invariants of the Right Cauchy-Green Deformation tensor, respectively are represented by I_1 and I_2**.**

These models can therefore represent the base matrix of the skeletal muscle, where the ψ_{MR} **(**Mooney-Rivlin) model is commonly used in skeletal muscle mechanics (Blemker, 2005; Röhrle & Pullan, 2007; Röhrle et al., 2012).

Whilst constitutive modelling lays down the foundation of skeletal muscle finite element modelling, skeletal muscle is a highly dynamic tissue that remodels in response to its mechanical environment. The next section discusses the growth and remodelling of skeletal muscles, in particular the physiological phenomena that occur during the remodelling of skeletal muscles.

3.1.6 Remodelling Phenomena of Skeletal Muscle

Skeletal muscle is a remarkable tissue that is capable of undergoing significant adaptations in response to mechanical cues. Whilst growth and remodelling may conventionally be considered synonymous, in the context of this thesis growth is considered to be the overall turnover of mass, hence volumetric growth (Rodriguez, et al., 1994), which occurs in response to a muscle's mechanical environment.

Remodelling meanwhile, is here considered to be the changes in mechanical response in relation to mechanical stimuli (Humphrey, 2002).

Whilst growth and remodelling of skeletal muscle tissue can occur upon cues from various stimuli (e.g. the chemical environment), only the mechanical response of the tissue will be considered here.

Muscle tissue is a hierarchical structure, it experiences changes across the molecular, subcellular, cellular, tissue and organ scales. These scales collaboratively contribute to macroscopic adaptations in overall muscle structure (Wisdom et al., 2015). The sarcomeres that are found at the subcellular level contribute to the growth and remodelling of skeletal muscle, where more sarcomeres are added in parallel in response to elevated forces produced by the muscle, hence building the muscle cross-sectional area (Johnson & Klueber, 1991; Farup, et al., 2012). Conversely, sarcomeres in parallel are lost in response to disuse (Yasuda et al., 2005; Narici & Maganaris, 2007; Campbell et al., 2013). Sarcomere numbers will increase in series - for example; when the muscle is stretched and held at a fixed length, or intermittently stretched to a perturbation of its homeostatic range, or decrease in series number when held in a shortened position (Baker & Matsumoto, 1988; Heslinga et al., 1995; Csapo, 2010), as observed in eccentric exercise (Lynn, 1994; Blazevich et al., 2007; Seynnes et al., 2007). The mechanical environments can be described as over- and under-stretch/loading. As such, the homeostatic range of different constituents are considered to be different, where the tendon and muscle constituents therefore could not only remodel at different rates, they may also have different homeostatic stretches and stresses which determine the onset of remodelling. Further investigation of this homeostatic range will be explored in this thesis, hence determining over – and under-stretch/loading.

Such mechanical environments in skeletal muscle mechanics include **overstretch**, which is interpreted as the extension of a muscle past its homeostatic operational range (Weerapong et al., 2004), and **understretch,** a reduction in the extension of a muscle below its homeostatic operational range. **Overloading** is the excessive production of force during muscle contraction, past the muscle's homeostatic threshold force operational range (this threshold is not necessarily its maximum force), for a prolonged period, as observed in resistance training, concentric and eccentric loading (Colliander & Tesch, 1990; Brooks et al., 1996). **Underloading** is therefore the opposite; the deficient production of force below the muscle's homeostatic operational range, as

observed in the disuse of muscles or Botulinum toxin (Botox) therapy (Ellman et al., 2013).

Overloading phenomena are observed during eccentric exercise and eventually enables muscle fibre lengthening through the increase of sarcomeres in series (Lynn, 1994; Brockett et al., 2001), as well as an increase in sarcomeres in parallel (Wisdom et al., 2015), as observed in anisotropic growth phenomena (Menzel, 2005; Tsamis et al., 2012). In contrast, individuals who decrease weight bearing on the triceps surea muscle group and keep them at a shortened length (understretch), when wearing high heels for instance, develop shorter muscles through the loss of sarcomeres in series (Csapo, 2010).

The current body of literature concerning growth and remodelling of skeletal muscle spans over different scales of skeletal muscle in specific mechanical environments for example; underloading limb suspension (Hackney & Ploutz-Snyder, 2012), or underloading in micro-gravity environments (Tabary et al., 1972; Trappe, 2002; Adams et al., 2003) and changes of the sarcomere numbers. Since the work carried out in this thesis concerns the passive mechanics of skeletal muscle, the mechanical stimuli and drivers of remodelling will focus on overstretch conditions.

3.1.7 Muscle Overstretch Physiological Mechanics

Muscle plasticity is synonymously referred to as muscle adaptation (Bottinelli & Reggiani, 2006), where the deformations caused by chronic lengthening are inelastic in that they neither store energy nor generate force (Go¨ktepe, et al., 2010). Whilst others have aimed to model the growth mechanics of sarcomerogenesis in a continuum mechanics regime (Zollner et al., 2012), here the remodelling from overstretch will be considered as a one-dimensional phenomenon (in the direction of loading), and then further developed into a three-dimensional finite element workflow. The remodelling from overstretch in this thesis is based on stress-driven remodelling, which results in changes of the material constituents. Physical mechanisms that can lead to overstretch include limb lengthening (Williams & Goldspink, 1971; Williams et al., 1998; Deyne, 2002; Lindsey, 2002; Boakes et al., 2007), immobilization in limb lengthened position (Tabary et al., 1972; Goldspink & Scutt, 1992; Pontén & Fridén, 2008) or stretch regimes (Goldspink, 1999; Nordez et al., 2009).

When the muscle is perturbed from its homeostatic operational range, growth or remodelling is thought to occur, where the muscle can increase or decrease in number

in series (growth) or it can increase or decrease in sarcomere length (remodelling). Such phenomena are illustrated in Figure 3.5.

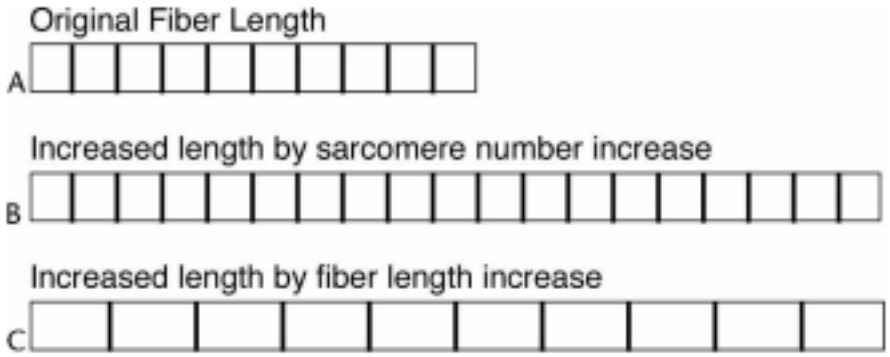

Figure 3.5 Possible nature of muscle fibre adaptation to chronic lengthening (A) muscle fibre length before growth or remodelling, (B) Increase in fibre length due to an increase in serial sarcomere numbers and (C) increase in fibre length due to an increase in the homeostatic length of sarcomeres (Boakes et al., 2007).

As the muscle is stretched and held at fixed length, the number of sarcomeres is thought to increase in series (Williams & Goldspink, 1971; Tabary et al., 1972; Simpson & Williams, 1995; Deyne, 2002; Lindsey et al., 2002; Boakes et al., 2007; Makarov et al., 2009). As demonstrated above, the sarcomere length is also thought to increase when the muscle is gradually stretched (Elsalanty et al., 2007; Makarov et al., 2009), which consequently increases the fibre length of the muscle (Lindsey, 2002; Elsalanty et al., 2007; Makarov et al., 2009).

The Myosin heavy chains that facilitate the sarcomere length changes and take longer to slide over each other, suggesting a stiffer material as the muscle is stretched more (Goldspink & Scutt, 1992; Deyne et al., 1999). As the passive stiffness of the muscle increases during overstretch (Williams et al., 1998; Reid & Mcnair, 2004), the extracellular matrix of the muscle is thought to increase (Pontén & Fridén, 2008), as does the collagen in the muscular and tendinous constituents (Williams et al., 1998). The pennation angle decreases and aligns more closely to the force-generating axis as the muscle experiences overstretch (Elsalanty et al., 2007).

3.1.8 Previous Continuum-Mechanics Models of Growth and Remodelling of Skeletal Muscles

Some of the first attempts made to simulate chronic adaptation of skeletal muscle in a fully three-dimensional finite element modelling framework were carried out relatively recently (Zöllner et al., 2012). The model produced by Zöllner et al. (2012), relied on a three-step procedure. They first project the whole muscle stress-strain onto local subcellular stretch and force, secondly, they consider the local generation or removal of sarcomeres in series or parallel, based on these strains and stress, and finally they use this information to predict the resulting stress-stretch across the muscle. Whilst this process is modular, and has been used successfully, the homeostatic stress and stretch of the skeletal muscle was thought to be one, hence if the muscle is *not* at rest, remodelling occurs, rather than allowing for an operational range where the muscle can function before the onset of remodelling.

Further work has been carried out to consider sarcomere loss when the muscle is held at a shortened configuration, namely the shortening of the gastrocnemius when high heels are worn (Zollner et al., 2015). Their case-study reported an overall 5% decrease of the gastrocnemius length, with extreme shortening of up to 22% in the central region of the muscle belly, when the heel was raised by 13 cm, whilst the Achilles tendon remains virtually unaffected. Due to the shortened configuration of the muscle, sarcomere loss occurred on average of 9%, up to a maximum sarcomere loss in the belly of the muscle of 39%. Whilst these values seem excessive after just ten weeks of wearing high heels, their tendon was modelled as an infinitely stiff material, and their critical stretch (threshold of the onset of modelling) was set to be 1. One can contend that these assumptions are contrary to what occurs in physiological phenomena, as this inherently assumes that remodelling will occur as soon as the tissue is not idle. Furthermore, the geometrical model used does not consider the muscle-tendon junction, or aponeurosis, which may cause erroneous remodelling distributions, as it has been established above that the morphology, and material property distribution, of skeletal muscles highly affect the stress and strains they experience: those stresses and strains are the main drivers of remodelling in the muscle.

Altan et al.'s model in (2016) modelled sarcomerogenesis during overstretch. This model was implemented through a continuum mechanics framework by a multiplicative split of the total deformation gradient $\mathbf{F}$, by the elastic deformation gradient $\mathbf{F}_e$, and the growth tensor $\mathbf{F}_g$. The deformation gradient and continuum mechanics methods are covered in Chapter 4, which is based on the work carried out by Rodriguez et al. (1994).

$$\mathbf{F} = \mathbf{F}_e\mathbf{F}_g \tag{3.12}$$

This multiplicative split allows for the deformation of the body to be defined with respect to reference B_0, current B, and an intermediate $\hat{\mathrm{B}}$ configurations, where the mapping between the reference and intermediate configurations involve the growth of each particle, individually. This may lead to voids and overlaps of individual parts within the body. Hence an elastic deformation configuration is used to restore its unity (Rodriguez et al., 1994). These states are shown conceptually in Figure 3.6.

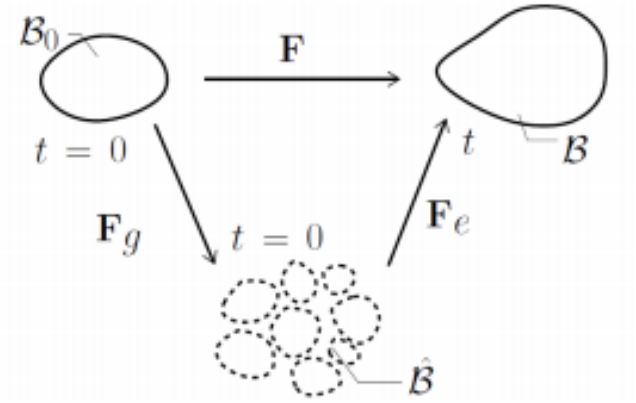

Figure 3.6 Kinematics of finite growth (Altan et al., 2016).

Altan et al., (2016) do however, employ an evolution equation that is used to determine the strain energy density function, which also accounts for the muscle's active force production activities. Altan et al., reported that the stress response of the skeletal muscle decreases over time, as the sarcomeres in series decrease whilst the muscle has contracted. However, they verified their growth model through a unit cube in uniaxial extension, rather than in compression, hence modelling overstretch, whilst making inference to under stretch mechanics. Whilst it is conventionally thought that sarcomere turnover in series occurs during over- and understretch phenomena, which predominantly consist of the passive mechanics of skeletal muscle, Altan et al.

included active mechanics of the skeletal muscle tissue by means of their strain energy density function. However, they did not consider the sarcomere turnover in parallel, which is driven by over- and-underloading – an active process. These are therefore, areas of possible limitations.

Altan et al. (2016) used the idea of an operational range of stretch of the muscle, as did Blemker et al. (2005), where muscle growth begins once the muscle is perturbed from this operational range. Neither study however, clearly stated this range, how it can be experimentally determined or how the fibres may constitutively behave in over– and understretch conditions (Blemker et al., 2005; Ehret et al., 2011; Calvo, 2010; Shearer, 2015). There has been speculation regarding the overlap of the operational range of the muscle and its homeostatic range, and it has been suggested that this is governed by the tissue's operational optimality (Cyron et al., 2015).

Whilst the optimal operational range, λ_{opt}, used by Altan et al. (2016) was not clearly determined, it was an extension of the work carried out by Zollner et al. (2012) and Goktepe et al. (2010), where the threshold optimal operational stretch was defined as **1,** hence suggesting that muscle growth occurs as soon as the muscle is no longer idle and moves from its resting position. Further, with the inclusion of finite growth, as the architecture and mass density of the constituents are thought to change, recent speculation has proposed that the homeostatic configuration will resultantly change, or *reset* upon each evolved step (Latorre & Humphrey, 2018) to an update homeostatic configuration. It is not currently known, however, how this homeostatic configuration changes during growth phenomena in skeletal muscle tissue.

Considering the current literature on the growth (changes in mass) and remodelling (changes in architectural structure and mechanical response), the kinematics of growth and remodelling require a multiplicative decomposition of the elastic and inelastic deformations. The work carried out in this thesis predominantly considers remodelling of skeletal muscle tissue and omits the effects of growth. When considering illustrative examples in which a skeletal muscle remodels, i.e. in limb lengthening, a subject specific finite element model can be highly personalised with specific considerations to the muscle's mechanical environment. For simplicity and reasonable inference, this thesis will only consider the remodelling regimes of the medial gastrocnemius.

The above review of the literature has elucidated areas of novelty that can be assessed, as well as what aspects of muscle architecture are important to include in the finite element model of skeletal muscle. These points are discussed in the next section.

3.2 Conclusions

Whilst constitutive modelling is a field of research that is well developed, with applications to a wide variety of soft fibre reinforced materials, its application to skeletal muscles is still relatively new. Whilst the recent advances in skeletal muscle models have looked towards modelling the muscle-tendon complex as a multi-scale model (Röhrle et al., 2017), with chemical, electrical and physiological phenomena (Mordhorst et al., 2015; Heidlauf & Röhrle, 2014), there are still areas of improvement to be made to each of these physiological phenomena and across the sub-cellular to organ scale. This thesis aims to address the following areas of novelty:

(i) How the aponeurosis region and the muscle-tendon junction of the medial gastrocnemius can be morphologically represented;

(ii) The effect the morphology and architecture of the muscle-tendon junction has on the medial gastrocnemius' mechanical response;

(iii) The constituent relationship and distribution between the muscle, tendon and muscle-tendon junction regions;

(iv) The remodelling regimes that may occur due to structural and morphological changes of the medial gastrocnemius in a perturbed mechanical environment.

From the review of literature carried out above, there are several other mechanisms that can be added to skeletal muscle models. For simplicity, only the areas outlined above will be investigated, to better understand the mechanical response of the medial gastrocnemius, the effects of different anatomical features and how its mechanical response changes over time in relation to its mechanical environment.

The next chapter details the mathematical methods that were used to develop the three-dimensional continuum finite element model of skeletal muscle tissue.

Chapter 4

The Exploration of a Mathematical Model of Skeletal Muscle and Tendon Tissue

The previous chapters have offered a general overview of the thesis and have discussed the anatomy and physiology of skeletal muscles. A chronological review of the literature concerning mathematical and finite element modelling of skeletal muscles was also undertaken. Together, these chapters underpin the subsequent work and outline the areas in which this thesis seeks to contribute to. The current chapter starts by reviewing the basics of non-linear solid mechanics and then justifies the selection of the constitutive relationships used in this thesis. From the constitutive relationships used, the benchmark analytical formulation is tested against a numerical simulation of an idealised cuboid in order to verify the accuracy of the numerical formulation.

4.1 Basics of Non-Linear Solid Mechanics

Bodies deforming in a space-time continuum can be defined using non-linear solid mechanics, meaning that each position vector on a body in its initial/reference state can be mapped onto its current/deformed state, with respect to time, as shown in Figure **4.1**. This transformation function is defined by means of a deformation tensor as derived below. The deformation and location of the body can be described using Eulerian (spatial cartesian) co-ordinates and Lagrangian (material) co-ordinates, where the Lagrangian coordinates deform with the material as it deforms.

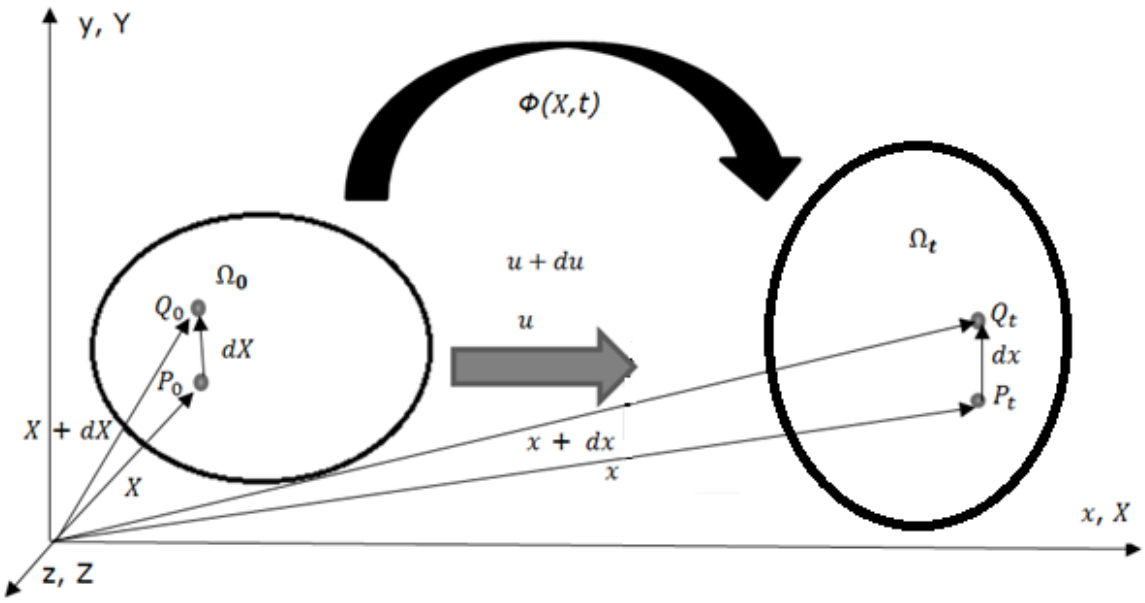

Figure 4.1 Initial reference and current configurations of a continuum body.

4.1.1 Lagrangian and Eulerian Co-ordinates

The position vector of a point on a material in the initial reference position can be given by the following relationship (Belytschko et al. (2000)):

$$\mathbf{X} = X_I \mathbf{E}^I \qquad \textbf{(4.13)}$$

X_I denotes the components of the position vector in the reference configuration ('spatial' or 'Lagrangian' co-ordinates), and $\mathbf{E^I}$ is the unit base vectors of a rectangular Cartesian coordinate system in the initial position.

The position vector of the deformed body in the current configuration is defined by the same relationship but denoted in lowercase lettering, as also shown in Figure **4.1**.

$$\mathbf{x} = x_I \mathbf{e^I} \qquad \textbf{(4.14)}$$

Here, x_I represent the components of the position vector in the current configuration ('spatial temporal' or 'Eulerian' co-ordinates) and $\mathbf{e^I}$ is the unit base vectors of a rectangular Cartesian coordinate system in the current position.

The motion and displacement of a body from its reference configuration can therefore be mapped onto its current configuration by mathematically defining its motion and displacement in the Lagrangian co-ordinate system.

4.1.2 Motion and Displacement

As shown by Shabana (2008), a point in the initial configuration can be mapped onto its current configuration at time t through the following direct relationship:

$$\mathbf{x} = \varphi(\mathbf{X}, t) = \mathbf{X} + u(\mathbf{X}, t) \qquad \textbf{(4.15)}$$

u(**X**,t) is the displacement of the material point through the deformation gradient – a matrix which defines the deformation of the body through a Eulerian co-ordinate system. This deformation gradient is described below.

4.1.3 Deformation Gradient

The deformation gradient, **F,** can be defined as (Belytschko et al. (2000)):

$$\mathbf{F}(\mathbf{x}) = \frac{\delta \varphi}{\delta x} = \sum \frac{\delta x_i}{\delta X_I} \cdot \mathbf{e}^i \mathbf{E}^I \qquad \textbf{(4.16)}$$

F can also be referred to as the Jacobian matrix of the mapping function φ, where the determinant of **F** is called the Jacobian (J) determinant, or the Jacobian, of the deformation gradient, as shown by Belytschko et al. (2000):

$$J = \det(\mathbf{F}) \tag{4.17}$$

The deformation gradient can therefore be compartmentalised into two parts that take into account, first, the related change in volume (the dilatational part) and, second, the change of shape of the deforming body (the deviatoric part), per unit volume of a homogenous substance, as shown by Flory (1961) in Equation **4.18**:

$$\begin{aligned} \mathbf{F} &= \mathbf{F}_{vol}.\mathbf{F}_{dev} \\ \mathbf{F}_{vol} &= J^{1/3}\mathbf{F} \\ \mathbf{F}_{dev} &= J^{2/3}\mathbf{F} \end{aligned} \tag{4.18}$$

where $\mathbf{F}_{vol}$ is the deformation gradient that attributes to the volumetric change and $\mathbf{F}_{dev}$ is the deviatoric part. It is important to note that the volumetric part is synonymously referred to as the isochoric and dilatational response in this context.

The determinant of the deviatoric deformation gradient is always 1, Therefore the determinant of the isochoric response is equal to the determinant of the whole response, which is equal to the Jacobian matrix J (Flory, 1961), for instance:

$$\det(\mathbf{F}_{vol}) = \det(\mathbf{F}) = J \tag{4.19}$$

Following on from these principles of solid mechanics, we can begin to derive and quantify the stress and strains associated with the material. The next section defines the following strains: Green Strain, the right and left Cauchy-Green deformation tensors and the principal stretches of the Cauchy-Green deformation tensors.

4.1.4 Strain Measures

The Green strain (also referred to as the Lagrangian strain) measures the squares' difference of an infinitesimal segment in the reference configuration and the current configuration, and can be given by the following relationship (Fung, 1993):

$$(d\mathbf{x})^2 - (d\mathbf{X})^2 = 2d\mathbf{X}\cdot\mathbf{E}\cdot d\mathbf{X} \qquad \textbf{(4.20)}$$

Provided:

$$d\boldsymbol{X}^2 = dX_i dX_i = \delta_{ij} dX_i dX_j$$

$$d\boldsymbol{x}^2 = dx_i dx_i = \delta_{ij} dx_i dx_j$$

Hence:

$$\mathbf{E} = \frac{1}{2}(\mathbf{F}^{\mathbf{T}}\mathbf{F} - \mathbf{I}) \qquad \textbf{(4.21)}$$

The Green strain tensor is denoted by $\mathbf{E}$ and $\mathbf{I}$ is a second order unit tensor – which can be considered as unity.

δ_{ij} is used in the Kronecker delta nomenclature: $\delta_{ij} = 1 \; if \; i = j$;and $\delta_{ij} = 0 \; if \; i \neq j$; again, note here that the lowercase letters refer to the current deformed configuration at time t, and the uppercase letters refer to the initial undeformed reference configuration when t=0. This means that the Green strain can be re-written in the following format:

$$E_{ij} = \frac{1}{2}(F_{ik}{}^{T} F_{kj} - \delta_{ij}) \qquad \textbf{(4.22)}$$

The right ($\mathbf{C}$) and left ($\mathbf{B}$) Cauchy-Green deformation tensors are shown below, respectively (Weiss (1996)):

$$\mathbf{C} = \mathbf{F}^{\mathbf{T}}\mathbf{F} = F_{iL}F_{iJ}\mathbf{E}^{\mathbf{I}}\mathbf{E}^{\mathbf{J}}$$

$$\mathbf{B} = \mathbf{C}^{-1} = \mathbf{F}\mathbf{F}^{\mathbf{T}} = F_{iI}F_{jJ}\mathbf{e}^{\mathbf{i}}\mathbf{e}^{\mathbf{j}} \qquad \textbf{(4.23)}$$

As such, we can eliminate the volume change factor and express the right and left Cauchy-Green deformation tensors as the following:

$$\mathbf{C} = \mathbf{F}^{T}\mathbf{F} = J^{2/3}\overline{\mathbf{C}} \qquad \textbf{(4.24)}$$

$$\mathbf{B} = \mathbf{F}\mathbf{F}^T = J^{2/3}\overline{\mathbf{B}}$$

Equating $\overline{\mathbf{C}}$ and $\overline{\mathbf{B}}$ as a volumetric-eliminated version of the right and left Cauchy-Green deformation tensors, respectively.

4.1.5 Stress Measures

Using the finite elasticity relationships, and based on the principle of least action, the principle of virtual work (governing equation) in the bodies of interest can be defined in terms of the internal (Cauchy) stress, the sum of the applied forces and inertial forces. These forces should reach an equilibrium, whereby the total energy is equal to zero (Yang et al., 2002; Baruh, 1999). Hence, the variational form of the principle of virtual work;

$$\delta W = \int_{\mathbf{v}} J\boldsymbol{\sigma} : \frac{\partial \mathbf{U}}{\partial \mathbf{X}} dVol - \int_{\mathbf{v}} \mathbf{b} \bullet \ \delta \mathbf{U} dVol - \int_{\mathbf{s}} \mathbf{Tr} \bullet \delta \mathbf{U} dS = 0 \qquad \textbf{(4.25)}$$

The field of virtual displacements are represented by $\partial\mathbf{U}$, $\mathbf{b}$ denotes the body force per unit mass and $\mathbf{Tr}$ represents the surface traction vector, W is the virtual work of a rigid body (which is a function of the strain energy density function), S is the surface of the body and Vol is the volume of the body. As expressed above, the volumetric part may be considered negligible (i.e. the second term in the integration function above may be considered as negligible). $\int_{\mathbf{v}} \mathbf{b}.\delta\mathbf{U} dV - \int_{\mathbf{s}} \mathbf{Tr}.\delta\mathbf{U} dS = 0$, therefore, only the first term will be used to derive the virtual work function:

$$\delta W = \int_{v} J\boldsymbol{\sigma} : \frac{\partial(\partial \mathbf{U})}{\partial \mathbf{X}} dVol$$

These integrals are performed over the initial undeformed volume and its surface area. As such, this is used to show the stress definitions expounded below.

$$\mathbf{P} = J\boldsymbol{\sigma}\mathbf{F}^{-\mathbf{T}}, \ \mathbf{S} = J\mathbf{F}^{-1}\boldsymbol{\sigma}\mathbf{F}^{-\mathbf{T}}, \ \mathbf{P} = \mathbf{F}\mathbf{S} \qquad \textbf{(4.26)}$$

Muscle can be considered as a quasi-incompressible hyper-elastic, transversely isotropic material (Namani & Bayly, 2010). The Jacobian and the hydrostatic pressure can therefore be modelled with the inclusion of a penalty function, where D is large, and J approaches and asymptotes towards 1.

$$\int_v \delta\rho_h \frac{1}{D_1}(J-1)dVol = 0 \qquad \textbf{(4.27)}$$

The hydrostatic pressure is denoted by ρ_h, which is to be derived, and the incompressibility parameter is defined as D_1. The Jacobian (det[**F**]) is J.

4.1.6 Determining Stress Measures Using Strain Energy Density Functions

When considering hyper-elastic materials, the second Piola-Kirchhoff stress is calculated from the strain energy function (SEF) (Belytschko et al. (2000)):

$$S = \frac{d\psi(\mathbf{E})}{d\mathbf{E}} = 2\frac{dW_{SEF}(\mathbf{C})}{d\mathbf{C}} \qquad \textbf{(4.28)}$$

Therefore, from the definition of $\mathbf{E}$ in Equation **4.28**:

$$W(\mathbf{C}) = \psi(2\mathbf{E}+\mathbf{I}) \qquad \textbf{(4.29)}$$

Thus, substituting Equation **4.28** into the Equation **4.26**, the Cauchy stress, $\boldsymbol{\sigma}$ can be calculated by:

$$\boldsymbol{\sigma} = 2J^{-1}\mathbf{F}\frac{dW_{SEF}(\mathbf{C})}{d\mathbf{C}}\mathbf{F}^{\mathbf{T}} \qquad \textbf{(4.30)}$$

4.2 Hyper-elastic Constitutive Relationships

The isotropy of a constitutive material can be expressed and represented by the invariants of the right Cauchy-Green deformation tensor. There are nine invariants ($I_{1\text{-}9}$) in total – however only five are required when modelling an isotropic constitutive relationship. A transversely isotropic material can be considered as an isotropic material with one family of fibres embedded in its matrix (Lieber & Friden, 2000), and therefore skeletal muscle has previously been modelled as an implicit fibre-

reinforced material (Limbert & Taylor, 2002). This simplification allows for the general mechanical response considerations of the fibres but limits the complexity of traction and visco-elasticity of the fibre-fibre interactions. An illustrative diagram of the implicit concept of the muscle as a fibre-reinforced material is shown in Figure **4.2**.

A transversely isotropic material models the base matrix as an isotropic material, and the fibre stretch will introduce anisotropy. These two factors can be incorporated in the total SEFs selected later. Accordingly, the fibres will deform according to the deformation configuration of the full body. This can be quantified by the following relationship given by Martins et al. (1998):

$$\lambda_f \mathbf{n} = \mathbf{F} \bullet \mathbf{N} \qquad \textbf{(4.31)}$$

where λ_f is the fibre stretch ratio in the direction of the undeformed fibre and **n** is a unit vector in the current configuration, with **N** a unit vector in the undeformed configuration (principal direction of the fibres).

Spencer states that the fourth and fifth invariants are the most appropriate for use to model the mechanical response induced by reinforced fibres, for transversely isotropic materials (Spencer, 1984). The concept of muscle tissue as a fibre reinforced material is illustrated in Figure **4.2**. The strain energy function can therefore be expressed with respect to invariants 1 to 5 of the right Cauchy-Green deformation tensor:

$$W(\boldsymbol{C}) = W(I_1, I_2, I_3, I_4, I_5)$$

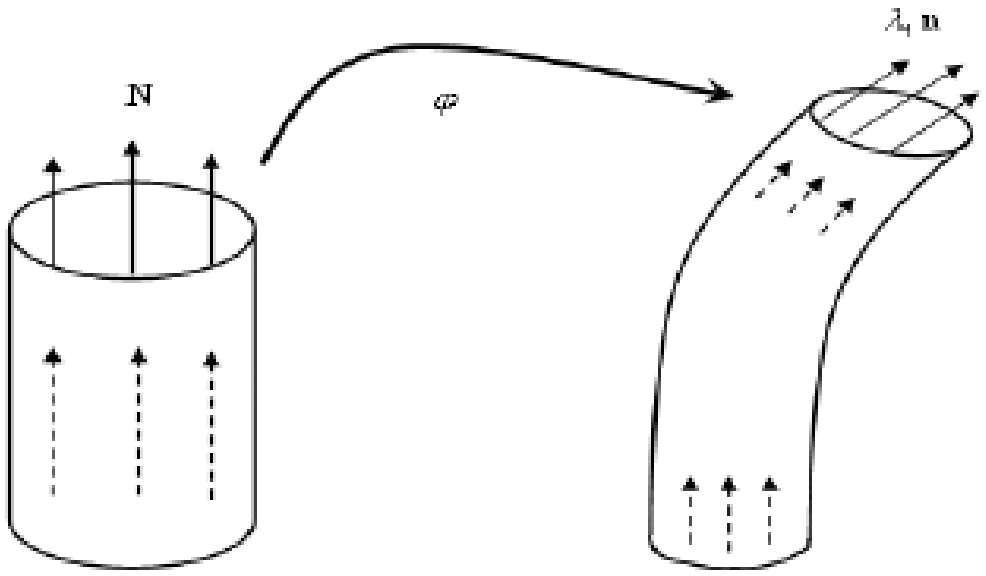

Figure 4.2 Representation of the fibre direction in an implicitly modelled fibre-reinforced material

Image taken from: Limbert, G. and Taylor, M. (2002).

The Piola-Kirchhoff stress of the body can therefore be derived using the following function irrespective of the loading conditions (uniaxial, biaxial or shear loading) (Weiss, 1996):

$$\mathbf{S} = 2\sum_{i=1}^{5} \frac{dW_{SEF}}{dI_1}\frac{dI_1}{d\mathbf{C}} + \rho\mathbf{C}^{-1} = 2\sum_{i=1}^{5} \frac{dW_{SEF}}{d\mathbf{C}} + \rho\mathbf{C}^{-1} \qquad \textbf{(4.32)}$$

Therefore,

$$\mathbf{S} = 2(W_1 + I_1W_2)\mathbf{I} - 2W_2\mathbf{C} + 2I_3W_3\mathbf{C}^{-1} + W_4\mathbf{N}\otimes\mathbf{N} + W_5(\mathbf{N}\otimes\mathbf{C}.\mathbf{N} + \mathbf{N}.\mathbf{C}\otimes\mathbf{N}) \qquad \textbf{(4.33)}$$

The invariants can therefore be expressed in terms of the principal stretches as derived by Spencer (1984).

$$for\ I(\lambda);$$

$$I_1 = \lambda_1^2 + \lambda_2^2 + \lambda_3^2 \qquad \textbf{(4.34)}$$

$$I_2 = \lambda_1^2\lambda_2^2 + \lambda_2^2\lambda_3^2 + \lambda_3^2\lambda_1^2 = \frac{1}{2}((tr\boldsymbol{C})^2 - tr\boldsymbol{C}^2) \qquad \textbf{(4.35)}$$

$$I_3 = \lambda_1^2\lambda_2^2\lambda_3^2 = det\boldsymbol{C} = J^2 \quad \textbf{(4.36)}$$

$$I_4 = \boldsymbol{N} \otimes \boldsymbol{N}: \boldsymbol{C} \quad \textbf{(4.37)}$$

$$I_5 = \boldsymbol{N} \otimes \boldsymbol{N}: \boldsymbol{C^2} \quad \textbf{(4.38)}$$

The derivatives of the right Cauchy-Green deformation tensor with respect to the invariants are therefore the following:

$$\frac{\partial I_1}{\partial \boldsymbol{C}} = \boldsymbol{I} \quad \textbf{(4.39)}$$

$$\frac{\partial I_2}{\partial \boldsymbol{C}} = I_1\boldsymbol{I} - \boldsymbol{C} \quad \textbf{(4.40)}$$

$$\frac{\partial I_3}{\partial \boldsymbol{C}} = I_2\boldsymbol{I} - I_1\boldsymbol{C} + I_3\boldsymbol{C}^{-1} \quad \textbf{(4.41)}$$

$$\frac{\partial I_4}{\partial \boldsymbol{C}} = \boldsymbol{N} \otimes \boldsymbol{N} \quad \textbf{(4.42)}$$

$$\frac{\partial I_5}{\partial \boldsymbol{C}} = \boldsymbol{N} \otimes \boldsymbol{C}.\boldsymbol{N} + \boldsymbol{N}.\boldsymbol{C} \otimes \boldsymbol{N} \quad \textbf{(4.43)}$$

Where $I_{1\text{-}5}$ = 1-5th invariants, **N** is a unit vector to represent the fibre direction in the undeformed configuration. **C** represents the right Cauchy-Green deformation tensor and **I** is a second order unit tensor.

Provided;

$$W_i = \frac{\partial W}{\partial I_i};\ i = 1,2,3,4,5 \quad \textbf{(4.44)}$$

Based on the mathematical formulations above we can separate the SEF into two compartments for a quasi-incompressible hyper-elastic material, where one

compartment accounts for the volumetric contribution expressed with respect to the Jacobian, and the other compartment is expressed considering the deviatoric contribution.

Therefore, the second Piola-Kirchhoff stress can be written as:

$$\mathbf{S} = \frac{dW_{vol}}{dJ} J\mathbf{C}^{-1} + 2J^{-2/3} DEV\left[\frac{dW_{dev}}{d\mathbf{C}}\right] \quad \textbf{(4.45)}$$

The Cauchy stress can therefore be derived as:

$$\boldsymbol{\sigma} = \frac{dW_{vol}}{dJ}\mathbf{I} + \frac{2}{J} dev\left[\bar{\mathbf{F}}\frac{dW_{dev}}{d\mathbf{C}}\bar{\mathbf{F}}\right] \quad \textbf{(4.46)}$$

The function dev[x] is defined by Weiss (1996) as shown below:

$$dev[x] = [x] - \frac{1}{3}(x:\boldsymbol{I})\boldsymbol{I} \quad \textbf{(4.47)}$$

These functions will therefore allow for the explicit Cauchy stress and stretch ratio to be calculated to compare the mechanical response of the materials, based on the constitutive equations chosen. The next section will explore this in more detail.

4.2.1 The Strain Energy Density Function of Skeletal Muscle Tissue

As skeletal muscle is a fibre reinforced transversely isotropic material, an equation that can define the fibrous anisotropic behaviour, as well as the isotropic base-matrix behaviour of the muscle and tendon constituents must be considered and used. The Holzapfel et al., (2000) constitutive relationship is one of the most widely used formula for modelling this type of material, where the isotropic response is expressed with respect to the first invariant (I_1), the first family of fibres are expressed in terms of the fourth invariant (I_4), and the second family of fibres are expressed in

terms of the sixth invariant (I_6). The strain energy function used in the current work is taken from Holzapfel et al. (2000) takes the form:

$$W_{SEF} = W_{SEF}(I_1, I_4, I_6) = c_1(I_1 - 3) + (\frac{k_1}{2k_2} e^{k_2(I_4-1)^2} - 1) + (\frac{y_1}{2y_2} e^{y_2(I_6-1)^2} - 1) \quad \textbf{(4.48)}$$

Where W is the strain energy function, and C_1 is the isotropic constant, usually measured in MPa. Parameters k_1 and y_1 are anisotropic constants of the first and second families of fibres, respectively, and are measured in MPa. Parameters k_2 and y_2 are also anisotropic constants of the first and second fibre families respectively, which are dimensionless. The isotropic response tends to represent the base or bulk response, while the anisotropic response represents the fibre response.

This strain energy function represents the isotropic and anisotropic summative contribution to the total Cauchy stress, based on the idealisation that muscle tissue consists of a family of two types of fibres embedded in an isotropic ground matrix.

These invariants are expressed in terms of the right (**C**) and left (**B**) Cauchy-Green deformation tensor, which takes the form:

$$\mathbf{C} = \begin{bmatrix} C_{11} & C_{12} & 0 \\ C_{21} & C_{22} & 0 \\ 0 & 0 & C_{33} \end{bmatrix} = \mathbf{F}^{\mathbf{T}}\mathbf{F}$$

since:

$$\mathbf{F} = \begin{bmatrix} F_{11} & F_{12} & 0 \\ F_{21} & F_{22} & 0 \\ 0 & 0 & F_{33} \end{bmatrix} = \begin{bmatrix} \lambda_{11} & \lambda_{12} & 0 \\ \lambda_{21} & \lambda_{22} & 0 \\ 0 & 0 & \lambda_{33} \end{bmatrix} \quad \textbf{(4.49)}$$

$\therefore$

$$\mathbf{C} = \begin{bmatrix} \lambda^2_{11} & \lambda_{12}\lambda_{21} & 0 \\ \lambda_{21}\lambda_{12} & \lambda^2_{22} & 0 \\ 0 & 0 & \lambda^2_{33} \end{bmatrix} = \mathbf{F}^{\mathbf{T}}\mathbf{F}$$

Note that;

$$\mathbf{C}^{-1} = \begin{bmatrix} C_{11}C_{33} & -C_{12}C_{33} & 0 \\ -C_{21}C_{33} & C_{22}C_{33} & 0 \\ 0 & 0 & C_{33}^{-1} \end{bmatrix} = \mathbf{B}$$

The Cauchy, first and second Piola-Kirchhoff stress terms can therefore be derived following the above conjecture, shown specifically in Equation **4.50**, and the strain energy function shown in Equation **4.48**, as the following:

$$\begin{aligned} \boldsymbol{\sigma} &= -p\mathbf{I} + 2W_1\mathbf{B} + 2W_4(\mathbf{m}\otimes\mathbf{m}) + 2W_6(\mathbf{n}\otimes\mathbf{n}) \\ \mathbf{P} &= \left(-p\mathbf{I} + 2W_1\mathbf{B} + 2W_4(\mathbf{m}\otimes\mathbf{m}) + 2W_6(\mathbf{n}\otimes\mathbf{n})\right)\mathbf{F}^{-T} \\ \mathbf{S} &= \left(-p\mathbf{I} + 2W_1\mathbf{B} + 2W_4(\mathbf{m}\otimes\mathbf{m}) + 2W_6(\mathbf{n}\otimes\mathbf{n})\right)\mathbf{F}^{-1}\mathbf{F}^{-T} \end{aligned} \qquad \textbf{(4.50)}$$

Where;

$$\begin{aligned} W_i &= \frac{dW}{dI_i} \\ i &= 1,4,6 \end{aligned} \qquad \textbf{(4.51)}$$

The invariants are expressed in terms of the axial stretches, as derived by Spencer (1984):

$$\begin{aligned} I_1 &= tr(\mathbf{C}) = \lambda^2{}_{11} + \lambda^2{}_{22} + \lambda^2{}_{33} \\ I_4 &= \mathbf{m}\otimes\mathbf{m} = \left(\lambda_{11}\cos\alpha + \lambda_{12}\sin\alpha\right)^2 + \left(\lambda_{21}\cos\alpha + \lambda_{22}\sin\alpha\right)^2 \\ I_6 &= \mathbf{n}\otimes\mathbf{n} = \left(\lambda_{11}\cos\beta + \lambda_{12}\sin\beta\right)^2 + \left(\lambda_{21}\cos\beta + \lambda_{22}\sin\beta\right)^2 \end{aligned} \qquad \textbf{(4.52)}$$

Noting the following from Holzapfel & Ogden (2009):

$$\begin{aligned} \mathbf{m} &= \mathbf{F}\begin{bmatrix} \mathbf{m}_1 \\ \mathbf{m}_2 \\ 0 \end{bmatrix} = \mathbf{F}\begin{bmatrix} \cos\alpha \\ \sin\alpha \\ 0 \end{bmatrix} = \begin{bmatrix} F_{11}\cos\alpha + F_{12}\sin\alpha \\ F_{21}\cos\alpha + F_{22}\sin\alpha \\ 0 \end{bmatrix} \\ \mathbf{n} &= \mathbf{F}\begin{bmatrix} \mathbf{n}_1 \\ \mathbf{n}_2 \\ 0 \end{bmatrix} = \mathbf{F}\begin{bmatrix} \cos\beta \\ \sin\beta \\ 0 \end{bmatrix} = \begin{bmatrix} F_{11}\cos\beta + F_{12}\sin\beta \\ F_{21}\cos\beta + F_{22}\sin\beta \\ 0 \end{bmatrix} \end{aligned} \qquad \textbf{(4.53)}$$

Hence enabling the evaluation of the following from Equation **4.51**:

$$\begin{aligned} W_1 &= c_1 1 \\ W_4 &= k_1 (I_4 - 1) e^{k_2 (I_4 - 1)^2} \\ W_6 &= y_1 (I_6 - 1) e^{y_2 (I_6 - 1)^2} \end{aligned} \tag{4.54}$$

For pure homogeneous planar biaxial deformation of the cuboid the Cauchy stress components can be written as:

$$\begin{aligned} &\sigma_{ij} = -p + 2W_1 B_{ij} + 2W_4 m_i m_j + 2W_6 n_i n_j \\ &i = 1, 2, \\ &j = 1, 2, \\ &\sigma_{33} = -p + 2W_1 B_{33} \end{aligned} \tag{4.55}$$

Adopting the assumption that $\sigma_{33} = 0$, ρ can be eliminated and the Cauchy stress term can be expressed so as to elucidate the specific stress terms that have been used for the analytical solution:

$$\begin{aligned} &\sigma_{ij} = -2W_1 B_{33} + 2W_1 B_{ij} + 2W_4 m_i m_j + 2W_6 n_i n_j \\ &i = 1, 2, \\ &j = 1, 2, \end{aligned} \tag{4.56}$$

4.2.2 Analytical Formulation of Uniaxial Loading

During uniaxial loading, the deformation gradient can be defined by the referential stretch according to the following relationship:

$$\mathbf{F} = \begin{bmatrix} F_{11} & F_{12} & 0 \\ F_{21} & F_{22} & 0 \\ 0 & 0 & F_{33} \end{bmatrix} = \begin{bmatrix} \lambda_{11} & \lambda_{12} & 0 \\ \lambda_{21} & \lambda_{22} & 0 \\ 0 & 0 & \lambda_{33} \end{bmatrix} = \begin{bmatrix} \lambda & 0 & 0 \\ 0 & \frac{1}{\sqrt{\lambda}} & 0 \\ 0 & 0 & \frac{1}{\sqrt{\lambda}} \end{bmatrix} \tag{4.57}$$

so that the condition of incompressibility is satisfied:

$$\lambda_{11}.\lambda_{22}.\lambda_{33} = 1$$

and as it is in homogenous uniaxial (or biaxial) tension, the following conditions must also be satisfied, where sheer stresses are not considered in the analytical and one-dimensional numerical investigations.

Material symmetry is a material property that considers the way in which a materials' mechanical response changes in relation to its axis of loading. Orthotropic materials have a material rotational symmetry order of 2 and isotropic materials have an infinite order of material rotational symmetry; that is – the material will respond uniformly in all directions (Humphrey, 2013; Holzapfel, et al., 2015). Transversely orthotropic materials are unique orthotropic materials that have only one order of material rotational symmetry, therefore only the orthogonal components are considered, hence:

$$\lambda_{12} = \lambda_{21} = 0$$

Therefore, the referential stretch can be defined as:

	$\lambda_{11} = \lambda$ $\lambda_{22} = \lambda_{33} = \frac{1}{\sqrt{\lambda}}$	**(4.58)**

4.2.3 Analytical Formulation of Biaxial Loading

During biaxial loading, like Equation **4.57**, the deformation gradient is defined by the referential stretch using the following definition:

$$\mathbf{F} = \begin{bmatrix} \lambda & 0 & 0 \\ 0 & \lambda & 0 \\ 0 & 0 & \frac{1}{\lambda^2} \end{bmatrix} \tag{4.59}$$

The orthogonal (principal) components of the referential stretch can therefore be defined as:

$$\lambda_{11} = \lambda_{22} = \lambda$$
$$\lambda_{33} = \frac{1}{\lambda^2}$$

These stretches can be used to determine the invariants of the Cauchy-Green deformation tensor, and hence the analytical formulation that will be used to verify the numerical implementation in ANSYS.

The numerical simulation is a cube of muscle tissue that is being loaded uniformly in one direction (uniaxial) and homogenously in two directions (biaxial). The mathematical formulations above explicitly show the analytical formulation that was used for comparison with the numerical simulations. The cubes that were extended numerically required material constants for the numerical model defined by the strain energy density function of Holzapfel et al. (2000). The material constants were carefully selected as reported below.

4.3 Determining the Material Constants

There are various material models that have been used to define strain energy functions that are like the constitutive model of Holzapfel et al. (2000). Whilst Holzapfel et al. (2000) created a model for arterial wall tissue, as shown in Equation **4.48**, their work has been widely used to model other biological fibrous tissues. Since the muscle and tendon lie adjacent to each other and their tissue constituents are similar (both modelled as fibre-reinforced materials), a careful selection of material constants has been carried out so that this model can be used to represent muscle and tendon tissue accurately in the current simulations as an assembly of different fibre reinforced materials. Firstly, a comprehensive search of constitutive models for

skeletal muscle or tendon tissue were considered and reviewed for similarities – some of the models considered are shown in Table **4.1**.

Table 4.1 Constitutive relationships from the literature with the tissue representation, constitutive equations and respective material constants used.

Author	Tissue Type	Const. Relationship	Material Constants
Taglialavoro et al. (2005)	Cyclic Loading Human Tendon	$\bar{\psi} = c_1(\bar{I}_1 - 3) + c_2(\bar{I}_2 - 3) + ...$ $...\left(\frac{c_3}{\gamma}\left(e^{\gamma(\bar{I}_4-1)^2} - \gamma(I_4 - 1) - 1\right)\right)$	C_1 = 1.0 [MPa]; C_2 = 2.0 [MPa]; C_3 = 4 [MPa]; γ = 10 [-];
Blemker et al. (2005)	Bicepts Bracchi Muscle, Tendon/Aponeurosis Fascicles	$f_{pass}^{fiber} = P_1(e^{P_2\left(\lambda/\lambda_{ofl}-1\right)} - 1);$ when $\lambda_{ofl} < \lambda < \lambda^*$ $\sigma^{tendon}(\lambda) = L_1(e^{L_2(\lambda-1)} - 1);$ when $1.0 < \lambda < \lambda^*$	P_1 = 0.05 [-]; P_2 = 6.6 [-]; λ^*_{musc} = 1.4 [-]; λ^*_{apon} = 1.03 [-]; L_1 = 2.7 [MPa]; L_2 = 46.4 [-];
Ehret et al. (2010)	Rat Tibialis Anterior Skeletal Muscle.	$\psi = \frac{\mu}{4}\left\{\frac{1}{\alpha}[e^{\alpha(I_p-1)} - 1] + \frac{1}{\beta}[e^{\beta(\tilde{\kappa}-1)} - 1]\right\}$	μ = 0.159 [kPa]; α = 19.69 [-]; β =1.19 [-];
Calvo et al. (2010a)	Rat Tibialis Anterior Skeletal Muscle	$\psi = \left[C_1(\bar{I}_1 - 3)\right] + \left[\frac{C_3}{C_4}\left(e^{C_4(\bar{I}_4-\bar{I}_{4_0})} - C_4(\bar{I}_4 - \bar{I}_{4_0}) - 1\right)\right],\ \bar{I}_4 > \bar{I}_{4_0} \text{ and } \bar{I}_4 < \bar{I}_{4ref}$ $\psi = \left[C_1(\bar{I}_1 - 3)\right] + \left[C_5\sqrt{\bar{I}_4} + \frac{1}{2}C_6\ln(\bar{I}_4) + C_7\right],\ \bar{I}_4 > \bar{I}_{4_{ref}}$	C_1=0.0088 [MPa]; C_3= 0.0099 [MPa]; C_4=2.237; C_5=3.064 [MPa]; C_6=-4.7596; C_7= -2.7635 [MPa];
Calvo et al. (2010b)	Rat Tibialis Anterior Tendon	$\psi = \left[C_1(\bar{I}_1 - 3)\right] + \left[\frac{C_3}{C_4}\left(e^{C_4(\bar{I}_4-\bar{I}_{4_0})} - C_4(\bar{I}_4 - \bar{I}_{4_0}) - 1\right)\right],\ \bar{I}_4 > \bar{I}_{4_0} \text{ and } \bar{I}_4 < \bar{I}_{4ref}$ $\psi = \left[C_1(\bar{I}_1 - 3)\right] + \left[C_5\sqrt{\bar{I}_4} + \frac{1}{2}C_6\ln(\bar{I}_4) + C_7\right],\ \bar{I}_4 > \bar{I}_{4_{ref}}$	C_1=0.081 [MPa]; C_3= 0.045 [MPa]; C_4=7.57; C_5=58.007 [MPa]; C_6=-66.7; C_7= -57.33 [MPa];
Roerhle et al. (2013)	Chemo-Electro-Mechanical Model	$\psi = c_1(I_1 - 3) + c_2(I_2 - 3) + \left(\frac{b}{d}(\lambda_f^d - 1) - b\ln\lambda_f\right)$	C_1=6.352e^{-10} [kPa]; C_2 = 3.627 [kPa]; b=2.75 e^{-5} [kPa]; d = 43.373 [-];
Shearer (2015)	Human Tendon	$\psi = (1-\phi)\frac{\mu}{2}(I_1 - 3),\ I_4 < 1,$ $\psi = (1-\phi)\frac{\mu}{2}(I_1 - 3) + \frac{\phi E}{6sin^2\theta_\sigma}\left(4\sqrt{I_4} - 3\log(I_4) - \frac{1}{I_4} - 3\right),$ $1 \le I_4 \le \frac{1}{cos^2\theta_\sigma},$ $\psi = (1-\phi)\frac{\mu}{2}(I_1 - 3) + \phi E\left(\beta\sqrt{I_4} - \frac{1}{2}\log(I_4) + \eta\right),$ $I_4 > \frac{1}{cos^2\theta_\sigma},$	$0 < \Phi < 1$; μ=0.01 MPa]; k_1 = 25 [MPa]; k_2 = 183 [-]; ΦE = 552 [MPa]; θ = 0.19 rad;
Bajuri et al. (2016)	Ageing Human Tendon	$\bar{\psi} = \frac{c_1}{2}(I_1 - 3) + \left(\frac{k_1^{'}}{k_2^{'}}\left(e^{k_2^{'}[\kappa\bar{I}_4 + (1-3\kappa)I_4 - 1)^2} - 1\right)\right)$	C_1 = 0.00046[MPa]; k_1 = 9.127 [MPa]; k_2 = 1.6 [-]; κ =0 [-];

Whilst Table **4.1** is not exhaustive, currently, no skeletal muscle data is available in the literature with exactly the same mathematical form as that used in this thesis (Holzapfel et al., 2000). The Holzapfel et al., (2000) constitutive relationship was chosen due to its wide application to previous soft tissue models (Bajuri, et al., 2016; Holzapfel & Ogden, 2009; Holzapfel, et al., 2000; Roehrle & Pullan, 2007), its availability in ANSYS for finite element modelling, and its ability to represent the structural features of the anatomical muscle model. The Holzapfel et al. (2000) constitutive relation contains several material properties (see Equation **4.48**). The stress-stretch response of this constitutive relationship can be plotted to illustrate the relative contribution of each parameter. These are shown in Figure 4, where the isotropic contribution of the model represents the base matrix constituent and the anisotropic contribution represents the fibrous. Please note arbitrary numbers within the representative range are used for C1, k1 and k2 in these plots.

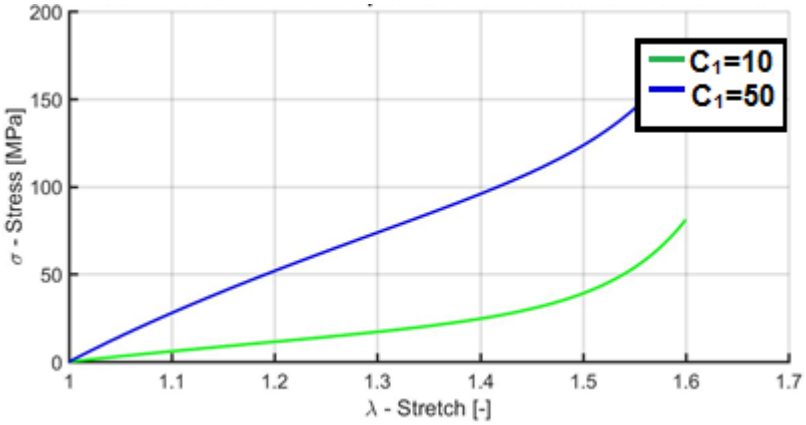

Figure 4.3a

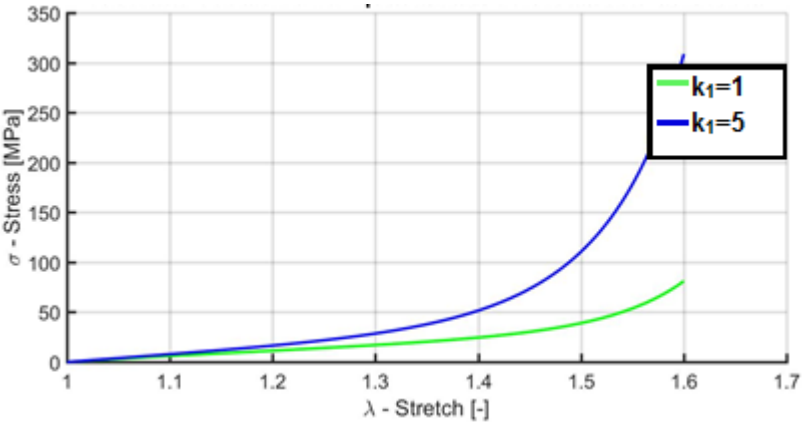

Figure 4.3b

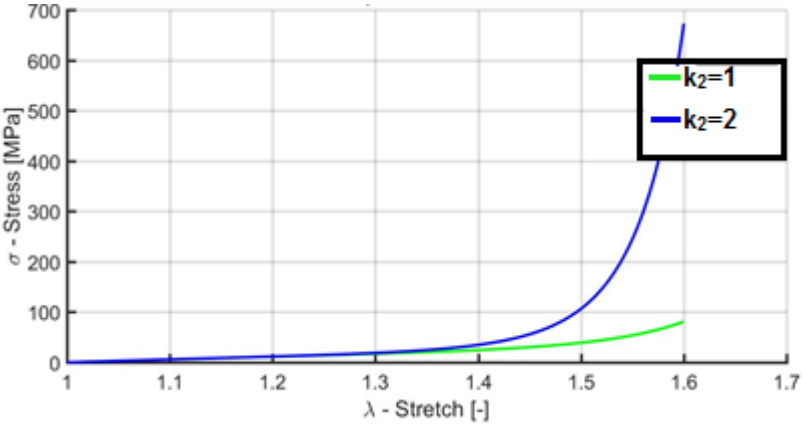

Figure 4.3c

Figure 4.3 Comparing the effects on the strain energy function used from Holzapfel et al. (2000) of changing C_1 (a), k_1 (b) and k_2 (c) in terms of the total stress contribution of the first Piola-Kirchhoff stress.

It is clear from Figures **4.3**a-c that k_1 has a marked effect on both the gradient and stiffness of the constitutive model for small to medium levels of stretches (e.g. stretch over 1.1), whereas k_2 has a much bigger effect at higher stretches (more than 1.4). The parameter k_2 provides a rapid stiffening response to prevent permanent tissue damage when approaching the stretch limit. The effect of C_1 lies predominantly within the isotropic linear region. Therefore, when estimating these parameters, particular care has been taken to optimise for k_1 and k_2, in order to ensure a reasonable non-linear response of the muscle and tendon tissues. The C_1 values for muscle and tendon were taken directly from the literature, if the same isotropic linear behaviour would be expected for the ground matrix substances.

4.3 Determining the Material Properties of the tendon

Calvo et al., (2010b) reported the stress-stretch data of rat tibialis anterior tendon tissues under uniaxial tension. It should be noted that Calvo et al., (2010a and b) used a slightly different form of constitutive equation compared with the one selected in this thesis from Holzapfel et al., (2000). It was assumed that the same C_1 value from Calvo et al., (2010b) could be used in Holzapfel et al., (2000). And parameters k_1 and k_2 were then optimised to fit the Calvo et al., (2010b) data using the Levenberg-Marquardt algorithm in MATLAB[1] (Levenberg, 1944) (see Figure 4.1). The final material parameters (C_1 and k_1) for muscle are listed in Tables 4.2. The value of Parameter k2 has been checked against that in Bajuri et al. (2016) to ensure it was within the range of those previously reported in the literature.

[1] Matlab is a multi-paradigm platform that is used for numerical computing. It provides a mathematical and engineering computing environment and consists of a proprietary programming language developed by MathWorks. www.mathworks.com

Determining the Material Properties of the Tendon

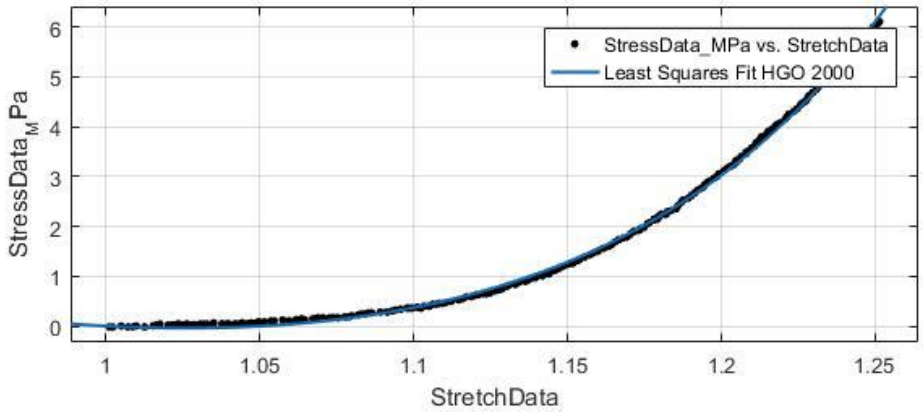

Figure 4.4 Final material parameters to be used for tendon. Parameters k1 and k2 have been optimised based on Calvo et al. (2010b) data. C1 is taken directly from the value used in Calvo et al. (2010b) as shown in Table 4.2.

Table 4.2 Final Material properties used for Tendon

Material constants	C_1 **[MPa]**	k_1 **[MPa]**	k_2 **[-]**	R^2 value
Tendon	0.08124	0.1047	0.1356	0.9986

A similar approach was adopted to determine the material constants for the muscle constituents using the same strain energy function. The methods used to determine the Material properties of the muscle are discussed in the next section.

Determining the Material Properties of the Muscle

For the muscle tissue, Calvo et al (2010a) provided stress-stretch data for rat tibialis anterior skeletal muscle. Like the tendon, the same C1 value estimated in Calvo et al (2010a) was assumed in Holzapfel et al., (2000) to reflect a similar isotropic response. In order to reduce the number of parameters to be optimised against experimental data, only k1 was optimised here against data reported in Calvo et al (2010a), unlike in the case of tendon where both k1 and k2 were optimised. The

decision to optimise k1 was based on the observation made in Figure 4.3, which showed k1 to be the most influential factor in a low to medium stretch range.

In order to find the muscle-specific parameter for k2, a muscle-tendon parameter ratio of 0.1083 was determined based on the two k2 values reported in the two Calvo et al (2010a and b) studies. This ratio was then applied to the k2 value estimated for tendon in the previous section in order to obtain the new k2 value for muscle in the Holzapfel et al., (2000) formula. The Calvo et al (2010a) data was then used to optimise for k1 as shown in Figure 4.5 below. The final parameters estimated for modelling muscle are illustrated in Table 4.3.

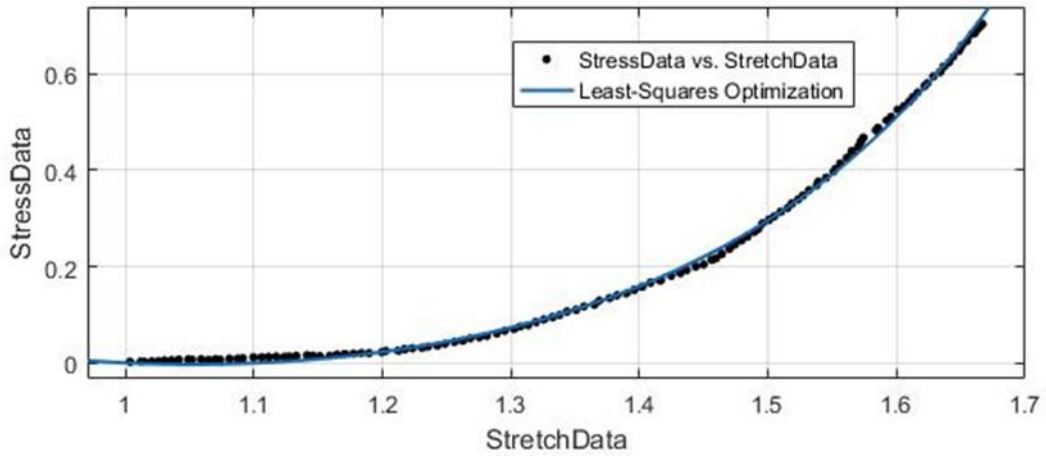

Figure 4.5 Final material parameters to be used for muscle. Parameters k1 and k2 have been optimised based on Calvo et al. (2010a) data. C1 is taken directly from the value used in Calvo et al. (2010a) as shown in Table 4.3

Table 4.3 Final material properties used for Muscle

Material constants	C_1 **[MPa]**	k_1 **[MPa]**	k_2 **[-]**	R^2 value
Muscle	0.0088	2.65	1.244	0.9992

4.4 Numerical Simulation Implementation and Verification

All finite element models with complex geometry and material property are solved numerically via an iterative process. The selection of the boundary constraints, material parameters and solution algorithms will affect model convergence. It would therefore be desirable to start with simplified FE models, before adding complexity, in order to check for predictive accuracy and resolve potential convergence issues. This was done by first using a cuboid geometry to approximate the muscle-tendon complex and compare its numerical results with benchmark analytical solutions. This section describes the boundary conditions and implementation process carried out to construct and verify the cuboid model.

4.4.1 ANSYS Numerical Implementation

Based on the derivation of the stress and strains in continuum mechanics, the strain energy function (W) used in ANSYS is similar to that defined in Equation **4.48**, which takes the form:

$$W = \sum_{i=1}^{3} c_i (\bar{I}_1 - 3)^i + \sum_{j=1}^{3} d_j (\bar{I}_2 - 3)^j + \frac{g_1}{2g_2}\left(e^{c_2(\bar{I}_4-1)^2} - 1\right) + \frac{E_1}{2E_2}\left(e^{E_2(\bar{I}_6-1)^2} - 1\right) \quad \textbf{(4.60)}$$

With c_i and d_i being the respective isotropic constants that attribute to the first and second invariants of the Cauchy-Green deformation tensor ($\bar{I}_1$ and $\bar{I}_2$), respectively. g_1 & g_2 and E_1 & E_2 are the anisotropic material constants for the first and second family of fibres, respectively, that attribute to the fourth and sixth invariants of the Cauchy-Green deformation tensor ($\bar{I}_4$ and $\bar{I}_6$), respectively.

This strain energy function was implemented into discrete elements in ANSYS by means of an input file that was applied to define the material model for one element in ANSYS. The block of code that was applied is shown by the **TB, AHYPER** command:

TB, AHYPER, , , EXPO
TBDATA, 1, $c_1, c_2, c_3, d_1, d_2, d_3,$
TBDATA,7, g_1, g_2, E_1, E_2

Note that the following model congruency from the strain energy density function from Holzapfel et al. (2000) (Equation **4.48**) and the strain energy density function from ANSYS apply as shown in Tables 4.4 and 4.5, where either the first or the second family of fibres were used (i.e., entered as 0, or their respective value, depending on the constituent)

Table 4.4a Congruency of material parameters used in strain energy functions from ANSYS and Holzapfel et al., (2000).

ANSYS Parameter	Holzapfel et al. (2000)	Value [Units]
c_1	C_1	0.081 [MPa]
c_2	n/a	-
c_3	n/a	-
d_1	n/a	-
d_2	n/a	-
d_3	n/a	-
g_1	k_1	35.04 [MPa] or 0
g_2	k_2	1.6 [-] or 0
E_1	y_1	0 or 4.10250 [MPa]
E_2	y_2	0 or 0.04728 [-]

The fibre directions are defined with respect to the unit vectors, as shown in Equation **4.53**, where **m** attributes to the fourth invariant $\bar{I}_4$ which concerns the unit vectors of the first family of fibres, and **n** attributes to the sixth invariant $\bar{I}_6$ which concerns the unit vectors of the second family of fibres. Hence, the following congruency exists when defining the fibre directions in ANSYS:

TB, AHYPER, , , AVEC
TBDATA,, A_1, A_2, A_3,

TB, AHYPER, , , BVEC
TBDATA,, B_1, B_2, B_3,

Table 4.5 Congruency of unit vectors used in strain energy functions from ANSYS and Holzapfel et al., (2000).

ANSYS Parameter	Holzapfel et al. (2000)	Value
A_1	m_1	1
A_2	m_2	0
A_3	m_3	0
B_1	n_1	0
B_2	n_2	1
B_3	n_3	0

Since the material model defined by Holzapfel et al. (2000) is an incompressible hyper-elastic transversely isotropic material, incompressibility had to also be enforced in ANSYS for the numerical implementation. The command that enabled this is shown below:

TB, AHYPER, , , PVOL
TBDATA,, D_1,

The PVOL command defines the volumetric potential of the material body, which is defined by its volumetric deformation ($\mathbf{F_{vol}}$) shown in Equation **4.18**. This can be explicitly defined as $\mathbf{F_{vol}} = \frac{1}{D_1}(\mathbf{J}-1)^2$, where D_1 is the incompressibility parameter with a unit of MPa^{-1} (or $\frac{1}{MPa}$), and acts as a penalty function, and hence enforcing incompressibility in each element.

4.4.2 Boundary Conditions

A cube was produced in ANSYS, of the dimensions 10mm x 10mm x 10mm. A tetrahedral mesh was fitted onto the cuboid, each with the longest side-length of 1mm. There were 2415 nodes and 1233 elements with a mesh density of 1.233 elements/mm^3. An image of the mesh is shown below;

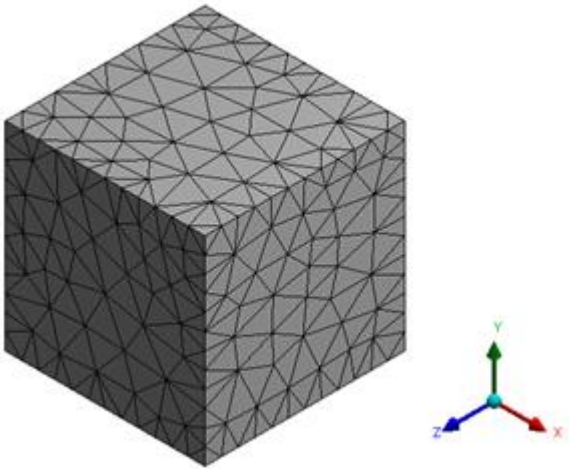

Figure 4.6 The mesh of the cube used for the simple numerical simulations to compare to analytical simulations.

A displacement of 1mm (10%) was applied in the X direction of the cuboid, where the opposing side was fixed across all nodes (Gauss points) in the X direction only, and free in the Z and Y, apart from the nodes at the corners (vertices) of the cube opposing the displaced face. As shown in Figure. 4.7(a) & Figure. 4.7(c). For stability, the node shown in Figure. 4.7(c) was fixed in the X, Y and Z direction. In Figure.

4.7(b) the node highlighted (yellow) was fixed in the X and the Y directions leaving the Z direction free, where Figure. 4.7(d) was fixed in the X and Z direction, but free to move in the Y. This was done to satisfy uniform uniaxial deformation in the numerical simulation.

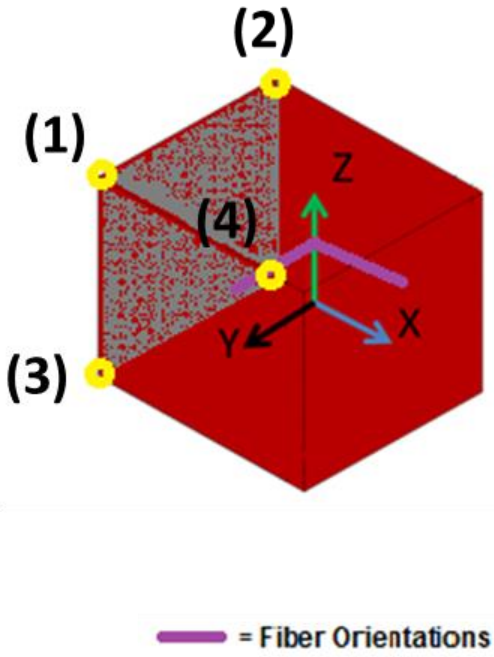

Figure 4.7 Boundary conditions for a cube with representative fibres directions (purple) in the x and y axes. Back face (grey) nodes were all fixed in x direction, free to move in z and y axes. Node 1 (yellow) was free to move in all directions. Node 2 was fixed in x and y directions, and free to move in z. Node 3 was fixed in x and z direction, and free to move in the y direction. Node 4 was fixed in X, Y and Z direction.

These boundary conditions were applied for uniaxial loading in the x direction, followed by equibiaxial loading in the x and y direction. This was done because the constituent is modelled as incompressible, therefore as deformation occurs, the cross-sectional area of the cube will change, correspondingly.

4.4.3 Numerical Verification of Uniaxial and Biaxial Loading against the Analytical Solution Results

The simulation for a uniaxially loaded 1 mm cube was carried out, as implemented from the boundary conditions in Figure 4.7. This was done to extrapolate uniform stress numerical results that could then be compared to the analytical solutions. The deformed cuboid is shown in the Figure **4.8** in both uniaxial and biaxial loading conditions.

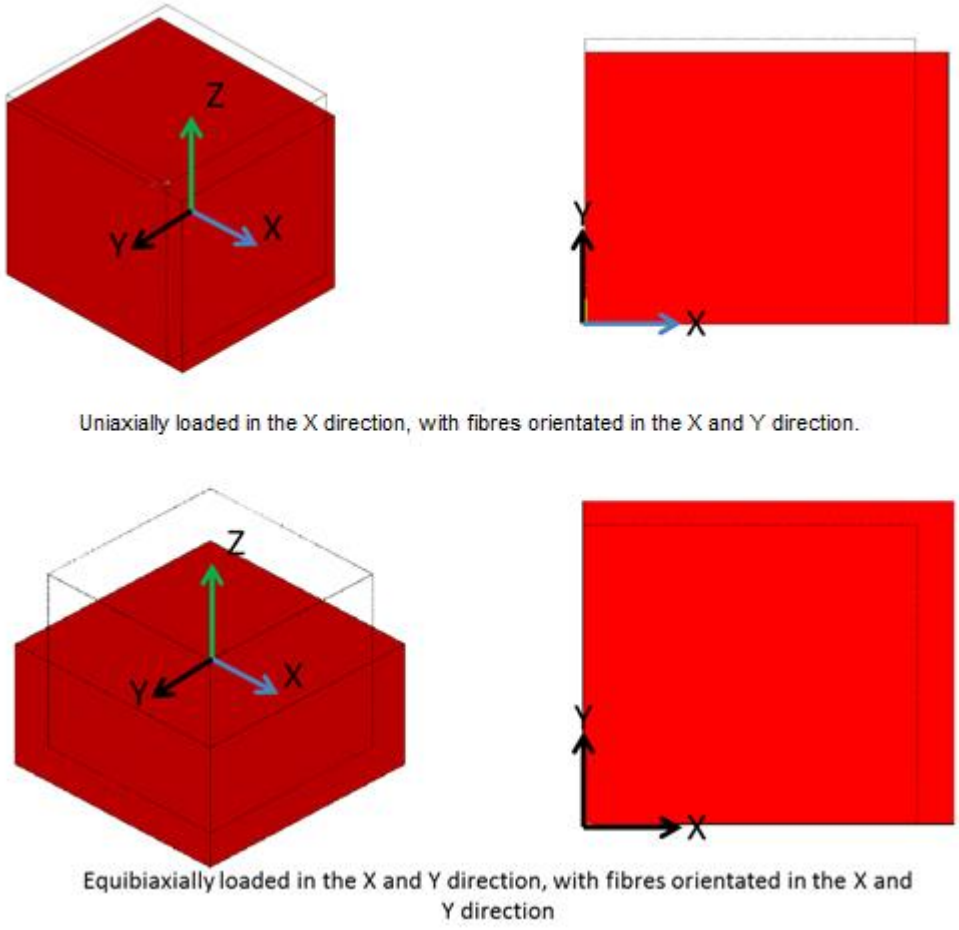

Figure 4.8 Uniaxial and equibiaxial extension deformation, with fibres orientated in the X and Y directions, respectively.

The total strain energy function (base matrix and fibre response) was then solved analytically at each stretch and plotted in Matlab and compared to the numerical results to assess the extent of congruency between the work-flow set up of the numerical simulation of a simple geometry and the analytical mathematical simulation derived

above. The comparisons of the analytical and numerical results are shown in Figures **4.9** and **4.10**.

The Cauchy stress tensor represents force measured per unit *deformed area* acting on an element of surface in the deformed configuration. The normal stress (or first Piola-Kirchoff stress) represents the forces acting on an element of surface in the deformed configuration but measured per unit undeformed area. The 2nd Piola-Kirchoff stress tensor represents force measured per unit deformed area, acting on an element of surface in the undeformed configuration. The stresses plotted in the analytical comparison below shows the three different stresses and how they change with the stretch, hence confirming that these stresses can be reliably predicted. These stresses are frequently referred to in numerical and experimental studies, and therefore it is important that they can be accurately estimated in the model.

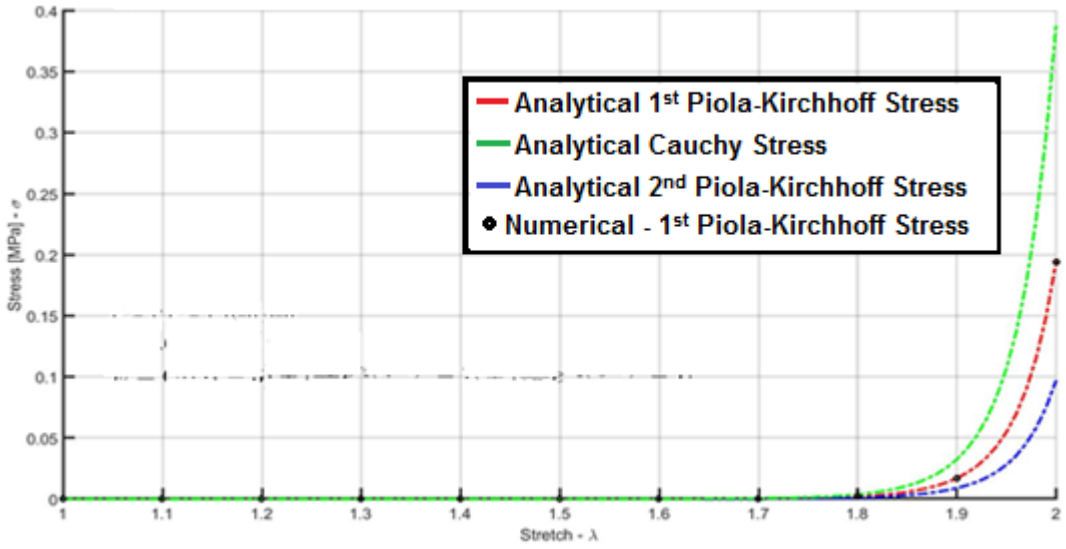

Figure 4.9 Numerical (black points) vs analytical (red line) comparison of uniaxial deformation in the X direction with 2 bodies of fibres in the X and Y axial direction.

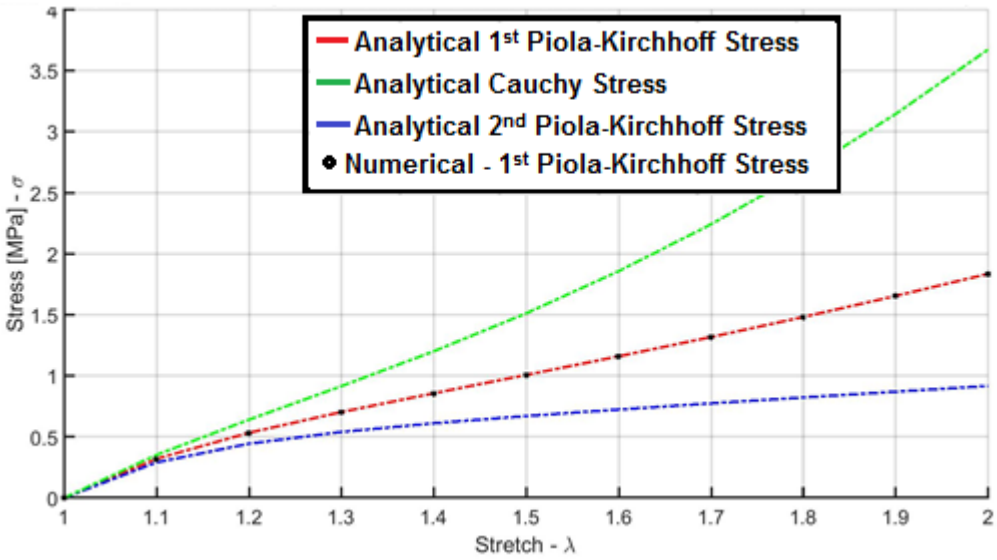

Figure 4.10 Numerical (black points) vs analytical (red line) comparison of equibiaxial deformation in the X direction with 2 bodies of fibres in the X and Y axial direction

From Figures **4.10** and **4.9**, it can be seen that the analytical solutions are very similar to the predicted numerical results by ANSYS, and hence validating this modelling approach. This would bring the thesis to the next step - where a more complex geometry of the skeletal muscle will be used for finite element simulations.

4.5 Discussion

From the simulations carried out, the one-dimensional model clearly coincides with the numerical implementation. The normal stress in ANSYS is numerically equivalent to the first Piola-Kirchhoff stress. It was found that the incompressibility had a detrimental effect on the stress results of the muscle, where an incompressibility parameter above 10 changed the stress response (however noting, that the larger the incompressibility parameter, the faster computational time and converges was observed).

Whilst a specific incompressibility parameter is not reported for skeletal muscle constitutive finite element simulations, the value chosen was 10, when using the MPa unit dimensions. The uniaxial model demonstrated that loading in the fibre direction causes a more anisotropic response than the biaxial simulation. More specifically, the

uniaxial simulation demonstrated the cross-fibre effects of the fibres in the y-axis, as the cube is loaded in the x axis. In contrast, the biaxial simulation showed a more linear stress-profile over the different stretches compared to the uniaxial response. This supports the corollary conclusion that fibre orientation highly affects the mechanical response of the muscle (Belytschko et al., 2000), in that the equal and opposite orientation of fibres cancels out its anisotropic effects on the overall stress response of the constitutive tissue (Holzapfel & Ogden, 2009).

As such, the verification above has established that the simulation was producing reasonable results, and the model can progress to anatomical simulations of the medial gastrocnemius.

Chapter 5

Numerical Simulation of the Medial Gastrocnemius – an Anatomical Study

The previous chapter discussed the constitutive and continuum mechanics upon which the current work is based. This chapter builds on the previous chapter to create a subject-specific finite element model of the medial gastrocnemius. A simulation has been carried out to investigate the effects of using certain anatomical features – such as anatomical fibre paths – in finite element modelling and how such detail affects the current skeletal muscle model.

5.1 Finite Element Models of the Medial Gastrocnemius

The anatomical features of the medial gastrocnemius muscle are comprehensively surveyed in Chapter 3. The medial gastrocnemius comprises of the muscle, tendon, aponeurosis and the muscle-tendon transition regions. The region at which the tendon dissipates into muscle tissue on the medial gastrocnemius muscle is known as the muscle-tendon junction. Very little is known about this transition zone, only that injuries attributing to medial gastrocnemius strains often occur in this region (Azizi et al., (2009)). This transition zone is thought to lie adjacent to the aponeurosis, which spans across the muscle mid-belly.

Whilst the anatomical geometry and location of the muscle is well understood, the mechanical behaviour of the skeletal muscle and how it is governed by its anatomical architecture, is still a subject of significant research. Two main types of models have previously been used; lumped parameter one-dimensional models, and continuum mechanics models. The differences between the two are discussed in Chapter 3, and briefly covered below.

Continuum mechanics models, which incorporate the three-dimensional structure of the muscle geometry, have used various computational techniques to define complex muscle fibre orientations (Blemker & Delp, 2005). Whilst the work done by Blemker et al. (2005) has shown good consistency with anatomical muscle fibre orientations, the model is based on a Bezier spline weighted algorithm, which adds extra computational demand to a subject specific finite element model. To address this, Zollner et al. (2015) have considered a compartmentalisation approximation, where the muscle is compartmentalised into six to eight divisions, and a general fibre orientation is applied to each compartment. Roerhle et al. (2012) also used a number of divisions, and generated the fibre orientations of the model using Diffusion Tensor Magnetic Resonance Imaging (DT-MRI), which was one of the first finite element models to use subject-specific fibre orientations (Roehrle, et al., 2012). Whilst the use of DT-MRI method displays diffusion of aqueous molecules which approximates individual fibre orientations (Bihan & Breton, 1985; Roehrle, et al., 2012), other

augmented and complex methods have been used to better represent and determine anatomical muscle fibres – for example – by means of normalized DT-MRI, Stimulated Echo Acquisition Mode (STEAM)-DTI and correction of directional (laterality) of the skeletal muscle orientation (McMillan, et al., 2011; Giraudo, et al., 2018). One commonality that stands across all these procedures is the requirement to further process the DT-MRI to clarify the fibre orientations (water content striations) within skeletal muscle tissue.

5.2 Applying Subject-Specific Data to a Finite Element Simulation

The anatomical muscle geometry and fibre orientations of the medial gastrocnemius from a female cadaver were acquired from the Living Human Digital Library (LHDL) (Viceconti, et al., 2007). The geometry acquired from the LHDL project required further processing (smoothing, cropping and fibre vector interpolation) before they could be meshed and used for a finite element study. A simplified process map of this work-flow is shown in Figure **5.1**.

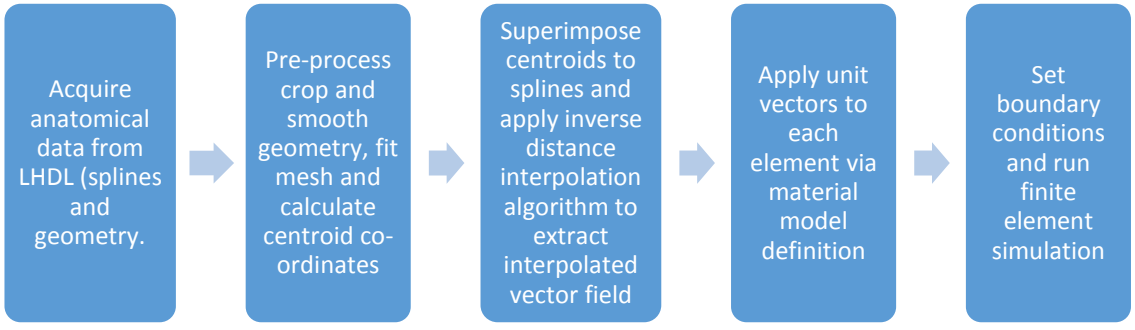

Figure 5.1 Process chart showing the procedures followed from original imaging data to finite element simulation.

The muscle was a surface membrane that had small discontinuities and only consisted of the posterior region of the muscle. Therefore, to get this to a geometry that could be used in finite element mechanics, the general order of pre-processing occurred as follows:

(i) The discontinuities were filled by an arbitrary automated hole fitting function.

(ii) A triangulation algorithm was applied, followed by a Delaunay three-dimensional function to re-create a close surface and three-dimensional volumetric geometry.

(iii) The geometry was then cropped, at specific regions to provide a musculo-tendon complex

(iv) The geometry was then smoothed using a Lagrangian function which therefore allowed a mesh to be fitted to the muscle.

This process is covered in detail below, and Figure 5.1 outlines the full process required to get the muscle geometry ready for meshing, and the process of incorporating the anatomical fibre orientation data into the finite element workflow. The muscle geometry of the medial gastrocnemius muscle acquired from the LHDL project is shown in Figure **5.4**a. The images acquired from LHDL consisted of the rough surface path of the posterior side of the muscle, as shown in Figure **5.3** a. Before the model could be used, the geometry needed to be processed and refined, as the surface of the geometry had discontinuities (small holes). These were resolved by using the 'hole-filing' function in the LHPBuilder[2] (Kohout & Clapworthy, 2012). This then provided a continuous anterior surface of the muscle. Some of the holes in the surface were very small, however have been shown in the image below (note, there were several holes on the surface and edge of the geometry, where most of them were situated towards the proximal end of the gastrocnemius. Figure 5.2 is representative of some of the miniscule holes that were present on the geometry surface and edge). Effectively, the holes consisted of small discontinuities in the surface of the muscle, as shown schematically in the image below. The hole filing algorithm has not been

[2] LHPBuilder is an application developed using the Multimod Application Framework that provide to the LHP participants a software tool to import, fuse, and store biomedical data on the Living Human Digital Library. www.swmath.org/software/6798

well documented in the LHPBuilder; however, the algorithm used is based on the mathematical framework reported in (Kohout & Clapworthy, 2012).

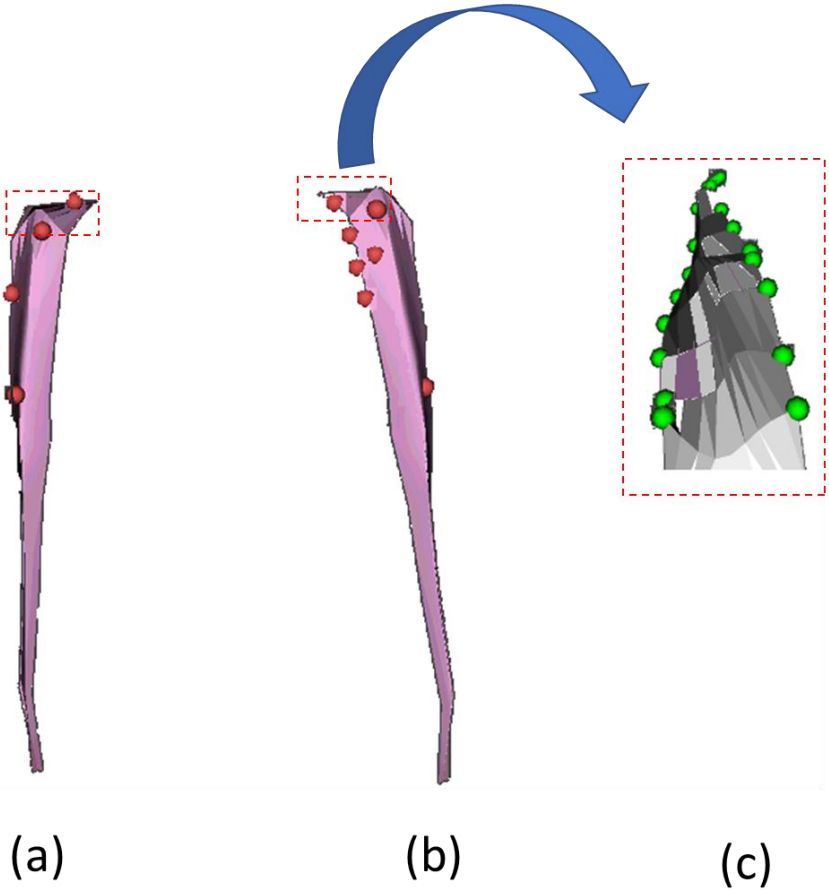

Figure 5.2 (a) The anterior view of the muscle showing areas in which the hole-filling algorithm was used in LHPBuilder (red elements). (b) Shows the posterior-lateral view of the geometry and (c) shows a closer view of the hole-filling algorithm by LHPBuilder as per element/pixel, where green dots denote geometry vertex boundaries automatically detected by LHPBuilder.

The continuous anterior surface was then imported into Paraview 5.2.0 – RC3[3] and the triangulate function was used there (Ayachit, 2016). This triangulate function created a boundary by creating surfaces between adjacent vertices. Consequently, the posterior surface of the muscle was estimated using the adjacent soleus muscle as a reference (as shown in Figure **5.3** b), to ensure that the estimated posterior side of the medial gastrocnemius does not penetrate the soleus muscle, as shown in Figure **5.4**.

[3] Paraview is an open source multiple-platform application for interactive, scientific visualization. www.paraview.org (Ayachit, 2016)

The 3D estimation of the muscle was based on creating a triangulation of the geometry information and its neighbouring points; so that the estimation a) created a closed 3D surface and b) ensured that one closed 3D surface did not extend/penetrate the geometry boundary of the neighbouring tissues. The three-dimensional Delaunay triangulation algorithm (Delaunay, 1934) - also available in Paraview, was used to define the entire closed surface of the 3D medial gastrocnemius.

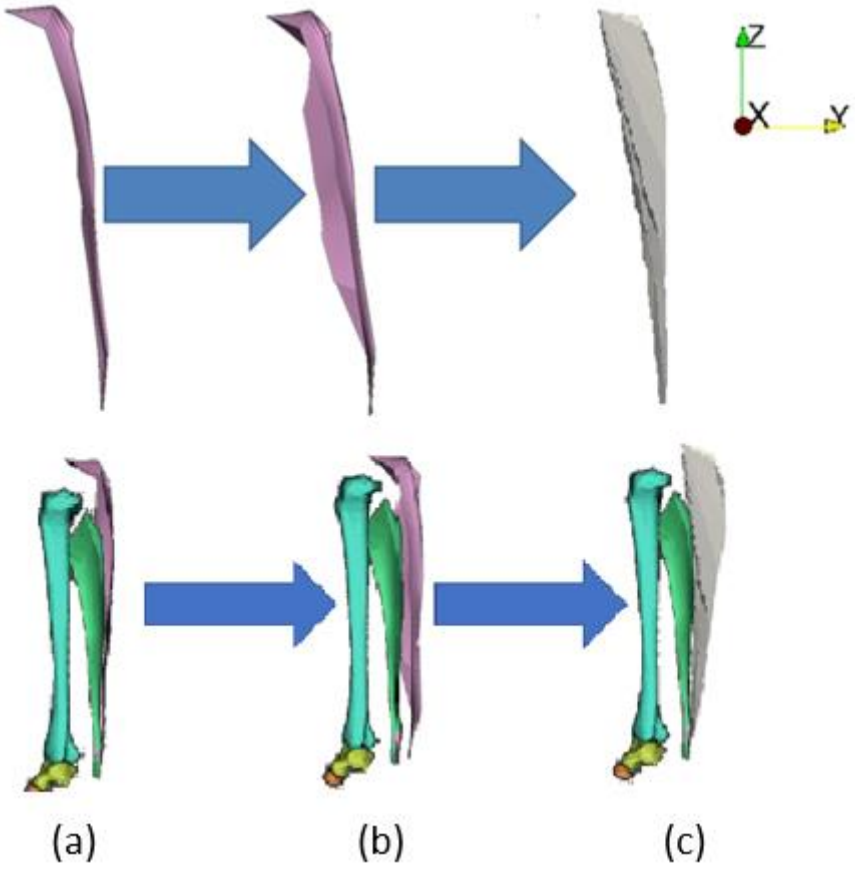

Figure 5.3 (a) The anterior surface geometry of the medial gastrocnemius obtained from LHDL data. (b) Processed surface after using the hole-filing function available in LHP Builder to fix discontinuity. (c) An enclosed surface describing the three-dimensional geometry of the medial gastrocnemius following three-dimensional triangulation.

The muscle was also cropped at the calcaneal distal tendon, so that while up to 40 mm of tendon at the insertion remained, the rest of the Achilles tendon was omitted,

as illustrated in Figure **5.4**. This was done by obtaining the muscle-tendon geometry co-ordinates of these geometrical regions and cross-checked visually using the data from the palpated landmarks from LHDL data. The landmarks marked where the muscle fibres on the geometry began and the tendon fibres ended, so it was visually easy to differentiate between the muscle tissue and the tendon tissue. The soleus is shown in Figure **5.4** to ensure that the 3D estimation of the gastrocnemius geometry did not penetrate the boundary of the Soleus muscle. This was also done to qualitatively determine the accuracy of the estimation of the gastrocnemius geometry.

Following the determination of the three-dimensional geometry outlined above, the surface of the muscle was still very coarse and could not be meshed for finite element simulations, therefore smoothing was carried out to ensure that a good mesh would fit the surface (Figure **5.4**b). This was done by exporting the surface geometry as a stereolithography ASCII (STL - ASCII) file and imported into an FE Bio module - Preview[4]. Once in Preview, smoothing was done using its Laplacian smoothing function. This smoothing function is widely used to smooth a polygonal mesh in various computational geometry models (Herrmann, 1976; Sorkine, et al., 2004). The general method this function follows is to smooth each vertex or node, by moving the vertex to a new location based on the average location of its neighbours. The smoothing operation per vertex can be described by the following Equation **5.61**:

$$\bar{x}_i = \frac{1}{N}\sum_{j=1}^{N} x_j \qquad \textbf{(5.61)}$$

Where N is the number of neighbouring vertices to node i. The position of the j-th neighbouring vertex is x_j and $\bar{x}_i$ is the new node location.

The number of iterations selected in this context was the minimum required to allow for a simple mesh to be fitted onto the geometry, with minimal element distortion (aspect ratio <1.1 and skewness <0.2).

The data points of the medial gastrocnemius were originally defined in an anatomical co-ordinate system, so the long axis (middle) of the muscle was not aligned

[4] PreView is a Finite Element (FE) preprocessor that has been designed specifically to set up finite element problems. Is was designed for FEBio, and is a module of the open source FEBio software. https://febio.org/preview

with any orthogonal axes. The data points therefore needed to be transposed which resulted in the x-axis running down the long axis of the muscle (Figure **5.4**c). The transposition was done to ensure that the displacement being applied at the insertion site was applied along the muscle axis, rather than at an angle to the muscle. This process of cropping, smoothing, transposition is illustrated in Figure **5.4**.

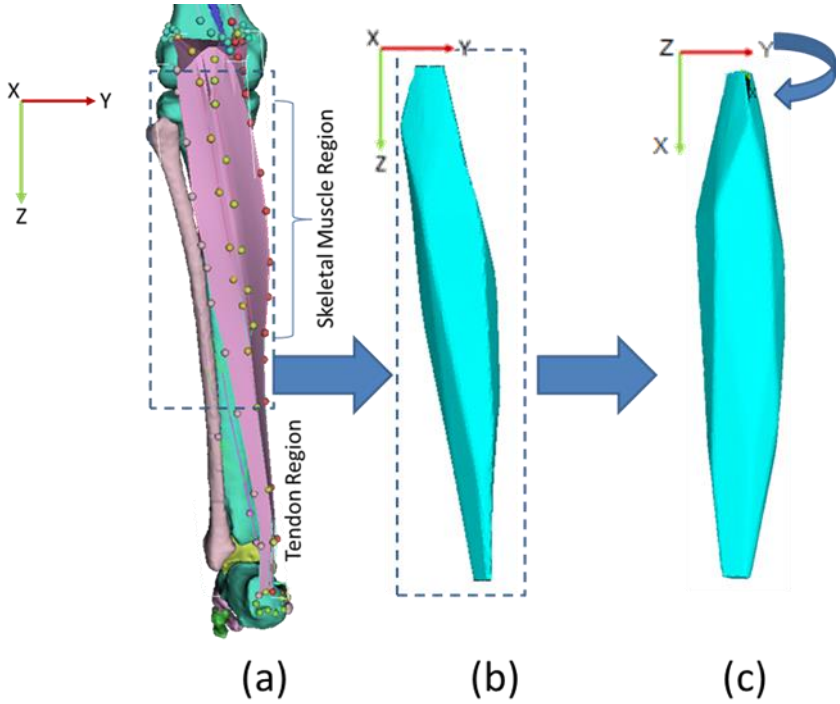

Figure 5.4 (a) Original anterior surface of the gastrocnemius muscle, showing the tendon and muscle region (blue box). (b) After the three-dimensional Delaunay triangulation function, the volumetric muscle geometry is cropped and smoothed, in its original co-ordinate system. (c) The muscle was then transposed into the new co-ordinate system with the x-axis running down the muscle length. The geometry is now ready for meshing.

Finally, the processed geometry was exported and meshed in ANSYS ICEM CFD[5]. A 10-node tetrahedral volumetric mesh was fitted with a maximum element size of 1 mm based on the mesh convergence analysis carried out later in this chapter. **The resulting mesh contains 144995 elements and 497016 nodes and a mesh density of 0.96 elements/mm^3, as shown in Figure 5.5.**

[5] A pre-processing and meshing module for use in ANSYS finite element simulations that provides sophisticated geometry tools, accurate and hybrid mesh generation for complex geometries.

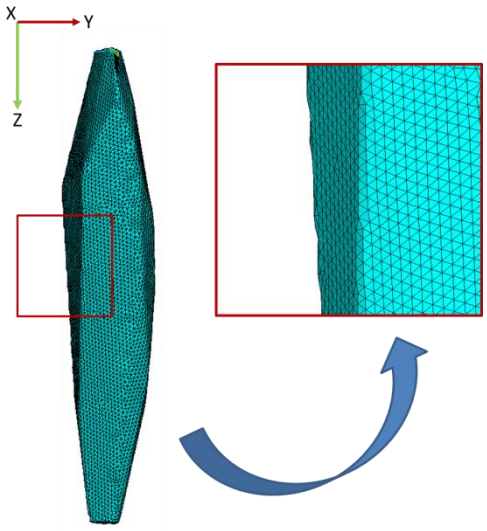

Figure 5.5 Mesh of the medial gastrocnemius muscle

It should be noted that the cuboid model was meshed with both hexahedral and tetrahedral elements, and the results were very similar between the two. Tetrahedral elements however, were chosen for the anatomical geometry, as the mesh fitted better over the surface of the muscle in comparison to the hexahedral elements.

5.3 Centroid Calculation

As previously discussed, the fibre orientation was defined for each element. As the fibre orientations of the muscle were non-uniform, the centroid location of each element had to be calculated in order to assign an averaged fibre orientation across that finite element. Although ANSYS has a built-in function to obtain these centroids, the python script was used to assign the fibre orientations to the centroids to reduce the disjoint of the algorithm work-flow and computational time. The centroid calculation was carried out by calculating the average x, y and z co-ordinates of the nodes making up each element.

This calculation was performed using a python script. Once the centroids were computed, their co-ordinates were then used to interpolate the fibre vectors from the vector field data provided by LHDL as shown in Figure **5.6**. It is important to note, however that the term ‘fibre vectors’ in relation to the raw data that was acquired from LHDL is used loosely in this thesis: the palpated landmarks were the general direction

of fibres, that emulated an estimated surface muscle fibre path. This is because the data was obtained from a cadaver of which only the surface directions were obtained – hence volumetric vector fields of the fibre directions were not acquired. A possible remedy to this issue could be to use DTI imaging, which enables a more comprehensive three-dimensional description of the fibres.

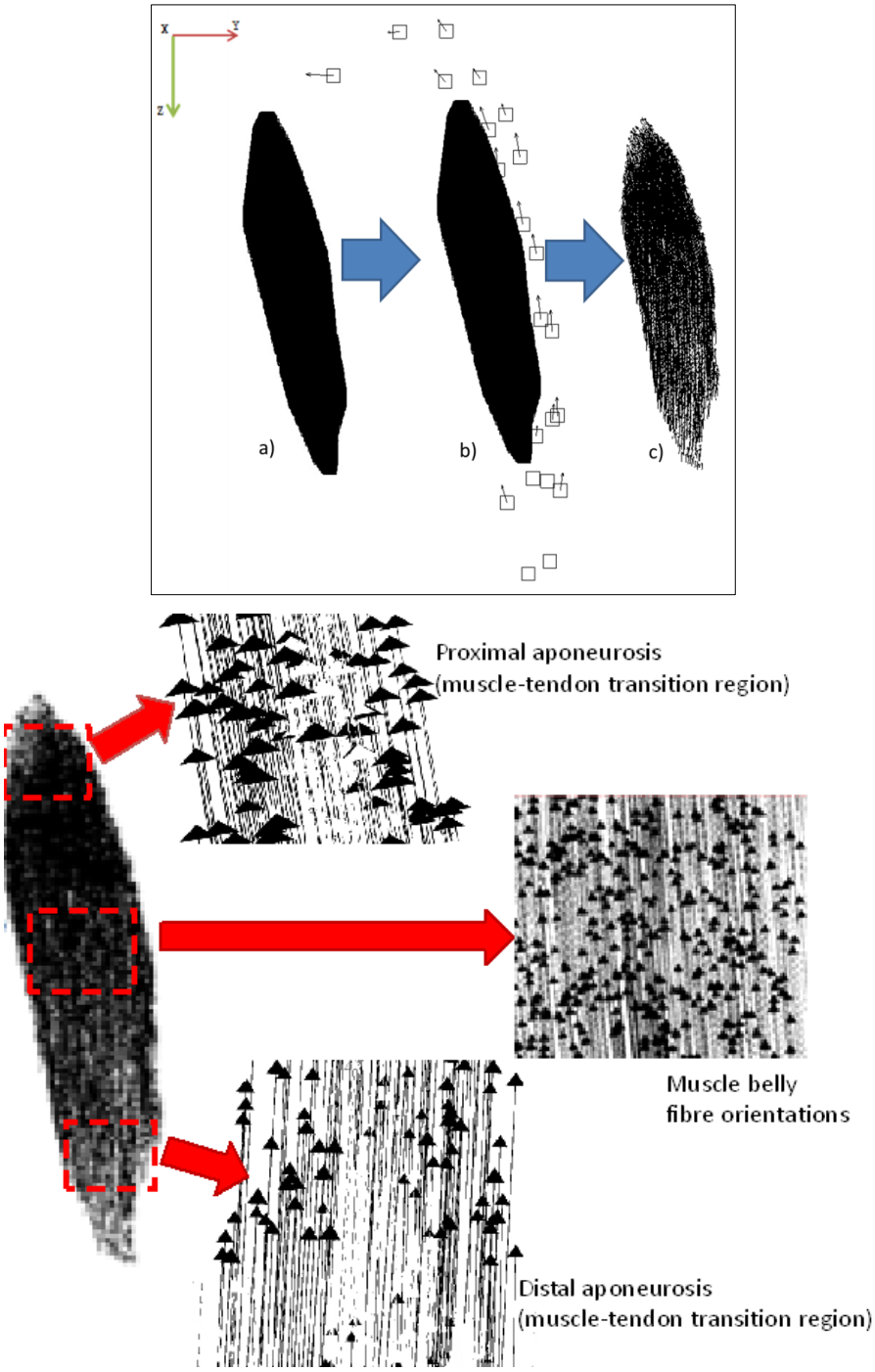

Figure 5.6 Interpolation process; (a) centroid point data ~144995 points, (b) superimposition of vector field from LHDL (square denotes the landmarks from LHDL data and arrows are the direction of spline at that point)

onto centroid points, (c) Using an inverse distance interpolation function showing the mapped fibre orientations. (d) Close up of the interpolated fibre orientations of each of the different regions (aponeurosis, muscle and tendon respectively) showing the difference and slight fibre orientations within each of the regions.

The changes in each of these regions as shown in Figure 5.6 highlight the general fibre orientation of the different regions. This is expected to affect the stress and strain response of these regions, which will be explored in the next section.

As shown from the image above, the vector directions are interpolated onto the centroid locations, so each centroid resultantly had a known vector assigned to it. The following section describes the interpolation of fibre orientations in detail.

5.3.1 Fibre Orientations from Anatomical Data to the Finite Element Simulation

The application of these anatomical fibres from cadavers has provided a valuable alternative to finite element modelling compared to previous literature (Blemker & Delp, 2005; Blemker, et al., 2005), where the fibre paths are either approximated in a few zones within the muscle, or derived from DTI-MRI images. All these methods carry some uncertainties, and therefore it will be useful to be able to compare and benchmark various approaches in the future. The fibre orientations obtained from LHDL are illustrated in Figure 5.2a. This was done by physically palpating the cadaveric medial gastrocnemius and determining 15 key-points for each approximated fibre orientation across the muscle. These 15 key points were joined up to make one spline, which was considered as one general fibre direction in that region. The medial gastrocnemius had four splines in total (i.e. four splines across the muscle), which ran from the proximal origin to the distal insertion site, with increasing curvature as the fibres approached the surface of the muscle. The path these 4 splines followed determined 4 general fibre paths.

The interpolation method allowed the superimposition of the fibre vector field to the centroids from the mesh. This deterministic multivariate interpolation method enabled the centroids in the study region (muscle geometry) to be calculated with a weighted average of the values from known neighbouring vector (i.e. from the four splines).

The result was therefore a known discrete assignment of the interpolated function (fibres onto centroids) in a specific region. The formula that relates this method incorporates the specific space explored, **D**, the known points and the unknown vector field, $\boldsymbol{u}(\boldsymbol{x})$, and is shown in Equation 5.62:

$$\boldsymbol{u}(\boldsymbol{x}): \boldsymbol{x} \rightarrow \mathbb{R}^{\boldsymbol{n}}, \boldsymbol{x} \in \mathbf{D} \qquad \textbf{(5.62)}$$

This formulation shows that the four splines were used to interpolate the vector direction at any centroid, where each ‘unknown point’ was determined by the vectors at the centroids and the known points were the direction vectors along the splines. This is illustrated in the Figure **5.6**, where $\boldsymbol{u}$ points are unknown fibre vectors at centroids,

and $\boldsymbol{w}$ represents the known direction vectors along the splines. Depending on how close $\boldsymbol{u}$ is from $\boldsymbol{w}$, the value of w is weighted to reflect the respective fibre vectors at $\boldsymbol{u}$. Note that the closer $\boldsymbol{u}$ is to $\boldsymbol{w}$, the more congruent their values will be; similarly, the further apart they are, the less congruent their values will be. This concept is illustrated visually in Figure **5.7.**

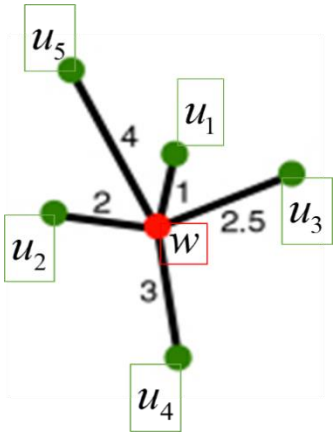

Figure 5.7 Schematic showing the inverse distance weighting interpolation of an unknown function (centroid vector) u_i in a specific field (muscle geometry); interpolating a known function (direction vectors along spline) w. The numerical values represent weighting between w and u.

The unknown value u_i of the function $u(x_i)$ where $\boldsymbol{i - 1, 2, \dots, N}$ can be calculated by finding the average weighted distance of known spline vectors onto the unknown fibre vectors at centroids by the relationship shown in Equation 5.63:

$$u(x) = \begin{cases} \dfrac{\sum_{i=1}^{N} w_i(x) u_i}{\sum_{i=1}^{N} w_i(x)}, & \text{when } d(x_i) \neq 0 \text{ for all } i \\ \therefore \\ u(x) = u_i, \text{when } d(x_i) = 0 \text{ for some } i \end{cases} \qquad \textbf{(5.63)}$$

Where w_i is the vector direction along the spline, d is the given distance from the known vector $w_i(x)$ to the centroid. Where the distance $d(x)$ is inversely proportional to the location of the known vector on the spline $w_i(x)$, as demonstrated by Shepard, (1968):

$$d(x) \propto \frac{1}{w_i(x)} \qquad \textbf{(5.64)}$$

With this information available, each centroid for each element on the mesh could be assigned a unique fibre orientation. The interpolated fibre orientations are shown in Figure **5.8** . The convergence criteria for each fibre was dependent on a weighted average of the distances between the vectors and the respective centroids.

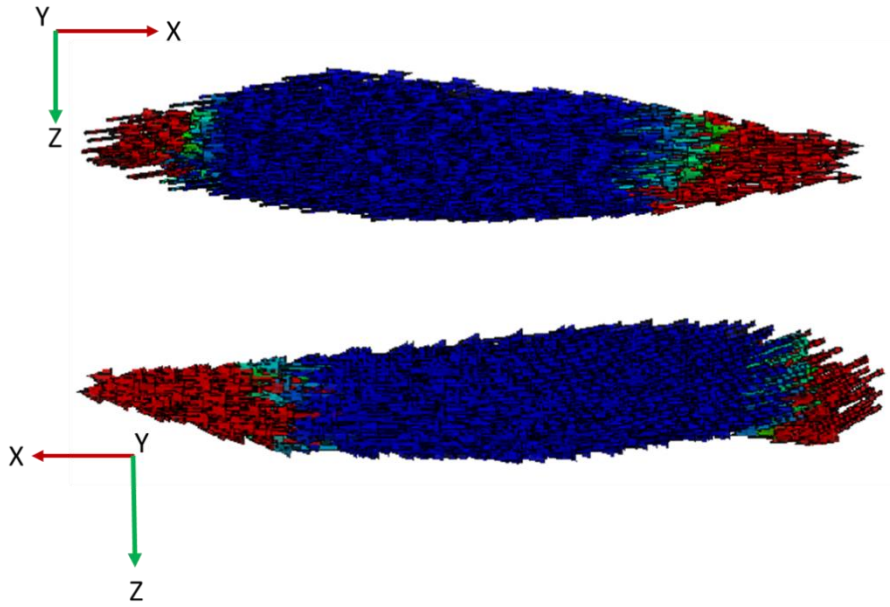

Figure 5.8 Interpolated vectors indicating fibre orientations at each element. (Blue is muscle tissue fibres, green is transition muscle-tendon junction and red is tendon tissue fibres.)

This procedure was carried out using Python 2.7[6] scripts. The centroids and fibre orientation data were combined into one file and then the fibre orientations were interpolated onto the centroid locations. This was defined for the finite element simulation in ANSYS and applied to the material description of each element. Since each element had a different fibre vector, therefore, each element also had a different constituent defined, based on the anatomical data from LHDL, and whether it was muscle or tendon.

The fibre orientations of the data were interpolated from four splines. Since these data originated from anatomical data, and were approximated using an inverse distance interpolation method to inform the finite element simulation, this work-flow

[6] Python is a high-level programming language for general-purpose programming. It features a dynamic type system and automatic memory management and supports object-oriented, imperative, functional and procedural programming paradigms. ywww.python.org

provides a different approach to estimate fibre orientations from physical palpation, as opposed to DT-MRI, thus adding to the current literature of muscle fibre modelling and enabling researchers to draw comparisons between different approaches to the modelling of fibre orientations. The process defined in the current workflow can be transferred to different muscle geometries with other muscle fibre orientations (excluding over-lapping asymmetrical fibre orientations).

To conclude this work, an illustrative finite element simulation was undertaken, and the boundary conditions and results are explained in detail below.

5.4 An Anatomical Finite Element Simulation of the Medial gastrocnemius

A simple simulation of the medial gastrocnemius muscle in extension was carried out. This was undertaken to ensure that the anatomical geometry and fibre orientations produced physically meaningful results. The muscle was extended at the distal insertion by 12 mm, which was within the range of extension experienced by the medial gastrocnemius when the ankle is in dorsi-flexion during slow walking. This extension is consistent with other investigators who reported strains of the medial gastrocnemius during slow walking with values between 10 mm – 16 mm (Lichtwark, et al., 2007; Fukunaga, et al., 2001; Kawakami, et al., 2002; Grieve, et al., 1978), The extension was applied at the insertion end only (in the x direction), since the distal insertion of the skeletal muscle is thought to move – during active and passive motion – whilst the origin of the muscle was anchored (fixed in the x, y and z direction) (Willert, et al., 2001). The side of the muscle adjacent to the lateral gastrocnemius was fixed in the y direction only, and the side adjacent to the soleus was fixed in the z direction only. The lengthening of the gastrocnemius is said to be homogenous from the distal to proximal ends (Lichtwark, et al., 2007), so the boundary conditions were set to mimic only the physiological phenomena. This inherently was applying Dirichlet boundary conditions – as a specified boundary condition for the solution was

applied to the elements at the boundary. Figure 5.7 shows the nodes selected and the respective boundary conditions on the geometry of the muscle. The fibres were applied to the muscle model as described in Section 5.3.1.

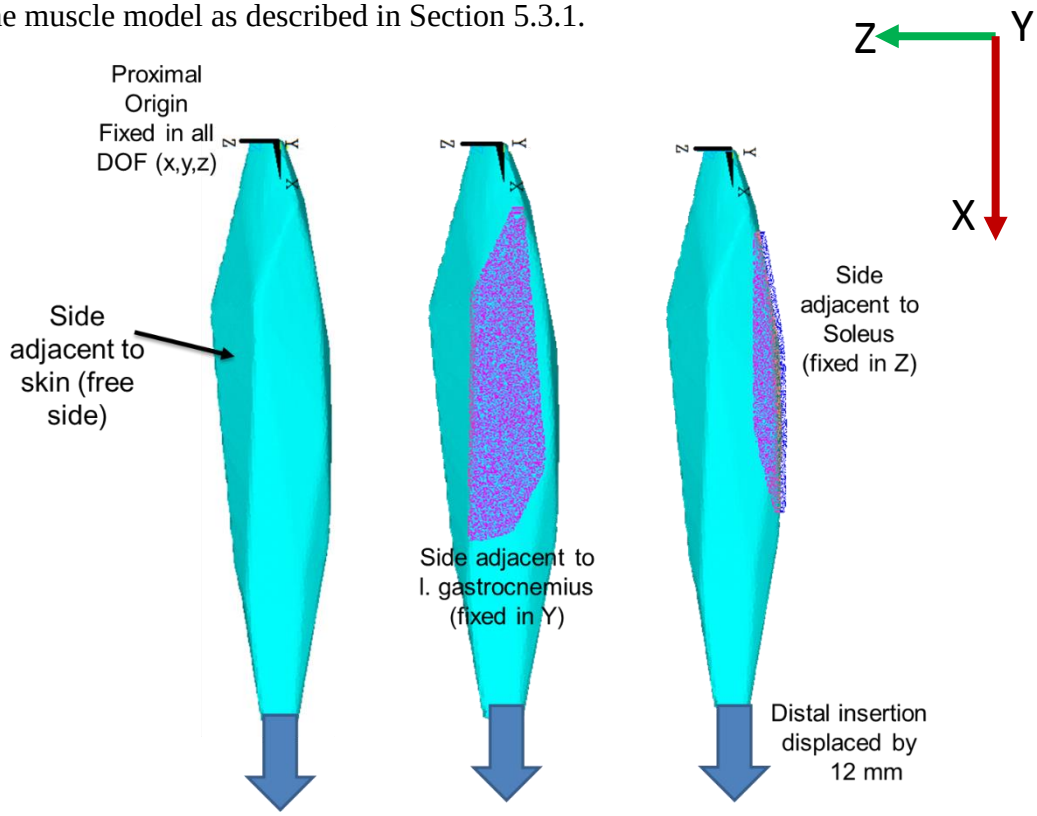

Figure 5.9 Applied boundary conditions for the medial gastrocnemius in the simple extension simulation.

A comparative simulation was done between the anatomical fibre orientation and a transversely-isotropic fibre orientation (fibres were aligned with the long axis in the x direction). This was done to assess the effect of anatomical fibre orientations on the finite element simulation. The constitutive model and material constants used for the subsequent simulations have been described in Chapter 4. The accuracy of the computed mesh was assessed by means of a mesh convergence analysis. This analysis was done on the anatomical meshed geometry and is reported in the next section.

5.4.1 Mesh Convergence Analysis and Finite Element Results

The mesh shown in Figure **5.5** was used and a convergence analysis was carried out to determine the optimal mesh (element) size.

The converged maximum first principal strain and stress were obtained from the region of interest in the muscle belly and the tendon region, then plotted against each mesh density increment. The regions of interest are illustrated in Figure 10 below.

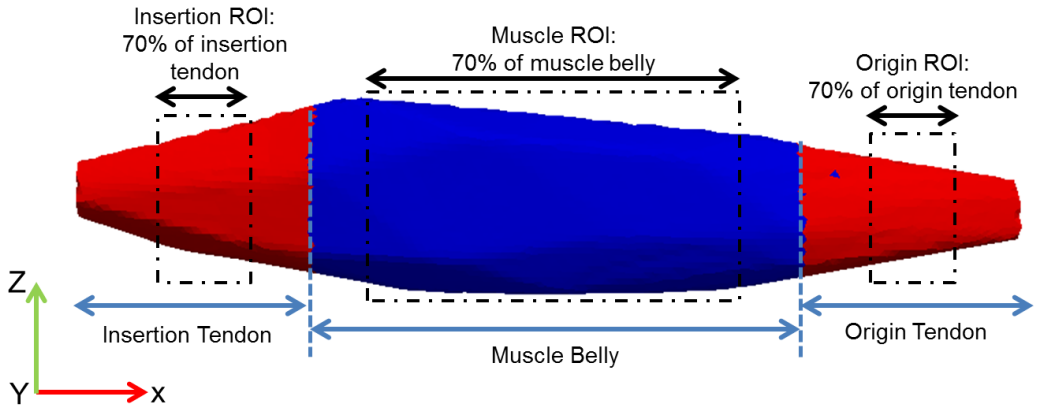

Figure 5.10 Illustrating the regions of interest selected (dashed lines) for the exploration of peak stress-strain values.

The region of interest is defined as follows; the muscle tissue and tendon tissue are easily determined by the contour as shown in Figure 5.9. Given that the length of the muscle and the tendon-aponeurosis complex were known, the nodes across a length of 70% of each tissue, in the centre of the constituent, were selected as regions of interest. Approximately 15% at each edge were omitted from the selection to avoid selecting an area too close to where the boundary conditions were applied. Approximately 70% of the length of each constituent was selected to ensure an adequate region of response was examined. The tendon tissue selected in the regions of interest at the insertion and origin ends were linked together in series so that the peak values across the regions of interest were explored at both ends, since they were both tendinous. The results from these regions were examined to determine the converged mesh density. The peak maximum first principal stress and strain for each mesh resolution are shown in Figure **5.11** for tendon, muscle and transition region (aponeurosis). The convergence criteria for the strain was set to an asymptotic precision of 10^{-1}, and the stress convergence criteria was set to a precision of 10^{-3} MPa.

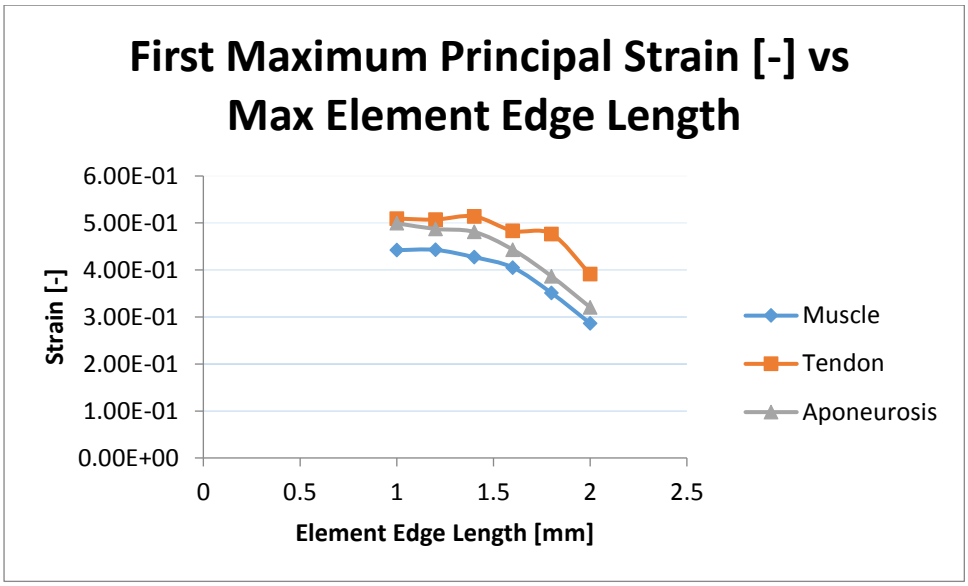

Figure 5.10a The predicted maximum first principal strain plotted against mesh density for muscle, tendon and aponeurosis.

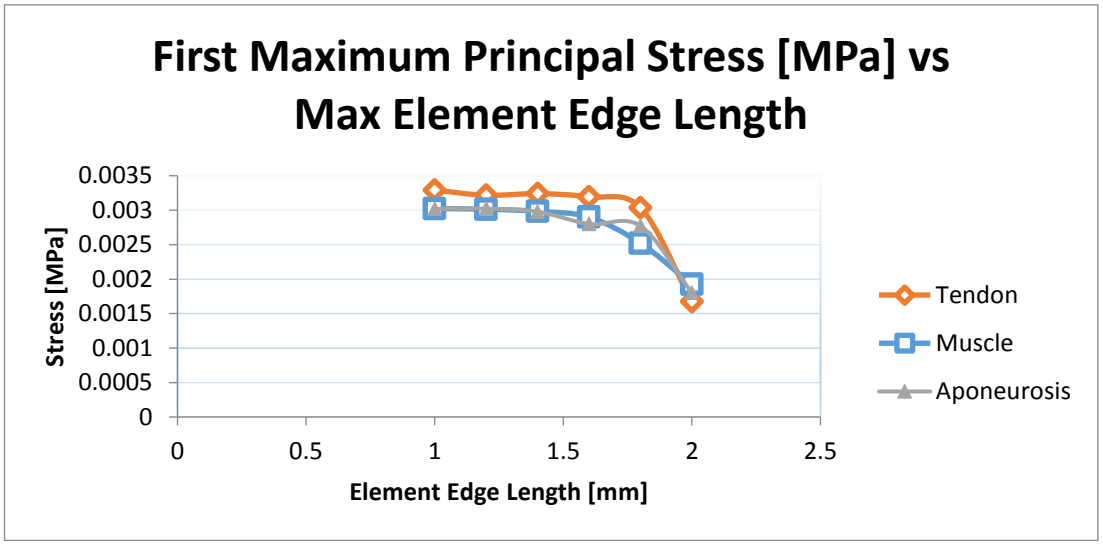

Figure 5.11b The predicted maximum first principal stress plotted against mesh density for muscle, tendon and aponeurosis.

As the maximum element size decreased (i.e. increasing mesh density), the strain and stress reached a plateau. The values reached convergence at a maximum element size of around 1.4mm. The chosen maximum element size of the mesh was therefore 1

mm, which provided a more accurate description of the geometry, as at this size, the element aspect ratio and skewness were minimal, whilst still maintaining an accurate solution upon convergence.

The same convergence analysis was also carried out on the models with different material constant distributions and with both transversely isotropic and anatomically-based fibre orientations. A similar trend was observed as shown in Figure **5.11**, with a 1 mm maximum element size guaranteeing mesh convergence across the various meshes fitted.

Using the selected mesh size (1 mm), an illustrative comparison of the stress-strain profiles of the simulations incorporating anatomical fibre orientations and transversely isotropic fibres are shown in Figures **5.12** and **5.13**.

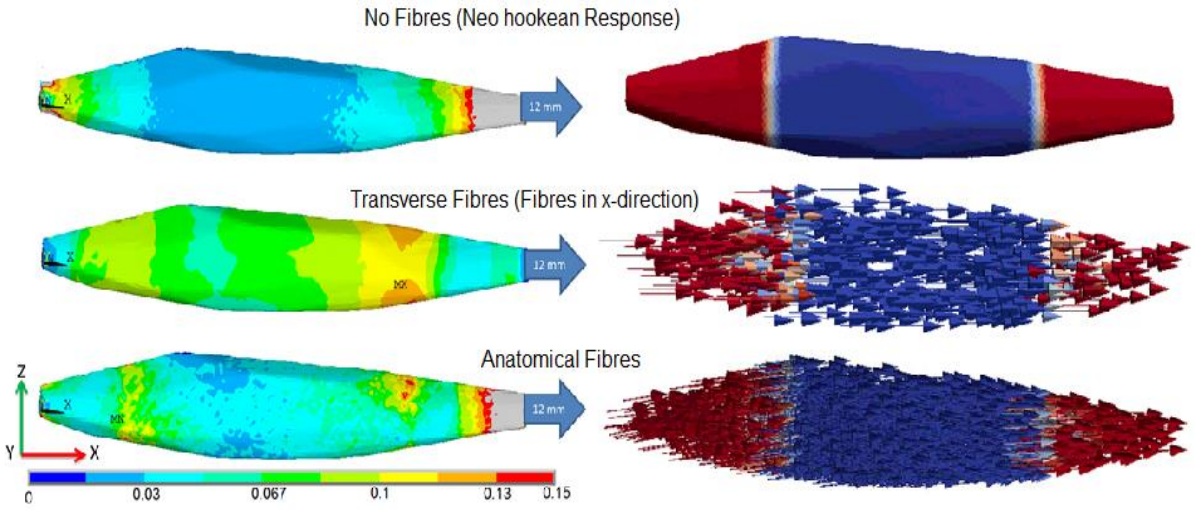

Figure 5.12 First principal strain of the medial gastrocnemius muscle belly when the knee is in extension and ankle is in dorsi-flexion at 12 mm extension of the transversely-isotropic muscle. The right-hand sides column shows corresponding fibre orientations in each case.

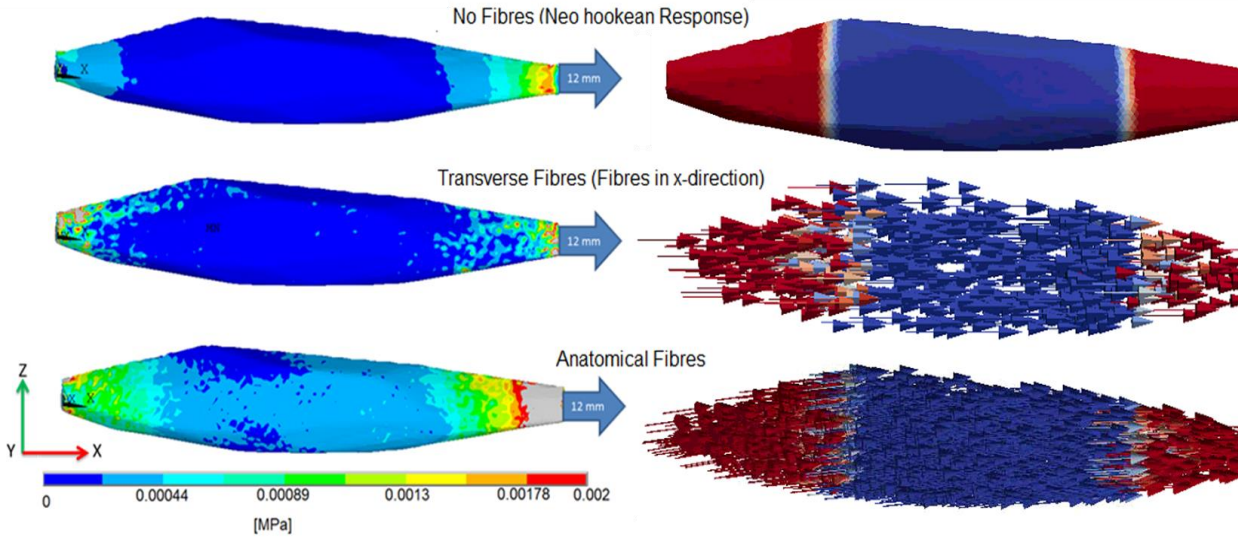

Figure 5.13 First principal stress of the medial gastrocnemius muscle belly when the knee is in extension and ankle is in dorsi-flexion equating to 12 mm extension of the muscle. The right-hand side column shows corresponding fibre orientations in each case.

From Figures **5.12** and **5.13**, it can be seen that there is a significant difference in the stress and strain results of the transverse fibre simulation compared to that of the anatomical fibres, and the no-fibre (isotropic Neo-Hookean) simulation. Specifically, the transverse fibres provide a more homogenous stress-strain response – particularly in the stress response of the transverse fibres, whereas the anatomical fibres displayed more differentiated strain and stress patterns, especially at the extremities (at the distal insertion end). The island of high strains observed in Figure **5.12** may be due to the anatomical geometry and fibre orientation of the muscle, in that the muscle is thinnest towards the distal end, as the muscle approaches the Achilles tendon. High strains and stresses are expected at the distal end under physiological loading during the extension of the medial gastrocnemius (Azizi & Roberts, 2009; Azizi, et al., 2009). This was more apparent in the anatomical fibre simulation than the transverse and in the no-fibre simulation.

5.5 Discussion

Considering the simulation of the medial gastrocnemius presented in this Chapter, the anatomical fibres seem to provide a more realistic presentation, as the highest stress-strain response is more localised, in the areas that are expected – the distal insertion, and moving towards the belly of the muscle (Azizi & Roberts, 2009) (Azizi, et al., 2009). The peak strains appear to be higher in the transversely isotropic fibres. From Figure **5.12** and Figure **5.13**, the fibre orientation had a significant effect on the mechanical response of the skeletal muscle, showing how important it is to have an accurate anatomical fibre orientation in the skeletal muscle model.

Whilst this model has used anatomical data in a finite element simulation, it currently does not represent the tendinous aponeurosis regions, which are important supporting structures for the muscle. The next chapter looks to enhance the anatomical description of the model by using mathematical and computational techniques to better mimic the 'wrapping' structure of the aponeurosis and the various material parameters that can be used for the muscle-tendon transition zone.

Chapter 6

Tendinous, Aponeurosis and Anatomical Muscle Representation

The morphology of a full muscle-tendon structure is complex. Considering the medial gastrocnemius, the full structure consists of tendinous regions, the aponeurosis, which spans across the surface of the muscle-tendon junction, and the muscle-tendon junction itself. The anatomical features of the medial gastrocnemius are the key elements in its mechanical response, meaning that it is important to consider the various structures within the muscle-tendon complex. The anatomical structure of the gastrocnemius aponeurosis, muscle, tendon and muscle-tendon junction are shown in Figure 6.1.

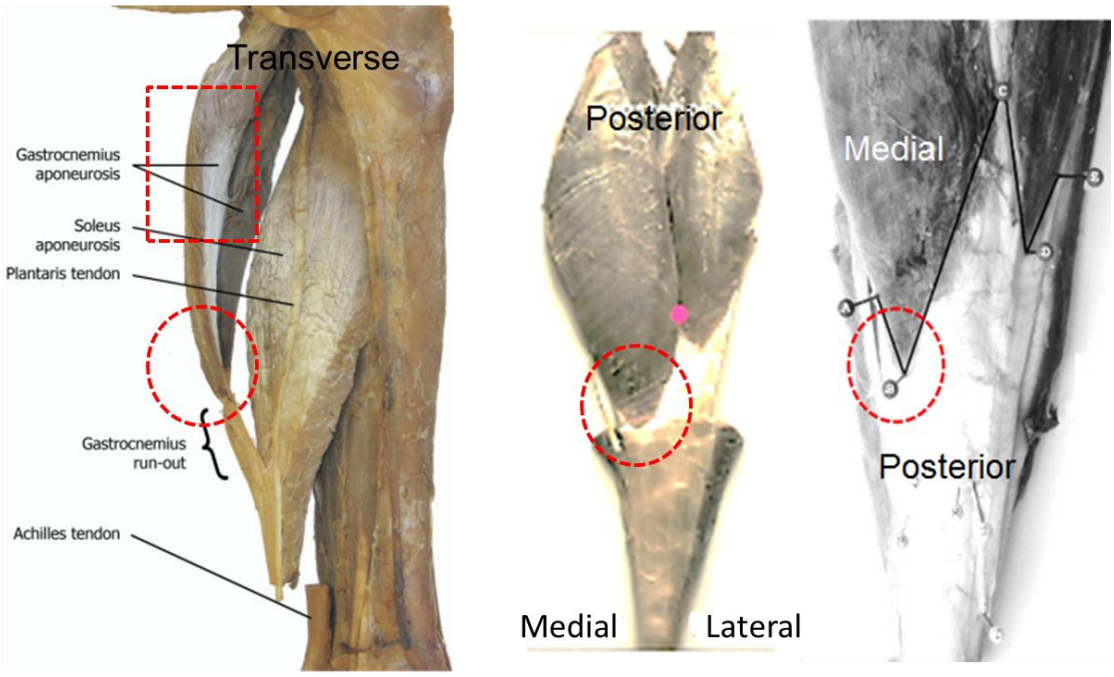

Figure 6.1 Anatomical features of the medial gastrocnemius aponeurosis (red square) and the muscle-tendon junction run-out shape (red circle) from the transverse plane and the posterior plane. Images taken from: (Blitz & Eliot, 2008) (Blitz & Elliot, 2007)

Figure 6.1 demonstrates that the gastrocnemius aponeurosis spans anteriorly over a large area of the muscle (red square), whilst the posterior side has a smaller region of muscle-tendon junction and aponeurosis area (red circle). Whilst it could be interpreted that the posterior junction meets the muscle at either a sharp or at a blunt cup apex, the exact apex could be argued to be rounded and cup like, rather than a sharp region, depending on how large the gastrocnemius muscle is. Therefore, there are three major features to consider when simulating the aponeurosis; i) The rounded or sharp apex, ii) the thin membrane spanning the aponeurosis up the belly of the muscle, iii) the muscle-tendon junction material parameters (where the aponeurosis meets the muscle).

Whilst there are several finite element models of skeletal muscles that consider some of the anatomical features of the muscle-tendon complex, there are few that

consider the aponeurosis morphology and even fewer that look to model the muscle-tendon junction. This chapter proposes a novel approach to represent the aponeurosis and muscle-tendon junction in a finite element muscle model.

6.1 The Constitutive Relationship of a Muscle – Tendon Complex

The active and passive mechanical characteristics of skeletal muscle tissue have been covered in detail in Chapter 3 and 4. Considering the anatomical arrangement, the medial gastrocnemius is an assembly of constituents in series - tendinous tissue, the aponeurosis and transition tissue (the muscle to tendon junction). Therefore, a good understanding of the constituents of the tendinous aponeurosis is required when developing a representative model of the muscle-tendon complex.

Various finite element studies have been developed to represent tendon tissue (Handsfield, et al., 2017; Blemker & Delp, 2005; Handsfield, et al., 2017) with comprehensive imaging data of specific tendon tissues (; Mithraratne, et al., 2017; Lin, et al., 2004; Neal M. Blitz, 2007; Toumi, et al., 2016).

Tendons are collagenous tissues, with a crimped collagen configuration at low strains, until the collagen begins to bear load, hence it has a visco-elastic nature (Herchenhan, et al., 2011). The mechanical responses of tendons are highly dependent on the orientation of the collagenous fibre (McPhedran, et al., 1965; Henneman, et al., 1965; Henneman & Olson, 1965). The collagenous orientations vary from muscle to muscle and change depending on the muscle's function (Thorpe C.T., 2013). Generally, the dry mass of tendons consists of about 86% collagen, (Jozsa, 1997), thus having a significant fibrous (anisotropic) response. The anisotropic non-linear behaviour of the collagen fibres is consequently expected to govern the mechanical response of tendinous and aponeurotic tissue.

Tendons respond to their mechanical environment much like skeletal muscles do; with studies showing a decrease in the collagen fibre thickness of the Achilles tendon due to disuse (Nakagawa, 1989), or a reduction in tendon stiffness due to microgravity (Reeves, 2005). It has previously been stated that modelling the muscle-tendon continuum alongside imaging data is imperative to gain an insightful and informed

understanding of the stress-strain profile of muscles (Blemker et al., 2005). This was shown in a model created for the bicep femoris longhead, which was used to explore strain injuries and ruptures of the hamstrings. The results showed that damage frequently occurred at the myotendon junction (Rehorna & Silvia S. Blemker, 2010). This model was comprehensive in showing the potential effect of the morphology of the aponeurosis on determining muscle injury susceptibility, despite using idealised geometries and fibre orientations (Rehorna & Silvia S. Blemker, 2010). A further study by Chi et al. (2010) also suggested that the complex strain mechanics of aponeuroses were highly influenced by their fibre orientations close to the transition zone (Chi, 2010).

The passive strains found in the fascicles are thought to counteract active strains in the gastrocnemius, causing local lengthening in the proximal insertion and shortening in the distal origin ends of the medial gastrocnemius (Karakuzua, et al., 2017). Although the active and passive response of the muscle's mechanical response can be amalgamated, these responses (active and passive) are decoupled in an additive split, as shown in Chapter 4. The tissues that make up the medial gastrocnemius consist of muscle, aponeurosis and tendon tissues and it is important to note again - only the passive contribution has been considered in this thesis. An active component can be added to the constitutive formulation (Equation **4.48**) shown in Chapter 4, as has been done with other similar formulations (Blemker, et al., 2005; Röhrle, et al., 2007), but is beyond the scope of this thesis.

Due to the tissue constituents of the tendon and aponeurosis, they have been modelled as transversely isotropic, fibre-reinforced quasi-incompressible materials (Roberts, 2009; Bajuri, et al., 2016; Holzapfel, et al., 2000; Lieber & Blevins, 1987). Since skeletal muscle is composed of various fibre-reinforced materials in series, each of these tissues is modelled with a strain-energy function, as explained in Chapter 3 and shown in Equation 6.70. The muscle and tendon tissues were considered to have one family of fibres each (Blemker, et al., 2005; Bajuri, et al., 2016), while the aponeurosis and muscle-tendon junction is considered to be a mixture of muscle and tendon tissue – i.e. a transition zone from muscle to tendon. The muscle-tendon junction areas have therefore been modelled with two families of fibres (muscle fascicles and collagenous tendon fibres), each with a respective volume fraction depending on the distance to muscle or tendon. It is assumed that the muscle and

tendon constituents had similar passive mechanical characteristics, with different material constants.

As shown in Chapter 4, the stresses and deformations of the constitutive tissues are related by means of a strain energy density function adapted from Holzapfel et al. (2000). Each of the respective tissues are therefore defined by the inclusion of a volume fraction as shown in Equation **6.65**. The total strain energy function of the muscle consists of a deviatoric (shape change) and volumetric isochoric (incompressible) part. The strain energy function defined in Equation **6.70** encompasses a further additive split of the passive response between the *isotropic* and *anisotropic parts*.

6.2 Mathematical Representation of the Tendinous Aponeurosis to Muscle Transition zone

Building on the strain energy function defined in Holzapfel et al. (2000), the aponeurosis and transitional zones between tendon and muscle have been represented by means of a volume fraction. This formulation separates the tendinous constituent and muscle constituent as separate mathematical terms, whilst defining the material constants of the transition zones of the muscle tendon junction. This has been done by introducing a new parameter – the volume fraction – to the conventional formulation developed by Holzapfel et al. (2000).

$$\begin{aligned} & f_T(x) \equiv \text{volume fraction of tendon} \\ & f_M(x) \equiv \text{volume fraction of muscle} \\ & \therefore \\ & f_T(x) + f_M(x) = 1 \end{aligned} \qquad \textbf{(6.65)}$$

Where:

$$0 \leq f_T(x) \leq 1$$

$$\bar{\psi}_{\text{Medial Gastrocnemius}} = f_T(x)\bar{\psi}_T + f_M(x)\bar{\psi}_M$$
$$\therefore \quad \textbf{(6.66)}$$
$$\bar{\psi}_{\text{Medial Gastrocnemius}} = f_T(x)\bar{\psi}_T + (1 - f_T(x))\bar{\psi}_M$$

The strain energy functions denoted as $\bar{\psi}_{\text{Medial Gastrocnemius}}$, $\bar{\psi}_{\text{T}}$, and $\bar{\psi}_{\text{M}}$ represent the medial gastrocnemius , tendon and muscle constituents, respectively.

As:

$$\bar{\psi}_{\text{T}} = \frac{c_1^T}{2}\left(\bar{I}_1 - 3\right) + \frac{k_1^T}{k_2^T}\left(e^{k_2^T(I_4-1)^2} - 1\right) \quad \textbf{(6.67)}$$

$$\bar{\psi}_{\text{M}} = \frac{c_1^M}{2}\left(\bar{I}_1 - 3\right) + \frac{k_1^M}{k_2^M}\left(e^{k_2^M(I_6-1)^2} - 1\right) \quad \textbf{(6.68)}$$

Where $c_1^{T,M}$ is the Neo-Hookean isotropic material constant for tendon or muscle tissue, respectively, and $k_1^{T,M}$ is the first anisotropic material constant for tendon or muscle tissue, respectively. These two constants are measured in MPa. $k_2^{T,M}$ is the second anisotropic material constant for tendon or muscle tissue and this parameter is dimensionless. The fourth invariant of the Cauchy-Green deformation tensor is represented by I_4, and represents the fibre directions for the tendon fibres in the constitutive relationship. I_6 is the sixth invariant of the Cauchy-Green deformation tensor and represents the fibre directions for the muscle fibres.

Following the assumptions above, the fibres governed by $\bar{I}_4$ are tendon fibres and the fibres defined by $\bar{I}_6$ are muscle fibres; thus the deviatoric part of the muscle and tendon tissues can be defined by;

$$\bar{\psi}_{\text{Medial Gastrocnemius}} = f_T(x)\left(\bar{\psi}_{iso} + \bar{\psi}_{aniso}\right)_T + \left(1 - f_T(x)\right)\left(\bar{\psi}_{iso} + \bar{\psi}_{aniso}\right)_M \quad \textbf{(6.69)}$$

Which leaves;

$$\overline{\psi}_{\text{Medial Gastrocnemius}} = f_T(x)\left(\frac{c_T}{2}(\bar{I}_1 - 3)\right) + f_T(x)\left(\frac{k^T{}_1}{2k^T{}_2}\left(e^{k^T{}_2(I_4-1)^2} - 1\right)\right) + \ldots$$
$$\ldots(1 - f_T(x))\left(\frac{c_M}{2}(\bar{I}_1 - 3)\right) + (1 - f_T(x))\left(\frac{k^M{}_1}{2k^M{}_2}\left(e^{k^M{}_2(I_6-1)^2} - 1\right)\right) \quad \textbf{(6.70)}$$

Further analysis now requires the exploration and selection of the correct material parameters to use for numerical simulations - which has been comprehensively discussed in Chapter 4.

It is important to note, however, that the specific and independent material properties of muscle and tendon are required in the formulation defined in Equation 6.70 because of the additional assumptions made about the muscle-tendon junction constituents.

6.3 Numerical Implementation of a Muscle-Tendinous Aponeurosis Junction

The mathematical representation of the transition zone, tendinous aponeurosis, muscle and tendon tissue has been defined in Chapter 6.1. The current section describes the numerical implementation in ANSYS, utilising the material parameters stated in Tables 4.2 and 4.3. The model was built in ANSYS, using anatomical data of the medial gastrocnemius geometry and fibre orientations. The strain energy function W_d used in ANSYS is defined in Equation 6.71.

$$W_d(\bar{\mathbf{C}}, \mathbf{A}\otimes\mathbf{A}, \mathbf{B}\otimes\mathbf{B}) = \sum_{i=1}^{3} c_i(\bar{I}_1 - 3)^i + \sum_{j=1}^{3} b_j(\bar{I}_2 - 3)^j + \ldots$$
$$\ldots\left(\frac{k_1}{2k_2}e^{k_2(\bar{I}_4-1)^2} - 1\right) + \left(\frac{E_1}{2E_2}e^{E_2(\bar{I}_6-1)^2} - 1\right) \quad \textbf{(6.71)}$$

From Equation **6.71**, As the terms have been defined above in Chapter 4, the new terms introduced here can be defined as follows. $\mathbf{A}$ is the vector field for the first

family of fibres. $\mathbf{B}$ is the vector field for the second family of fibres and c_i and b_i can be defined by the first and second isotropic material constants, respectively, that relate to the distortional response usually measured in MPa. The first anisotropic material constant related to the distortional response is represented by k_1 for the first body of fibres and by E_1 for the second body of fibres. The second anisotropic material constant related to the distortional response, meanwhile, is represented by E_2 for the first body of fibres and k_2 for the second body of fibres. These second material constants are dimensionless.

The constitutive relationship that is used in this thesis, as shown in Equation 6.70, consists of only one isotropic term (therefore 'b' = 0), where the 'k' material constants refer to the tendon tissue and the 'E' material constants refer to the muscle tissue in Equation 6.71. The transitional tissue is represented by a mixture of the two, derived through the volume fraction parameter, which is defined with respect to the x-coordinate of each centroid (linear dependence) and the perpendicular distance of each centroid to the central line (radial dependence). These dependencies are described in detail below.

6.3.1 Linear Dependence

The transitional zone was represented with a measure of the volume fraction f(x), ranging between $0<f_T(x)<1$. This volume fraction was used to differentiate: the muscle tissue, the tendon tissue and the transitional muscle-tendon junction. Using the material constants reported in Tables4.2 and 4.3, two families of fibres were defined (muscle and tendon), each with their own material constants, with the tendon constituent (when f(x) = 1) being stiffer than the muscle (when f(x) = 0). The function in Equation 6.72 then defines the linear dependence of the volume fraction, which is reliant on the distance of each centroid from the origin. Figure 6.2 provides a schematic of the linear distance dependant function.

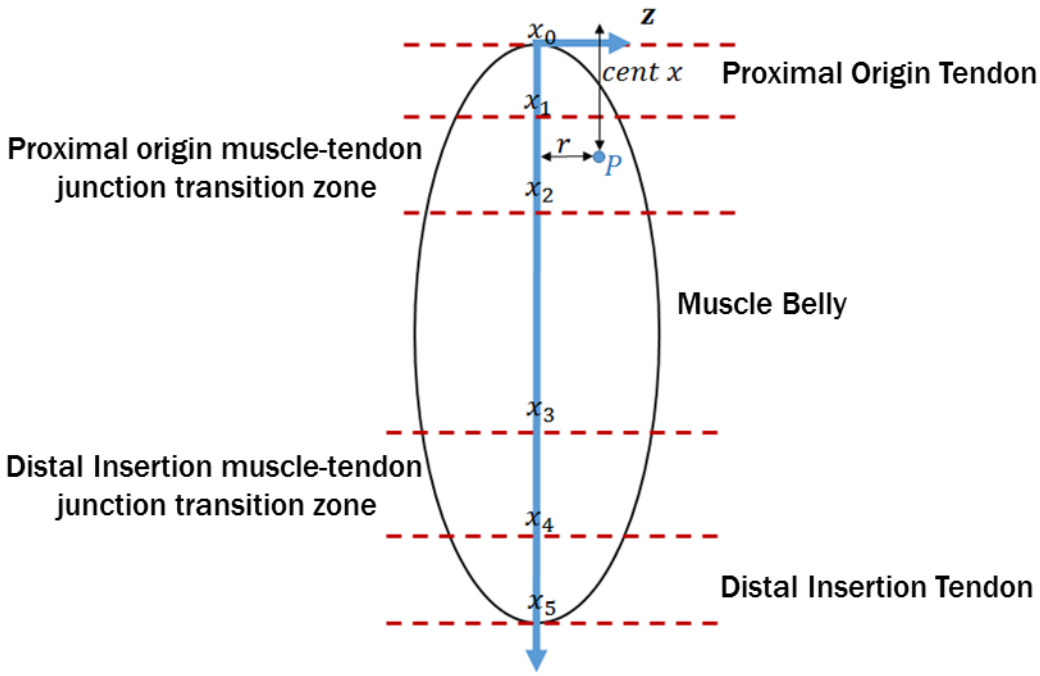

Figure 6.2 Schematic showing the linear dependence of the discretised muscle-tendon complex

The zones defined in Figure 6.2 can be mathematically represented by a volume fraction f(x) using the following piece-wise function.

$$1-f_M(x)=f_T(x)=\begin{pmatrix}1\\(x_2-x_C)/(x_2-x_1)\\0\\(x_C-x_3)/(x_4-x_3)\\1\end{pmatrix}=\begin{pmatrix}x_0\le x<x_1\\x_1\le x<x_2\\x_2\le x<x_3\\x_3\le x<x_4\\x_4\le x<x_5\end{pmatrix}=\begin{pmatrix}\text{Origin Tendon}\\\text{Transition}\\\text{Muscle}\\\text{Transition}\\\text{Insertion Tendon}\end{pmatrix} \quad \textbf{(6.72)}$$

Where x_C is the x-coordinate of the centroid along the long axis of the muscle, and x_{0-5} are the known x-coordinates that determine the different tissue boundaries, as shown in Figure 6.2 .

This means that the calculated centroid location of each element at the muscle-tendon junction will have a different volume fraction f(x), and each element will have different material parameters, being either muscle, tendon, or a constitutive mixture

of the two, where any centroid point ‘P’ will be more muscular or tendinous based on its proximity to those respective tissues.

A schematic to show the distribution of the volume fraction with linear dependence is shown in Figure 6.3

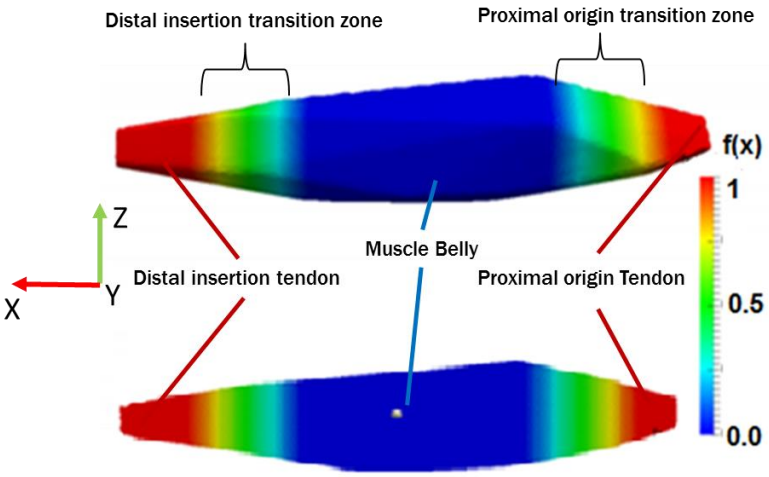

Figure 6.3 Contour of volume fraction of tendon dispersion across the body of the tendon-muscle complex.

The linear dependence algorithm was then used to define the radial dependence which further improved the morphological description of the aponeurosis and muscle-tendon junction. This is described in the next section.

6.3.2 Radial Dependence

Whilst the linear dependence defined in Figure 6.3. showed the efficacy of the concept of a transition zone, the linear degradation of material properties is quite crude compared to the real anatomical structure, since the morphology of the aponeurosis is such that it spans over the body of the muscle with an encapsulating apex-like morphology. The radial dependence aims to follow the general anatomical structure of the muscle through a mathematical algorithm that closely ties in with the finite element mesh.

The radial dependence function was created by first calculating a central line. This is necessary because the x-axis does not necessarily run along the long-axis of the muscle belly. The central line was defined by first isolating planes across the muscle geometry, every 1 mm down the x-axis in the y-z plane. The coordinates of each

centroid (of each element), within each respective plane, were collected as shown in Figure 6.4. The average y and z coordinates of all the centroid points within a plane were calculated to estimate the central line.

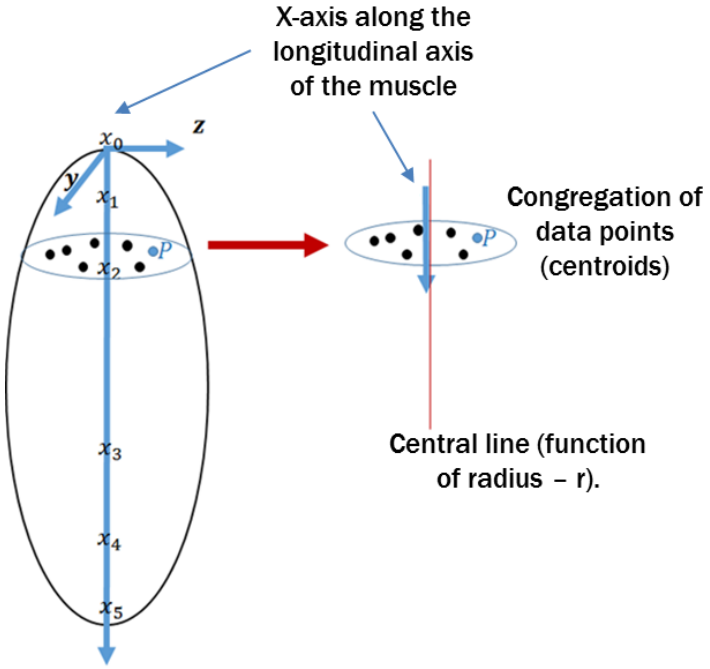

Figure 6.4 Schematic of the tendon-muscle complex showing the z-y approximation used to calculate the geometrical central line, in relation to the x-axis based on centroid points 'P'.

It is important to note from Figure 6.4 that the x-axis of the skeletal muscle was independent of the central line. Specifically, the central line was calculated by getting the mean value of all y and z-coordinates across each plane, defined in Equation 6.73 and Equation 6.74, respectively.

$$\bar{y}_0 = \frac{\sum_{i=1}^{n} y_i}{n_C} \tag{6.73}$$

Where $\bar{y}_0$ is the central averaged y coordinate across a selected plane, y_i is the y coordinate of each respective centroid on a selected plane and n_C is the number of centroids specifically on a selected plane.

$$\bar{z}_0 = \frac{\sum_{i=1}^{n} z_i}{n_C} \quad \textbf{(6.74)}$$

$\bar{z}_0$ is the central averaged z coordinate across a selected plane and z_i is the z coordinate of each respective centroid on a selected plane. This provides a range of key points from each plane, with varying x-coordinates along the centre of the planes, projected along the centre of the muscle:

$$(x_i^C, \bar{y}, \bar{z}) \quad \textbf{(6.75)}$$

Where x_i^C = the varying x-coordinates along the central line. The radius that f(x) was to depend upon, was calculated by the perpendicular distance from a centroid point P to the central line coordinates, calculated in Equation 6.75 and defined using the parameters shown in Figure 6.4. This radius was calculated using the Euclidean distances of the y and z coordinates for each point, as shown in the Equation 6.13.

$$r = \sqrt{(y_i - \bar{y}_0)^2 + (z_i - \bar{z}_0)^2} \quad \textbf{(6.76)}$$

Where r is the radius of the perpendicular distance of a centroid point 'P' to the central line. This provided a respective radius and x-coordinate x_i, that was on the axis of the muscle for each centroid point - P_i which is defined with respect to r and x_i by:

$$P_i = (r, x_i) \quad \textbf{(6.77)}$$

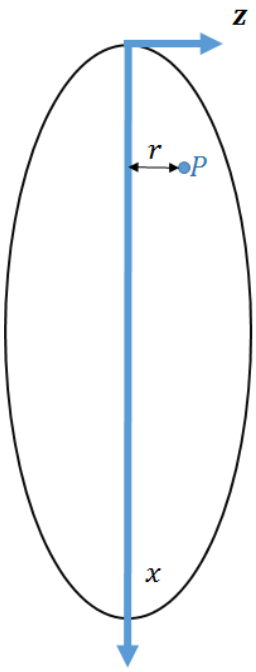

Figure 6.5 Schematic showing the function of 'r' radius for each defined centroid point shown here as 'P'.

The transition zone between the muscle and tissue was represented by a cone shape. A simple linear equation was used to define the known points A and B. A was determined by the anatomical base point on the central line where the tendon ended and the transition zone started, as shown in Blitz et al. (2007). B was the outermost point that the 'cone' shape reached on the muscle geometry surface, also congruent with anatomical landmarks reported in Blitz et al. (2007). B was also the largest x coordinate on the muscle geometry surface where the transition zone began, and the tendon zone ended. This was then rotated along the x-axis to define a projected 3D cone-like structure of the tendinous-aponeurosis transition and muscle junction. This process was repeated for points DEF as shown in Figure 6.6.

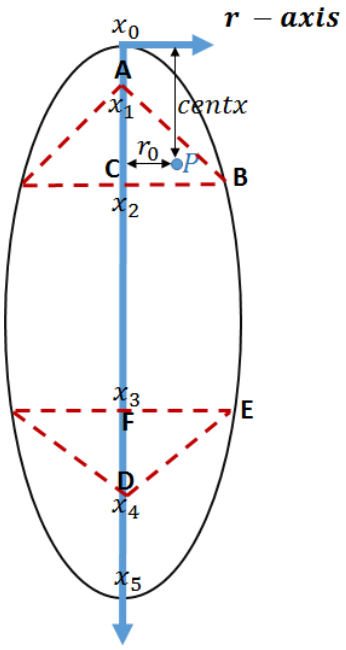

Figure 6.6 Schematic showing the discretisation of the muscle-tendon complex with the muscle-tendon origin and insertion junction defined within ABC and DEF, respectively.

The aim was then to define any point within this triangular structure as a transition zone becoming muscle, and anything outside of this triangular zone as aponeurotic/tendinous. To this end, the piece-wise function for the linear dependence shown in Equation 6.72 was slightly amended to show instead the piece-wise function for the radial dependence shown in Equation 6.78:

$$1-f_M(x)=f_T(x)=\begin{Bmatrix}1,\\ \frac{x_2-x_i}{x_2-x_1}\bullet\frac{r}{f_{AB}^{-1}(x_i^C,r_0)}\\ 0\\ \frac{x_4-x_i}{x_4-x_3}\bullet\frac{r}{f_{DE}^{-1}(x_i^C,r_0)}\\ 1\end{Bmatrix},\begin{pmatrix}x_0\le x<x_1\\ x_1\le x<x_2\\ x_2\le x<x_3\\ x_3\le x<x_4\\ x_4\le x<x_5\end{pmatrix},\begin{pmatrix}\text{Origin Tendon}\\ \text{Transition}\\ \text{Muscle}\\ \text{Transition}\\ \text{Insertion Tendon}\end{pmatrix} \quad \textbf{(6.78)}$$

$f_{AB}^{-1}(x_i^C,r_0)$ can be defined as the volume fraction of the origin transition zone defined in triangle ABC and transposed in a 3D fashion, with the radius of each centroid r_0 being dependent on its perpendicular central line x-coordinate x_i^C. $f_{DE}^{-1}(x_i^C,r_0)$ represents the volume fraction of the insertion transition zone defined in triangle DEF and transposed in a 3D fashion, with the radius of each centroid r_0 being dependent on its perpendicular central line x-coordinate x_i^C.

Figure 6.7 provides a graphical representation of the volume fraction f(x) distribution across the muscle using the radial function described in Equation 6.78.

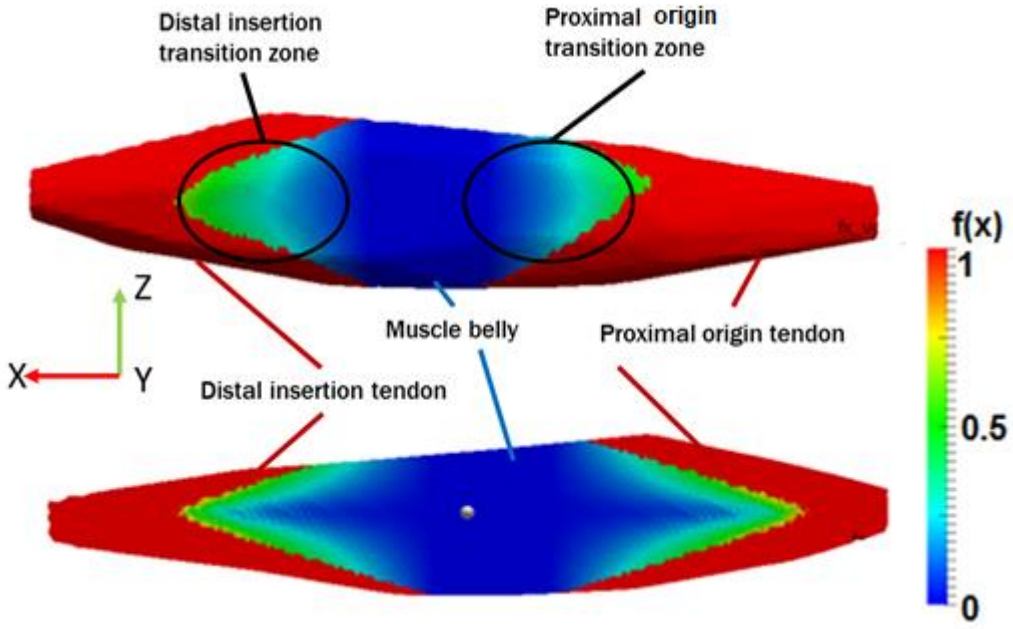

Figure 6.7 Colour separation of the tendon - muscle distribution f(x), according to the radial dependence, which served to define the material constant distribution. Three-dimensional model (top) and sliced section plane in the z axis (bottom).

Whilst the current model elucidated an enhanced description of the medial gastrocnemius aponeurosis, there were still some issues surrounding the region in which the muscle penetrated the tendon. At these transition regions, the apex was very sharp, as shown in Figure 6.7. Therefore, further erudition of the model was employed, where this apex was modelled as a blunt 'cupping' feature using an ellipsoidal function.

6.3.3 Ellipsoid Apex Enhancement

The cone model presented in the previous section has a few limitations, one of which is the sharp apex at which the muscle penetrates tendon. Therefore, an alternative model is presented in this section, using a 3D half-ellipsoid, to provide a more accurate description of the core geometry and to ease the penetration angle at the apex. This is shown in Figure 6.8 .

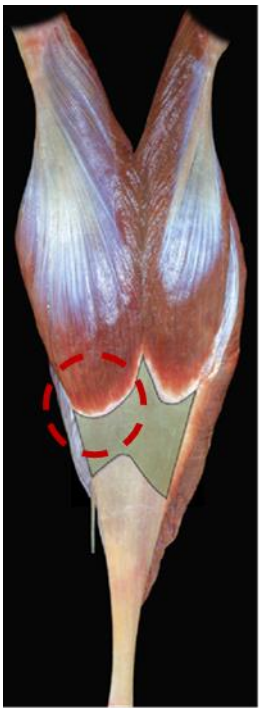

(a)

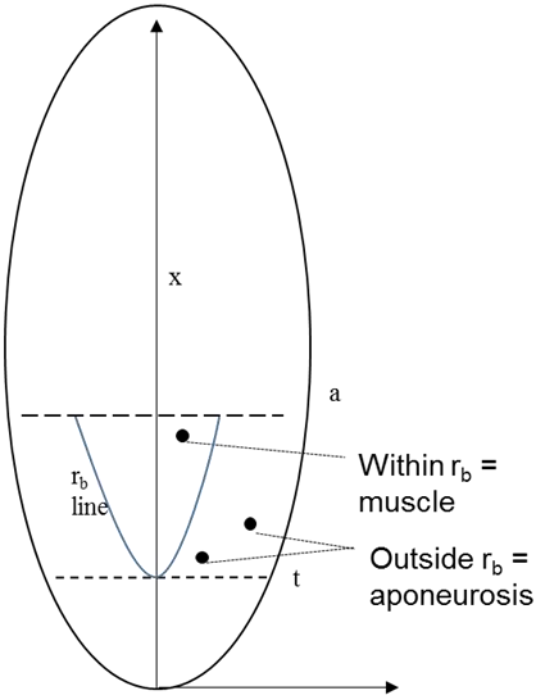

(b)

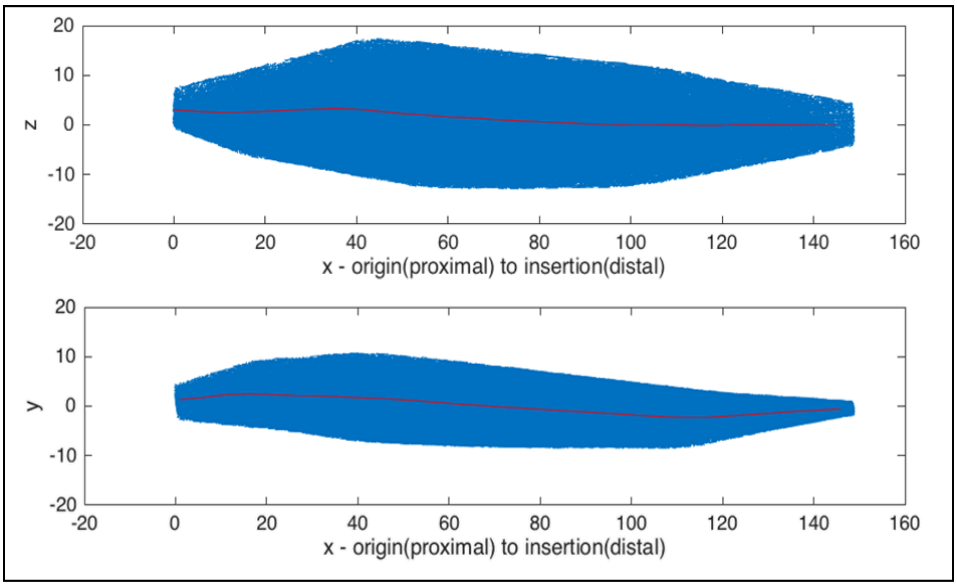

(c)

Figure 6.8 (a) Anatomical representation of the gastrocnemius muscle, showing a cup-like radius (red circle). (b) Half-ellipsoid schematic representation of radial boundaries (r_b), of the cup. (c) The muscle geometry with central line as defined in Equations 6.73, 6.74 and 6.75 (Patterson & Watton, 2018).

This geometrical representation of the cup was implemented where a point along the pre-defined centre line (c) of the muscle co-ordinate system, at an x-axis position, was used for the radial dependence, as described in section 6.3.2. The formula for an ellipsoid, (*Equation* **6.79***)* was then applied to every centroid within the aponeurosis region, hence resulting in a value for the volume fraction, $f_T(x)$, as shown in Equation **6.78**.

$$f_T(x) = \left[\left(\frac{(x-x_1)^2}{a^2}\right)+\left(\frac{(y-y_1)^2}{b^2}\right)+\left(\frac{(z-z_1)^2}{c^2}\right)\right] \qquad \textbf{(6.79)}$$

x_1, y_1 and z_1 indicate the co-ordinates for the central points of the ellipsoid, x, y and z determine the centroid co-ordinates and a, b and c represent the variable dimensions of the ellipsoid in the x, y and z directions, respectively. The parameters that represent the ellipsoid dimensions are taken from the anatomical study done by Blitz & Rush., (2007) and Blitz & Eliot (2008). This half ellipsoid model implemented, is illustrated in Figure 6.9.

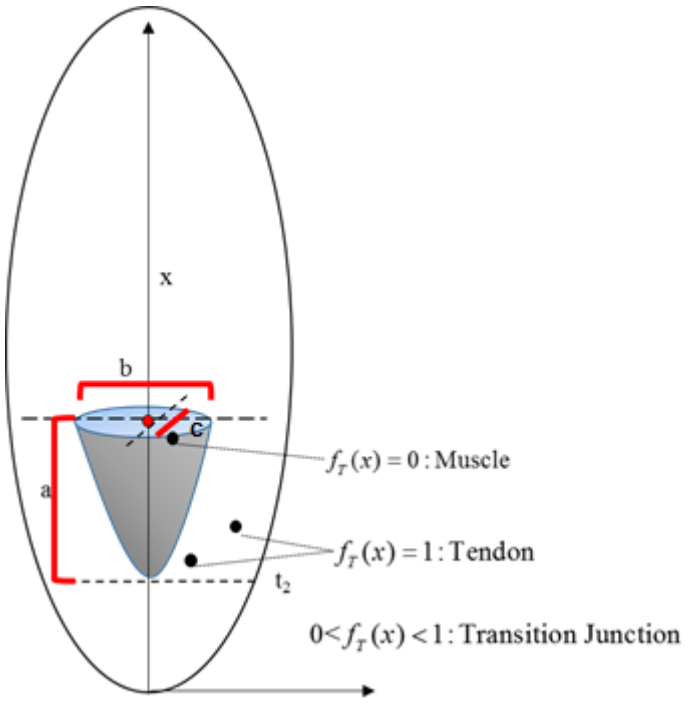

Figure 6.9 Schematic illustrating the implementation of the half ellipsoid muscle-tendon cup apex geometry. The red dot indicates the centre point of the ellipsoid.

The values of $f_T(x)$ vary between 0 and 1, hence determining the constituents in each element being either muscle, tendon or transition depending on its proximity to muscle or tendon tissue within the ellipsoid region.

As an ellipsoid is an idealised shape within an axisymmetric muscle geometry, further modifications were required to provide a more accurate anatomical description of the aponeurosis. Therefore, flat boundaries were applied to the ellipsoidal model, in a tapered fashion as illustrated in Figure 6.10

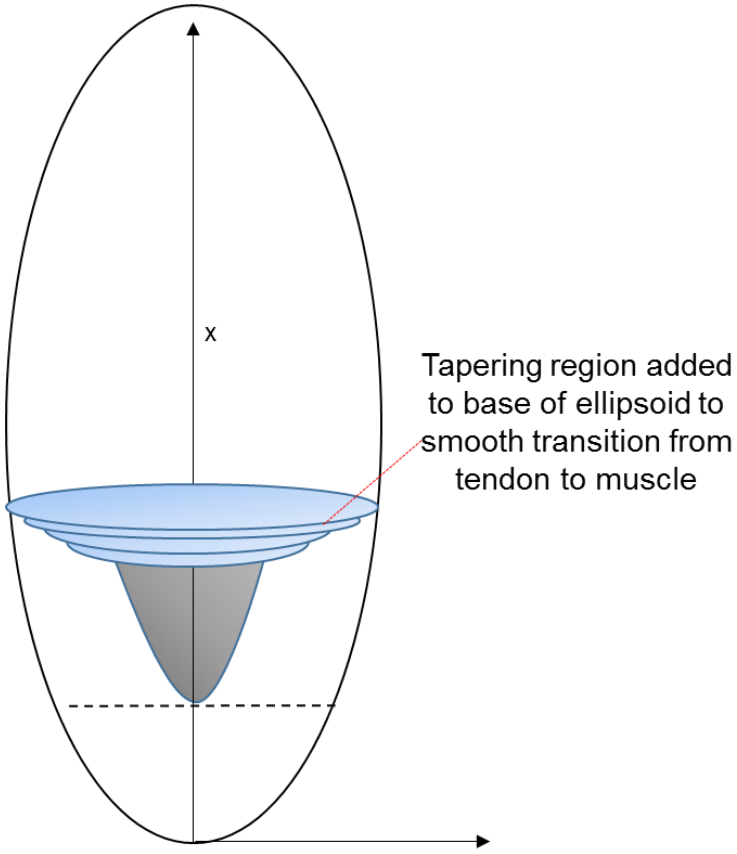

Figure 6.10 Schematic representation of the tapering base added to the half-ellipsoid muscle-tendon junction, using an increasing radius.

The tapering base was achieved by using a two-dimensional boundary that increased in radius in the y-z plane, as the x-axis increased along the central line. Therefore, any centroids within this region became part of the muscular penetration, and the centroids outside this region were tendon. The transition region in this area was still radially dependant, as defined in Equation **6.79**. The length and gradient of

the tapering region can be changed by increasing the radial length along the central line, e.g. a 10% increase in radial length per 1mm increase in the central line.

The final ellipsoid model with the tapering edges are shown in Figure 6.11.

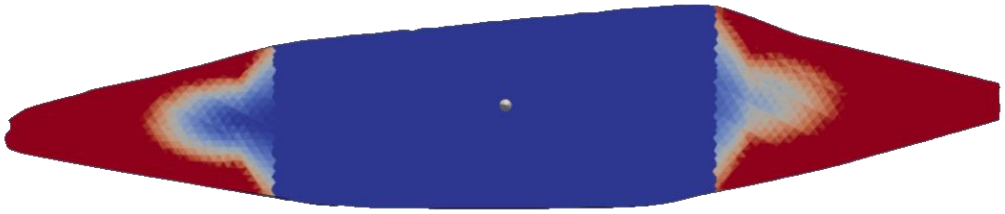

Figure 6.11 with the volume fractions f(x) = 1 (red) tendon, f(x) = 0 (blue) muscle and 0<f(x)<1 (white shade) transition region.

The linear, radial and ellipsoidal algorithms of the material constant distribution were applied to the muscle geometry, and simulations were carried out to determine the stress-strain profile, and hence the mechanical response of the muscle. The muscle was fixed at the proximal origin and extended by 12 mm at the distal insertion to simulate the muscle in dorsi-flexion. The sides of the muscle adjacent to the lateral gastrocnemius and soleus were fixed in the y and z directions, respectively.

The boundary conditions used for this simulation are identical to those used and described in Chapter 5

6.3.4 Finite Element Results of the Various Aponeurosis Morphologies

The predicted stress-strain distribution is shown in Figure 6.12. The four cases presented are: (1) A sharp junction (i.e. no muscle-tendon transition zone); (2) A linear distance dependence as defined in Section 6.2.1; (3) A radial dependence as defined in Section 6.2.2; and (4) An ellipsoid apex model defined in Section 6.3.3.

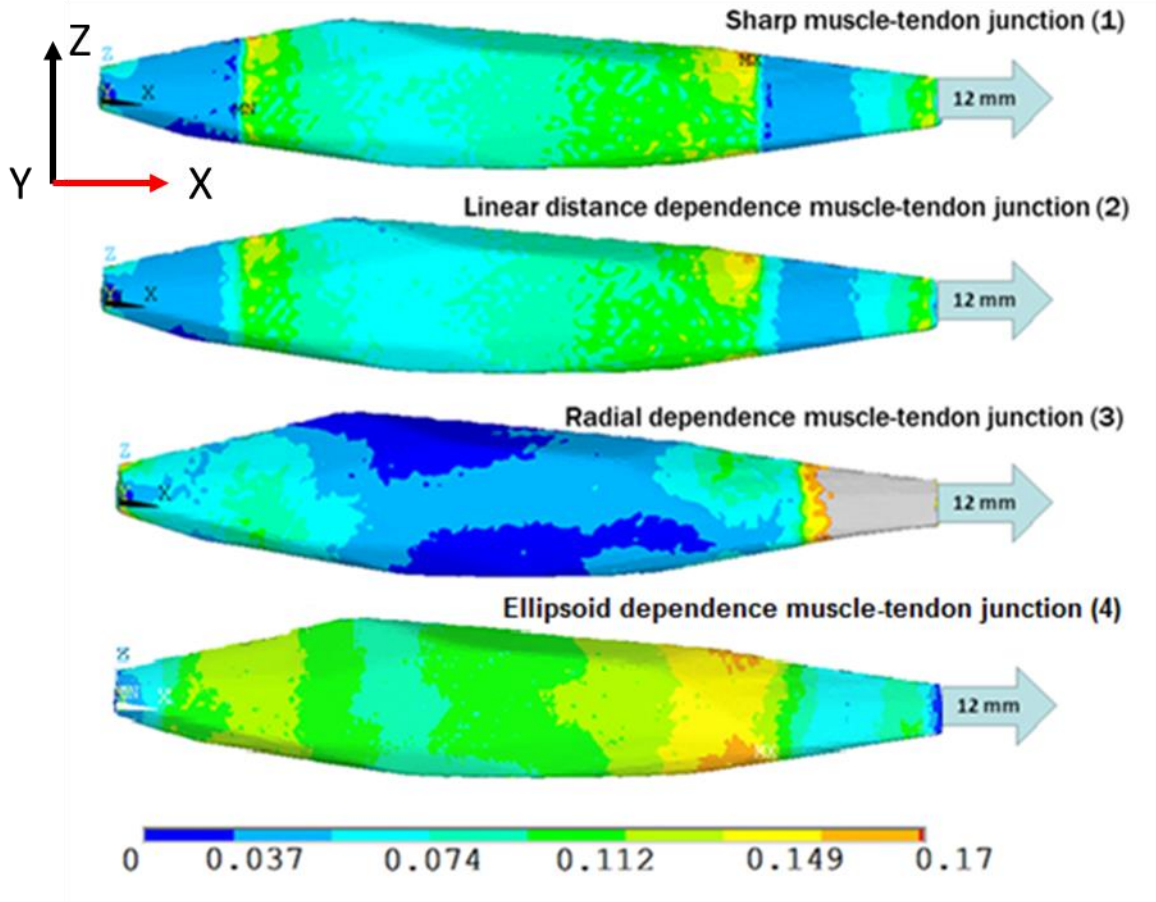

Figure 6.12 First principal strain results of case (1) with a sharp transition region, linear case (2), radial case (3) and finally ellipsoid case (4) dependence of f(x) muscle - tendon transition junction. Shown in anterior view (side adjacent to the soleus) with the muscle extended by 12 mm.

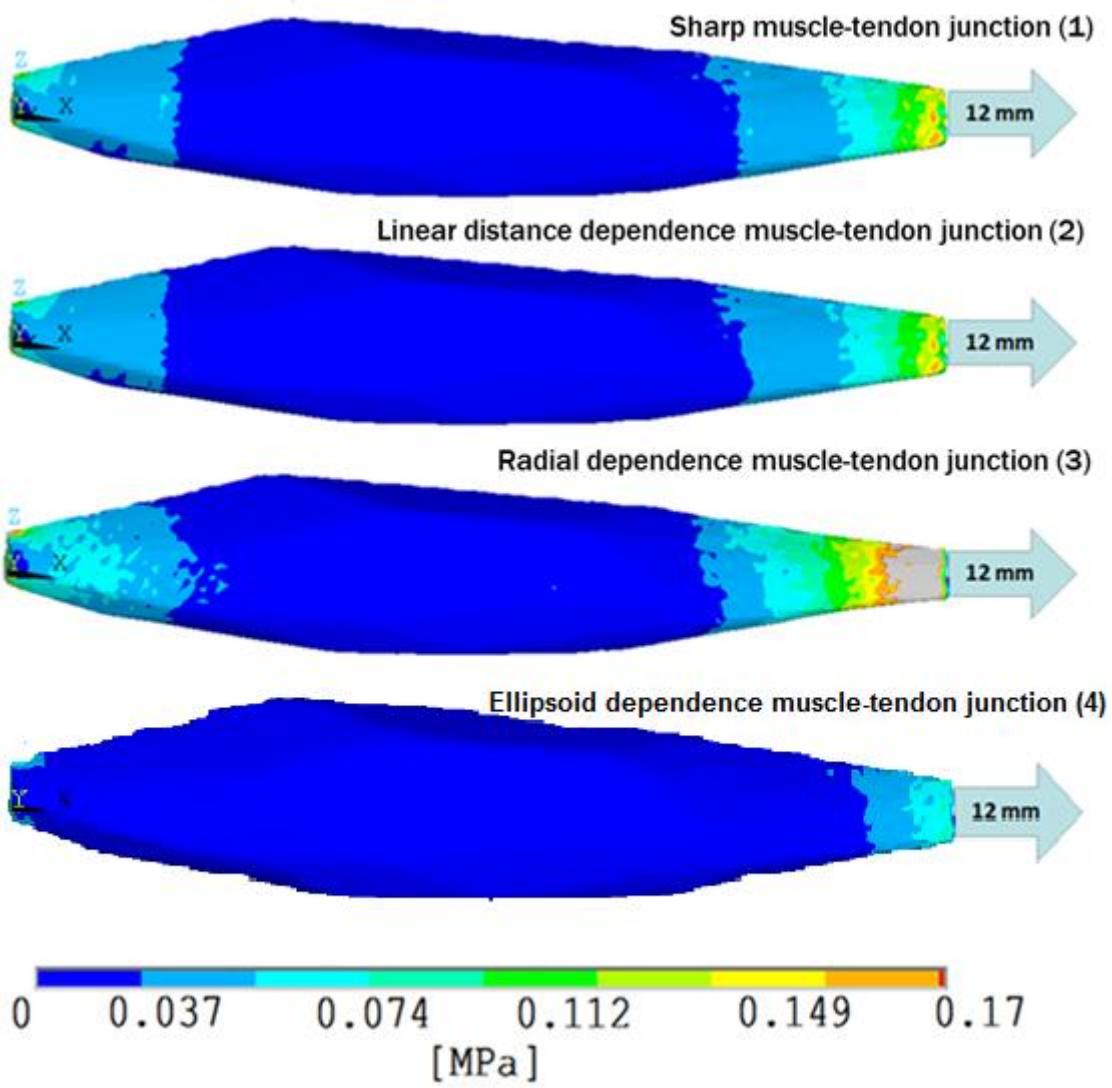

Figure 6.13 First principal stress results of case (1) with a sharp transition region, linear case (2) and radial case (3) and finally ellipsoid case (4) dependence of f(x) muscle - tendon transition junction. Shown in anterior view (side adjacent to the soleus) with the muscle extended by 12mm.

Figures 6.12 and 6.13 show the strain and stress results, respectively, of the muscle-tendon junction. The muscle-tendon junction (transition zone) has been mathematically applied as above, according to the material constants of the constitutive relationship shown in Equation 6.70 (Holzapfel, 2000). The arbitrary dependence case (1) has no transition zone, in other words the muscle-tendon junction is acute and goes straight from muscle to tendinous constitutive tissue. Figures 6.12 and 6.13 reveal that the arbitrary and linear dependence stress and strain results are not qualitatively different, with a similar 'band' or transverse region of intensity across

both methods and cases (1 and 2). In Figure 6.12, the strain results show a region of high strain intensity at the muscle-tendon transition region of the muscle geometry. These regions have been labelled anatomically in Figure 6.7 and Figure 6.3 , and these islands are located at the side close to the skin of the medial gastrocnemius . However, there is a clear difference between the strain results for cases (2) and (3). In the radial dependence (case 3) simulation, the island of intensity previously found in cases (1) and (2) has reduced. This suggests a more physiologically accurate strain distribution with the radial implementation in case (3). Higher strains are also present at the distal insertion or myotendinous junction of the muscle (towards the Achilles tendon), which agrees with experimental findings with respect to high strain injuries of the medial gastrocnemius (Azizi & Roberts, 2009; Prakash, et al., 2017; Gilbert, et al., 1996; Severance & III, 1982; Bianchi, et al., 1998; Delgado, et al., 2002; Koulouri, et al., 2007; Cibulka, et al., 2017). Compared with cases (1) and (2), case (3) also predicted lower strains in the belly of the muscle. This is however, in contrast to case (4), which appeared to have higher strains in the belly of the muscle, although the resultant strains and stresses in the tendinous region are much lower, which are expected as the Achilles tendon has been previously reported to be more than 4 times stiffer than muscle tissue (Kawakami, et al., 2008). The next section discusses the inference of these results, and which setup maybe more favourable for subsequent simulations.

6.3.5 Discussion

Whilst case (4) is more favourable in that it emulated a more uniform strain distribution with generally higher strains in the belly of the muscle; during high displacements the musculotendinous junction and the tendon has been shown to be the main area of strain injury when the muscle has been exposed to high displacements during dorsi-flexion. As such, case (4) suggests the areas of highest strain will occur in the belly of the muscle, (as opposed to the myotendinous junction) which is contrary to other physiological findings (Armfield, et al., 2006), and experimental studies which reported that almost no strains were present in the proximal medial gastrocnemius when the muscle is in maximum dorsi-flexion of -30° (Kawakami, et al., 2008; Hobara, et al., 2012; Whitting, et al., 2013).

Having carried out these illustrative simulations, the aponeurosis representation emulates a finite element solution that suggests that case 3 – the aponeurosis with

radial dependence – offers a more physiologically representative result, hence the model used in the following sections. However, it should be noted that case (4) should be further explored in future to provide a better understanding of the difference in mechanical response of the changes in aponeurosis representation.

Using the converged mesh defined in Section 5.2.1, simulations were carried out to investigate the effects of the geometry of the muscle-tendon transition zone on the stress-strain response of the muscle. Three scenarios were considered: (i) the muscle under high strains, (ii) the aponeurosis increasing in length and (iii) the tendon healing over a period of 21 days after a prior laceration.

6.4 The Effects of High Strains on the Muscle-Tendon Complex

The individual muscles that comprise of the triceps surae (the calf muscle including soleus, gastrocnemius and plantaris) often experience injury induced by high strains. This trio of muscles join to form the aponeurosis of the Achilles tendon (Dixon, 2009). Localised injuries in these muscles, particularly in the soleus and gastrocnemius muscle, are particularly important for the accurate prognosis, treatment and deterrence of recurrent injury (Dixon, 2009).

Although strain injury rates of the triceps surae are low (Coughlin et al., 2006; (DeLee et al., 2003; Brukner & Khan, 2002; Garrett, 1996), when they occur, they are predominantly found in athletes (Armfield et al., 2006), which may be due to the high strains the triceps surae muscles are exposed to when the ankle is in extreme dorsi-flexion and the knee is in extension during strenuous sporting activities such as running.

Triceps surae injuries are commonly found in the medial head of the gastrocnemius muscle (Brukner & Khan, 2002), which were initially associated with playing tennis, referred to as *'Tennis Leg' (*Fu & Stone, 2001). The classic presentation of this injury is when the knee suddenly extends with the foot in dorsi-flexion, which passively extends the triceps surae muscles. This type of rapid extension results in immediate pain, disability and swelling which can last from months up to years depending on the

severity of the injury, and the efficacy of treatment (Coughlin et al., 2006). The medial gastrocnemius not only covers two joints (ankle and knee), it also contains many type two fast twitch muscle fibres, which inherently increase the risk of injury; which in the case of this muscle occurs particularly in relation to tennis-leg type strain injuries (Simon et al., 2006; DeLee et al., 2003; Garrett, 1996; Armfield, et al., 2006). In addition, the diarthrodial architecture of the muscle, along with excessively forceful and rapid stretching, also contribute to muscle injury. This mechanism conjures the image of a 'cracking whip' which consequently and has historically, been referred to as *'coup de fouet'* (directly translated as *'snap of the whip'* (Fu & Stone, 2001)).

Although previous studies have tried to localise areas of damage during high strain injuries in the gastrocnemius by using palpation and physical examinations (Armfield et al., 2006), the full anatomical location of the injury is not fully known (Dixon, 2009).Hence, the benefit of a finite element model that can show distributions of strain along the muscle pose great potential in physical therapy diagnosis.

Gastrocnemius strains are often characterised by tenderness in the medial belly or at the muscular-tendinous junctions (Dixon, 2009), thus suggesting the most likely areas of damage in the gastrocnemius. Palpation, strength testing and stretching are all physical measures that can be done to help diagnose strains of the medial gastrocnemius head, but an accurate diagnosis of the extent of damage is required to gain a better understanding of strain injuries, particularly in the medial gastrocnemius muscle. Such an understanding would help localise and determine areas of high risk as well as determine the amount of strain that could lead to injury.

6.4.1 Boundary Conditions

The boundary conditions were prescribed to mimic extreme strains in the medial gastrocnemius. These were similar to those described in Chapter 5, with the exception that the muscle-tendon complex was stretched to the furthest length (convergence allowed), which was approximately 20% of its original length (29 mm, as opposed to the 12 mm as described in Chapter 5.) to assess the effects of extreme strains on the muscle-tendon complex of the medial gastrocnemius muscle and to also determine the limit of strain the muscle would extend to.

The length, depth, radial dependence and thickness of the myotendinous junction, aponeurosis, tendon and muscle constituents were kept constant, with the distal

insertion muscle-tendon junction being set at 15 mm and the distal insertion tendon at 18 mm. The muscle only region had a length of 100 mm. The proximal origin muscle-tendon junction and tendon were set at 5 mm and 10 mm, respectively. This anatomical configuration is shown in Figure 6.14 and was done to mimic the full medial gastrocnemius muscle-tendon configuration as comprehensively discussed by Blitz et al. (2007). All material constants were the same as those reported in Chapter 4, Table 4.2.

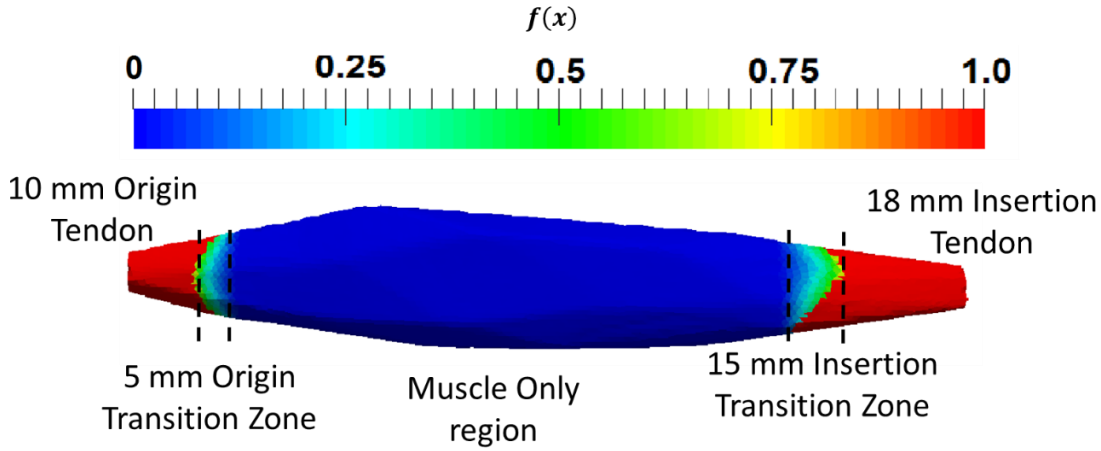

Figure 6.14 Sections in the muscle-tendon model. The spectrum shows the volume fraction.

6.4.2 Simulation Results of High Strains on the Medial gastrocnemius Muscle.

This section describes the simulation results of the medial gastrocnemius tendon-muscle complex after being stretched to its computational limit of 20% of its original length (29 mm). The distribution of the first principal strain and stress are shown in Figure 6.15. The contours of the strains were plotted up to 0.17, since this was the contour range that allowed for a clear distribution across all the various simulations.

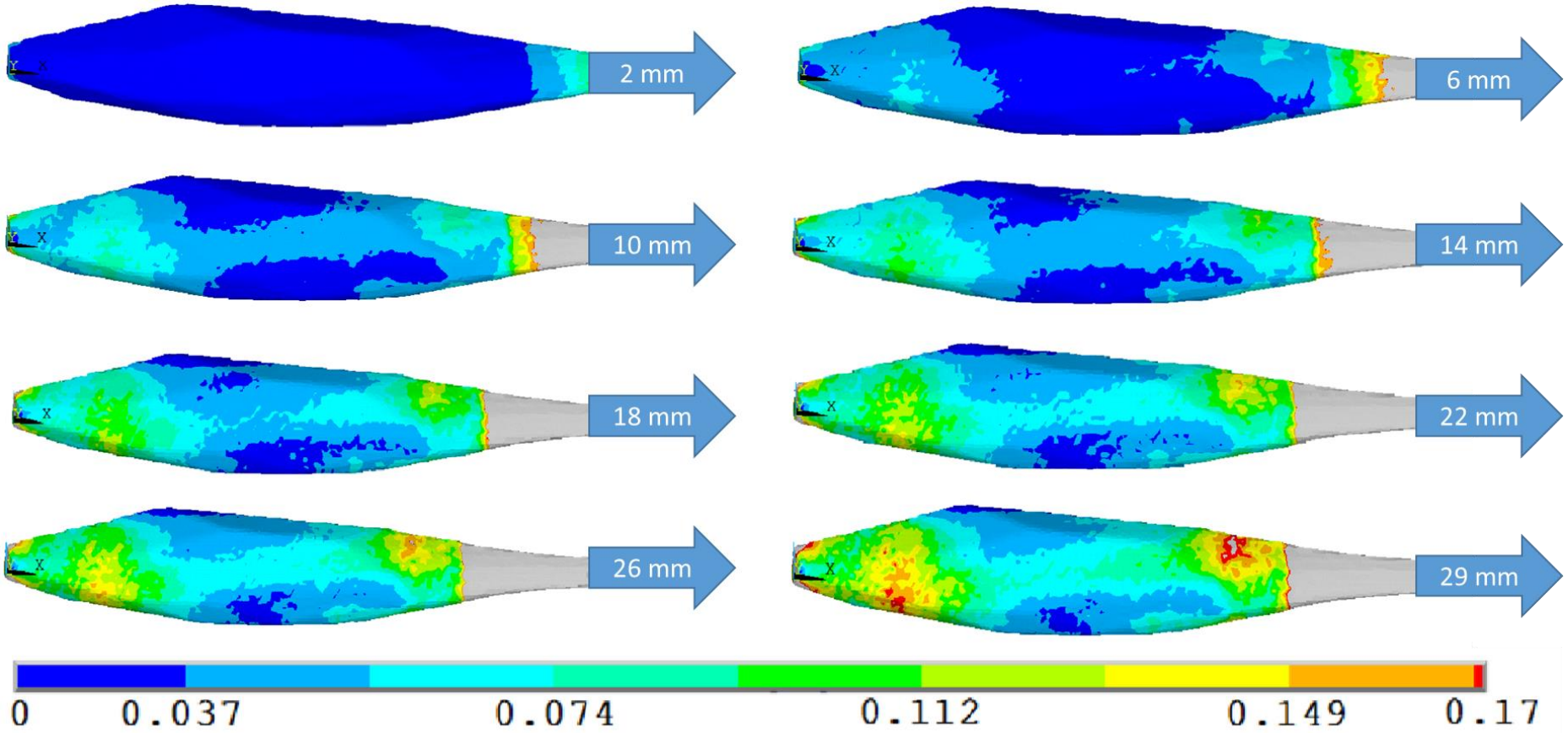

Figure 6.15 Results of the first principal strain distribution of the muscle-tendon complex of the medial-gastrocnemius having been stretched from 2 mm to 29 mm. The grey areas in the images show strains higher than 0.17.

.

The peak strains observed in Figure 6.15 were located at the extremities of the muscle, with the highest strains occurring at the distal insertion. The strains in the belly of the muscle increased as the muscle was extended. After a 10 mm extension, however (approximately 6.7% of the muscle's original length), an intensity of strain is apparent around the muscle-tendon junction transition zones. This is thought to be due to the changes in material parameters in the transition zone, as the volume fraction f(x) was dependent on location and radial distance. The change in material properties in this heterogeneous model appeared to be an area of weakness as the muscle-tendon complex resulted in areas where damage or rupture is likely to occur. Consequently, strain injuries, pain and remodelling are most likely to occur in the transitional regions of the muscle-tendon structure, especially when the muscle experiences higher strains. In contrast, the strains found in the belly of the muscle were relatively low.

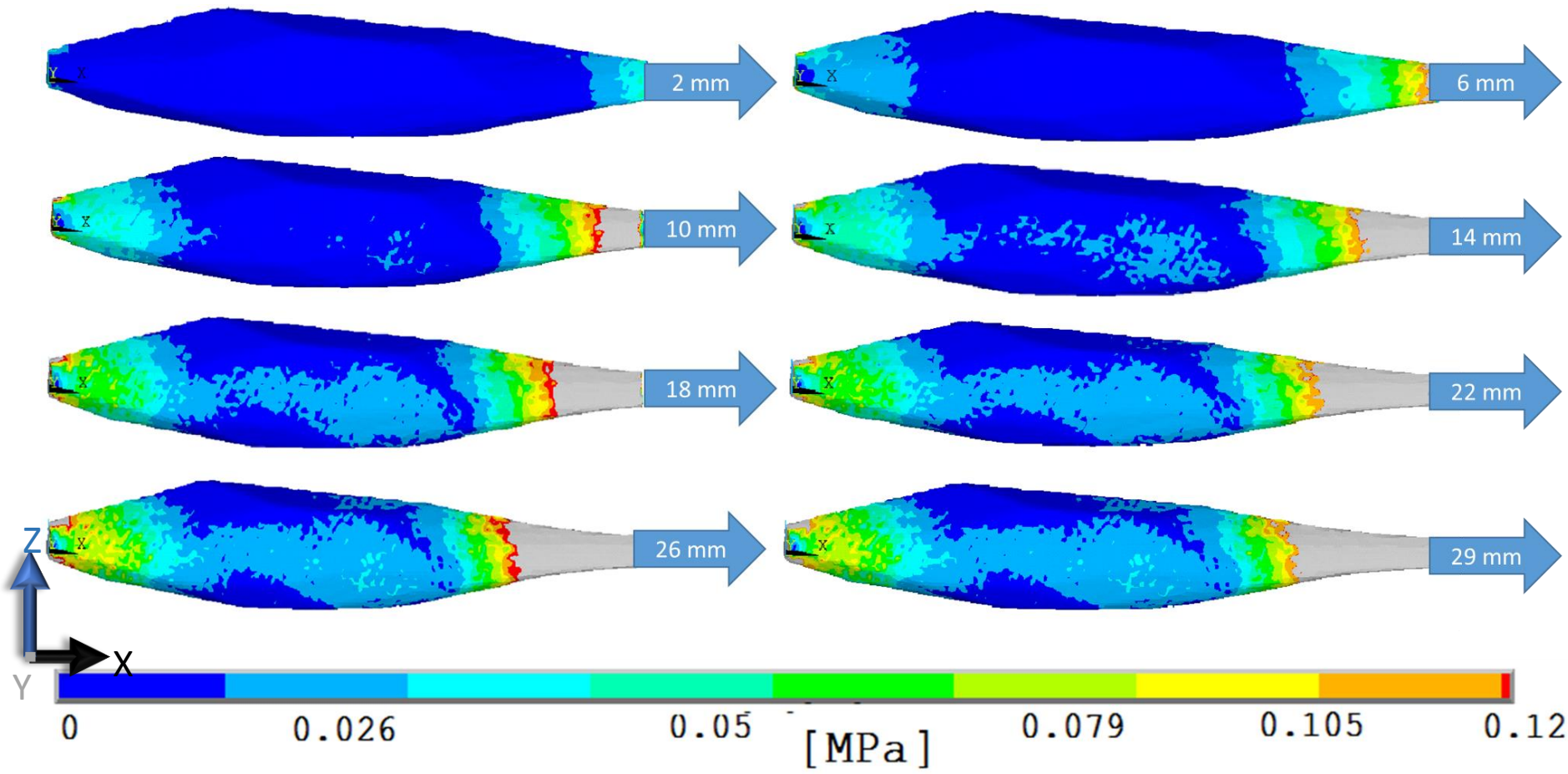

Figure 6.16 First principal stress of the muscle-tendon complex of the Medial-Gastrocnemius having been stretched from 2 mm to 29 mm.

The general pattern of the stress distribution was like that of the strain, as shown in Figure 6.16. The higher the extension at the insertion end, the higher the stresses in the muscle, with almost no stress being experienced at very low strains (2 mm-10 mm or approximately 1.3% - 6.7%). The peak stresses were, once again, largest at the extremities, namely the distal insertion end, and slowly increased across the belly of the muscle as the amount of extension increased. The stresses at the proximal origin became more apparent at strains of 14 mm and above (approximately 9.4%). Whilst the current simulations provide valuable insights into the high strain and stress regions in the medial gastrocnemius muscle, future work in a finite element context may consider the stress and strain thresholds that will induce injury. With that information, it could be possible to predict regions of high risk of injury.

6.4.3 Discussion

Whilst the above analysis acknowledges that future work will involve determining areas of high risk of injury, the regions of high strains in the muscle strain-distribution results above also suggest the areas that are most likely to undergo sarcomerogenesis strain-driven growth when the medial gastrocnemius muscle is extended (Zollner et al., 2015). However, these high-risk areas may induce different remodelling regimes when the muscle is exposed to prolonged and intensive cyclic loading. Concentrated strains were consistently observed at the proximal origin, suggesting an increased risk of injury in the ankle region. When the muscle was stretched excessively, the model also showed an increased strain around the soft tissues of the knee towards the insertion end of the muscle. The muscle belly only began to bear more load when the muscle-tendon complex experienced higher displacements. This model provides a preliminary anatomical map of the likely areas of injury associated with over-stretch in the medial gastrocnemius.

There are a few limitations of this model. The current approach did not consider active contraction of the muscle. This is likely to affect the mechanical response of the muscle and needs to be explored in the future.

Although the muscle tissue is very compliant and can withstand high strains, the tissues surrounding the muscle, namely the tendon and surrounding soft tissues, may limit the amount of excessive stretch experienced by the muscle-tendon complex. Furthermore, the current model only simulated the instantaneous effects of the mechanical response of the muscle tissue; long term growth and remodelling features also need to be considered in the future to gain insights into tissue repair and remodelling post-injury. One approach could be to simulate remodelling in the areas of high stress – this proposition will be discussed in Chapter 7.

6.5 The Effects of Aponeurosis Lengthening on the Mechanical Response of the Medial gastrocnemius

The distal end of the gastrocnemius aponeurosis and the superficial tendinous region of the soleus attach over a range of lengths that are unique to individuals (Blitz, 2007). This distal muscle-tendon junction plays an important role in the mechanics of the medial gastrocnemius, and changes in this junction may alter the normal function of the muscle. For example, one surgical intervention, known as ‘gastrocnemius or aponeurotic recession’ has been used to assist several foot and ankle conditions (Fulp & McGlamry, 1974; Joolan et al., 1999; (Lin et al., 1996). This technique is based on relieving tension in the triceps surae, in the gastrocnemius complex, to restrict the dorsi-flexion of the ankle joint. The tendon of the triceps surae is lengthened by making a lateral incision on the Achilles tendon from the posterior plane and either leaving it to heal or suturing it loosely to adjacent tissue. Consequently, a wound is created, and as the tendon heals the scar

tissue results in the tendon being longer, allowing for intramuscular and aponeurotic lengthening, hence restoring the foot and ankle function (Blitz & Rush, 2007; Tashjian et al., 2003; Blitz & Elliot, 2007).

Although the surgical process of aponeurosis recession has been extensively studied, and the resultant physiological effects observed are consistent (Tashjian et al., 2003; Joolan et al., 1999), not much is known about the long-term changes to the mechanics of the medial gastrocnemius -tendon complex following aponeurotic recession or tendon lengthening.

This section investigates the effects of the aponeurotic lengthening at the muscle-tendon aponeurotic junction, to demonstrate how this will affect the mechanical response of the medial gastrocnemius. This has been done by changing the length of the distal tendinous aponeurosis at the insertion end in the model, which in turn changes the transition zone at the muscle-tendon junction.

6.5.1 Boundary Conditions

The simulation was designed to mimic the changes in the transition zone at the muscle-tendon junction and the effects of aponeurosis regression/lengthening. Hence, the boundary conditions applied were the same as those reported in Chapter 5. Both the length of the aponeurosis and transition length were varied over a physiological range determined by the anatomical work in Blitz (2007).

The distal insertion muscle-tendon junction was defined to range from 0 mm (direct attachments) to approximately 25 mm, in 5 mm increments, which was the minimum length increment that allowed a qualitative difference to be observed in the results. The proximal origin tendon was defined to be approximately 10 mm in length, with a small 5 mm transition zone (see Figure 6.17). All other parameters were kept constant in the simulation in congruence with the material parameters defined in Chapter 4, and boundary conditions described in Chapter 5, where each muscle-tendon complex was extended by 12 mm at the insertion end.

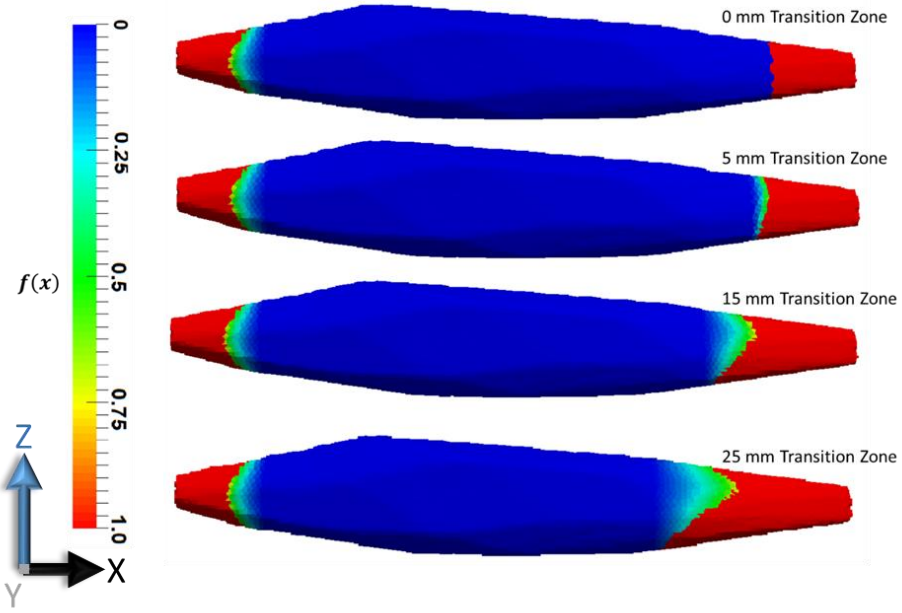

Figure 6.17 Varying muscle-tendon junction transition zone from 0mm to 25mm.

6.5.2 Numerical Results of the Medial gastrocnemius with Aponeurosis Lengthening

The simulations were carried out to examine the effects of a lengthened muscle-tendon junction, which mimics the results of an aponeurosis regression intervention (Blitz & Rush, 2007). The first principal strain results are shown in Figure 6.18. The sagittal cross-sectional plane of the muscle has been displayed, as this provides a direct view of the mechanical response across the transition zone.

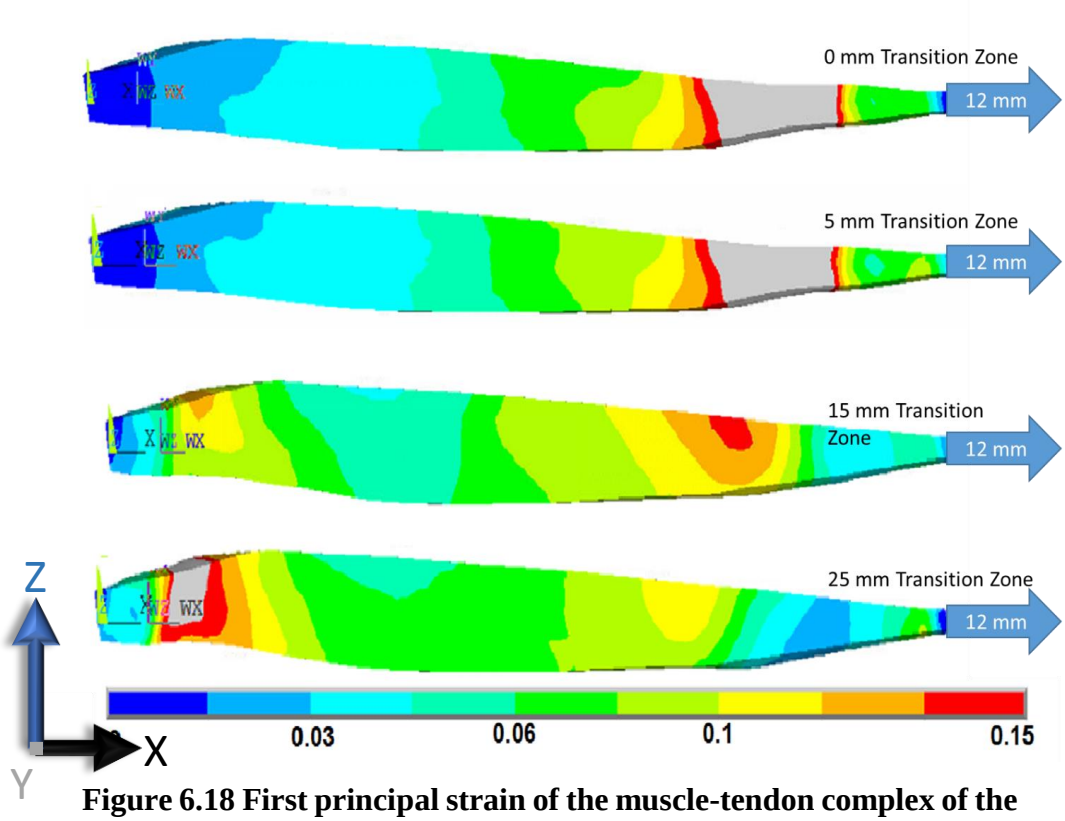

Figure 6.18 First principal strain of the muscle-tendon complex of the medial-gastrocnemius with a varying muscle-tendon junction from 0 mm to 25 mm.

The strain results show the changes in the strain distribution as the transition zone was lengthened in the model. The highest strains were observed at the distal insertion, particularly in the transition zone, suggesting that this region is at higher risk of damage. The area with the smallest strains were at the thickest cross-section of the muscle belly.

Although the transition zones at the proximal origin remained at 5 mm, when the transition zone length increased to above 5 mm at the insertion end (15 mm and 25 mm), the strains at the proximal origin began to increase. Indeed, when the length of the transition zone at the distal insertion reached 25 mm, the highest strains were observed at the proximal origin, indicating a shift in the strain distribution towards the proximal end when the distal transition zone was increased.

The stress results (not shown here for the sake of concision) showed a similar trend as the strain results.

6.5.3 Discussion

As the transition zone lengthened, the maximum strains reduced at the distal insertion end, thereby changing the strain intensity distribution across the muscle so that it became more homogenous. As the aponeurosis and muscle-tendon junction lengthened, the region of high strain/stress gradually shifted from the distal to the proximal end; at the same time the mechanical response became more uniformly distributed across the muscle. The lengthening of the aponeurosis therefore suggests a positive outcome in that the strain distribution is more homogenised across the belly rather than being exclusively localised at the distal and proximal extremities of the muscle-tendon complex. These results indicate that it is important to consider the effects of different anatomical features on the overall mechanical response of the muscle-tendon region and aponeurosis of the medial gastrocnemius muscle.

The next section considers the effects of damaged tendon, the mechanical stress-strain profile of the medial gastrocnemius , which will bring further insight on stretching exercises that are carried out in rehabilitation regimes following damaged tendon and how long healing should take place before a tendon can be safely exposed to strains in the normal ranges of motion of the medial gastrocnemius .

6.6 The effects of a Damaged Tendon on the Mechanical Response of the Medial gastrocnemius

Damage to the muscle and/or tendinous tissues of the calf can occur in strain injuries with partial or whole tears (rupture). Rupture of the distal myotendon junction at the insertion end is one of the most common sports-related injuries (Miller, 1977). Although most people who suffer from this injury experience partial tears, sometimes the damage could be severe enough to cause the detachment of muscle fibres at the medial head distal aponeurosis (Bianchi et al., 1998).

Experimental findings have shown that the muscle-tendon junction is most susceptible to injuries under extreme loading (McMaster, 1923) - a sudden contraction of the muscle, with concomitant overstretching when the knee is in extension, often leads to excessive tensile force and stretching, thus causing injury. Such injuries can take months (or years) to fully heal (Bajuri et al., 2016). Although it is believed that mechanical loading of tendinous tissues could improve mechanically induced healing processes (Andersson & Aspenberg, 2009; Killian et al., 2012; (Schepull et al., 2009; Wang et al., 2012), the optimal mechanisms of this phenomenon in respect to the tendon and muscle remain unclear.

This section therefore aims to explore a simple case of damage of the tendinous tissue and how this affects the stress-strain profile of the muscle-tendon complex of the medial gastrocnemius. This was done by extracting the material constants used in a previous study (Bajuri et al., 2016), which applied a similar constitutive relationship to healing medial gastrocnemius tendon tissue from a murine medial gastrocnemius model.

6.6.1 Estimation of the Damaged Tendinous Material Properties

The tendon's mechanical response changes during its various healing stages (Bajuri et al., 2016). This was modelled by changing the material constants of the constitutive relationships based on Bajuri et al.'s (2016) well-established constitutive relationship that takes into account non-symmetric fibre dispersions and structural parameters, as defined in Equation 6.80. This constitutive relationship is similar to its former version, which has been used in the finite element simulations in this thesis (Equation 6.80) (Holzapfel et al., 2000).

A murine model of the Achilles tendon was examined at the distal insertion and cut transversely, proximal to the calcaneal insertion. A 3 mm segment of the Achilles tendon was removed, and the wound was closed and allowed to heal over 3 days, 8 days, 14 days and 21 days (Eliasson et al., 2009). The tendons were then tested mechanically, which expounded the stress-strain relationship of each of the healing tendons (Eliasson et al., 2009). These data were then fitted to the Bajuri et al., (2016) model, which had the following formulation, as shown in Equation 6.80:

$$\bar{\psi} = \frac{c_1}{2}(I_1 - 3) + \left(\frac{k_1^{'}}{k_2^{'}} \left(e^{k_2^{'}[\kappa \bar{I}_4 + (1-3\kappa) I_4 - 1)^2} - 1 \right) \right) \qquad \textbf{(6.80)}$$

Where: c_1 is the Neo-Hookean isotropic material constant for the isotropic tissue, and k_1 is the first anisotropic material constant for the anisotropic tissue, respectively. These two constants are measured in MPa. k_2 is the second anisotropic material constant for the constituent fibres, which is dimensionless. The fourth invariant of the Cauchy-Green deformation tensor is signified by I_4, which represents the fibre directions for one family of fibres in the constituent. κ is the structural parameter representing the symmetry of the fibre dispersion.

The material parameters used in this constitutive relationship are shown in Table 6.1, where one simulation was done for each healing time-phase.

Table 6.1 Material constants used in the constitutive relationship for tendon tissue (Bajuri et al., 2016).

Healing Phase	C_1 [MPa]	k_1 [MPa]	k_2 [-]	κ [-]
Day 3	0.1669	1.110	5.802	0.25
Day 8	0.0807	1.915	13.864	0.24
Day 14	0.1791	2.271	7.077	0.23
Day 21	0.1066	1.238	3.870	0.22
Intact	0.00046	9.127	1.6	0

The ratio of the relative stiffness of the muscle to that of the tendon was calculated by scaling each material constant ratio separately (C_1, K_1 and K_2). This was undertaken since the constitutive relationship defined in this thesis is slightly different to the one reported in Bajuri et al. (2016). The tendon values for the healing phases (i.e. all phases apart from intact phase) were therefore scaled to eliminate the κ constant. The material properties reported in Bajuri et al. (2016) are shown in Table 6.2.

The stress response was derived according to Nanson's formula from the strain energy function used in Bajuri et al., (2016), as shown in Equation 6.80. The stress response was plotted analytically using the material constants in Table 6.2, as shown in Figure 6.19. This reveals the stress response of the tendon tissue during each healing phase. In Bajuri et al.'s (2010) work the intact healthy tendon was the only tendon that had a κ value of 0, thus, according to Equation 6.80, the strain energy function was exactly the same as that used in this thesis, as shown in Equation **4.48**. Since κ was not 0 for the healing tendon (Equation **6.80**), however, the stress ratio was calculated from the ratio of the healthy stress value (45.4043 MPa) to that of the healing stress values (0.6670 MPa at 3 days, 1.3060 MPa at 8 days, 1.6627 MPa at 14 days and 0.9712 MPa at 21 days) using a maximum tendon stretch of 1.2. This ratio was used to scale the material parameters of the strain energy function used in this thesis (Equation **6.70**). This was done to determine the ratio required to scale the parameters from healthy tendon, which was used to

scale the parameters for the constitutive relationship used here (Holzapfel, 2000). These scaled values are shown in Table 6.2.

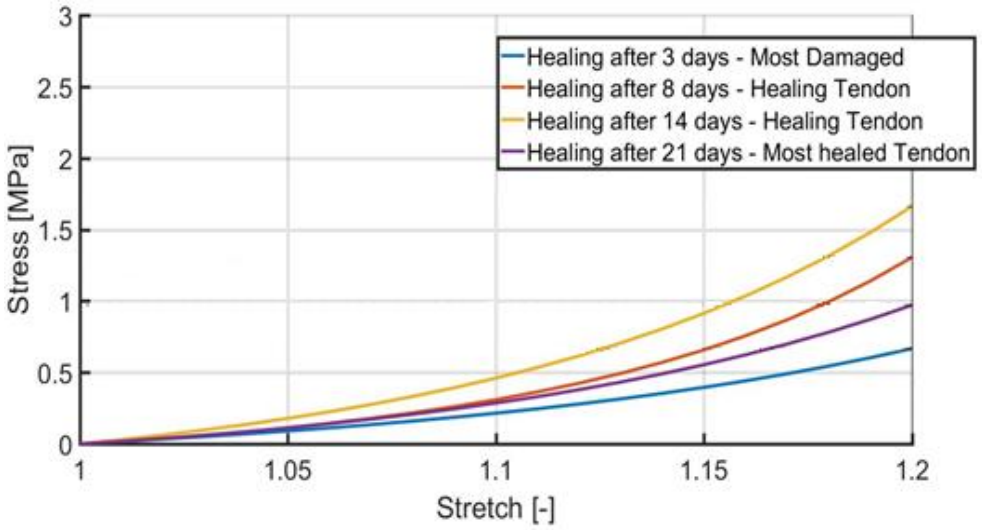

Figure 6.19 Analytical solution (first Piola-Kirchhoff Stress) of the tendon tissue across different healing phases.

Table 6.2 Scaled material constants of muscle and tendon tissue for the simulation of the healing tendon.

Constitutive relationship:

$$_{m.Gastro} = f_x^T \left(C_1^T (I_1 - 3) + (\frac{k_1^T}{2k_2^T} e^{I_4 - 1} - 1) \right) + f_x^M \left(C_1^M (I_1 - 3) + (\frac{k_1^M}{2k_2^M} e^{I_6 - 1} - 1) \right)$$

Material Constant	**C_1 [MPa]**	**K_1 [MPa]**	**K_2**
Muscle	*0.0228*	*0.1938*	*0.0039*
Tendon (intact)	0.00046	9.127	1.6
Tendon (3day)	0.001566	0.13407	0.0235
Tendon (8day)	0.003066	0.262527	0.0460
Tendon (14day)	0.003904	0.33423	0.0585
Tendon (21day)	0.00228	0.19522	0.0342

6.6.2 Simulation Boundary Conditions

The boundary conditions of the radial dependant transition zone and the aponeurosis anatomical configuration are the same as those reported in Section 6.3.2.

A simulation was done according to the healing phase (3 days, 7 days, `4 days, 21 days and intact), where the material parameters were applied as shown in Table 6.2. This was used to simulate the way in which the healing tendon's mechanical response changed over time.

6.6.3 Simulation Results

The following results (see Figures 6.20 and 6.21) show the damaged tendon and how the tendon healed over the 21 day period, by examining the distribution of the first principal strains in the muscle-tendon complex.

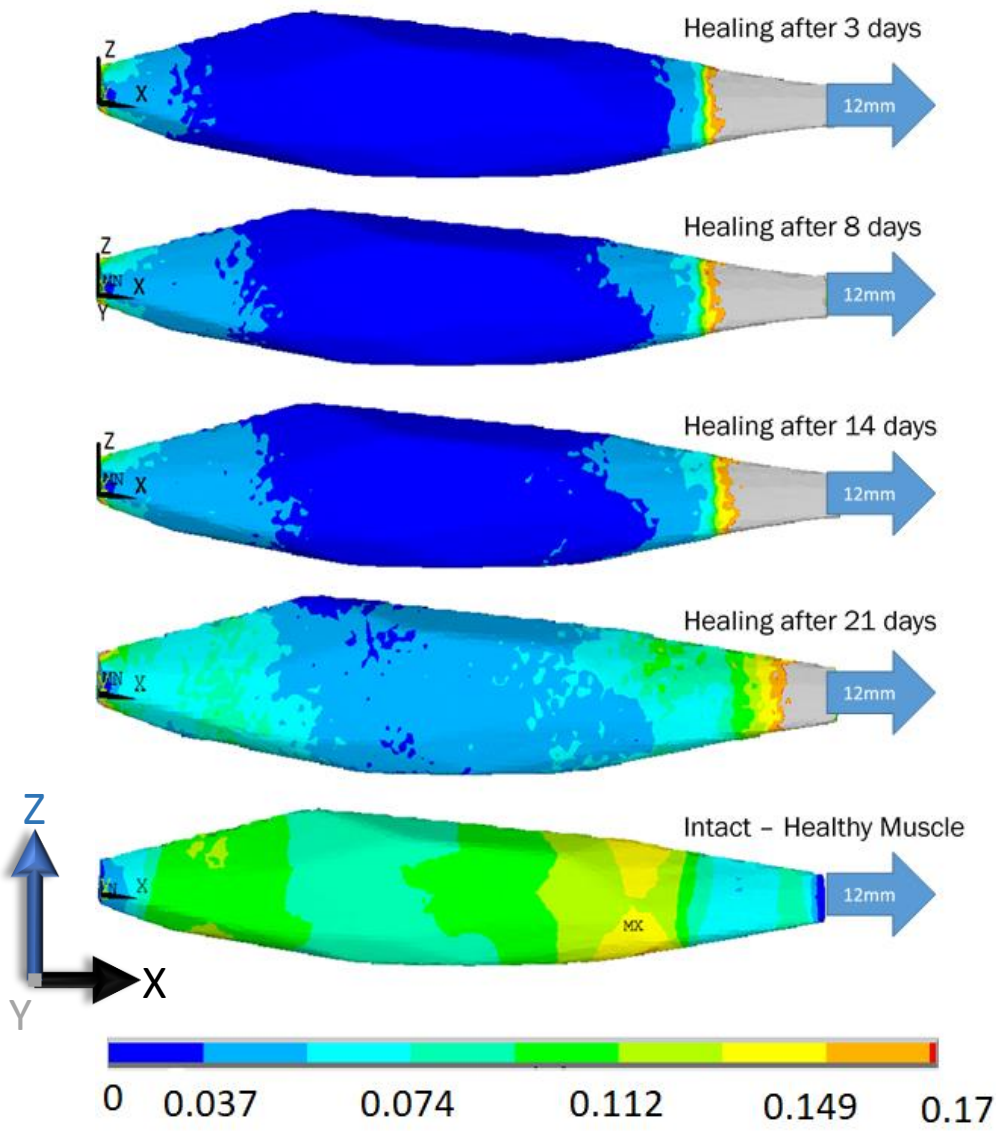

Figure 6.20 Anterior view of the first principal strain of the muscle-tendon complex of the medial-gastrocnemius in the case of a healing tendon.

Figure 6.20 shows the distribution of the first principal strains of the simulation as the tendon healed from the most damaged (after 3 days) to the most healed (after 21 days) phases, compared to the response of a healthy tendon. Note that only the tendon has undergone the 'healing' process here, and the muscle is simulated as healthy tissue throughout all simulations.

As the tendon healed, the strains at the distal insertion decreased and the strains across the belly of the muscle increased. The load appeared to be more evenly distributed with a healthy tendon compared to a damaged tendon.

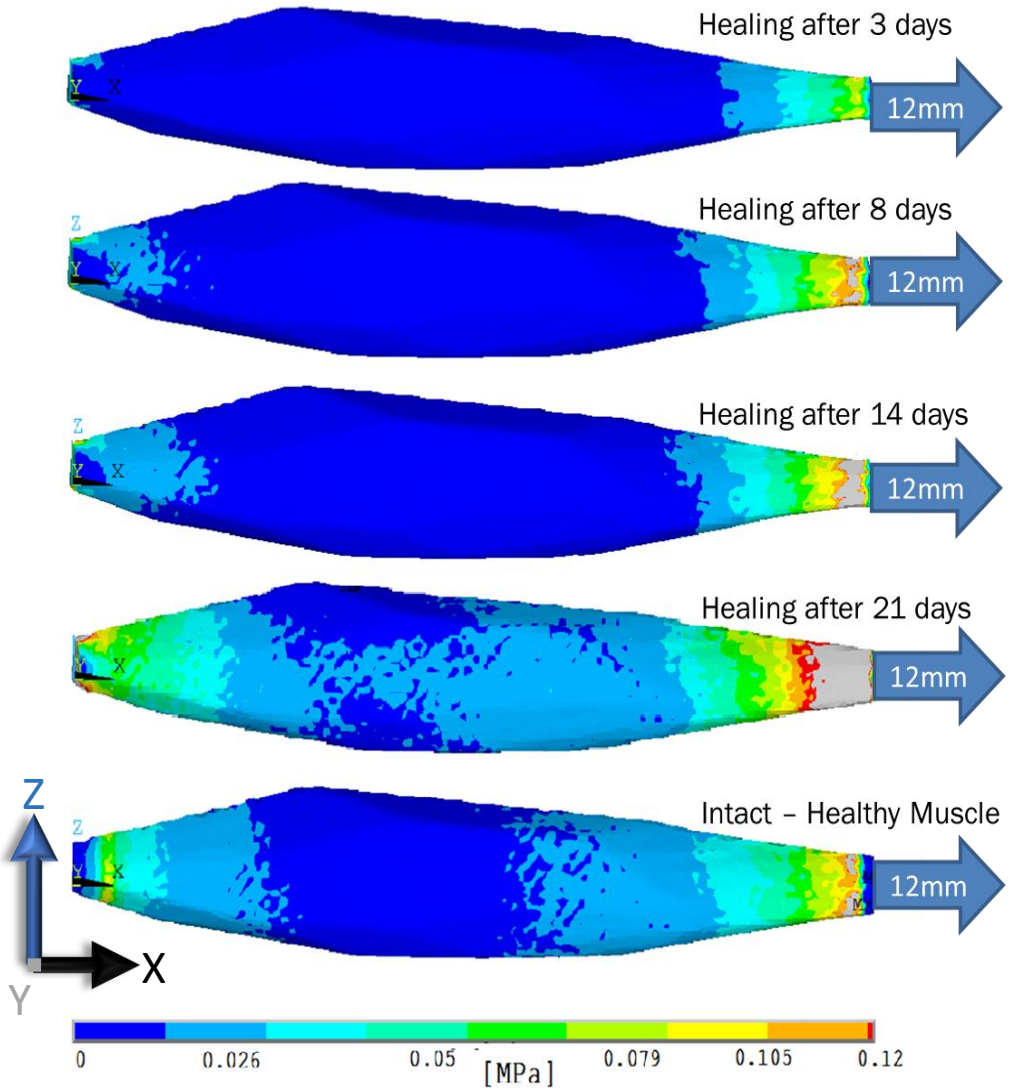

Figure 6.21 Anterior view of the first principal stress of the muscle-tendon complex of the medial-gastrocnemius with healing tendon.

Similar trends were also observed in the predicted stress distribution of the muscle; in that the stress was more evenly distributed across the muscle belly as the tendon healed, compared to its damaged counterpart. It is worth noting, however, that the maximum stresses were always found at the insertion and distal ends of the muscle regardless of the state of the tendon. This could potentially be an effect of the boundary conditions applied at both ends.

6.6.4 Discussion

The material parameters used here were directly scaled from the material constants used in a similar constitutive relationship of healing tendons (Bajuri et al., 2016), where C_1 (the Neo-Hookean shear modulus of the non-collagenous matrix) reduced as healing progressed and k_1 increased as expected. In Bajuri et al. (2016), however, k_2 decreased as healing progressed, where it increases in the current simulation – noting that the strain energy functions in Bajuri et al. contain the fibre dispersion parameter κ, whereas the simulations in this thesis have scaled the parameters to eliminate κ.

It is well recorded that the elastic modulus increases during healing of tendon tissue (Eliasson et al., 2009; Schepull, 2007; Schepull, 2013). These phenomenological parameters are thought to represent tissues like ligaments and arteries when considering their rate independent elastic behaviour (Weiss & Gardiner, 2001). The selection of the parameters used (an optimisation algorithm in MATLAB called the Levenberg–Marquardt Algorithm) is highly dependent on the initial values selected and the parameter space being explored, however, meaning that there could be several different combinations of optimised material parameters that result in the same overall stress-strain response. Nevertheless, the results showed some insight into the effects of tendon damage on the medial gastrocnemius muscle.

It is important to consider the different healing stages of the muscle, specifically, the stress response of the muscle that rendered an anomaly at day 21 of the healing process. Bajuri et al. (2016) acknowledge a change in the stress response at day 21 of the healing process related to up or downregulation of genes, suggesting that the formation of scar or residual tissue at this stage. This suggests that the change of the tissue resulted in a change in the stress response in comparison to the other healing phases. One possible explanation for this observed increase in stiffness could be the formation of scar tissue.

It is important to note, however, that the extent of damage of the murine tendon was excessive – a healing 3 mm incision. Such damage will not only cause anatomical changes in the muscle-tendon complex, as explored earlier

in this chapter, but will also lead to a much longer healing processes than the 21 days studied (Eliasson et al., 2009). Future work could include an exploration of minor to moderate damage of the tendon, and experimentation on the mechanical response over a longer period, until the tendon is fully recovered.

This exploration suggested that stretching a damaged tendon beyond its physiological limit during the healing phase may cause more damage and should be avoided; hence the implication that the rehabilitation and loading regime of the healing tendon must be carefully considered.

The growth and remodelling formulation proposed in the next chapter can be used to explore such phenomena in future.

6.7 Discussion and Conclusions

A number of previous models of the muscle-aponeurosis/tendon complex have been created and used in finite element simulations (Blemker, et al., 2005; Chi, 2010; Pamuk, et al., 2016; Chi, 2010). Few of these models however, have been able to capture the anatomical path of the fibres appropriately (Blemker & Delp, 2005). The current work not only presents a unique method to use anatomical fibres for the computational finite element modelling of skeletal muscles, but also provides a novel model that considers the muscle-aponeurosis/tendon complex with a transitional myotendon region. In addition, most other finite element muscle-tendon work-flows have used a manual or semi-automatic process, where a region of tendon or muscle tissue is assumed and manually selected according to their anatomical locations on the mesh, and material constants assigned thereafter (Blemker, et al., 2005; Chi, 2010). The drawback of such an approach is that it requires a good understanding of the anatomical location of each region, which can be difficult to identify in different individuals (Neal M. Blitz, 2007). In contrast, the muscle-tendon/aponeurosis model presented here uses a distance method to determine the exact material constants for each region. The results shown in this chapter demonstrated that the transitional zone and tendon/aponeurosis morphology will influence the mechanical behaviour of the muscle, and this is further investigated in the next chapter by investigating a range of parameters defined in the model and their effects on the stress-strain prediction.

From the arbitrary formulation case (1), (no distance dependence) and linear distance-dependence formulation case (2), the stress-strain results exhibit a lamellar pattern, where transverse ‘bands’ of intensity are presented. This is not consistent with physiological phenomena in the cases of high strain locations of the medial gastrocnemius in that the most common localisation of medial gastrocnemius tears are found at the muscle-tendon junction (the transition zone) in the case of high strain injuries of the Triceps Surae. These tears are expected to occur closer to the posterior side of the muscle – the side adjacent to the skin (Dixon, 2009; Bianchi, et al., 1998). Although the

quantitative stress-strain profile of the medial gastrocnemius muscle is not clearly understood, from medical convention with respect to such strain injuries, it is clear to see that the radial dependence simulation applied in this chapter has rendered results that are more analogous to the physiological phenomena when the muscle is stretched (Bianchi, et al., 1998; Dixon, 2009). When the muscle is stretched extensively, additional disruption and partial tears are found to occur around the muscle belly (Bianchi, et al., 1998). These extensive stretches of the muscle will be explored further in Chapter 7.

This investigation highlights the importance of having a more accurate anatomical representation of the muscle-tendon transition zone. Further analysis therefore needs to be done to explore the skeletal muscle model created here more fully, along with other pathological phenomena such as tendon healing or the effect of anatomical features on the stress-strain profile of the muscle. Such studies will provide further insights into the mechanical response of skeletal muscle tissue and indeed, a full anatomical muscle-tendon complex. To begin this work, this chapter goes on to explore the effects of the radial dependent anatomical configuration of the skeletal muscle, comparing the stress-strain effects of the skeletal muscle over three cases; (i) excessive strains on the medial gastrocnemius, (ii) lengthening of the aponeurosis and muscle-tendon transition zone and (iii) healing tendon.

Changes in the mechanical environment surrounding a muscle often affect the behaviour and performance of that muscle. Consequently, the lengthening of the aponeurosis beyond a critical length may lead to regions of high strain (e.g. after a 25 mm transition length), where higher strains are observed in the proximal origin than the distal insertion. Similar effects are also observed when the medial gastrocnemius muscle-tendon complex is stretched beyond 10% of its original length.

Previous finite element models of muscles have used idealised geometries, fibre orientation and approximated material parameters to explore the mechanics of skeletal muscle (Blemker et al., 2005; Blemker & Delph, 2005; Zollner et al., 2015; Tang et al., 2007). Although these models have enabled the exploration of the intended research question, the current model offers a novel framework to provide an anatomical geometry,

anatomical fibre orientation and a comprehensive exploration on the material constants used.

The results shown above suggest an ‘optimum’ region for muscle displacements and aponeurosis muscle-tendon lengths which needs to be further confirmed by experimentation. The current work-flow has demonstrated the mechanical response of a specific skeletal muscle and how it responded to mechanical stimuli. The limitations of the current model lie in the transition zone of the muscle-tendon junction. This is currently modelled as a cone with a sharp radial edge, but has been enhanced by a smoother transition, and a blunt cup-like apex to more closely mimic the true anatomical structure of the skeletal muscle.

The long-term effects of loading on the muscle’s mechanical response can be explored by means of the growth and remodelling formulation proposed in Chapter 3. Other similar models have been proposed that use a mixed constrained method that considers myosin heavy chain isoforms, serial sarcomere numbers, parallel sarcomere numbers, pennation angles, and extracellular matrix composition (Wisdom et al., 2015). Models built on these formulations, however, have not comprehensively considered the muscle-tendon complex, its mechanical behaviour or the muscle-tendon junction (Zollner et al., 2015). Further, although the finite element model proposed by Zollner et al. (2015) suggests a novel and comprehensive model of sarcomere genesis, and uses relatable foundations of sarcomere genesis in series and parallel with the muscle’s mechanical environment, the model does not explicitly consider the mechanical response of the muscle-tendon junction, or the aponeurosis over the gastrocnemius muscle, and the tendon was modelled as an infinitely stiff component adjoined to the muscle tissue.

Future work can shadow the work-flow of Roerhle et al. (2008), to incorporate the anatomical specificity and higher dimensionality of multi-scale models. Simulations of the mechanics, and the growth and remodelling regimes of the medial gastrocnemius muscle, however, must be explored to gain further insight into the temporal behaviour of the muscle’s mechanics. The next chapter explores the growth and remodelling of the medial gastrocnemius, whilst under different mechanical stimuli.

Chapter 7

Growth and Remodelling of Skeletal Muscle: Application to Limb Lengthening

Chapter 6 explored the different anatomical structures required to achieve a more representative finite element model of the medial gastrocnemius. Because skeletal muscle tissue responds to its mechanical environment and MSDs are degenerative diseases that progress over time, useful research of skeletal muscle mechanics will require the inclusion of a temporal domain. Whilst the quasi-static stress-strain profile of the muscle-tendon complex has been demonstrated, the longer term changes the muscle experience during various mechanical environments (e.g. during overstretch) have not yet been investigated in this thesis.

This chapter will explore the application of the remodelling formulation to simulate overstretching of the muscle during limb lengthening, considering work performed by Boakes et al., (2006). Boakes et al. stated that muscle adaptability limits the outcome of reconstructive limb lengthening surgery. In

their study, the limb was lengthened incrementally over a quarter of a year and then held at fixed length for the remaining nine months as the muscle was left to adapt. The study showed that the procedure was successful, and the muscle lengthened accordingly over that timescale, however the lengthening regime was governed by the remodelling time of the muscle – hence the requirement to explore what possible timescales could be considered for muscle tissues. The example illustrated by Boakes et al., (2006) will inform the boundary conditions and simulation time (one year) of the remodelling formulation proposed in this thesis. This will test the current remodelling formulation and allow for the investigation of what appropriate simulation parameters are required to achieve a muscle that will remodel to its homeostatic configuration.

This chapter shows 3 modelling approaches to simulate the remodelling of muscle-aponeurosis-tendon tissue;

(i) An analytical model, with the consideration and inclusion of a homeostatic range of values.

(ii) An idealized finite element model with a cuboid geometry, uniaxially loaded.

(iii) An anatomically realistic finite element model of the medial gastrocnemius - as described in Chapter 6.

These models build on the previous work of this thesis and progressively inform one another as follows:

The analytical model (i) uses constitutive parameters described in Chapter 4, to derive the remodelling rate parameters - hence informing the succeeding finite element models. The cuboid model (ii), introduces the axial variation of constituent properties and remodelling, which is independent of the anatomical features and their effects on the mechanical response of the muscle-tendon complex. The third approach brings together the anatomical geometry developed in Chapter 6, and the proposed remodelling framework, to assess what remodelling regime is most useful to use, to produce a predictive finite element simulation of the overstretched gastrocnemius.

7.1 Growth and Remodelling Finite Element Models of Skeletal Muscle

Skeletal muscle modelling has seen great advances in the last two decades, with three-dimensional models coupled with chemical and electrical pathways now able to provide significant insight into muscle physiology and function (Oomens et al., 2003; Lemos et al., 2004; Blemker & Delph, 2005; Böl & Reese, 2008; Röhrle et al., 2008; Böl, 2010; Röhrle, 2010). Such models have been further enhanced by elucidating the interactions between biochemistry, metabolism and force production (Dash et al., 2007; Murtada et al., 2012). Despite such advances in the skeletal muscle finite element modelling community, models that can reliably predict the longer-term response of skeletal muscle are surprisingly rare (Kuhl, 2014). Whilst other models have provided valuable insight into the adaptation of skeletal muscle in response to chronic under- and over-stretch in one-dimension (Wren, 2003), three-dimensional continuum mechanics models are still currently lacking in this regard. Having comprehensively reviewed - in Chapter 3 - previous finite element models of skeletal muscle adaptation, when they are exposed to different mechanical environments, the next section expands on the modelling approaches used to model overstretch phenomena in skeletal muscles.

7.1.1 Modelling Overstretch and its Mechanical Phenomena

To model overstretch, the muscle is extended and held at a fixed length, which increases the length and/or number of sarcomeres in series (Makarov et al., 2009), and this in turn increases the length of the muscle-tendon complex. The passive stiffness of the muscle-complex is thought to increase, and the fibres of the muscles are thought to align more towards the direction of loading (Williams et al., 1998; Elsalanty et al., 2007). Overstretch in this context is defined as the maximum stretch the medial gastrocnemius maybe subjected to, during various activities, above its maximum homeostatic value – such as when the muscle is extended and held at fixed length. In contrast, understretch in this context is defined as the minimum stretch the medial gastrocnemius will be subjected to, below its minimum homeostatic value.

The next section inspects various homeostatic stretches that are thought to lie within the physiological range of the motion of muscle, as well as how they are used to define the homeostatic stress values of the muscle-tendon complex model.

7.1.2 The Definition of the Homeostatic Configuration and Constituent Remodelling

Here, we propose a distinction between the homeostatic range of motion and the operational range of motion of the medial gastrocnemius. The homeostatic range is the stretch range within which the muscle can operate before the onset of remodelling occurs. The operational range is a stretch of 0.9 – 1.15. Hence the supposition of the ‘homeostatic range’ which is different from the ‘operational range’ of the muscle.

It is well accepted that passive stretch beyond a physiological threshold initiates the process of sarcomerogenesis (Caiozzo et al., 2002), however the exact cascade of mechanotransduction events that trigger serial sarcomere adaptation remains largely unknown (Lieber & Fridén, 2000). Furthermore, it is unclear how to define a homeostatic range. As a start, we review the homeostatic ranges of muscular tissues, soft collagenous tissues and tissues

with unidirectional fibres are shown in Table 7.1, and from there, their homeostatic anisotropic contribution of the Cauchy stresses are calculated using the methods described in Chapter 4.

Table 7.1 Homeostatic stretches of muscular, unidirectional fibres and soft tissues as reported in various sources of literature.

Reference	**Study Type (Experimental/ Computational)**	**Tissue (Muscle/Tendon)**	**Homeostatic Stretch range, λ**
Zöllner et al. (2012)	Computational	Biceps Brachii Skeletal Muscle tissue	1.00
Gordon et al. (1966)	Experimental	Frog Skeletal Muscle	0.95 – 1.07
Wisdom et al. (2015)	Computational	Analytical Skeletal Muscle tissue	1.0
Hamedzadeh & Gasser (2018)	Computational	Collagenous Soft Biological Tissues	1.04
Lanir (2015)	Computational	Tissues with Unidirectional fibres	1.03~1.067

It should be noted that different constitutive relationships will inherently have different homeostatic stresses. The smallest and largest values have been selected from Table 7.1 to help provide a benchmark value for the homeostatic stretch range and hence a homeostatic Cauchy stress range. This range of homeostatic stress values is interpreted as the following;

$$\sigma_{aniso,h(\min)} < \sigma_{aniso,h} < \sigma_{aniso,h(\max)} \qquad \textbf{(7.81)}$$

Whilst the model discussed by Wisdom et al. (2015) and the model developed by Zöllner et al. (2012) each determine the homeostatic state to be identical with the reference configuration, considering the material parameters of the strain energy function used in this thesis (Equation **6.60**), the material parameter k_2 has been selected to evolve and bring the anisotropic stresses back to their homeostatic values. This is because during remodelling the muscle is expected to stiffen, which results in a right-ward shift of the stress-strain relationship (as shown in Figures 4.a-c), and this shift is most sensitive

to the value of k_2. The anisotropic stresses are used to drive remodelling, as they govern the total stress response of both muscle and tendon constituents at higher strains. Based on the strain energy function in Equation **6.70**, the modified strain energy function can be written as:

$$\psi = \psi(f_T(x), I_1, I_4, I_6) = f_T(x)\left[\frac{c_1^T}{2}(I_1-3)+(k_1^T\ e^{k_2(t)(I_4-1)^2}-1)\right]... \\ ...+(1-f_T(x))\left[\frac{c_1^M}{2}(I_1-3)+(k_1^M e^{y_2(t)(I_6-1)^2}-1)\right] \quad \textbf{(7.82)}$$

To model overstretch, k_2t (for tendon) and k_2m (for muscle) stiffness parameter defined in Chapter 6 (Equation 6.60) is evolved using the following relationship;

$$\frac{dk_2t(t)}{dt} = -\beta^T\left(\frac{\sigma_{aniso}-\sigma|aniso,h(\max)}{\sigma|h(\max)}\right)_T \\ \frac{dk_2m(t)}{dt} = -\beta^M\left(\frac{\sigma_{aniso}-\sigma|aniso,h(\max)}{\sigma|aniso,h(\max)}\right)_M \quad \textbf{(7.83)}$$

The *t* subscript represents the evolution of the tendinous constituent of k_2, and the *m* subscript represents the evolution of the muscular constituent of k2. The remodelling constant β, will therefore be specific to the type of tissue constituents. As such, the evolution of the stiffness parameter, k_2 t, is driven by the deviance of the anisotropic contribution of Cauchy stress values σ_{aniso} from their homeostatic anisotropic stress values, $\sigma_{aniso,h}$. Whilst this thesis only models overstretch, the model could be extended by considering that the homeostatic Cauchy stress comprises of a range of values. The over- and understretch phenomena are produced when the stresses satisfy the following conditions:

$$\sigma_{aniso,h(\max)} \le \sigma_{aniso} \Rightarrow \text{Overstretch} \\ \sigma_{aniso,h(\min)} \ge \sigma_{aniso} \Rightarrow \text{Understretch} \quad \textbf{(7.84)}$$

σ_{aniso} of the muscle-tendon complex is the anisotropic contribution of the Cauchy stress of a tissue constituent when held at fixed length during the remodelling regime. Therefore, as the anisotropic 1st Piola Kirchoff stress is the first derivative of the strain energy function ψ with respect to the stretch λ, the anisotropic Cauchy stress term for tendon and muscle are then multiplied by the stress to obtain the Cauchy anisotropic stress.

$$\begin{aligned} \sigma_{Anisotropic} &= 4k_1t \cdot k_2t(t)\lambda(\lambda^2-1)e^{k_2t(t)(\lambda^2-1)^2} \Rightarrow Tendon \\ \sigma_{Anisotropic} &= 4k_1m \cdot k_2m(t)\lambda(\lambda^2-1)e^{k_2m(t)(\lambda^2-1)^2} \Rightarrow Muscle \end{aligned} \quad \textbf{(7.85)}$$

In the context of this remodelling algorithm, the maximum homeostatic stretch value is taken from the range used by Lanir et al. (2015) for unidirectional fibres of collagenous tissues, where the stretch ranges from 1.03 ~ 1.067. The maximum homeostatic strains of the medial gastrocnemius complex are therefore estimated to lie around 3%-6.7% of the complex's original length. In order to determine the boundary conditions of the models, the upper bound of this range was used, at 6.7% of strain. Considering that the original length of the muscle-tendon complex is 149 mm, the muscle's maximum homeostatic stretch will therefore be approximately 6.7% of that value, which equates to 10 mm. It is from this stretch that the maximum homeostatic Cauchy stress to drive the remodelling of k_2t and k_2m, is calculated.

The next section explores the proposed model using analytical solutions.

7.2 An Analytical Investigation of Limb Lengthening of the medial gastrocnemius

Bone lengthening surgery is a reconstructive therapy that often results in complications in muscle contracture and loss of joint motion. This is often observed where the muscle adaptive capacity seems to limit the extent of possible lengthening of the limb (Boakes et al., 2006) hence posing the question – 'how quickly can the bone be lengthened, to achieve optimum muscle adaptation?' It is also important to consider the modelling of the soft tissues (muscle, tendon and myotendinous tissues) attached to the bone. Whilst many studies showed the need of the cat soleus muscle remodelling during sarcomerogenesis or sarcomere-loss (Tabary et al., 1972; Tardieu et al., 1982; Goldspink & Scutt, 1992), others have shown that other muscles remodel to a lesser extent than the soleus (Simard et al., 1982; Spector et al., 1982). It is therefore imperative to explore the different remodelling rates – defined as β^T and β^M in Equation **7.83** for tendon and muscle constituents, respectively – of the medial gastrocnemius muscle, tendon and myotendinous junction tissue.

An illustrative example of overstretch from limb lengthening leading to sarcomerogenesis has been provided by Boakes et al. (2006). This will be modelled by considering the evolution of k_2t and k2m (Equation **7.83**), to adapt the muscle stresses back to homeostasis when in overstretch. A 4 cm lengthening of the femoral bone was achieved incrementally (0.5 mm per day over 80 days), referred to as the 'distraction' period, and the leg was then left to heal for a total of 285 days, post-surgery – during the consolidation phase. Hence, the lengthening of the limb is interpreted to be linear over the reported timescales, and a simple linear interpolation was used to define the remodelling regime of the system, as shown in Figure **7.1**.

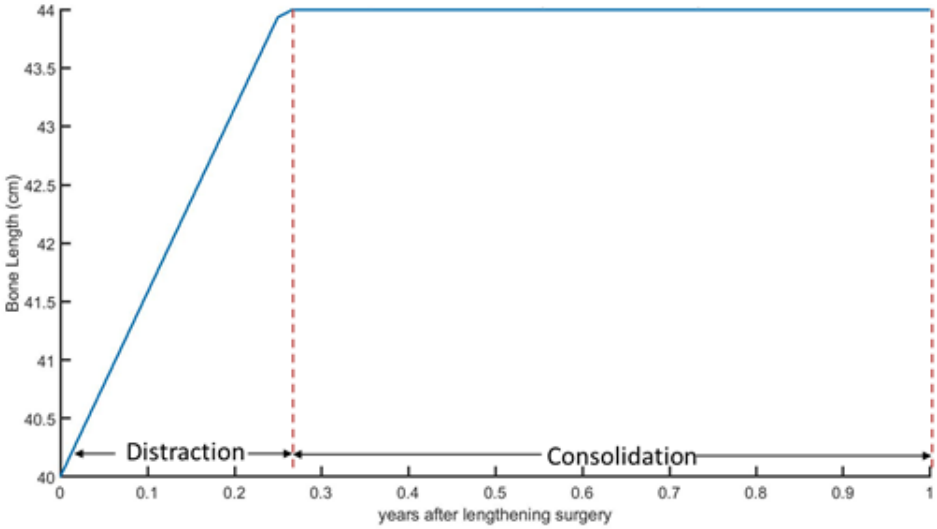

Figure 7.1 Derived lengthening of the femoral bone across 1 year post surgery.

The bone was increased by a total of 10% of its original length, i.e. a 4 cm increase (Boakes et al., 2006) – hence the deduction that the original bone was originally 40 cm and increased to 44 cm. Whilst it is acknowledged that the bone lengthened in Boakes et al., (2006) was the femoral bone, rather than the tibial bone (which is closer to the medial gastrocnemius), the increases have been scaled, so that normalised values of the lengthening are obtained and applied to the current model of the medial gastrocnemius muscle system.

This remodelling regime was explored so that the remodelling rate parameters of the current model could be calibrated against the data defined in Boakes et al. (2006) in order to extrapolate parameters - in particular the remodelling rate constant β - for overstretch during limb lengthening. This exploration was done analytically. The strain energy function used is that described in Equation **6.70**, and the material parameters used for C_1, $k_1$and $k_2\big|_{t=0}$ for muscle and tendon are taken from Chapter 4, Table 4.2.

From the Equation **7.83**, k_{2t} and k2m evolve at rates ($\beta^T$and β^M) dependant on their initial values, homeostatic ($\sigma_{aniso,h}$) and operational σ_{aniso} Cauchy stress values. The initial stress values for the analytical

solutions shown in Figure **7.1** were taken to be the upper bound inferred Cauchy stress value calculated from Lanir (2015) as shown in Table 7.1 as 1.3910 MPa

To infer a suitable range of values for beta, both and tendon have been assumed to remodel to homeostasis within a year. These rate parameters are expected to differ for the tendinous and muscular constituents. The proposed way in which k_2 and k2m evolve is shown in Figure **7.2** and **7.3** for different values of β^T and β^M and for muscle and tendon constituents, respectively.

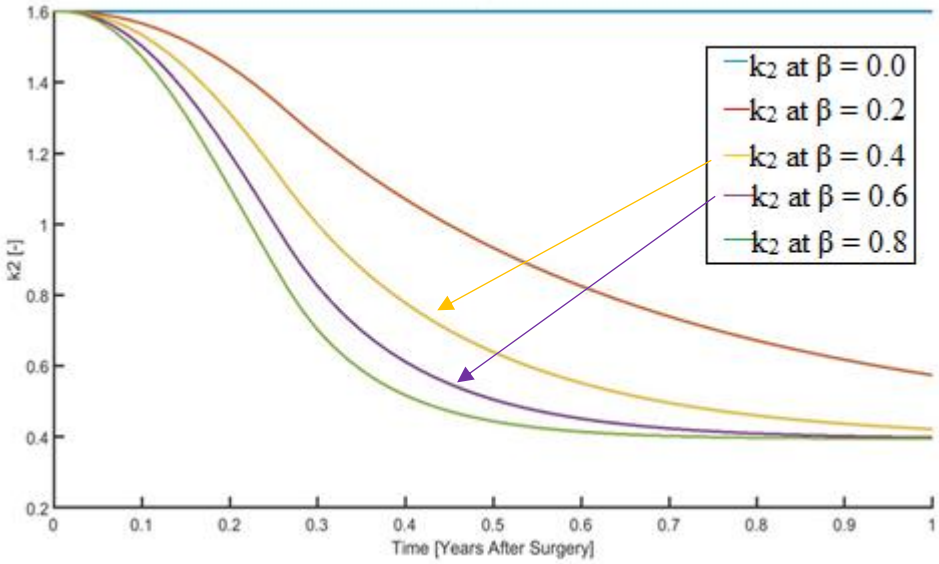

Figure 7.2 Evolution of k_2t in the 12 months post-surgery, with varying values of the remodelling rate parameter β for tendon tissue.

For the remodelling scenario defined by Boakes et al. (2006), k_2 is expected to asymptote within 1 year, hence suggesting that favourable values of the tendinous remodelling rate parameter lies within $0.4 \leq \beta^T \leq 0.6$, as shown in Figure **7.2**.

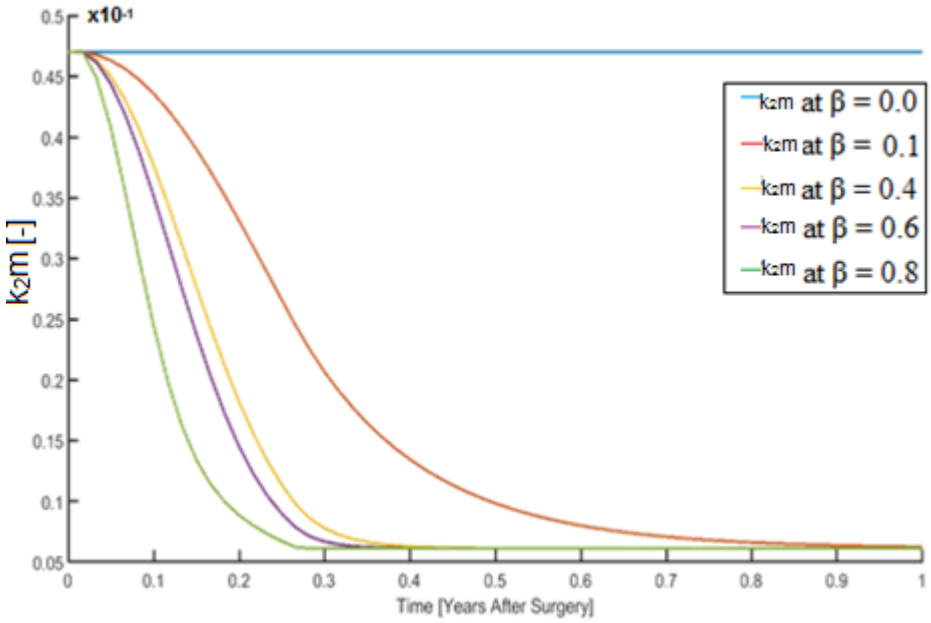

Figure 7.3 Evolution of k2m in the 12 months post-surgery, with varying values of the remodelling rate parameter β for muscle tissue.

β^M must be prescribed similarly to how β^T has been, with its own respective material parameters. Since the remodelling scenario defined by Boakes et al. (2006), k2m is expected to asymptote within one year, favourable values of the muscular remodelling rate parameter are approximately $\boldsymbol{\beta^M \geq 0.1}$, as shown in Figure **7.3**.

These are the parameters used in the subsequent remodelling work-flow to simulate overstretch during limb lengthening. The Cauchy stress was analytically calculated for the varying values of β^M and β^T to show how the stress changes and asymptotes to its homeostatic value (maximum dorsi-flexion in its homeostatic range), as shown in Figures **7.4** and **7.5**.

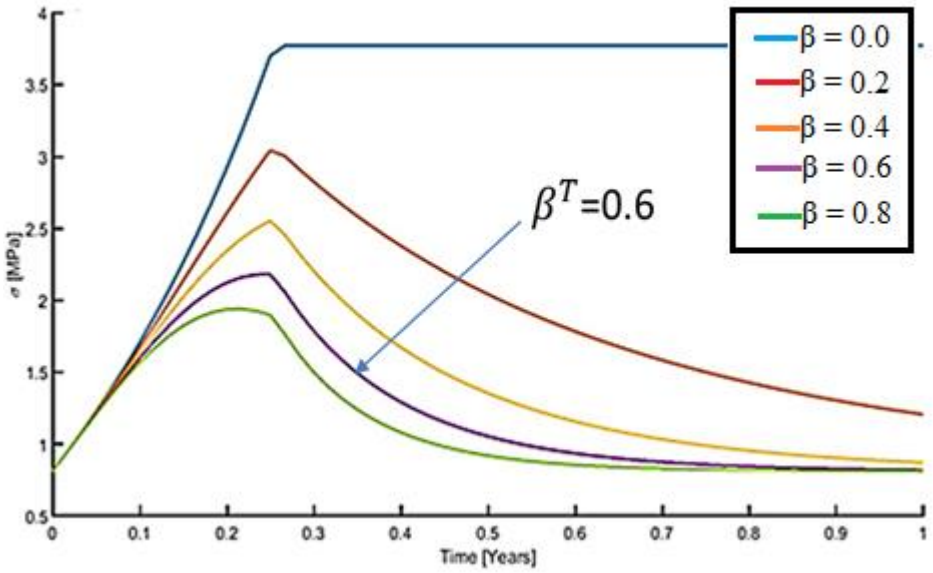

Figure 7.4 Illustrative example of Maximum anisotropic stress values [MPa] for different remodelling parameters of β^T (Tendon) in the overstretch remodelling regime of limb lengthening during the first year post-surgery (Boakes et al., 2006).

There are peak anisotropic stresses that are experienced by the tendon constituent for each value of β^T as shown in Figure **7.4.** This value is thought to lie around the same time ~ 0.25 years (which equates to 80 days) when the distraction period had ended, and the bone is no longer being incrementally extended. Following this, the muscle then left to remodel for the remaining 0.75 years (285 days) and this is shown as the anisotropic stress values decrease over time.

This analytical simulation confirms that the prescribed β^T calibrated to 0.6 (purple curve) in Figure **7.4** presents a Cauchy stress profile that remodels back to its original maximum homeostatic stress in maximum dorsiflexion of the medial gastrocnemius tendon, hence showing the behaviour of the model, the calibration of β^T and its boundary conditions and the efficacy the current model for the specific case study presented by Boakes et al. (2006). Congruent methods were carried out for the muscular constituents.

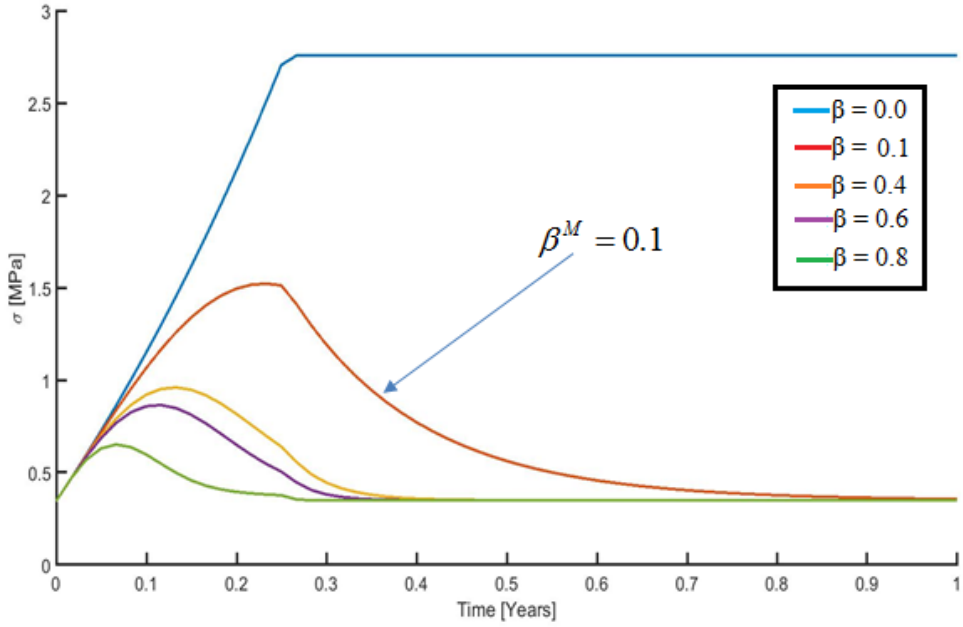

Figure 7.5 Illustrative example of Maximum anisotropic stress values [MPa] for different remodelling parameters of β^M (Muscle) in the overstretch remodelling regime of limb lengthening during the first year post-surgery (Boakes et al. 2006).

Contrary to the peak anisotropic stresses that are experienced by the tendon constituent for each value of β^T, the peak anisotropic stresses of the muscle constituent are all different, for different values of β^M as shown in Figure **7.5.** The value selected for β^M has the peak stresses experienced at approximately 0.25 years (80 days) which is also around about the end of the distraction period, and when the muscle was held at fixed length and left to remodel over the remainder of the year. When β^M is 0.1, the anisotropic stresses of the muscle are shown to decrease over time and asymptote at the homeostatic value.

This analytical simulation confirms that the prescribed β^M calibrated to 0.1 (red curve) in Figure 7.5, presents a Cauchy stress profile that remodels back to its original maximum homeostatic stress in overstretch of the medial gastrocnemius muscle tissue within a year, hence showing the behaviour of

the model, the calibration of β^M and the simulation boundary conditions that are able to represent the specific case study presented by Boakes et al. (2006).

The evolution equations proposed are stress-driven. As such, the tendon is expected to remodel faster as the same displacement boundary condition is applied to both muscle and tendon constituents, which is confirmed by the analytical simulations and the calibration of the remodelling parameter values of β^T and β^M.

7.3 A Numerical Investigation of Limb Lengthening of the medial gastrocnemius

The remodelling framework used above was applied to numerically test a cuboid of skeletal muscle tissue extended uniaxially. The cuboid constituents comprised of muscle, tendon and a linear myo-tendinous region. A 10 cm x 2 cm x 2 cm cuboid was used to represent a small cuboidal section of skeletal muscle complex, the constituent material properties are identical to those stated in Chapter 4, Table 4.2. The dimensions of the cuboid were chosen to represent a simplistic model of the morphology of the muscle, whilst also being able to loosely represent the geometry of the medial gastrocnemius complex – hence the selection of a cuboid, rather than a cube.

The muscle comprised of 50% of the total cuboid volume, the tendon consisted of 35% whilst the remaining 15% comprised of the muscle-tendon transition region. The transition region was not incorporated here since the individual constituents were to be explored. Hence, each of the constituents had the following volume fraction values, with an abrupt constituent junction applied, as illustrated in Figure 7.6.

$$f(x) = 1 \Rightarrow \textit{Tendon}$$
$$f(x) = 0 \Rightarrow \textit{Muscle}$$
$$f(x) = 0.5 \Rightarrow \textit{Junction}$$

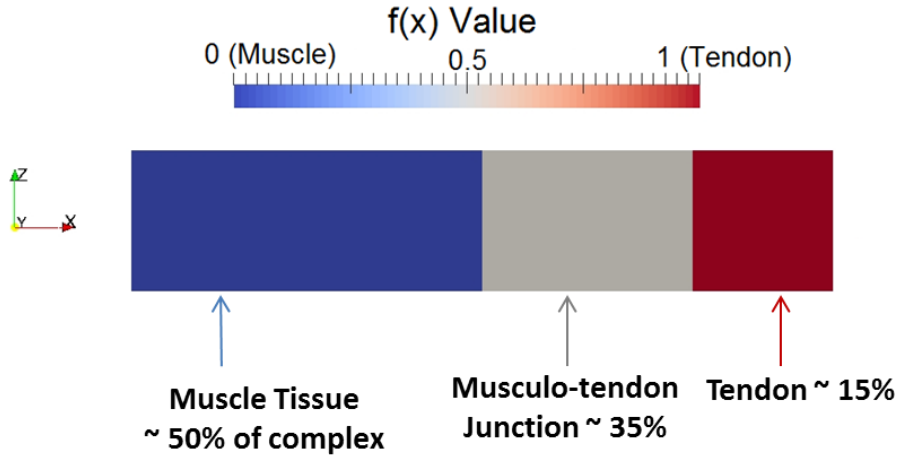

Figure 7.6 Simple material distribution of volume fraction f(x) in sample cuboid

Whilst the analytical model proposed in section 7.2 was computed in Matlab, it was numerically incorporated into the finite element workflow using a Python script to assign features such as fibre orientation and constituent distribution. To link the remodelling algorithm with the updated k_2 values, a custom Perl[7] script was used to orchestrate the remodelling workflow and ANSYS (?).

Further details of this, and the Perl code used are shown in Appendix A. This scheme was then used to inform the numerical analysis that was carried out in ANSYS. A brief description of this framework is illustrated in Figure 7.7, taken from Dandapani et al. (2017):

[7] Practical Extraction and Reporting Language (Perl) is a combination of two high-level multi-purpose dynamic programming languages – Perl 5 and Perl 6. It is a general-purpose scripting language, which derives broadly from C language. www.perl.org

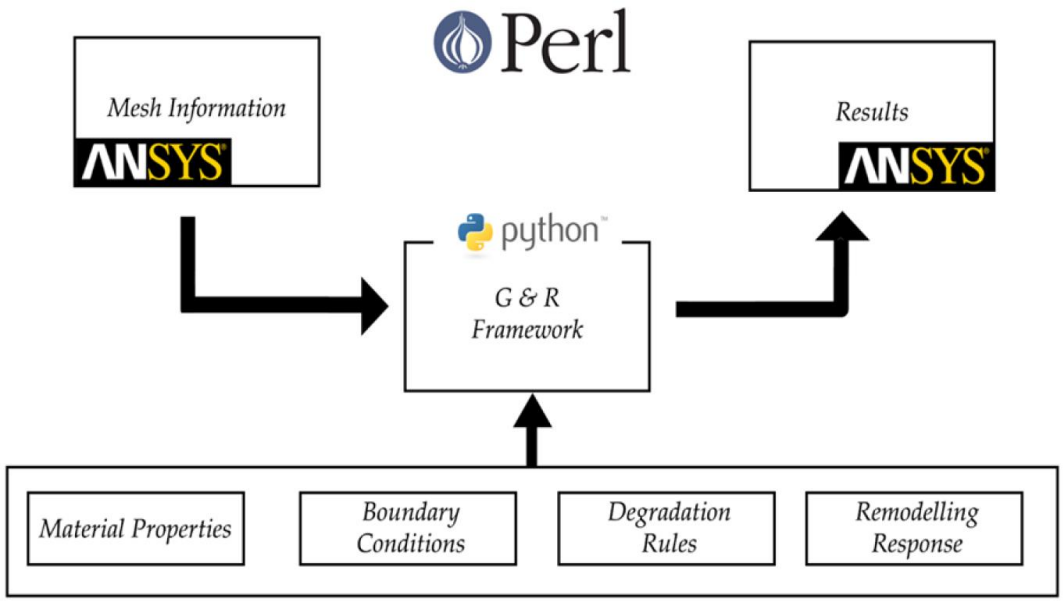

Figure 7.7 General Remodelling framework applied in Perl, Python and ANSYS. Inc (Dandapani et al., 2017).

The tissues that comprise of the medial gastrocnemius are fibre reinforced unidirectional soft tissues. For simplicity, the assumption that an axial alignment of fibres along the direction of loading is adopted. This numerical testing was undertaken to understand the remodelling regime of the medial gastrocnemius tissue more clearly, without the inclusion of geometrical and anatomical effects on the finite element analysis. The cuboid, its material property distribution, growth rates and boundary conditions are discussed in the next section.

7.3.1 Boundary Conditions

The k_2t and k2m were degraded incrementally, over several time-steps. This was done over 1 year to illustrate the incremental evolution of k_2t and k2m. The total time steps that were carried out to achieve homeostasis were 30 time steps, carried out over 1 year. (i.e. Since each remodelling time step was calibrated to the time for the simulation being 1 year, hence each remodelling time. The cuboid was constrained to Dirichlet conditions where the origin face was fixed in the X direction, and the nodes in the corners were

fixed to allow for uniaxial deformation as illustrated in Section 4.4.2, Figure 4.7. The (Figure 7.8) and then extended by 10% of its original length, which equates to 1 cm hence representing the maximum homeostatic stretch of the cuboidal muscle complex. The perturbed state of the cuboid was represented by extending the cuboid to 2 cm.

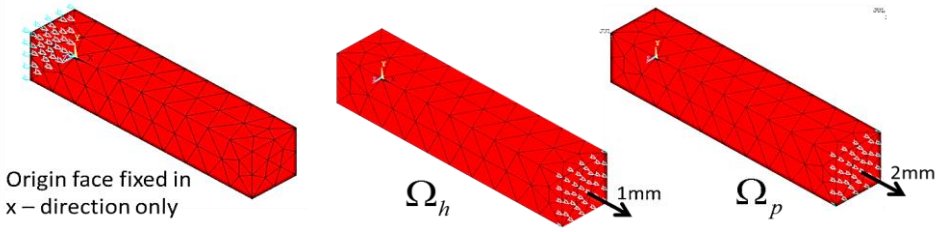

Figure 7.8 Cuboid of skeletal muscle-tendon complex boundary conditions for the homeostatic configuration and its perturbed configuration.

The cuboid was extended, and the remodelling workflow was left to run over 30 steps. The muscle and tendon remodelling constants (β^T and β^M) were varied during different simulations using the prescribed values of β^T and β^M from the analytical simulations above. In Simulation (a) only the muscle was set to remodel, with β^T= 0 and β^M= 0.1. In Simulation (b) only the tendon was set to remodel with β^T= 0.6, β^M=0, and finally, in simulation (c) both the tendon and muscle were made to remodel, with β^T= 0.6 and β^M= 0.1. This was done to i) assess the effects of the remodelling of individual constituents at the calibrated rates and ii) to illustrate how differential rates of remodelling of tendon/muscle can affect the evolution of the muscle-tendon complex. Hence highlighting the importance of correctly specifying remodelling rates for the tendon and muscle constituents so they can evolve 'physiologically'. Variation of the volume fraction of muscle – tendon and aponeurosis

From the literature, the muscle constituent of the medial gastrocnemius on average comprised approximately 50 - 55% of the full muscle-tendon unit and the tendon constituent compromises of 40 - 45% (Kalkman, et al., 2018; Boakes, et al., 2007). As there is little to no information on the aponeurosis,

various proportions of the tendon and muscle regions have been selected, leaving approximately 10% of the full muscle tendon complex as the aponeurosis region, as illustrated in Figure 7.9. For this model, a 10cm x 2cm x 2cm cuboid was used to represent a section of the medial gastrocnemius. The cuboidal model consisted of a central muscle region, two tendinous regions at each end and the transition regions, separating the muscle and tendon. This series arrangement more closely represents the anatomical arrangement of the MG constituents than the 1D model reported in Section 7.3.2.

In the previous section, the remodelling rates of each of the constituents have been investigated in order to define appropriate remodelling parameters in the current model. The remodelling regime of the tendon and muscle volume fraction has not yet been considered and will therefore be explored in the next section.

This variation was done to explore potential changes in the remodelling algorithm of the muscle-tendon unit based on increased tendinous regions (e.g. healing anatomical tissues may become more tendinous as observed in the build-up of scar tissue), or increased muscle regions (Bajuri, et al., 2016). Note that the tendon tissue is much more fibrous and denser compared to aponeurotic tissue and muscle tissue. Therefore, the following section could provide insight into such physiological phenomena and hence highlight how the stresses experienced by the evolving tissues can be impacted by their changing material compositions and properties.

Three simulations were carried out, where the proportion of tendon volume fraction was increased in Simulation B, compared to Simulation A, and then reduced (more muscle compromised of the muscle tendon complex) in Simulation C. The representative volume fractions and constituent proportions are shown in Table 7.2.

Table 7.2 Volume fraction variation of the muscle, tendon and aponeurosis constituents in the representative cuboidal geometry

	Muscle Constituent	Tendon Constituent	Aponeurosis Constituent

Simulation A	50%	40%	10%
Simulation B	75%	15%	10%
Simulation C	15%	75%	10%

The selection of the proportions chosen were based on approximate anatomical data of the different tissue regions in the gastrocnemius muscle (Boakes, et al., 2007), albeit the location and proportion of the transition, muscle and tendon regions are difficult to determine. Therefore, the proportions chosen here are only representative values.

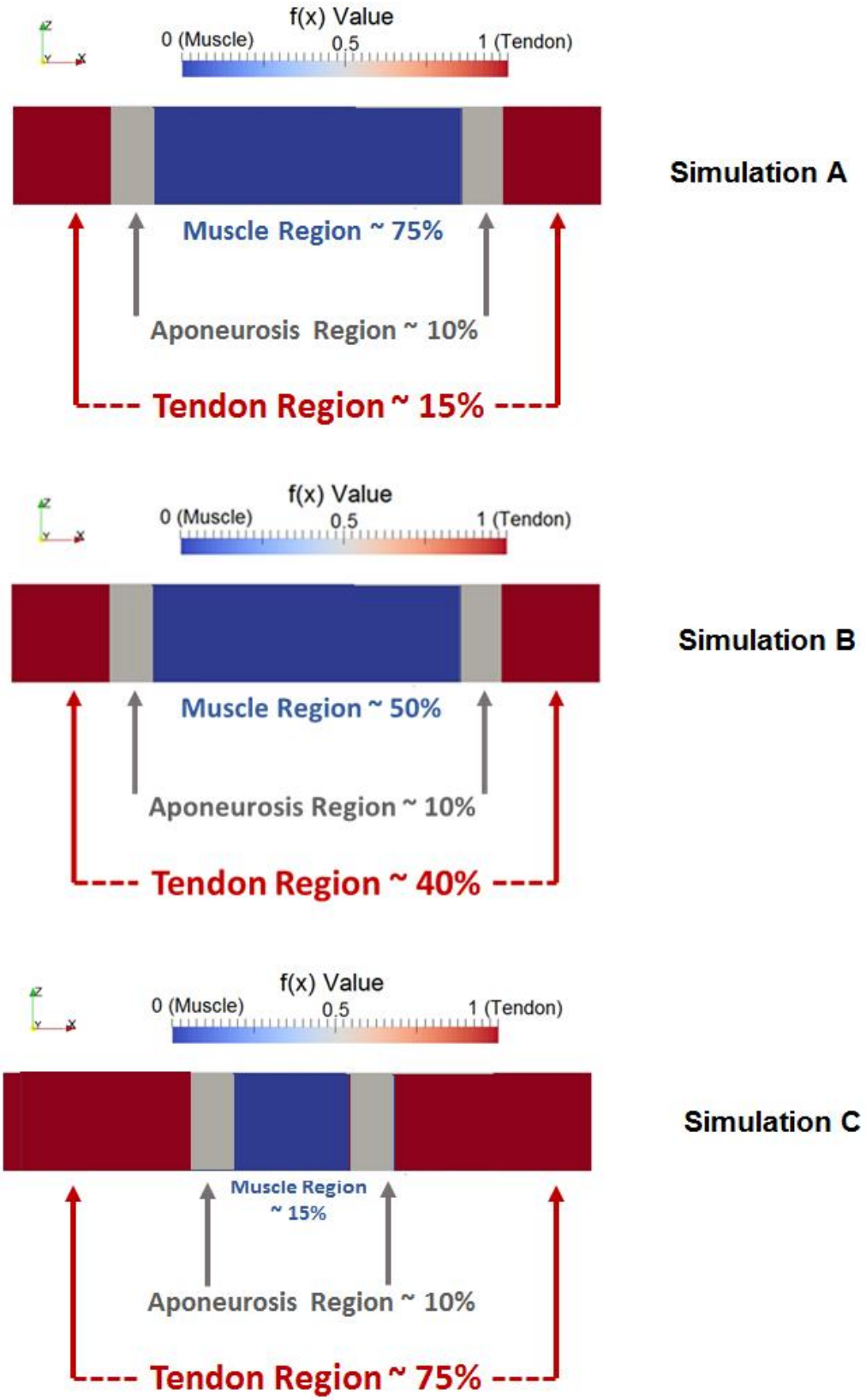

Figure 7.9 Schematic representation of the volume fractions of the muscle, tendon and aponeurosis tissue in the cuboidal geometry.

The cuboidal numerical models were developed from the studies done on the analytical studies shown in Section 7.2. It allowed for different variations of spatial configuration observed anatomically to be explored. This simplified geometry, however is by no means a true representation of the medial gastrocnemius muscle. Therefore, for the exploration of the difference in volume fractions on remodelling algorithms, a more comprehensive geometry has been created compared to that shown in Figure 7.6. This geometry is comprehensive, as it has a representation of transition regions and tendon regions of the distal insertion and proximal origin of the gastrocnemius muscle, as well as boundary constraints.

The cuboid was constrained using Dirichlet conditions as shown in Figure 7.8, however the origin face was fixed in all 3 degrees of freedom (X, Y and Z) to better represent the boundary conditions the anatomical muscle geometry would be subjected to. The insertion face of the cuboid was extended by 1% of its original length, which equates to 1 cm (10mm) hence representing the maximum homeostatic stretch of the cuboidal muscle complex.

In the current remodelling framework shown in Section 7.1, Equation **7.83**, the anisotropic stress is the main driver of remodelling, and hence its return to homeostasis is the main indicator of a successful remodelling algorithm. The results in Figures 7.10, 7.11 and 7.12 show the anisotropic contribution of the Cauchy stress of the representative cuboidal geometry over three Simulations A, B and C, respectively.

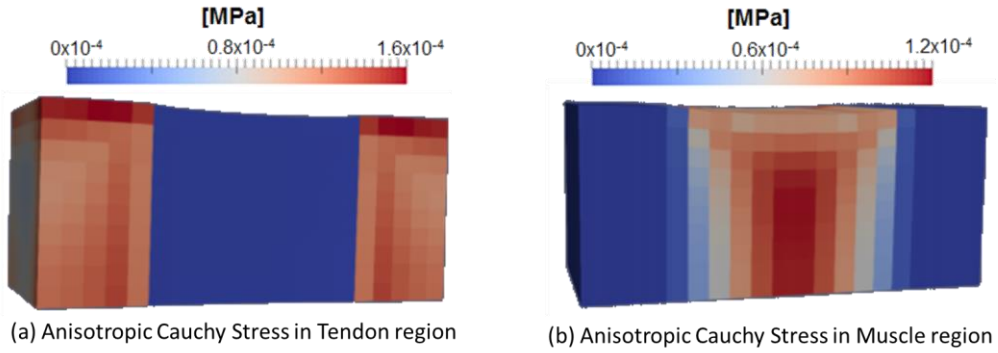

(a) Anisotropic Cauchy Stress in Tendon region (b) Anisotropic Cauchy Stress in Muscle region

Figure 7.10 Simulation A: muscle ~ 50%, tendon ~ 40% and aponeurosis ~ 10%. (a) Red regions showing the result of the tendon anisotropic stress (muscle stress is displayed as 0, therefore is blue) and (b) Red regions showing the result of the muscle anisotropic stress (tendon stress is displayed as 0, therefore in this section tendon is blue).

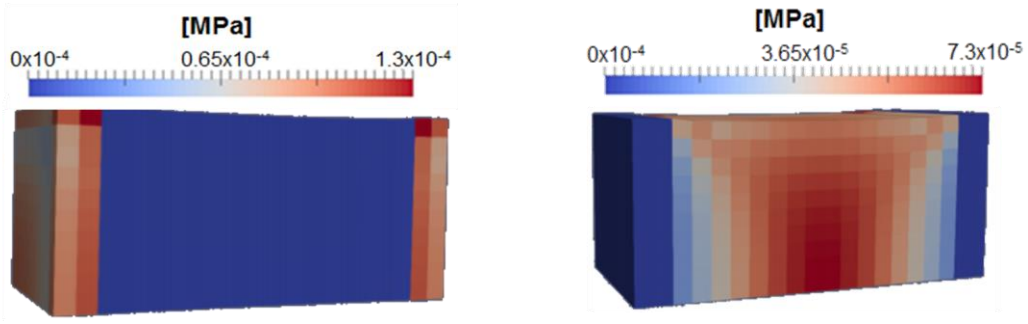

(a) Anisotropic Cauchy Stress in Tendon region (b) Anisotropic Cauchy Stress in Muscle region

Figure 7.11 Simulation B: muscle ~ 75%, tendon ~ 15% and aponeurosis ~ 10%. (a) Red regions showing the result of the tendon anisotropic stress (muscle stress is displayed as 0, therefore is blue) and (b) Red regions showing the result of the muscle anisotropic stress (tendon stress is displayed as 0, therefore in this section tendon is blue)

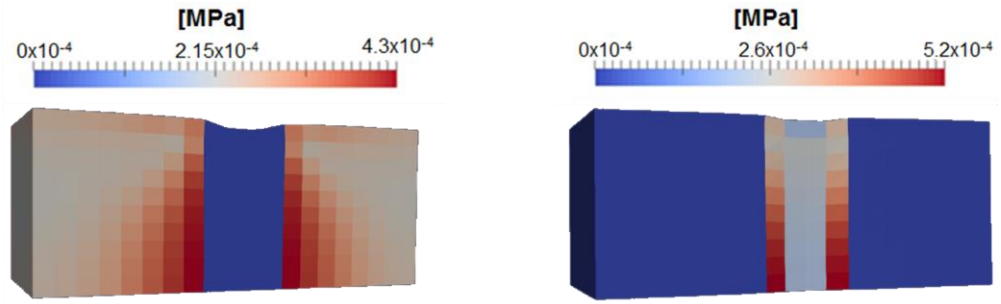

(a) Anisotropic Cauchy Stress in Tendon region

(b) Anisotropic Cauchy Stress in Muscle region

Figure 7.12 Simulation C: muscle ~ 15%, tendon ~ 75% and aponeurosis ~ 10%. (a) Red regions showing the result of the tendon anisotropic stress (muscle stress is displayed as 0, therefore is blue) and (b) Red regions showing the result of the muscle anisotropic stress (tendon stress is displayed as 0, therefore in this section tendon is blue)

Due to the graphical constraints of Paraview, and the additive split of the anisotropic stress terms of the muscle and tendon constituent, the stress of the muscle and tendon were plotted separately. For clarity, the first images (a) consider only the anisotropic contribution of the Cauchy stress term of the tendon and therefore does not show the stress in the muscle and vice versa for images (b) in Figure 7.27.

The peak stress in the tendon was generally higher in simulations A and B as expected, however when the tendon volume fraction in Simulation A was 15% where it was 40% in Simulation B. A consistent observation in the above simulations is that the aponeurosis tissue and muscle tissue experienced the least stress when the tendon was shorter as opposed to when it was longer. This suggests that the length of the tendon tissue affects the stress response of the muscle-tendon unit overall, as observed in the results in Chapter 6 (in tendon lengthening studies). Both the physiological changes and the remodelling process could affect the mechanical response of the recovering muscle, which needs to be further investigated in order to provide insight on how such changes can affect therapeutic treatments, and later determine the efficacy of these treatments (e.g. limb lengthening techniques). This is explored in the next section through illustrative results of a remodelling cuboid.

7.3.2 Illustrative Results of the Remodelling Algorithm on a Cuboid

Figure 7.13 shows the numerical study carried out on the perturbation of the anisotropic stress from its homeostatic value on the cuboid of the tendon constituent as k_2 remodels over 14 days (one casting cycle). Figure 7.14 shows the numerical study carried out on the perturbation of the anisotropic stress from its homeostatic stress value – therefore showing normalised stress values of the muscle constituent as k2m evolves over 14 days (one casting cycle).

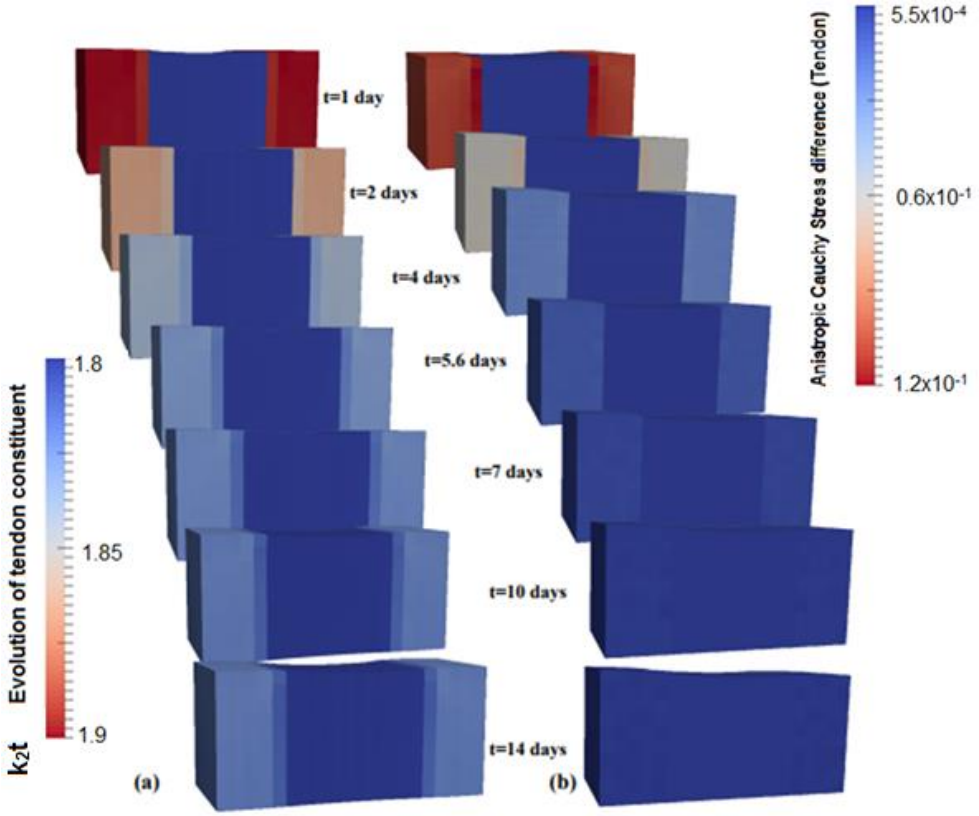

Figure 7.13 (a) Evolution and contour map of k_2 evolving with respect to time over 14 days, and (b) evolution of anisotropic stress distribution of the tendon tissue in Simulation A – tendon ~40%, muscle~ 50% and aponeurosis ~10%.

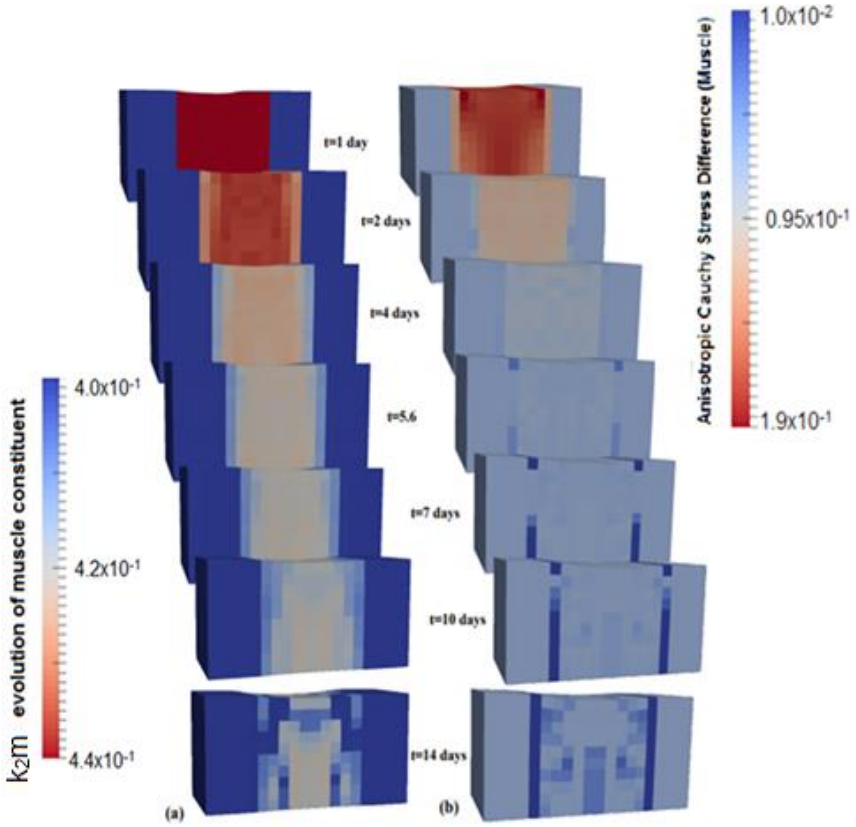

Figure 7.14 (a) Evolution and contour map of k2m evolving with respect to time over 14 days, and (b) evolution of anisotropic stress distribution of the Muscle tissue in Simulation A – tendon ~40%, muscle~ 50% and aponeurosis ~10%.

Previous literature suggests that when held in extension, the anisotropic stress of the tissue gradually returns to homeostasis as k_2 and k2m return to their original configurations as shown in the Figures 7.13 and 7.14.

It was expected that Simulation C, where the tendon had the largest volume fraction, would have remodelled the slowest. However, the predicted remodelling results of Simulation A, B and C were very similar, regardless of the lengths of the constitutive regions, as illustrated in Figures 7.13 and Figure 7.14. This suggests that the constituents are remodelling to their required states, synchronously. Since the remodelling of the tissue here is driven by the anisotropic stress, the remodelling regime is therefore responding to the stress experienced to return the cuboid to its homeostatic configuration regardless of the constitutive configuration of the cuboid. Since the

homeostatic stress of the cuboidal complex is not homogenous, the stress difference could be 0, as this shows the deviance of the resultant stress from its homeostatic value for each element. Therefore, the stress difference shows a more quantitative representation of distribution of remodelling in the muscle geometry.

For each simulation, rapid progress towards the homeostatic stress was made over the first 7 days where stresses in the tendon were within 2% of homeostasis and the stress difference in muscle was negligible. It is important to consider the stress difference here as it explicitly shows the deviance of the stresses from its homeostatic value and hence is clearly indicative of remodelling regions in the muscle. By day 10, stresses in the tendon and muscle regions had reached homeostasis across all simulations. However, in each simulation, k_2t (the tendon material parameter) began to converge to 1.78 after seven days and k2m (the muscle material parameter) converged towards 0.4 generally (given, that there was variation in the distribution of values across the geometry).

Generally, the simulations above have shown that increasing the length of the tendon had a larger effect on the muscle response than on the tendon. The results suggest that the lengths of the muscle and tendon volume fractions do not influence remodelling time but are still important to consider as they largely influence the tissue's strain and stress response.

The current cuboidal model has shown the various interactions in remodelling and stress-strain experienced in the muscle geometry which highlights the value of its implementation in exploring the overall muscle-tendon-aponeurosis behaviour.

7.3.3 Discussion

In this chapter, the anisotropic contribution of the Cauchy stresses and strains were computed. The stress difference (remodelled stress – homeostatic stress) distribution explicitly shows the areas of remodelling as the remodelling is driven by the anisotropic stress and its deviance from the homeostatic stress, and finally illustrate that the model is behaving as

expected where the stress difference in the cuboidal model returns to homeostasis. The anisotropic stress results showed that only remodelling regime (c) (both the muscle and tendon were remodelling) resulted in the cuboidal muscle complex returning to its homeostatic anisotropic stress value. The higher anisotropic stresses observed in the muscle constituent in regime (b) when tendon remodelled in isolation, showed that the other constituents did not return to their homeostatic anisotropic stress value after remodelling, similar results were also observed in the tendon region when muscle was remodelled in isolation for case (a).

In remodelling regime (c), the highest strains after remodelling were found in the muscle constituent, followed by the tendon tissue and then the transition zone. The *difference* of strains in the homeostatic and remodelled configurations represent the potential extent of lengthening of the constituent – which indicates regions of sarcomerogenesis (increase of sarcomere number, in this context sarcomere number in series). It is important to note that it is the *change of strain* from each constituent's homeostatic value to its remodelled state that is indicative of sarcomerogenesis, rather than the mere presence of strain in either configuration. Therefore, the quantification of this phenomenon; as future work, could elucidate further results on sarcomerogenesis and growth or further development of the cuboidal skeletal muscle complex, since the current model is based on stress-driven remodelling only.

These results support the idea that in order to extrapolate a representative remodelling regime of overstretch in skeletal muscle-tendon complexes from a perturbed configuration back to homeostasis, both the tendon and muscle constituents should be considered to remodel, albeit at different rates. It is noteworthy, therefore, that other models have remodelled only the muscle constituent (remodelling regime (a)), in a muscle-tendon anatomical complex (Zöllner et al., 2012; Zöllner et al., 2015), and those results should be reviewed with caution.

The volume fraction and its effect on the muscle-tendon unit has also been explored in Simulations A, B and C in Section 7.3.3. Whilst these simulations provide some insight on increasingly tendinous evolution or increasingly

muscular evolution in the muscle-tendon-aponeurosis complex, it has been concluded that the volume fraction and lengths of the various constituents affects the stress response – further strengthening the conclusion in Chapter 6, as these lengths do not affect the remodelling regime of the muscle-tendon complex.

Note that future work could explore the theory that mechanical homeostasis of the muscle lies within a range, rather than at a set threshold value as has previously been defined in (Zöllner, et al., 2015). This highlights the novelty in including a homeostatic *range* into a finite element model of the medial gastrocnemius in overstretch. Collaboratively, the maximum and minimum stretches in this context could be referred to as the muscle's range of motion for this future work.

Before the onset of remodelling, the muscle is assumed to operate within a homeostatic range, which is below the critical threshold that determines the onset of remodelling. After this threshold homeostatic range, the muscle is thought to be operating in a perturbed environment, where remodelling occurs. This concept of a range of motion coincides with a homeostatic range of values which have been discussed by other authors (Latorre & Humphrey, 2018). Therefore, this highlights the importance to carefully consider the homeostatic configuration of the muscle and how to define it, as it is this configuration that determines the onset of remodelling in future work.

The next section explores the remodelling regimes described above (a, b and c) using the anatomical geometry described in Chapter 6 with anatomical fibre paths, aponeurosis and constituent distribution. This last simulation is used to predict and provide further insights into the remodelling regimes an anatomical medial gastrocnemius muscle may experience during limb lengthening.

7.4 An Anatomical FE Investigation of Limb Lengthening of the medial gastrocnemius

The previous section explored the way in which each of the constituents remodelled, and the qualitative impact this had on the stress-strain relationship of a muscle-tendon complex. Whilst the cuboid with allocated constituents was an insightful simulation, the anatomical features were not considered. This section, therefore, investigates the same remodelling regimes. This exploration will be used to assess how such regimes will impact the overall stress-strain profile of the medial gastrocnemius, in an overstretched mechanical environment during limb lengthening, as defined in Boakes (2006). The boundary conditions inferred from this work and applied to the anatomical simulation are covered in more detail in the next section.

7.4.1 Boundary Conditions

The boundary conditions for this simulation are like those described in Chapter 5, with the exception that the muscle was extended by 10 mm initially at the insertion end, which represented the maximum homeostatic stretch the muscle might experience, and then further extended to 15 mm to represent the perturbed configuration as taken from the previous section. These values represent the anisotropic homeostatic stretches which attribute to the fibre response of the constituents.

Since the length of the muscle-tendon complex is 149 mm, 6.7% of this equates to approximately 10 mm extension. The boundary conditions of the muscle are identical to those used in Chapter 5, with the exception that the muscle was extended by 10mm first, followed by 15mm in its perturbed configuration. The material constants used are identical to those described in Chapter 4, Table 4.2.

7.4.2 Results

As the fibre stress exceeds the homeostatic stress, remodelling occurs to restore the fibre stress towards homeostatic levels. This is achieved by reduced k2 material parameter in both muscle and tendon (see Fig 7.4 and 7.5). The homeostatic and perturbed anisotropic stress and k_2 values for muscle and tendon are shown in Figure 7.15 and Figure 3.11 respectively.

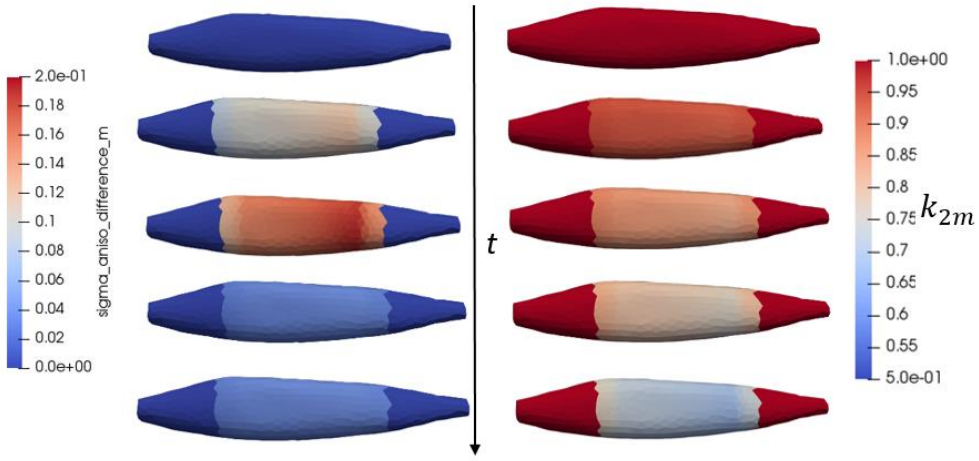

Figure 7.15 (left) Muscle fibre stress difference fraction from homeostatic levels. Initially at t=0 (top image), the stress is equal to homeostatic values throughout domain and hence stress difference is zero. As axial displacement is increased, the stress difference increases to 0.2 (a 20% elevation above homeostatic levels). The increase is due to stress driven remodelling of k2m (right). As k2m reduces (to around 0.65), the stress differences are restored to within 2% of homeostatic values.

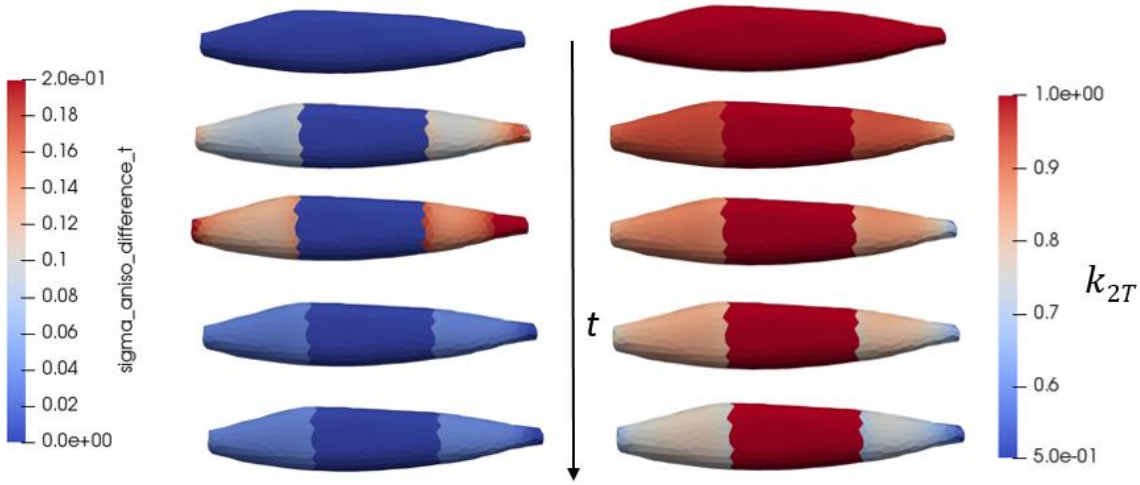

Figure 7.16 (left) Tendon fibre stress difference fraction from homeostatic levels. Initially at t=0, the stress is equal to homeostatic values throughout domain and hence stress difference is zero. As axial displacement is increased, the stress difference increases to 0.2 (a 20% elevation above homeostatic levels). The increase is due to stress-driven remodelling of k2 (right). As k2 reduces (to around 0.5), the stress differences are restored to within 2% of homeostatic values.

In the first-time step (top images in Figures 7.30 and 7.31), the muscle was extended to the upper bound of the homeostatic range (e.g. 10 mm). The second row shows the onset of the perturbed configuration, where the muscle was extended to 15mm. Note that remodelling had not begun. Subsequent rows showed further time steps as remodelling occurs with time. The process is driven by the anisotropic stress difference (from homeostatic state), which in turn forced k2 to evolve in order to bring the stress back to the homeostatic value, as illustrated in the final row of the figures. This verifies that the remodelling algorithm is working on the anatomical model, and therefore further studies could be done to calibrate such a model to patient specific parameters to hence determine a more bespoke remodelling process for bone-lengthening scenarios. In the above case, both k_2m and k_2t had to decrease, so that the stress could return to its homeostatic state. The evolution of k_2m and k_2t represents permanent changes of the material behaviour after the tissue was perturbed.

Figure 7.32 highlights how the anisotropic stress difference of tendon (a) and muscle (b) returned to 0 in the above simulation. Note that the simulation was run for 30 remodelling time steps, representing 1 year in real life. Therefore, each remodelling time step represented approximately 12.2 days. The stress difference started at 0 when t=0 (homeostatic state). The muscle-tendon complex was then extended to 15mm at t=2. After that, the remodelling algorithm kicked in and the stress difference reached maximum at t=3, which in turn drove the evolution of k2 parameters. The model was able to return to homeostasis within 14 time steps, or 170 days.

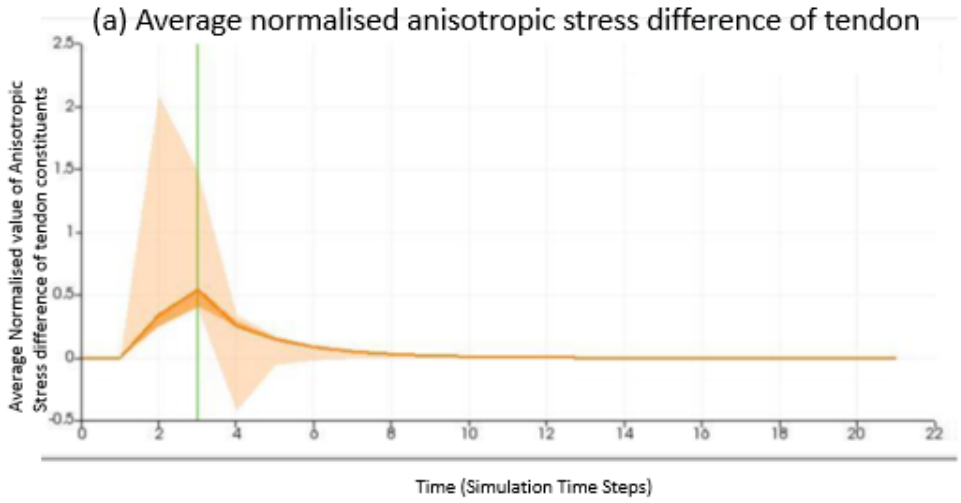

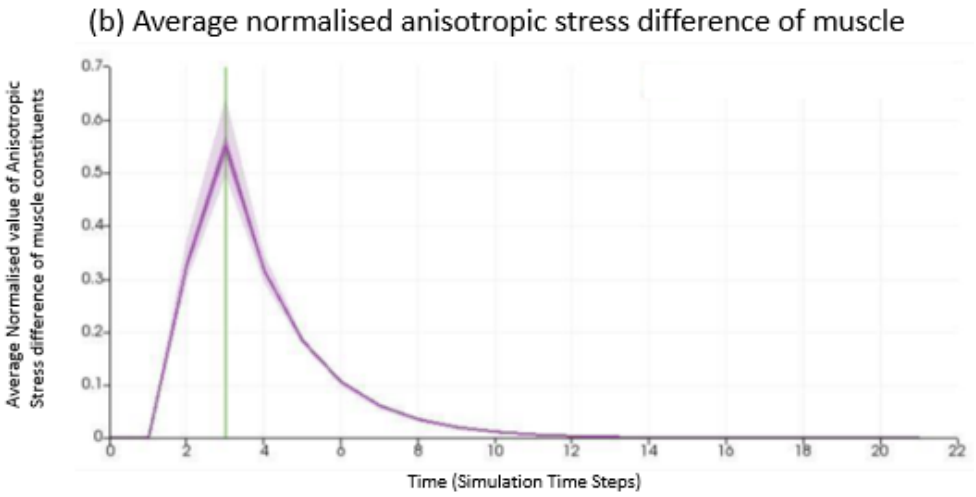

Figure 7.17 Evolution of the average distributions in the stress difference ratio (from homeostatic stress) for tendon (a) and muscle (b). At t=0, the stresses are equal to the homeostatic stress distributions, i.e. stress difference is zero throughout the domain. For 0<t<3, the stresses increase to reach maximum. For t>2, the displacement is fixed, and stress distributions are gradually restored back to homeostatic levels (stress difference is zero at around t=14) as k2t and k2m remodels.

7.4.3 Discussion

From the results shown in Figure 7.31 and Figure 7.32, it is clear that remodelling both the muscle and tendon is imperative to getting the muscle back to its homeostatic state, specifically when looking at anatomical muscle geometries that have both muscle and tendon components.

From Figure 7.17, it is clear to see that the muscle and tendon constituents remodel at different rates, over different remodelling cycles. The tendon has a faster remodelling rate, which is due to the tendon region having a smaller cross-sectional area and a stiffer response.

Because the current remodelling algorithm is stress-driven, the strain distributions were not shown here for these models. Nevertheless, the stress results are verified by the results extrapolated from the cuboidal muscle complex simulations.

7.5 Discussion

The work in this chapter showed a novel remodelling framework for the medial gastrocnemius, which allows for the exploration of various remodelling algorithms in both muscle and tendon components of the skeletal muscle, which has not been explored previously (Böl & Reese, 2008; Zöllner et al., 2012; Zöllner et al., 2015). From the results shown in section 7.3, the description of the different constituents and their material distribution in a complex structure, such as skeletal muscle, has a powerful impact on the overall mechanical response. From the analytical, cuboid and anatomical simulations, results suggested that it is necessary to include the remodelling of both tendon and muscle components in order to capture the different remodelling rates in each material.

Whilst other models (Zöllner et al., 2012; Zöllner et al., 2015) have attempted to disregard the tendinous mechanical response by setting it to a disproportionately stiff material, and not considering any muscle-transition zone, concern may arise around the initial structural analysis of the muscle, and around the accuracy of their muscles' remodelled state. From the results in this section, it is therefore concluded that both the muscle and tendon constituents are required to model – potentially at different rates – in order to get the combined muscle-tendon constituent back to its homeostatic configuration.

Whilst the proposed model offers a contribution to the current body of knowledge on skeletal muscle remodelling, there are some limitations that need to be acknowledged. The re-alignment of the muscle fibres during remodelling was informed by the structural analysis in section 7.3, however the degree to which the fibres realign in tendon, muscle and transition tissue needs further investigation. The proposed model has been formulated so that the fundamental idea of a muscle remodelling back to its homeostatic configuration can be satisfied. However, the exact homeostatic values of the muscle and tendon tissue are largely unknown and should be determined through future experiments.

The remodelling algorithm used here relied on the evolution of k_2t and k2m in order to bring the anisotropic stresses back to homeostasis after perturbation. The homeostatic stresses are heterogeneous and calculated from Equation 7.83. This was shown in the analytical results in Section 7.2.

In this study, homeostatic stretch range of the full muscle-tendon complex of the medial gastrocnemius was taken from Lanir et al. (2015) because they represented unidirectional collagenous fibrous tissues. This coincided well with the current assumption that the muscle-tendon complex were made up of different fibres. However, it should be acknowledged that the homeostatic stretch ranges could be different between muscle and tendon. This needs to be further investigated in the future.

Furthermore, whilst the remodelling is stress based, the actual growth of the muscle-tendon complex (i.e. the increase in sarcomere number and volume) has not been modelled. This could be investigated in the future by incorporating and evolving mass-density variables. This might help represent the general mass turnover of the muscle. However, additional knowledge of how the different components (muscle, tendon and muscle-tendon transition) change during over- and under-stretch will need to be examined, which is currently not clearly understood.

In conclusion, this chapter presented a remodelling framework that can propose an adaptive mechanism when the medial gastrocnemius is in overstretch. Results showed that the remodelling regimes of *each* constituent must be carefully considered, in order to simulate remodelling of muscle from a perturbed configuration back to its homeostatic configuration. The proposed remodelling algorithm works on the anatomical model, which is verified using results from the numerical cuboidal simulations as well as the analytical simulations. A series of assumptions has been made in the model, and further studies should be conducted to better inform and validate the model against physiological parameters.

The overall conclusions of the thesis, discussions and future work are covered in the next and final chapter.

Chapter 8

Conclusions and Future Work

The overall aim of this thesis was to develop an anatomical model of the medial gastrocnemius that can be used to explore its mechanical response

Firstly, the medial gastrocnemius anatomical model was produced from a cadaveric geometry and fibre orientations from LHDL, and further sophisticated to accommodate the morphology and material constant distribution of the myotendon junction and aponeurosis. Secondly, the model was used to explore several different mechanical environments – lengthening of the myotendon junction, high strains and healing tendon. Finally, the muscle as applied to a preliminary remodelling framework that explored different remodelling regimes and which regimes might best describe the mechanical response of the muscle as it changes temporally.

This Chapter summarises the general conclusions of the work of this thesis and discusses the results generated from the present investigations, hence giving guidelines for future research.

8.1 Key Findings

The key findings and areas of future publication of this thesis are highlighted here and separated into three summarized points;

(i) A descriptive model of the anatomical morphology of the medial gastrocnemius muscle has been developed that proposed a unique approach to defining the anatomical fibre orientations and the constitutive description of the myotendon transition region and the aponeurosis.

(ii) Further extrapolation of this model found that excessive strains shift the location of peak strains in the medial gastrocnemius, however, the maximum stresses and strains experienced at the distal insertion decreased as the transition zone lengthens and stretching damaged tendon may render higher stresses across the whole muscle-tendon structure - resultantly causing more damage.

(iii) The final key aspect concerned the preliminary findings of remodelling different constituents in a composite constitutive geometry, in that adaptation of all constituents are imperative to consider, whilst they remodel at different rates.

These areas of key findings provide a significant contribution to the current body of knowledge as the point (i) provides a unique and relatively simple method to incorporate anatomical fibre orientations from a cadaver (and possibly in vivo fibre orientations) into a finite element formulation. Whilst there have been more complex computational methods used to determine fibre orientations of different muscles (Blemker & Delp, 2005; Lu, 2011), the use of an interpolation vector field onto centroid locations provides a sufficient solution to determining anatomical fibre orientations, which are not exclusive to fusiform muscles, but could be used for a number of other types of muscles, such as bipennate or multipennate muscles – provided the anatomical data used to inform the model is comprehensive.

8.2 Limitations

The preliminary remodelling formulation can provide some insight on the mechanical response of an anatomical medial gastrocnemius muscle in overstretch, over a temporal domain. It also has the potential to inform multi scale models for use in kinematics and dynamics models. Whilst this connection has been previously made between finite element muscle models and multi scale muscle models (Röhrle, et al., 2017), the current model offers a descriptive three-dimensional model of which can be used to improve precision of accuracy in stress-strain distributions.

Such models can be used to holistically model MSDs, by incorporating the current model into multiscale models that have been used to investigate specific MSDs and hence better inform the area of research concerning musculoskeletal systems, therapies, diagnosis and latently, cost reduction strategies. Therefore, the current model has the potential to inform a variety of applications, however in order to do this efficiently, the limitations of the thesis must be clearly acknowledged and are discussed here.

8.2.1 The Skeletal Muscle Geometry

Whilst this model has used anatomical data in a finite element simulation, it incorporated the tendon and aponeurosis regions using idealised shapes to represent the geometry of the aponeurosis. The current shapes rendered good results however, further scrutiny could be carried out to improve the shape of the aponeurosis – in particular the tapering angle at the aponeurosis edge, or the penetration depth of the muscular transition zone into the tendon.

Another geometrical limitation concerns the fibre orientations of the muscle where the fibre vectors used in the simulation were augmented from only 4 splines that were palpated from the cadaver. If there were more splines made available, then the interpolation and fibre vector allocation would be more accurate. More descriptive data of muscle fibre orientations can be obtained from DT-MRI, as discussed in Chapter 3. This would better inform the current model, and hence provide an accurate interpolation of the vectors

at each centroid element – which would provide a more accurate stress-strain profile of the medial gastrocnemius.

In addition, the acquired geometry had to go through several pre-processing steps before finite element simulations commenced. The geometry had to be triangulated, cropped and smoothed. Whilst these processes may have altered the volume of the geometry, with further estimation of the geometry boundaries using surrounding soft tissues, the final geometry was able to provide a geometrical representation of the medial gastrocnemius for finite element simulations. A more accurate description of the 3D geometry (e.g. from MRI scans) of the medial gastrocnemius would considerably reduce the amount of pre-processing required and provide a more accurate description of the anatomy. This ought to be investigated in the future.

8.2.2 Remodelling Formulation

Whilst the proposed remodelling formulation offers a contribution to the current body of knowledge on models of skeletal muscle remodelling, there are several limitations that need to be acknowledged. The formulation proposed in Chapter 7 is unique however preliminary. The remodelling formulation proposed in this thesis is mainly stress based, however the actual growth of the muscle-tendon complex (i.e. the increase in sarcomere number) has not been modelled - although this could be easily incorporated into the model by evolving the volume fraction parameters, f(x). Whilst growth might represent the general mass turnover of the muscle, additional knowledge of the change in distribution and location of the different constituents (muscle, tendon and muscle-tendon transition) are expected to change during over- and under-stretch/loading phenomena. It is also expected that the distribution of constituents, and how they grow and remodel, will vary across different muscles. Therefore, rigorous and gradual experimentation is required to inform this area of research.

8.3 Future Directions

8.3.1 Incorporation of skeletal muscle active mechanics and antagonistic pairs

The current model has only considered the passive mechanics of the medial gastrocnemius, due to the mathematical nature of the mechanical contribution of the passive and active parts (additive split). However, there are some aspects of the active mechanics that will affect the passive mechanics of the muscle– such as the increase of PCSA found in stress-based remodelling, or muscle tonus which tends to increase the stiffness of the muscle tissue. An active component can be incorporated into the current model by means of an ANSYS subroutine, which will enable further studies to be carried out, and elucidate further insights on under/over loading mechanics of the muscle. The inclusion of an active component will enable the remodelling phenomena of over – and underloading mechanics – such as parallel sarcomerogenesis, increase in force generation and PCSA.

Further, since the passive medial gastrocnemius was studied in isolation, the inclusion of surrounding tissues – such as the lateral gastrocnemius, and soleus are thought to have an impact on the active mechanics of medial gastrocnemius. The inclusion of these structures in a full finite element simulation may provide further insight into the physiological behaviour of the muscle.

8.3.2 Further analysis on the geometrical representations of the transition region and aponeurosis

As highlighted in Chapter 6, further geometrical models could be used to represent the geometry of the aponeurosis, for example two ellipsoids representing the penetration of muscle into the transition region, and further

the transition region into the tendon region. Case (4) - the tapered ellipsoid could also be improved, and the effects of the tapering angle used could be investigated in a parametric study. The number of morphologies proposed in Chapter 6 however, offer a few ways to represent the aponeurosis and transition region in a variety of muscles – some which may have a linear-like transition and aponeurosis. The linear dependence case (2) could be used for the most fusi-form, bi-pennate and multipennate muscles; Sartorius, for example, which is a long thin muscle with a fusi-form fibre orientation and has a small linear like aponeurosis that joins from its proximal origin to the distal insertion. Another muscle that could also be modelled using Case (2) morphology is the tensor fascia lata, which has a similar fibre orientation to the Sartorius but has a much smaller muscle belly and longer tendinous aponeurosis at its insertion end. This shows the versatility of the approaches proposed in Chapter 6.

The fibre orientations and how they evolve will provide more detailed insight into the final mechanical response of the muscle. The current model does not show the fibres upon remodelling due to computational and algorithm constraints, however this could be developed through further sophistication of the model and future work.

The constitutive model adopted through-out this thesis is taken from Holzapfel et al., (2000), where the inclusion of a volume fraction equation has allowed for the representation of the different constituents. Whilst this model has allowed for the general fibre direction of each of the constituents to be modelled through I_4 and I_6, it assumes that the material symmetry is homogenous. This may not be the case in highly collagenous tissues such as the tendon constituent; hence the inclusion of a structural tensor which can be used to statistically determine the asymmetry of fibre orientations (Gasser, et al., 2006).

8.3.3 Methods used to model growth and remodelling mechanics of muscles in over/under stretch/loading

In Chapter 7, whilst the current formulation has proposed a method to model the return of anisotropic stresses to their homeostatic value during overstretch, future work may include the investigation of other methods to simulate the mechanics of over/under stretch/loading and determine the efficacy of such methods, since only one method has been adopted in this thesis. Other methods could be used to remodel the stiffness k_1 base matrix of the muscle, or to evolve the fibre orientations of the muscles as it is in over- and under-stretch/loading. The degree to which the fibre orientations realign during different remodelling regimes will also better inform the current model, with further enhancement by including the growth and mass turnover of the muscle and its distribution of material constituents.

Further investigations need to be carried out with the current remodelling algorithm – such as specific and gradual experimentation to calibrate the parameters and values in the model. This can help elucidate further insight into the medium to long term changes a skeletal muscle may undergo. The work carried out in Chapter 7 is preliminary, and focus has lied around exploring the remodelling regimes and definition of the homeostatic configuration. Future work could be done to provide a more comprehensive understanding of skeletal muscle remodelling, as only one scenario has been explored – limb lengthening.

8.3.4 Validation

The current model has a range of different areas that have been estimated from anatomical data. The model also incorporates a range of assumptions, such as fibre orientations, material properties, boundary constraints, as well as remodelling algorithms and parameters. Therefore, it is important to consider how the modelling pipeline can be validated. Although the numerical workflow has been verified by analytical solutions using a simple geometry, further validation of the numerical work-flow could be carried out using experimental data on isolated tendon, muscle, and aponeurosis

constituents under uniaxial loading. This would provide additional data to validate the assumptions on geometry, fibre orientation, material properties and boundary constraints.

The validation of the remodelling algorithm is more challenging, as it would be difficult to track the behaviour of a piece of soft tissue over a period. Previous work has investigated the force generation of cardiac muscle kept in isolation *in vitro* over a period of time (Lopez & Kramer, 2019) and other growth and remodelling finite element models have been verified and applied to abdominal aortic aneurysms (Horvat, et al., 2019). A similar approach could be applied to skeletal muscles considering the long-term remodelling effects of limb lengthening – where the initial mechanical response of the gastrocnemius muscle (and its isolated constituents) are experimentally determined and upon remodelling measured again. This could be done to ensure that the remodelling of the parameter chosen is an accurate reflection of the underlying mechanical changes in the gastrocnemius. Furthermore, there has been extensive recent advance in the use of digital image correlation (DIC) and digital volume correlation (DVC) techniques to validate finite element modelling frameworks (Holak, et al., 2015; Sopher, 2017; Huang, et al., 2019). These techniques provide a detailed stress/strain map of the material under deformation and would help to further elucidate the change in material composition and behaviour during remodelling.

8.4 Summary

This thesis developed an anatomical finite element model of the medial gastrocnemius muscle-tendon complex and proposed an approach to represent the aponeurosis region and the muscle tendon junction. From this work, further analysis has been carried out to assess the effect various morphologies have on the passive mechanics of the medial gastrocnemius

muscle. The model was then used to explore different remodelling regimes in a preliminary remodelling formulation that may occur when the muscle operates within a specific mechanical environment specifically – overstretched during limb lengthening.

The main novelties of this thesis lie in the following areas;

(i) The incorporation of cadaveric fibre paths into a finite element workflow in an anatomical simulation of the medial gastrocnemius,

(ii) An innovative approach adopted to represent the morphology of the medial gastrocnemius aponeurosis,

(iii) The inclusion of a simplistic method to determine the material constituent distribution with a radial dependence in the muscle-tendon transition zone,

(iv) The exploration of remodelling mechanisms of the passive medial gastrocnemius during overstretch (limb lengthening).

The current model can be used to predict areas of high strains and low strains across the passive mechanics of skeletal muscle, This research has provided an informative model, that can be used in multi-scale models and further the research in MSD (Musculo-skeletal disorders), which can intrinsically alleviate the disease burden on the world economy (World Health Organisation, 2013).

References

Abbott, B. & Richie, J., 1951. The onset of shortening in striated muscle. *Journal of Physiology,* Volume 113, pp. 336 - 345.

Adams, G., Caiozzo, V. & Baldwin, K., 2003. Skeletal muscle unweighting: spaceflight and ground-based models. *J Appl Physiol (1985),* 95(6), pp. 2185-201.

Altan, E., Zöllner, A., Avici, O. & Röhrle, O., 2016. Towards modelling skeletal muscle growth and adaptation. *PAMM Proceedures of Applied Mathematics and Mechanics,* Volume 16, pp. 921-924.

Ambrosi, D. et al., 2011. Perspectives on Biological Growth and Remodelling. *Journal of Mechanical Phys Solids,* 59(4), pp. 863-883.

Anderson, F. & Pandy, M., 1984. Dynamic Optimization of humnan walking. *Journal of Biomechanical Engineering,* 106(3), pp. 280-282.

Andreassen, S. & Arendt-Nielsen, L., 1987. Muscle fibre conduction velocity in motor units of the human anterior tibial muscle: a new size principle parameter.. *Journal of Physiology,* Volume 391, pp. 561-71.

Arendt-Nielsen, L., Gantchev, N. & Sinkjær, T., 1992. The influence of muscle length on muscle fibre conduction velocity and development of muscle fatigue. *Electroencephalography and Clinical Neurophysiology/Evoked Potentials Section,* 85(3), pp. 166-172.

Armfield, D. et al., 2006. Sports Related muscle Injury in the Lower Extremity. *Clinical Sports Medicine,* Volume 25, pp. 803-842.

Ayachit, U., 2016. *The Paraview Guide; Community Edition - Updated for ParaView version 5.0.* s.l.:Paraview 5.2.0 RC3.

Azizi, E., Halenda, G. M. & Roberts, T. J., 2009. Mechanical properties of the gastrocnemius aponeurosis in wild turkeys. *Journal of Integrative and Comparative Biology,* pp. 51-58.

Azizi, E. & Roberts, T., 2009. Biaxial strain and variable stiffness in aponeuroses. *Journal of Physiology,* p. 4309–4318.

B. Calvo, A. R. A. A. J. G. F. S. R. O. M. M., 2010. Passive nonlinear elastic behaviour of skeletal muscle: Experimental results and model formulation. *Journal of Biomechanics,* 43(2), p. 318–325.

Bajuri, M., Isaksson, H., Eliasson, P. & Thompson, M., 2016. A hyperelastic fibre-reinforced continuum model of healing tendons with distributed collagen fibre orientations. *Biomechanics and modeling in mechanobiology*, 15(6), pp. 1457-1466.

Bajuri, M., Isaksson, H., Eliasson, P. & Thompson, M. S., 2016. A Hyperelastic Fibre-Reinforced Contunuum Model of Healing Tendons with Distributed Collagen Fibre Orientations. *Journal of Biomechanics and Models in Mechanobiology*, pp. 15: 1457 - 1466.

Baker, J. & Matsumoto, D., 1988. Adaptation of skeletal muscle to immobilization in a shortened position. *Muscle Nerve,* 11(3), pp. 231-44.

Baker, J. & Matsumoto, D., 1988. Adaptation of skeletal muscle to immobilization in a shortened position. *Muscle Nerve ,* 11(3), pp. 231-44.

Baker, J. & Matsumoto, D., 1988. Adaptation of skeletal muscle to immobilization in a shortened position. *Muscle Nerve,* 1(3), pp. 231-44.

Balbi, V., Shearer, T. & Parnell, W., 2018. A modified formulation of quasi-linear viscoelasticity for transversely isotropic materials under finite deformation. *Fibre-reinforced Materials,* Issue 39.

Bavel, H. V. et al., 1996. Strain distribution on rat medial gastrocnemius (MG) during passive stretch. *J. Biomech,* 29(8), p. 1069–1074.

Bélaise, C., Michaud, B., Maso, F. D. & Mombaur, K., 2018. Which data should be tracked in forward-dynamic optimisation to best predict muscle forces in a pathological co-contraction case?. *Journal of Biomechanics,* 68(2018).

Bevan, T. et al., 2018. A biomechanical model for fibril recruitment: Evaluation in tendons and arteries. *Journal of biomechanics,* Volume 74, pp. 192-196.

Bianchi, S. et al., 1998. Sonographic Evaluation of Tears of the Gastrocnemius Medial Head ("Tennis Head"). *Journal of Ultrasound Medicine,* Issue 17, pp. 157-162.

Bianchi, S. et al., 1998. Sonographic Evaulation of Tears if the Gastrocnemius Medial Head ("Tennis Leg"). *Journal of Ultrasound in Medicine,* Volume 17, pp. 157-162.

Bihan, D. L. & Breton, E., 1985. Imagerie de diffusion in-vivo par résonance magnétique nucléaire. *C R Acad Sci. 301,* 301(15), pp. 1109-1112.

Bihan, D. L. & Breton, E., 1985. Imagerie de diffusion in-vivo par résonance magnétique nucléaire. *C R Acad Sci,* 301(15), p. 1109–1112..

Blazevich, A., Cannavan, D., Coleman, D. & Horne, S., 2007. Influence of concentric and eccentric resistance training on architectural adaptation in human quadriceps muscles.. *J Appl Physiol (1985),* 103(5), pp. 1565-75.

Blemker, S., 2005. A 3D model of the muscle reveals the causes of nonuniform strains in the biceps brachii. *J. Biomech.*, pp. 657-665.

Blemker, S., 2005. Three-Dimensional Representation of Complex Muscle Architectures and Geometries. *Annals of Biomedical Engineering,* pp. 661-673.

Blemker, S. & Delp, S., 2005. Three-Dimensional Representation of Complex Muscle Architectures and Geometries. *Journal of Analysis of Biomedical Engineering,* 33(5), pp. 661 - 673.

Blemker, S. & Delp, S., 2005. Three-Dimensional Representation of Complex Muscle Architectures and Geometries. *Annals of Biomedical Engineering*, 33(5), pp. 661 - 673.

Blemker, S. S., Pinskya, P. M. & Delp, S. L., 2005. A 3D model of muscle reveals the causes of nonuniform strains in the biceps brachii. *Journal of Biomechanics Award,* pp. 38: 657-665.

Blitz, N. & Eliot, D., 2007. Anatomical Aspects of the Gastrocnemius Aponeurosis and Its Insertion: A Cadaveric Study. *J. Foot Ankle Surg,* 46(2), p. 101–108.

Blitz, N. & Eliot, D., 2008. Anatomical Aspects of the Gastrocnemius Aponeurosis and its Muscular Bound Portion: A Cadaveric Study Part II. *The Journal of Foot and Ankle Surgery ,* 47(6), pp. 533-540.

Blitz, N. & Eliot, D., 2008. Anatomical Aspects of the Gastrocnemius Aponeurosis and its Muscular Bound Portion: A Cadaveric Study-Part II. *J Foot Ankle Surg,* 47(6), p. 533–540.

Blitz, N. & Elliot, D., 2007. Anatomical aspects of the gastrocnemius aponeurosis and its insertion: a cadaveric study. *Journal of Foot and Ankle,* 46(2), pp. 101-108.

Blitz, N. & Rush, S., 2007. The Gastrocnemius Intramuscular Aponeurotic Recession: A Simplified Method of Gastrocnemius Recession. *Journal of Foot and Ankle Surgery,* 46(2).

Boakes, J., Foran, J., Ward, S. & Lieber, R., 2006. Muscle Adaptation by Serial Sarcomere Addition 1 Year after Femoral Lengthening. *Journal of Clinical Orthopaedics and Related Research,* 1(456), pp. 250 - 253.

Boakes, J., Foran, J., Ward, S. & Lieber, R., 2007. Muscle adaptation by serial sarcomere addition 1 year after femoral lengthening. *Clin Orthop Relat Res.* , Volume 456, pp. 250-3.

Boakes, J., Foran, J., Ward, S. & Lieber, R., 2007. Muscle Adaptation by serial sarcomere addition in 1 year after femoral lengthening. *Clinical Orthopeadics and Related Research,* Volume 456, pp. 250-253.

Bol, M., Sturmat, M., Weichert, C. & Kober, C., 2011. A new approach for the validation of skeletal muscle modelling using MRI data. *Computational Mechanics*, 33(5), pp. 591-601.

Böl, M., Sturmat, M., Weichert, C. & Kober, C., 2011. A new approach for the validation of skeletal muscle modelling using MRI data.. *Comput Mech,* 47(5), p. 591-601.

Bolserlee, B., Gandevia, S. & Herbert, R., 2016. U&ltrasound Imaging of the human Medial Gastocnemius muscle: How to otient the transducer so that muscle fascicles lie in the image plane. *Journal of Biomechanics,* 49(7), pp. 1002 - 1008.

Bottinelli, R. & Reggiani, C., 2006. *Skeletal muscle plasticity in health and disease Advances in Muscle Research.* 2 ed. s.l.:Springer.

Boyce, M. & Arruda, E., 2000. Constitutive models of rubber elatsticity: A review. *Stanford University,* pp. 504-522.

Brennan, S., Cresswell, A., Farris, D. & Litchwark, G., 2017. The effect of cadence on the muscle-tendon mechanics of the gastrocnemius muscle during walking. *Scandinavian Journal of Medicine and Science in Sports,* Volume 27, pp. 289-298.

Brockett, C., Morgan, D. & Proske, U., 2001. Human hamstring muscles adapt to eccentric exercise by changing optimum length. *Med Sci Sports Exerc,* 33(5), pp. 783-90.

Brooks, G., Fahey, T. & White, T., 1996. *Exercise Physiology: Human Bioenergetics and Its Applications. (2nd ed.). Mayfield Publishing Co.*. 2nd ed. s.l.:Mayfield Publishing Company.

Burkholder, T., Fingado, B., Baron, S. & Lieber, R., 1994. Relationship between muscle fiber types and sizes and muscle architectural properties in the mouse hindlimb. *Journal of Morphology,* pp. 177-190..

Campbell, E. et al., 2013. Skeletal muscle adaptations to physical inactivity and subsequent retraining in young men. *Biogerontology,* 14(3), pp. 247-59.

Carlos, Q. et al., 2018. Influence of the Musculotendon Dynamics on the Muscle Force-Sharing Problem of the Shoulder—A Fully Inverse Dynamics Approach. *J of Biomech Eng,* 140(7).

Chanaud, C., Pratt, C. & Loeb, G., 1991. Functionally complex muscles of the cat hindlimb. II. Mechanical and architectural heterogenity within the biceps femoris.. *Experimental Brain Research,* 85(2), pp. 257-270.

Chi, S.-W., 2010. Finite Element Modeling Reveals Complex Strain Mechanics in the Aponeuroses of Contracting Skeletal Muscle. *Journal of Biomechanics,* 43(7), pp. 1243 - 1250.

Cibulka, M. et al., 2017. Variation in Medial and Lateral Gastrocnemius Muscle Activity with Foot Position. *Journal of International Sports Physical Therapy,* 12(2), pp. 233-241.

Colliander, E. & Tesch, P., 1990. Effects of eccentric and concentric muscle actions in resistance training. *Acta Physiol. Scand,* 140(1), pp. 31-9.

Craig, G. A. a. A., 2002. *Numerical Analysis and Optimization:An Introduction to Mathematical Modelling and Numerical Simulation.* 1st ed. Oxford: Oxford University Press.

Criscione, J., Douglas, A. & Hunter, W., 2001. Physically based strain invariant set for materials exhibiting transversely isotropic behaviour. *Journal of Mechanics and Physics* , Volume 49, pp. 871-897.

Csapo, R., Maganaris, C., Seynnes, O. & Narici, M., 2010. On muscle, tendon and high heels.. *J Exp Biology. ,* 213(Pt 15), pp. 2582-8..

Cyron, C. & Humphrey, J., 2017. Growth and Remodelling of Load-Bearing Biological Soft Tissues. *Meccanica,* 52(3), pp. 645-664.

Cyron, C., Wilson, J. & Humphrey, J., 2015. *Mechanobiological Stability: a new paradigm to understand growth and remodeling in soft tissue.* Leganés-Madrid, Spain , 9th European Solid Mechanics Conference ESMC 2015.

Dandapani, S., 2014. *Maters Thesis: Reconstruction of the Arterial Bifurcation Prior to Cerebral Aneurysm Formation - A Novel Approach.* Sheffield: University of Sheffield Dissertation Archives.

Delaunay, B., 1934. Sur la sphère vide. *Bulletin de l'Académie des Sciences de l'URSS, Classe des sciences mathématiques et naturelles,* Volume 6, pp. 793-800.

Delgado, G. et al., 2002. Tennis Leg: Clinical US Study of 141 Patients ane Anatomic Investigation of Four Cadavers with MR Imaging and US. *Musculoskeletal Imaging and Radiology,* 224(1).

Delp, S. et al., 2007. Opensim: Open-source software to create and analyze dynamic simulations of movement. *IEEE Transactions on Biomedical Engineering,* 11(54), pp. 1940 - 1950.

Delp, S. & Loan, S., 2000. A computational framework for simulating and analyzing human and animal movement. *Computing in Science and Engineering,* pp. 46-53.

Deyne, P. D., 2002. *Lengthening of muscle during distraction osteogenesis.* s.l.:s.n.

Deyne, P. D. et al., 1999. Muscle regeneration and fiber-type transformation during distraction osteogenesis.. *J Orthop Res.,* 17(4), pp. 560-70.

Dixon, J., 2009. Gastrocnemius vs. Soleus strain: How to differentiate and deal with calf muscle injuries. *Current Revisions in Musculoskeletal Medicine,* Issue 2, pp. 74 - 77.

Dixon, J., 2009. Gastrocnemius vs. Soleus Strain: How to differentiate and deal with Calf Muscle Injuries. *Journal of Current Revisions to Muscluloskeletal Medicine,* 2009(2), pp. 74-77.

Dr. Stephen H. Scott, D. G. E. L., 1995. Mechanical properties of aponeurosis and tendon of the cat soleus muscle during whole-muscle isometric contractions. *Journal of Morphology,* pp. 73-86.

Ehret, A. E., Bol, M. & Itskov, M., 2011. A continuum constitutive model for the active behavour of skeletal muscle. *Journal of the mechanics and Physics of solids,* 59(3), pp. 625-636.

Ellman, R. et al., 2013. Partial Reductions in Mechanical Loading Yield Porportional Changes in Bone Density, Bone Architecture, and Muscle Mass. *Journal of Bone and Mineral Research,* 28(4), pp. 875-885.

Elsalanty, M. et al., 2007. Changes in pennate muscle architecture after gradual tibial lengthening in goats.. *Anat Rec (Hoboken),* Volume 290, p. 461–467.

Farup, J. et al., 2012. Muscle morphological and strength adaptations to endurance vs. resistance training. *J Strength Cond Res.,* 26(2), pp. 398-407.

Flory, P., 1961. Thermodynamic relations for high elastic materials. *Transactions of the Faraday Society ,* Volume 57, pp. 829-838..

Fukunaga, T. et al., 2001. In Vivo behaviour of human muscle tendon during walking. *Proceedinggs of the Royal Society of London B Biological Sciences,* Volume 268, pp. 229-233.

Fung, Y., 1993. Skeletal Muscle. In: *Biomechanics: Mechanical Properties of Living Tissues.* s.l.:Springer-Verlag, p. 568.

GA Holzapfel, T. G. R. O., 2000. A New Constitutive Framework for Arterial Wall Mechanics and a Comparative Study of Material Models. *Journal of elasticity and the physical science of solids,* 61(1), p. 1–48.

Gasser, T., Ogden, R. & Holzapfel, G., 2006. Hyperelastic modelling of arterial layers with distributed collagen fibre orientations. *Journal of the Royal Society Interface,* 3(6), pp. 15-35.

Gilbert, T., Bullis, B. & Griffiths, H., 1996. Tennis calf or tennis leg. *Orthopedics,* Volume 19, pp. 179-184. [Medline].

Giraudo, C. et al., 2018. Normalised STEAM-based diffusion tensor imaging provides a robust assessment of muscle tears in football players:

preliminary results of a new approach to evaluate muscle injuries. *Journal of European Radiology,* 28(312), pp. 1-8.

Go¨ktepe, S., Abilez, J., Parker, K. & Kuhl, E., 2010. A multiscale model for eccentric and concentric cardiac growth through sarcomerogenesis. *J Theor Bio,* Volume 265, p. 433–442.

Goktepe, S., Abilez, O., Parker, K. & Khul, E., 2010. A multiscale model for eccentric and concentric cardiac growth through sarcomerogenesis. *Journal of Theoretical Biology,* 265(3), pp. 433-442.

Goldspink, G., 1999. Changes in muscle mass and phenotype and the expression of autocrine and systemic growth factors by muscle in response to stretch and overload. *J Anat.,* Volume 194, p. 323–334.

Goldspink, G. & Scutt, A., 1992. Gene expression in skeletal muscle in response to stretch and force generation.. *Am J Physiol Integr Comp Physiol,* Volume 262, pp. 356-363.

Goldspink, G. & Scutt, A., 1992. Gene expression in skeletal muscle in response to stretch and force generation.. *Am J Physiol Integr Comp Physiol,* Volume 262, p. R356–R363.

Gordon, A., Huxley, A. & Julian, F., 1966. The Variation in Isometric Tension with Sarcomere Length in Vertebrate Muscle Fibres. *Journal of Physiology,* Volume 184, pp. 170-192.

Gossman, M., Sahrmann, S. & Rose, S., 1982. Review of length-associated changes in muscle. Experimental evidence and clinical implications.. *Phys Ther,* Volume 62, p. 1799–1808.

Grasa, J. et al., 2011. A 3D active-passive numerical skeletal muscle model incorporating initial tissue strains. Validation with experimental results on rat tibialis anterior muscle.. *Biomech Model Mechanobiol.,* pp. 779-87.

Grasa, J. et al., 2011. A 3D active-passive numerical skeletal muscle model incorporating initial tissue strains. Validation with experimental results on rat tibialis anterior muscle. *Biomechanics and Modelling in Mechanobiology,* 10(5), pp. 779-787.

Grieve, D., Pheasant, S. & Cavanagh, P., 1978. Perdiction of Gastrocnemius Length from Knee and Ankle Joint Posture. *Proceedings of the Sixth International Congress of Biomechanics 2A,* pp. 405-412.

Griffin, M. et al., 2004. Patterning, Prestress and Peeling Dynamics of Myocytes. *Biophysical,* 86(2), pp. 1209-1222.

Gunther, M., Schmitt, S. & Wank, V., 2007. High Frequency Oscillations as a consequence of neglected serial damping in hill-type muscle models. *Journal of Biological Cybernetics,* 97(1), pp. 63-79.

Hackett, R., 2018. Hyperelasticity Primer. In: *Strain Energy Functions.* s.l.:Springer, pp. 19-28.

Hackney, K. & Ploutz-Snyder, L., 2012. Unilateral lower limb suspension: integrative physiological knowledge from the past 20 years (1991-2011). *Eur J Appl Physiol,* 112(1), pp. 9-22.

Haeufle, D., Gunther, M., Bayer, A. & Schmitt, S., 2014. Hill-Type muscle model with serial damping and eccentric force-velocuty relation. *Journal of Biomechanics,* 47(6), pp. 1531-1536.

Hamedzadeh, A., Gasser, T. & Federico, S., 2018. On the constitutive modelling of recruitment and damage of collagen fibresin soft biological tissues. *European ourna of Mechanics / A Solids,* Volume 72, pp. 483 - 496.

Hamilton, N. & Luttgens, K., 2001. *Kinesiology: Scientific Basis of Human Motion.* 10th ed. s.l.: McGraw-Hill.

Handsfield, G. G. et al., 2017. A 3D model of the Achilles tendon to determine the mechanisms underlying nonuniform tendon displacements. *Journal of Biomechanics*, pp. 17 - 25.

Heidlauf, T. & Roehrle, O., 2015. A Multiscale chemo-electro-mechanical skeletal muscle model to analyze muscle contraction and force generation for different muscle fiber arrangements. *Frontiers in Physiology*, Volume 5, p. 498.

Heidlauf, T. & Röhrle, O., 2014. A multiscale chemo-electro-mechanical skeletal muscle model to analyze muscle contraction and force generation for different muscle fiber arrangements. *Frontiers in physiology*, 5(498).

Henneman, E. & Olson, C., 1965. Relations between structure and function on the design of skeletal muscles. *Journal of Neurophysiology*, pp. 581-598.

Henneman, E., Somjen, G. & Carpenter, D., 1965. Functional significance of cell size in spinal motoneurons. *Journal of Neurophysiology*, pp. 560-580.

Herchenhan, A. et al., 2011. Tenocyte contraction induces crimp formation in tendon-like tissue". *Biomechanics and Modeling in Mechanobiology*, pp. 11 (3-4): 449–459.

Herrmann, L., 1976. Laplacian-isoparametric grid generation scheme. *Journal of the Engineering Mechanics Division, ,* 102(5), p. 749–756.

Heslinga, J., G, G. t. K. & Huijing, P., 1995. Growth and immobilization effects on sarcomeres: a comparison between gastrocnemius and soleus muscles of the adult rat. *Eur J Appl Physiol Occup Physiol. ,* 70(1), pp. 49-57.

Heslinga, J., Kronnie, G. t. & Huijing, P., 1995. Growth and immobilization effects on sarcomeres: a comparison between gastrocnemius

and soleus muscles of the adult rat. *Eur J Appl Physiol Occup Physiol. ,* 70(1), pp. 49-57.

Hill, A., 1938. The Heat of Shortening and they Dynamic Constants of Muscle. *Section of Biophysics, Department of Physiology,* Volume 612.745, pp. 136-195.

Hoang, P., Herbert, R. & Gandevia, S., 2007. Effects of eccentric exercise on passive mechanical properties of human gastrocnemius in vivo.. *Med Sci Sports Exerc,* 39(5), pp. 849-57.

Hobara, H., Kato, E., Kobayashi, Y. & Ogata, T., 2012. Sex differences in relationship between passive ankle stiffness and leg stiffness during hopping. *Journal of Biomechanics,* 45(16), pp. 2750-2754.

Holak, K. et al., 2015. The use of digital image correlation in the study of the achilles tendon strain field. *Mechanics and Control,* 34(1).

Holzapfel, G. A., Gasser, T. C. & Ogden, R. W., 2000. A New Constitutive Framework for Arterial Wall Mechanics and a Comparative Study of Material Models. *Journal of Elasticity and the Physical Science of Solids,* pp. 61 (1): 1 - 48.

Holzapfel, G., Gasser, T. & Ogden, R., 2000. A New Constitutive Framework for Arterial Wall Mechanics an a Comparitive Study of Material Models. *Journal of Elasticity and the Physical Science of Solids,* 61(1-3), pp. 1-48.

Holzapfel, G., Gasser, T. & Ogden, R., 2000. A New Constitutive Framework for arterial wall mechanics and a comparative study of material models. *Journal of Elasticity,* Volume 61, pp. 1-48.

Holzapfel, G. et al., 2015. Modelling non-symmetric collagen fibre dispersion in arterial walls. *The Royal Society Interface,* 12(106).

Holzapfel, G. & Ogden, R., 2009. OnPlanar Biaxial Tests for Anisotropic non-linearly elastic solids. A continuum mechanical framework. *Mathematics and Mechanics of Solids*, Volume 14, pp. 474-489.

Horvat, N. et al., 2019. A finite element implementation of a growth and remodeling model for soft biological tissues: Verification and application to abdominal aortic aneurysms. *Computer Methods in Applied Mechanics and Engineering*, 352(1), pp. 586 - 605.

Huang, L., Korhonen, R., Turunen, M. & Finnila, M., 2019. Experimental mechanical strain measurement of tissues. *Peer J*, Volume 7.

Humphrey, J., 1999. Remodeling of a Collagenous Tissue at Fixed Lengths. *Journal of Biomedical Engineering*, 121(6), pp. 591-597.

Humphrey, J., 2013. *Cardiovascular solid mechanics: Cells, Tissues and Organs.* 1 ed. s.l.:Springer.

Humphrey, J., Dufresne, E. & Schwartz, M., 2014. Mechanotransduction and extracellular matrix homeostasis. *Nat Rev Mol Cell Biol*, 15(12), pp. 802-12.

Humphrey, J., Strumph, R. & Yin, F., 1990. Deterimnation of a constitutive relation for massive myocardium, I. A new functional form. *ASME Journal of Biomechanics and Engineering*, Volume 15, pp. 333-339.

Humphrey, J. & Yin, F., 1987. On constitutive relations and finite deformations of passive cardiac tissue: 1. A pseudostrain-energy function.. *Journal of Biomechanical Engineering*, Volume 109, pp. 298-304..

Humphrey, J. & Yin, F., 1989. Constitutive relations and finite defromations of passive cardiac tissue II: Stress analysis in the left ventricle. *Circulation Research*, 65(3), pp. 805-817.

Janmey, P. et al., 2006. Negative normal stress in semiflexible biopolymer gels. *Nature Materials,* Volume 6, pp. 48-51.

JD Humphrey, K. R., 2002. A constrained mixture model for growth and remodeling of soft tissues. *Math. Models Methods Appl. Sci,* Volume 12, p. 407–430.

JH Poynting, R.-p., n.d. *Philosophical Magazine,* 9(1905), pp. 393-406.

Johnson, T. & Klueber, K., 1991. Skeletal muscle following tonic overload: functional and structural analysis. *Med Sci Sports Exerc,* 23(1), pp. 49-55.

Jozsa, L. a. K. P., 1997. *Human Tendons: Anatomy Physiology, and Pathology. Human Kinetics.* Champaign Illinois: s.n.

Kainz, H. et al., 2017. Effects of hip joint cedntre mislocation on gait kinematics of children with cerebral palsy calculated using patient-specific direct and inverse kinematic models. *Journal of Gait and Posture,* Volume 57, pp. 154-160.

Kalkman, B. et al., 2018. Muscle and tendon lengthening behaviour of the medial gastrocnemius during ankle joint rotation in children with cerebral palsy. *Experimental Physiology,* 103(10), pp. 1367-1376.

Karakuzua, A. et al., 2017. Magnetic resonance and diffusion tensor imaging analyses indicate heterogeneous strains along human medial gastrocnemius fascicles caused by submaximal plantar-flexion activity. *Journal of Biomechanics,* pp. 54: 69-78.

Kawakami, Y., Kanehisa, H. & Fukunaga, T., 2008. The Relationship Between Passive Ankle Plantar Flexion Joint Torque and Gasrocnemius Muscle and Tendon Stiffness: Implications for Flexibility. *Journal of Orthopaedic & Sports Physical Therapy,* 38(5), pp. 269-276.

Kawakami, Y. et al., 2002. In Vivo muscle fibre behaviour during counter-movement excersise in humans reveals a significant role for tendon elasticity. *Journal of Physiology,* Volume 540, pp. 635-646.

Kinugasa, R., Yamamura, N., Sinha, S. & Takagi, S., 2016. Influence of intramuscular fiber orientation on the Achilles tendon curvature using three-dimensional finite element modeling of contracting skeletal muscle. *J. Biomechanics,* 49(14), pp. 3592–3595,.

Kjaer, M., 2004. Role of extracellular matrix in adaptation of tendon and skeletal muscle to mechanical loading. *Physiol Rev,* 84(2), pp. 649-98.

Kohout, J. & Clapworthy, G., 2012. *Morphable Muscluloskeletal Model, VPHOP - Technology to fight Osteoporosis,* s.l.: 7th Framework Programme; Work Package 10: Morphable Musculoskeletal Model.

Kojic, M., Mijailovic, S. & Zdravkovic, N., 1998. Modeling of muscle behavior by the finite element method using Hill's three-element model. *International Journal for numerical methods in engineering* , Volume 43, pp. 941-953..

Koulouri, G. et al., 2007. Magnetic resonance imaging findings of injuries to the calf muscle complex.. *Skeletal Radiolog,* 36(10), pp. 921-7..

Kuhl, E., 2014. Growing matter: a review of growth in living systems.. *J Mech Behav Biomed Mater.,* Volume 29, pp. 529-43.

Kupczik, K. et al., 2015. Reconstruciton of muscle fascicle architecture from iodine-enhanced microct images: A combined texture mapping and stremline approach. *Journal of Theoretical Biology,* Volume 382, pp. 34-43.

Lanir, Y., 2015. Mechanistic micro-structural theory of soft tissues growth and remodelling: Tissues with Unidirectional fibers. *Biomechanical modelling and Mechanobiology*, Volume 14, pp. 245-266.

Latorre, M. & Humphrey, J., 2018. Critical Roles of Time-Scales in Soft Tissue Growth and Remodeling. *APL Bioengineering,* 2(2).

Latorre, M., Mohammadkhah, M., Simms, C. & Montans, F., 2018. A Continuum model for tension-compression assymetry in skeletal muscle. *Journal of the Mechanical Behaviour of Biomedical Materials,* Volume 77, pp. 455-460.

Levenberg, K., 1944. A Method for the Solution of Certain Problems in Least Squares. *Quart. Applied Mathematics,* Volume 2, pp. 164-168.

Lichtwark, G., Bougoulias, K. & Wilson, A., 2007. Muscle Fascicle and Series Elastic Element Length Changes Along the Length of the Human Gastrocnemius During Walking and Running. *Journal of Biomechanics,* Volume 40, pp. 157-164.

Lieber, R. & Blevins, F., 1987. Skeletal muscle architecture of the rabbit hindlmix functional implications of muscle design. *Journal of morphology,,* pp. pp. 93-101,.

Lieber, R. & Bodine-Fowler, S., 1992. Skeletal Muscle mechanics: Implications for Rehabilitation. *Journal of Physical Therapy ,* pp. 844-856.

Lieber, R. & Friden, J., 2000. Functional and Clinical Significance of Skeletal Muscle Architecture. *Journal of Muscle and Nerves,* pp. 23(11): 1647 - 66.

Lieber, R. & Fridén, J., 2000. Functional and clinical significance of skeletal muscle architecture. *Muscle Nerve,* 23(11), pp. 1647-66.

Lieber, R. & Friden, J., 2002. "Functional and clinical significance of skeletal muscle architecture". *Muscle & Nerve,* Volume 23, p. 1647–1666.

Lieber, R. et al., 2018. Skeletal Mucle Mechanics, Energetics and Plasticity. *Journal of NeuroEngineering and Rehabilitation*, 14(108).

Limbert, G. & Taylor, M., 2002. On the constitytive modelling of biological soft connective tissues: A general theoretical framework and explicity forms of the tensors of elasticity for strongly anisotropic continuum fibre-reinforced composites at finite strain.. *International Journal of Solids and Structures*, 8(39), pp. 2343-2358.

Lindsey CA, M. M. S. S. B. J. B. P. C. A. W. R. S. M., 2002. The effect of the amount of limb lengthening on skeletal muscle. *Clin Orthop Relat Res,* Volume 402, pp. 278-87.

Lindsey, C. et al., 2002. The effect of the amount of limb lengthening on skeletal muscle. *Clin Orthop Relat Res,* Issue 402, pp. 278-87.

Lin, T. W., Cardenas, L. & Soslowsky, L. J., 2004. Biomechanics of tendon injury and repair.. *Journal of Biomechanics.* , p. 37 (6): 865–877..

Lopez, D. & Kramer, C., 2019. Acute Myocardial Infarction: Ventricular Remodeling. *Jounral of Cariovascular Magnetic Resonance,* Issue 4, pp. 251 - 261.

Lu, Y., 2011. *Soft Tissue Modelling and facial movement simulation using the finite element method.* Cardiff: Schools of Engineering and Dentistry.

Mahon, T., 1984. Fundamental muscle mechanics. In: *In muscles, reflexes and Locomotion.* Princeton, New Jersey: Princeton University Press, pp. 11, Fig 1.7.

Makarov, M., Birch, J. & Samchukov, M., 2009. The role of variable muscle adaptation to limb lengthening in the development of joint contractures: an experimental study in the goat. *Journal of Pediatrics and Orthopeadics,* Volume 29, p. 175–181.

Marey, E., 1874. *Animal MechanismsL A treatise on Terrestrial and Aerial Locomotion.* New York: Appleton.

Markert, B., Ehlers, W. & Karajan, N., 2005. A general polyconvex strain energy function for fiber reinforced materials. *Proceedings in Applied mathematics and mechanics,* 5(1), pp. 245-246.

McMaster, P., 1923. Tendon and Muscle Ruptures: Clinical and experimental studies on the causes and location of subcutaneous ruptures. *Journal of Bones and Journal of Surgery,* Volume 15, p. 705.

McMillan, A., Shi, D., Pratt, S. & Lovering, R., 2011. Diffusion Tensor MRI to Assess Damage in Healthy and Dystrophic Skeletal Muscle after Lengthening Contractions. *J Biomed Biotechnology,* 10(1155), pp. 1-10.

McPhedran, A., Wuerker, R. & Henneman, E., 1965. Properties of Motor Units in a homogeneous red muscle (soleus) of the cat. *Journal of Neurophysiology,* pp. 71-84.

Menzel, A., 2005. Modelling of anisotropic growth in biological tissues - A new approach and computational aspects. *Biomech Model Mechanobiol,* Volume 3, p. 147–171.

Merboldt, K., Hanicke, W. & Frahm, J., 1985. Self-diffusion NMR imaging using stimulated echoes. *Journal of Magnetic Resonance,* 64(3), pp. 479-486.

Merboldt, K., Hanicke, W. & Frahm, J., 1985. Self-diffusion NMR imaging using stimulated echoes. *Journal of Magnetic Resonance,* 64(3), p. 479–486. .

Mihai, L. & A Goriely, 2011. Positive or negative Poynting effect? The role of adscititious inequalities in hyperelastic materials. *Proceedings of the Royal Society A* , Volume 467, pp. 3633-3646.

Mihai, L. & Goriely, A., 2013. Numerical simulation of shear and the Poynting effects by the finite element method: An application of the generalised empirical inequalities in nonlinear elasticity. *International Journal of Non-Linear Mechanics* , Volume 49, pp. 1-1.

Miller, W., 1977. Rupture of the musculotendinous juncture f the medial head gastrocnemius muscle.. *AM Journal of Sports Medicine,* 5(191).

Mithraratne, M. A., Herbert, R. D. & Fernandez, J., 2017. A 3D Ultrasound Informed Model of the Human Gastrocnemius Muscle. *BIVPCS 2017, POCUS Imaging for Patient-Customized Simulations and Systems for Point-of-Care Ultrasound,* pp. 27-34.

Monti, R., Roy, R. & Edgerton, V., 2001. Role of motor unit structure in defining function.. *Muscle Nerve,* Volume 24, p. 848–866.

Mordhorst, M., Heidlauf, T. & Röhrle, O., 2015. Predicting electromyographic signals under realistic conditions using a multiscale chemo–electro–mechanical finite element model. *Interface focus,* 5(2).

Nakagawa, Y., 1989. Effect of disuse on the ultra structure of the Achilles tendon in rats. *European Journal of Applied Physiology.* , p. 59: 239–242.

Namani, R. & Bayly, P., 2010. Shear wave propagation in anisotropic soft tissues and gels. *Conference Proceesings IEEE Eng. Med. Biol Society,* pp. 1117-1122.

Narici, M. & Maganaris, C., 2007 . Plasticity of the muscle-tendon complex with disuse and aging.. *Exerc Sport Sci Rev,* 35(3), pp. 126-34.

Neal M. Blitz, F. a. D. J. E., 2007. Anatomical Aspects of the Gastrocnemius Aponeurosis and Its Insertion: A Cadaveric Study. *The Journal of Foot and Ankle Surgery,* pp. 46(2) 101-108.

Nordez, A., Casari, P., JP, J. M. & Cornu, C., 2009. Modeling of the passive mechanical properties of the musculoarticular complex: acute effects of cyclic and static stretching.. *J Biomech*, Volume 42, p. 767–773.

O Roerhle, J. D. & Pullan, A., 2012. A Physiolgically based, multi-scale model of skeletal muscle structure and function. *Frontiers of Physiology*, 3(358).

Oliveira, L. F. d., Peixinho, C. C., Silva, G. A. & Menegaldo, L. L., 2016. In vivo passive mechanical properties estimation of Achilles tendon using ultrasound. *Journal of Biomechanics*, pp. 507 - 513.

Pamuk, U. et al., 2016. Combined magnetic resonance and diffusion tensor imaging analyses provide a powerful tool for in vivo assessment of deformation along human muscle fibers. *J. Mech. Behav. Biomed. Materials*, pp. 63: 207-219.

Patterson, J. & Watton, P., 2018. *A Biomechanical Model for Muscle-Aponeurosis-Tendon Complex*, Sheffield, UK: University of Sheffield, Whiterose.

Pinney, S., Sangeorzan, B. & Hansen, S., 2004. Surgical Anatomy of the Gastrocnemius Recession (Strayer Procedure). *Foot Ankle Int*, 25(4), p. 247–250.

Pollard, T. & Korn, E., 1973. "Acanthamoeba myosin. I. Isolation from Acanthamoeba castellanii of an enzyme similar to muscle myosin". *The Journal of Biological Chemistry. ,* 248(13), p. 4682–90.

Pomarino, D., Llamas, J., Martin, S. & Pomarino, A., 2017. Literature Review of Idiopathic Toe Walking - Etiology, Prevalence, Classification and Treatment. *Journal of Foot and Ankle Specialist*, 10(4), pp. 337-342.

Pontén, E. & Fridén, J., 2008. Immobilization of the rabbit tibialis anterior muscle in a lengthened position causes addition of sarcomeres in series and extra-cellular matrix proliferation. *J Biomech.,* Volume 41, pp. 1801-1804.

Pontén, E. & Fridén, J., 2008. Immobilization of the rabbit tibialis anterior muscle in a lengthened position causes addition of sarcomeres in series and extra-cellular matrix proliferation. *J Biomechanical Modelling,* Volume 41, p. 1801–1804.

Poynting, J., 1909. On pressure perpendicular to the shear-planes in finite pure shears, and on the lengthening of loaded wires when twisted. *Proceedings of the Royal Society A ,* Volume 82, pp. 546-559.

P, P. D. D., 2002. Lengthening of muscle during distraction osteogenesis. *Clin Orthop Relat Res,* Volume 403S.

Prakash, A. et al., 2017. Connective Tissue Injury in Calf Muscle Tears and Return to Play: MRI Correlation. *British Journal of Sports Medicine,* Issue 2017.

Proske, U. & Morgan, D., 1984. Stiffness of Cat Soleus Muscle and Tendon During Activation of Part of Muscle. *Hournal of Neurophysiology,* 52(3).

Public Health England, N., 2018. *State of Musculoskeletal Health,* s.l.: Public Health England, Arthritis Research UK.

R Csapo, C. M. O. S. M. N., 2010. On muscle, tendon and high heels. *J Exp Biol,* 213(15), pp. 2582-8.

R Lynn, D. M., 1994. Decline running produces more sarcomeres in rat vastus intermedius muscle fibers than does incline running. *J Appl Physiol 1994,* 77(3), pp. 439-44.

Reeves, N., 2005. Influence of 90-day simulated micro-gravity on human tendon mechanical properties and the effect of restiveness countermeasures. *Applied Physiology.*, p. 98 (6): 2278–2286.

Rehorna, M. R. & Silvia S. Blemker, 2010. THE EFFECTS OF APONEUROSIS GEOMETRY ON STRAIN INJURY SUSCEPTIBILITY EXPLORED WITH A 3D MUSCLE MODEL. *J Biomech. 17; 43(13),* p. 2574–2581.

Rehorn, M. & Blemker, S., 2010. The effects of aponeurosis geometry on strain injury susceptibility explored with a 3D muscle model. *Journal of Biomechanics,* 43(13), p. 2574–2581.

Reid, D. & Mcnair, P., 2004. Passive Force, Angle, and Stiffness Changes after Stretching of Hamstring Muscles. *Med Sci Sport Exerc.,* Volume 36, p. 1944–1948.

Roberts, E. A. a. T. J., 2009. Biaxial strain and variable stiffness in aponeuroses. *Journal of Physiology*, pp. 4309 - 4318.

Rodriguez, E., Hodger, A. & McCulloch, A., 1994. Stress-Dependant finite growth in soft elastic tissues. *Journal of Biomechanics,* 27(4), pp. 455-467.

Rodriguez, E., Hoger, A. & McCulloch, A., 1994. Stress-Dependant Finite Growth in Soft Elastic Tissues. *Journal of Biomechanics,* 27(4), pp. 455-467.

Roehrle, O., Davidson, J. & Pullan, A., 2012. A Physiologically based, multi-scale model of skeletal muscle structure and function. *Frontiers in Physiology.*

Roehrle, O. & Pullan, A., 2007. Three-Dimensional Finite Element modelling of muscle forces during mastication. *Journal of Biomechanics*, 40(15), pp. 3363 - 3372.

Roerhle, O., 2018. *Multiscale Modelling of Skeletal Muscles.* Sheffield, UK, SoftMech, MultiSim Joint Event.

Roerhle, O., Davidson, J. & Pullan, A., 2008. Bridging scales: a three dimensional electromechanical finite element model of skeletal muscle. *SIAM Journal on Scientific Computing*, 30(6), pp. 2882-2904.

Roerhle, O. & Pullan, A., 2007. Three-dimensional finite element modelling of muscle forces during mastication. *Journal of Biomechanics*, 40(15), pp. 3363-3372.

Roger, E. & Pearson, G., 2013. "The motor unit and muscle action". In: A. J. Hudspeth, ed. *Principles of Neural Science.* New York: NY: McGraw-Hill Medical. .

Röhrle, O., Davidson, J. & Pullan, A., 2007. Bridging scales: a three-dimensional electromechanical finite element model of skeletal muscle. *Journal of Computer Science*, Issue 30, p. 2882–2904.

Rohrle, O., Davidson, J. & Pullan, A., 2012. A Physiologically based multi-scale model of skeletal muscle structure and function. *Frontiers in Phusiology*, 3(358), pp. 1-14.

Rohrle, O. & Pullan, A., 2007. Three dimensional finite element modelling of muscle forces during mastication. *Journal of Biomechanics*, pp. 3363-3372.

Röhrle, O. & Pullan, A., 2007. Three-dimensional finite element modelling of muscle forces during mastication. *J Biomech*, 40(15), p. 3363-3372.

Röhrle, O., Sprenger, M. & Schmitt, S., 2017. A two-muscle, continuum-mechanical forward simulation of the upper limb. *Biomechanics and modeling in mechanobiology,* 16(3), pp. 743-762.

Rupp, T. et al., 2015. A forward dynamics simulation of human lumbar spine flexion predicting the load sharing of inverterbral discs, ligaments and muscles.. *Biomechanics and Modelling in Mechanobiology,* 14(5), pp. 1081-1105.

Severance, H. & III, F. B., 1982. Rupture of the plantaris: does it exist?. *J Bone Joint Surg Am,* Volume 64, pp. 1387-1388..

Seynnes, O., M, M. d. B. & Narici, M., 2007. Early skeletal muscle hypertrophy and architectural changes in response to high-intensity resistance training. *J Appl Physiol (1985),* 102(1), pp. 368-73.

Shearer, T., 2015. A New Strain Energy Function for Modelling Ligaments and Tendons whose fascicles have a helical arrangement of Fibrils. *Journal of Biomechanics,* 48(12), pp. 3017-3025.

Shepard, D., 1968. *A two-dimensional interpolation function for irrelgularly-spaced data*. s.l., Proceedings of the 1968 ACM National Conference, pp. 517-524.

Siebert, T. et al., 2008. Nonlinearities make a difference: Comparison of two common hill-type models with real muscle. *Biological Cyberneetics,* 98(2), pp. 133-143.

Siebert, T., Stutzig, N. & Rode, C., 2018. A hill-type muscle model expansion accounting for effects of varying transverse muscle load. *Journal of Biomechanics,* 66(2018), pp. 57-62.

Simo, J. & Taylor, R., 1991. Quasi-incompressible finite elasticity in principal stretches: Continuum basis and numerical examples. *Computational Methods of Applied Mechanical Engineering,* Volume 51, pp. 273-310.

Simpson, A. & lengthening., P. W. T. r. o. m. t. l., 1995. *J Bone Jt Surg,* Volume 77, pp. 630-636.

Simpson, A. & Williams, P., 1995. The response of muscle to leg lengthening. *J Bone Jt Surg,* Volume 77, p. 630–636.

Sopher, R., 2017. *Loading and Joint Replacement of the Knee,* London: Imperial College.

Sorkine, O. et al., 2004. *"Laplacian Surface Editing". Proceedings of the 2004 Eurographics/ACM SIGGRAPH Symposium on Geometry Processing.* France, SGP '04 ACME, p. 175–184..

Spencer, A., 1984. *Continuum theory of the mechanics of fibre-reinforces composites.* New York: Springer-Verlag.

Stojanovic, B. et al., 2006. An extension oHill's three-component model to include different fibre types in finite element modelling of muscle.. *International Journal for Numerical Methods in Engineering ,* 7(71).

Tabary, J., Tabary, C. & Tardieu, C., 1972. Physiological and structural changes in the cat's soleus muscle due to immobilization at different lengths by plaster casts. *J Physiol ,* Volume 224, p. 231–244..

Tabary, J., Tabary, C. & Tardieu, C., 1972. Physiological and structural changes in the cat's soleus muscle due to immobilization at different lengths by plaster casts. *J Physiology,* Volume 224, p. 231–244.

Taber, L., 1998. Biomechanical growth laws for muscle tissue.. *J Theor Biol,* 193(2), pp. 201-13.

Tang, C., Stojanovic, B., Tsui, C. & Kojic, M., 2005. Modeling of muscle fatigue using Hill's model. *Bio-Medical Materials and Engineering* , Volume 15, pp. 341-348..

Tang, C., Tsui, C., Stojanovic, B. & Kojic., M., 2007. Finite element modelling of skeletal muscle coupled with fatigue. *International Journal of Mechanical Sciences*, Volume 49, pp. 1179-1191..

Tardieu, C., Tabary, J., Tabary, C. & Tardieu, G., 1982. Tardieu C, Tabary JC, Tabary C, Tardieu G. Adaptation of connective tissue length to immobilization in the lengthened and shortened positions in cat soleus muscle.. *J Physiol (Paris);* , Volume 78, p. 78:214–220.

Taylor, D. & Bushell, M., 1985. The spatial mapping of translational diffusion coefficients by the NMR imaging technique. *Physics in Medicine and Biology*, 30(4), pp. 345-349.

Thorpe C.T., B. H. C. P. S. H., 2013. The role of the non-collagenous matrix in tendon. *Int J ExpPathol.*, pp. 94;4: 248-59..

Toumi, H. et al., 2016. Implications of the calf musculature and Achilles tendon architectures for understanding the site of injury. *Journal of Biomechanics.*

Trappe, S., 2002. Effects of spaceflight, simulated spaceflight and countermeasures on single muscle fiber physiology. *J Gravit Physiol*, 9(1), pp. 323-6.

Truesdell, C., 1952. A Programme of Physical Research in Classical Mechanics. *Zeitschrift f ur Angewandte Mathematik und Physik*, Volume 3, pp. 79-95.

Tsamis, A. et al., 2012. Kinematics of cardiac growth - In vivo characterization of growth tensors and strains.. *Journal of Mechanical Behaviour in Biomedicine,* Volume 8, pp. 165-177.

Valentin, J., Sprenger, M., Pfluger, D. & Roehrle, O., 2018. Gradient-based optimization with B-splines on sparse grids for solving forward-dynamics simullations fo three-dimensional, continuum-mechanical muculoskeletal system models. *Journal for Numerical Methods in Biomedical Engneering,* Issue 02965.

Valentin, J., Sprenger, M., Pflüger, D. & Röhrle, O., 2018. Gradient-based optimization with B-splines on sparse grids for solving forward-dynamics simulations of three-dimensional, continuum-mechanical musculoskeletal system models. *International J Numerical Methods in Biomedical Engineering,* 34(5).

Viceconti, M. et al., 2007. Towards the Multiscale Modelling of the Muculoskeletal System. In: Y. G. a. M. Cerrolaza, ed. *Bioengineering Modeling and Computer Simulation.* Spain: CIMNE, Barcelona, Spain, pp. 1-13.

Watkins, C., 2007. 4.8 The Centroid of a Tetrahedron. In: *From Advanced Engineering Mathematics: A Computer Approach, Seventh Edition.* s.l.:s.n.

Watton, P., Hill, N. & Heil, M., 2004. A mathematical model for the growth of the abdominal aortic aneurysm. *Biomechanics and modeling in mechanobiology,* 3(2), pp. 98-113.

Watton, P., Ventikos, Y. & Holzapfel, G., 2009. Modelling the mechanical response of elastin for arterial tissue. *Journal of biomechanics,* 42(9), pp. 1320-1325.

Weerapong, et al., 2004. Stretching: Mechanisms and Benefits for Sports Performance and Injury Prevention". *Physical Therapy Reviews,* 9(4), pp. 189-206.

Weiss, A., Maker, B. & Govindjee, S., 1996. Finite Element Implementation of Incompressible, Transversely Isotropic Hyperelasticity. *Computational Methods in Applied Mechanical Engineering,* Volume 135, pp. 107-128.

Weiss, J. & Gardiner, J., 2001. Computational modeling of ligament mechanics.. *Critical Reviews Biomedical Engineering 303–371,* Volume 29, pp. 303-371.

Weiss, J. M. B. a. G. S., 1996. Finite element implementation of incompressible, transversely isotropic hyperelasticity.. *Computer Methods in Applied Mechanics and Engineering,* Volume 135, pp. 107-128..

Wellcome Trust, N. M. R. C., 2017. *Medical Research: Whats it worth? A breifing on the economic benefits of musculoskeletal disease research in the UK,* London: Wellcome Trust.

Whitting, J., Steele, J., McGhee, D. & Munro, B., 2013. Passive dorsiflexion stiffness is poorly correlated with passive dorsiflexion range of motion. *Journal of Science and Medicine in Sport,* 16(2), pp. 157-161.

WHO, W. H. O., February 2018. *Musculoskeletal Condition: Global Burden of Disease,* s.l.: WHO.

Widmaier, E., Raff, H. & Strang, K., 2010. Muscle. In: *Vander's Human Physiology: The Mechanisms of Body Function.* 12th ed. New York: NY: McGraw-Hill., pp. 250 - 291.

Willert, et al., 2001. *Taber's Cyclopedic Medical Dictionary.* 19 Illustrated in Full Color ed. Philadelphia: FA Davis Co..

Williams, P. & Goldspink, G., 1971. Longitudinal growth of striated muscle fibres.. *J Cell Sci.,* Volume 9, p. 751–767.

Williams, P. & Goldspink, G., 1973. The effect of immobilization on the longitudinal growth of striated muscle fibres.. *J Anatomy,* Volume 116, p. 45–55.

Williams, P. & Goldspink, G., 1978. Changes in sarcomere length and physiological properties in immobilized muscle.. *J Anatomy,* Volume 127, p. 459–468.

Williams, P. & Goldspink, G., 1984. Connective tissue changes in immobilised muscle. *Journal of Anatomy,* Volume 138, p. 343–350.

Williams, P. et al., 1998. The morphological basis of increased stiffness of rabbit tibialis anterior muscles during surgical limb lengthening. *J Anatomy,* Volume 193, p. 131–138.

Williams, P. et al., 1998. The morphological basis of increased stiffness of rabbit tibialis anterior muscles during surgical limb lengthening. *J Anat,* Volume 193, pp. 131-138.

Williams, P. et al., 1998. The morphological basis of increased stiffness of rabbit tibialis anterior muscles during surgical limb lengthening. *J Anatomy,* Volume 193, p. 131–138.

Wisdom, K., Delp, S. & Khul, E., 2015. Review. Use it or lose it: Multiscale skeletal muscle adaptation to mechanical stimuli. *Journal of Biomechanical Modelling and Mechanobiology,* 14(2), pp. 195-215.

World Health Organisation, W., 2013. *Predictions 2015 - 2030, Global Burden of Diseases Projections.* [Online] Available at:

http://www.who.int/healthinfo/global_burden_disease/projections/en/ [Accessed 30 June 2015].

Wren, T., 2003. A computational model for the adaptation of muscle and tendon length to average muscle length and minimum tendon strain.. *J Biomech. 2003,* 36(8), pp. 1117-24.

Yasuda, N. et al., 2005. Sex-based differences in skeletal muscle function and morphology with short-term limb immobilization.J Appl Physiol (1985). 2005 Sep. *J Appl Physiol,* 99(3), pp. 1085-92.

York Health Economics, N., 2017. *The cost of Arthritis, Calculation conducted on behalf of Arthritis Research UK,* s.l.: Public Health UK.

Zajac, F., 1989. Muscle and Tendon: Properties, Models, Scaling and Application to Biomechanics and Motor Control. *Critical Reivews in Biomedical Engineering,* 17(4), pp. 359-411.

Zollner, A., Abilez, O., Bol, M. & Khul, E., 2012. Stretching Skeletal Muscle: Chronic Muscle Lengthening through Sarcomerogenesis. *PLos One,* 7(10).

Zöllner, A., Abilez, O., Böl, M. & Kuhl, E., 2012. Stretching skeletal muscle: chronic muscle lengthening through sarcomerogenesis. *PLoS One.* , 7(10).

Zollner, A. et al., 2015. On high heels and short muscles: A multiscale model for sarcomere loss in the gastrocnemius muscle. *Journal of Theoretical Biology,* 21(365), pp. 301 - 310.

Zöllner, A. et al., 2015. On high heels and short muscles: A multiscale model for sarcomere loss in the gastrocnemius muscle. *Journal of Theoretical Biology,* Volume 365, pp. 301-310.

Appendix A

The material properties, which were defined according to the mesh and geometry of the muscle (Chapter 6) were one of the inputs for the model. Other inputs included; the boundary conditions (simple uniaxial tension) remodelling and degradation conditions (Equation **7.83**) and the remodelling response (updated k_2 and k2m values run through an updated numerical analysis). These various components were orchestrated by a Perl script, and upon a remodelling simulation, a new structural analysis was carried out.

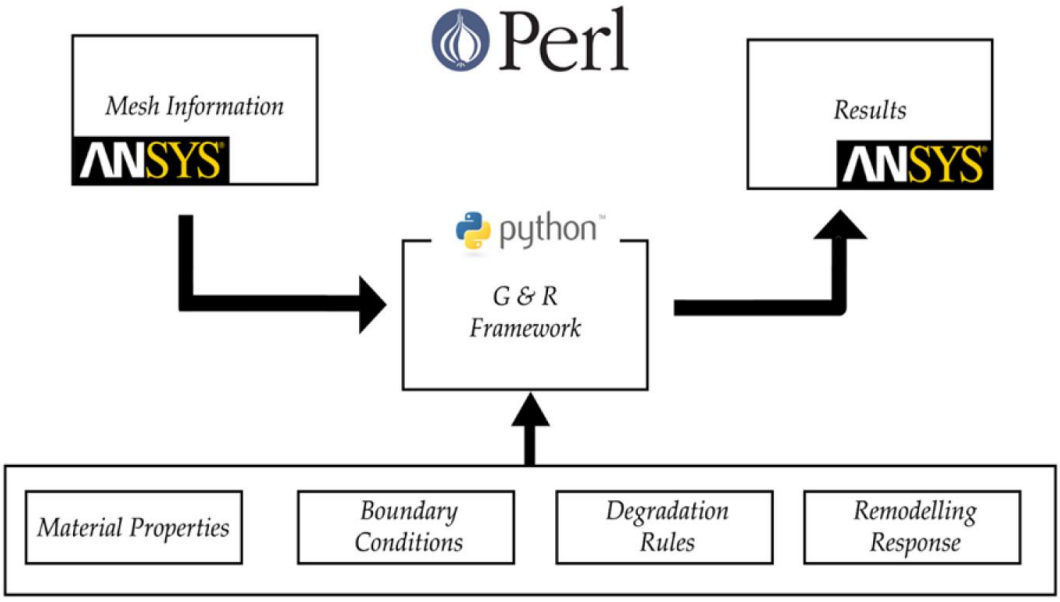

Orchestrating Perl Script used in this thesis augmented from (Dandapani, 2018):

```
#!usr/bin/Perl
use warnings;
use strict;
use Cwd;
use libraries::RemodellingRoutines::check_file;
use libraries::RemodellingRoutines::execute_ansys;
use File::Copy;
my $datestring = localtime();
print "Start Time: ", $datestring;
# ---------------------------------------------------------------------------- #
# 1. Run the first time step with a displacement of 2
# 2. Run the second step with a displacement of 4
# 3. Deploy the remodelling algorithm :)
# 4. This absolutely all that you need
# 5. Get the results done
# ---------------------------------------------------------------------------- #
my $time_counter = 0;
my $max_time = 11;
my $job_name_clean = "gr_step_";
my $job_name = "gr_step_".$time_counter;
my $python_file_name_gr = "gr_hgo_model.py";
my $input_file = 'ansys_job.inp';
my $file_stress = 'stress_list.txt';
my $file_strain = 'strain_list.txt';
my $file_homeo_stress = 'stress_list_0.txt';
my $file_homeo_strain = 'strain_list_0.txt';
my $material_values_homeo = "material_values_homeo.csv";
# Homeostatic Step
open(my $fh, '>', 'max_time.txt');
print $fh "max_time=".$max_time;
close $fh;
```

```
print "\nmax displacement file created\n";
system("python", $python_file_name_gr);
rename "material_values_0.csv", $material_values_homeo;
execute({
   input_file => $input_file,
   job_name => $job_name
});
my $exists_file_stress = check_file_existence({filename=>$file_stress});
my $exists_file_strain = check_file_existence({filename=>$file_strain});
# Rename stress, strain lists to _0.txt -> homeostatic state
if ($exists_file_stress){
   rename $file_stress, $file_homeo_stress;
   rename $file_strain, $file_homeo_strain;
   print "\n Homeostatic state Saved";
   # rename $file_nlist, "renamed_n_list.txt";
}
 #Total time for remodelling
$max_time = 16;
$time_counter += 1;
# Rename to a new step.
$job_name = "gr_step_".$time_counter;
open(my $fh2, '>', 'max_time.txt');
print $fh2 "max_time=".$max_time;
close $fh2;
print "max displacement file created\n";
system("python", $python_file_name_gr);
rename "material_values_0.csv", "material_values_1.csv";
execute({
   input_file => $input_file,
   job_name => $job_name
});
my $file_secondary_stretch_stress = 'stress_list_1.txt';
my $file_secondary_stretch_strain = 'strain_list_1.txt';
```

```
# Rename stress_list strain_list
if($exists_file_stress){
   copy($file_stress, $file_secondary_stretch_stress);
   copy($file_strain, $file_secondary_stretch_strain);
   print "\n Secondary Stretched Muscle State Saved";
}
#number of remodelling steps taken
$time_counter += 1;
my $step_limit = 20;
my $prev_material_values = "";
my $remodelled_material_values = "";
for(my $i = $time_counter; $i < $step_limit; $i++ ){
   # 1. Read in all the names
   # 2. $job_name to include "_rem_".$i; (if first step read in from
   #    second stage of stretch)
   # 3. renam stress, strain all results to "_rem_".$i;
   # 4. Feed that back into the next step
   # 5. Loop it up
   print "\n Step: ", $i;
   #my $file_mat_curr = "material_values_rem_".$i.".csv";
   my $file_mat_new = "material_values_rem_".$i.".csv";
   my $new_job_name = $job_name_clean."rem_".$i;
   if ($i == 2){
      $prev_material_values = "material_values_1.csv";
   } else {
      $prev_material_values = "material_values_rem_".($i-1).".csv";
   }
   # Remodelling Python Script
   system("python",
            "remodelling_hgo.py",
          $file_strain,
          $file_homeo_strain, # needs to be defined
          $file_stress,
```

```
            $file_homeo_stress, # needs to be defined
            $prev_material_values,
            "materials.inp",
            $file_mat_new,
            $material_values_homeo,
            "time_info.txt"
        );
        my $new_rem_stress_list = "stress_list_rem_".$i.".txt";
        my $new_rem_strain_list = "strain_list_rem_".$i.".txt";
            execute({
            input_file => $input_file,
            job_name => $new_job_name
        });
        if($exists_file_stress){
            copy($file_stress, $new_rem_stress_list);
        }
        if($exists_file_strain){
            copy($file_strain, $new_rem_strain_list);
        }
    }
```